Nonlinear stall-induced instability analysis of a parked rotor

Master Thesis

Jonas E. Lohmann

Delft University of Technology

TU Delft

Nonlinear stall-induced instability analysis of a parked rotor

by

Jonas E. Lohmann

to obtain the degrees of

Master of Science
in Wind Energy
at Technical University of Denmark

Master of Science
in Aerospace Engineering
at Delft University of Technology

To be defended on October 10, 2024

Supervisors:	Wei Yu	TU Delft
	Georg Pirrung	DTU
	Qingshen Meng	TU Delft
Defence committee:	Roland Schmehl	TU Delft
	Mac Gaunaa	DTU
Start date:	November 1, 2023	
End date:	September 11, 2024	
Student numbers:	s223685	DTU
	5856426	TU Delft

An electronic version of this thesis is available at
https://repository.tudelft.nl and https://findit.dtu.dk

The code written for this thesis is available on GitHub

Danmarks Tekniske Universitet DTU

TU Delft

DTU Wind and Energy Systems

Nonlinear stall-induced instability analysis of a parked rotor

Author:
Jonas Erik Lohmann
DTU Wind-M-0770
July 2024

Author:
Jonas Erik Lohmann

Title:
Nonlinear stall-induced instability analysis of a parked rotor

DTU Wind-M-0770
July 2024

ECTS: 45

Education: Master of Science

Supervisors:

Georg Pirrung
DTU Wind & Energy Systems

Wei Yu
Qingshen Meng
TUDelft

Remarks:
This report is submitted as partial fulfillment of the requirements for graduation in the above education at the Technical University of Denmark.

DTU Wind & Energy Systems is a department of the Technical University of Denmark with a unique integration of research, education, innovation and public/private sector consulting in the field of wind energy. Our activities develop new opportunities and technology for the global and Danish exploitation of wind energy. Research focuses on key technical-scientific fields, which are central for the development, innovation and use of wind energy and provides the basis for advanced education at the education.

Technical University of Denmark
Department of Wind and Energy Systems
Frederiksborgvej 399
4000 Roskilde
Denmark
www.wind.dtu.dk

Preface

In quieter moments, I am overwhelmed with gratitude thinking about the support I have received from people around me during the work on this thesis and the whole master's programme. Placing only my name in big letters on the title page does not do justice to everyone feeding my enthusiasm, listening to challenges I had, making me laugh, and making all of this worthwhile.

For this thesis, I am sincerely thankful for the effort my supervisors Wei, Georg, and Qingshen have consistently week after week put into the progress of my thesis. Your availability for my questions, curiosity, and challenges led me further than I would have ever managed myself. Thank you also for being open and flexible in letting me explore new thesis objectives not just once but twice. I understand that none of this is by any means something every student can take for granted.

To my friends: I am deeply in your debt to return energy and time spent together. It is again that I understand to not take for granted the patience I have received from you when my enthusiasm for the master's led to many late nights studying. I have learned from the experience and I am excited to for coming times together.

At last, I would not be here were it not for the two-and-a-half decades of incredible love, joy, and unconditional support from you, Jaki, Mama, and Papa. I cannot wait to see you in person again.

Jonas E. Lohmann
Copenhagen, September 2024

Abstract

Numerous dynamic stall models exist to improve aerodynamic modelling. As such, they play an integral part in aeroelastic analyses. In numerous publications, their qualitative damping effect on stall-induced instabilities of wind turbine blades compared to using quasi-steady aerodynamics has been proven. However, often different dynamic stall models are used without consideration of quantitative differences between aeroelastic predictions. Thus, the goal of this thesis is to quantify the damping effect of dynamic stall models on stall-induced instabilities. A model used in HAWC2, openFAST, one developed by IAG, and one unpublished model are compared amongst each other and in comparison to predictions with quasi-steady aerodynamics. A typical blade section at $75\,\%$ *span of the DTU* $10\,\mathrm{MW}$ *reference wind turbine is modelled. The blade the section belongs to is facing vertically up at a pitch angle of* $90°$ *in parked conditions. The inflow ranges from* $5\,\mathrm{m/s}$ *to* $50\,\mathrm{m/s}$ *with yaw-misalignment angles from* $-25°$ *to* $25°$*. In comparison to using quasi-steady aerodynamics, the dynamic stall model from openFAST reduces the amplitude of edgewise limit cycle oscillations from maxima of* $22.5\,\mathrm{m}$ *to* $7.2\,\mathrm{m}$*. The model from HAWC2 further reduces the maxima to* $5.4\,\mathrm{m}$*. No edgewise limit cycle oscillations occur using the IAG or unpublished model. Instabilities other than limit cycle oscillations are not predicted. Analyses of the time series of dynamic stall parameters, dynamic lift, drag, and moment power, as well as the unsteady force and moment coefficient loops and aeroelastic damping ratios, did not trivially explain the models' different predictions.*

Table of Contents

List of Figures

List of Tables

List of Algorithms

Abbreviations

Abbreviation	Description	Page List
DOF	degree of freedom	viii, 6, 7, 9, 48
DS	dynamic stall	viii–xii, 1–5, 8, 9, 13, 18, 20, 21, 23, 25, 29, 38, 39, 48, 55, 56, 58, 59, 64–66, 68–71, 86, 88, 90, 92–95, 97–99, 105–107
EOM	equation of motion	9–11, 17, 45, 108, 109
LCO	limit cycle oscillation	xii, 1, 13, 25, 42, 46, 47, 55, 56, 58–61, 63–66, 68–74, 93, 94, 96–99, 103, 105–107
OOP	object-oriented programming	7, 9
SIV	stall-induced vibrations	9

Nomenclature

Notation	Unit	Description	Page List
k	–	Reduced Frequency	38
C_d	–	Polar Drag Coefficient	17, 18, 24, 25, 38, 41, 48, 97
C_l	–	Polar Lift Coefficient	17, 18, 24, 25, 32, 35, 37, 38, 41, 96
C_m	–	Polar Moment Coefficient	17, 38, 48
C_n	–	Normal Force Coefficient	23–26, 29, 83
C_t	–	Tangential Force Coefficient	24, 25, 29, 40
$C_{d,\text{us}}$	–	Unsteady Drag Coefficient	3, 35, 40–42, 71–74, 76, 78, 80, 82, 83, 94–96
$C_{l,\alpha}$	–	Lift Slope	23, 24, 32, 39, 48, 93, 94, 97
$C_{l,\text{us}}$	–	Unsteady Lift Coefficient	3, 35, 40, 41, 71–74, 76, 78, 80, 82, 83, 94–96
$C_{m,\text{us}}$	–	Unsteady Moment Coefficient	40, 41, 83
$C_{n,\alpha}$	–	Normal Force Slope	23–25, 29
$C_{n,\text{i}}$	–	Impulsive Normal Force Coefficient	29
$C_{t,\text{p}}$	–	Potential Flow Lift Coefficient	32
$C_{t,\text{p}}$	–	Potential Flow Tangential Force Coefficient	29
$C_{t,\text{us}}$	–	Unsteady Tangential Force Coefficient	40
D_{ind}	N	Induced Drag	21

Notation	Unit	Description	Page List
D	N	Drag	15–18, 21, 51, 71–74, 76, 78, 80, 82, 83, 93, 95, 96
L_{cent}	N	Centrifugal Lift	21
L_{circ}	N	Circulatory Lift	21
L_{iner}	N	Inertial Lift	21
L	N	Lift	15–18, 21, 51, 71–74, 76, 78, 80, 82–84, 93, 95, 96
M_{aero}	N	Aerodynamic Moment	16–18, 71, 72, 76, 78, 80, 82, 96, 98
α^{HHT}	–	Damping Parameter For The HHT-α^{HHT} Algorithm	46, 47
$\alpha_{0,\text{l}}$	rad	Zero Lift Angle Of Attack	23, 32, 39
$\alpha_{0,\text{sEq}}$	rad	Equivalent Steady Angle Of Attack	32
α_{eff}	rad	Effective Angle Of Attack	ix, xi, 8, 20, 21, 25, 26, 29, 32, 35, 37, 41, 42, 49, 68, 72–74, 76, 78, 80, 82, 95–98, 103, 106
α_{qs}	rad	Quasi-steady Angle Of Attack	viii, ix, 11, 12, 18–22, 25, 29, 35, 37, 38, 41, 50, 60, 61, 72, 73, 84, 93, 94, 97, 98

Notation	Unit	Description	Page List
α	rad	Geometric Angle Of Attack	7–9, 11–13, 16–19, 24, 25, 32, 35, 40–42, 48, 58
$\boldsymbol{C}$	$\mathrm{N\,s\,m^{-2}}$ and $\mathrm{N\,s\,rad^{-1}}$	Damping Matrix In The xy Coordinate System	10, 45, 47, 48, 51, 56
$\boldsymbol{K}$	$\mathrm{N\,m^{-2}}$ and $\mathrm{N\,rad^{-1}}$	Stiffness Matrix In The xy Coordinate System	10, 17, 45, 47, 48, 51, 56
$\boldsymbol{M}$	$\mathrm{kg\,m^{-1}}$ and $\mathrm{kg\,m\,rad^{-1}}$	Mass (Inertia) Matrix In The xy Coordinate System	10, 47, 48, 51, 56
$\boldsymbol{f}_{\mathsf{aero}}$	$\mathrm{N\,m^{-1}}$	Aerodynamic Forces Vector	9, 17, 18
$\boldsymbol{f}_{\mathsf{ext}}$	$\mathrm{N\,m^{-1}}$ and N	External Forces And Moments Vector	10
$\boldsymbol{f}_k$	$\mathrm{N\,m^{-1}}$ and N	Structural Stiffness Force And Moment Vector	51
$\boldsymbol{u_0}$	$\mathrm{m\,s^{-1}}$	Wind Inflow Vector	11, 15, 16, 55
$\boldsymbol{u}$	$\mathrm{m\,s^{-1}}$	Quasi-steady Inflow Vector	12, 17
$\boldsymbol{x}$	m and rad	Positional Coordinates	10
γ	rad	Torsional Coordinate	9, 11, 13, 16–18, 45, 50
ϕ_{qs}	rad	Relative Quasi-steady Inflow Angle	11, 12
ϕ	rad	Wind Inflow (Here Also Yaw Misalignment) Angle	11, 12, 16–18, 48
ρ	$\mathrm{kg\,m^{-2}}$	Air Density	17
c	m	Chord	11, 17, 20, 23, 32, 38
f	$-$	Separation Point	viii, 23–25, 29, 35, 37
k_e	$\mathrm{N\,m^{-2}}$	Spring Stiffness Along e	11
k_f	$\mathrm{N\,m^{-2}}$	Spring Stiffness Along f	11
q	$\mathrm{N\,m^{-3}}$	Dynamic Pressure	17, 29, 32
u_0	$\mathrm{m\,s^{-1}}$	Wind Inflow Magnitude	viii, 12, 16, 29, 38–44, 48
u	$\mathrm{m\,s^{-1}}$	Quasi-steady Inflow Magnitude	12, 17, 19, 29

1 Introduction

In peer-reviewed scientific literature, anthropogenic-caused global warming is an undeniable reality of modern humankind (Lynas et al., 2021). On top of that, our energy demand, one of global warming's main contributors, is still expected to grow – amplifying existing challenges (Ruijven et al., 2019). Expanding the use of less climate-detrimental renewable energy sources is evident and ample research has been done on the transition thither. A key journal paper by (Gielen et al., 2019) argues that two-thirds of the world's energy demand can be supplied by renewable energies with wind energy providing the second biggest amount (24% of renewable energies). Exponential growth in installed wind turbine capacity (33 years for the first installed Terra Watt, 10 years for the second) based on engineering, social, and political advancements back that claim (Hutchinson et al., 2023).

However, especially wind turbine blades face climatological drawbacks such as using Balsa wood from the Amazon (Behrend, 2022), being hard to impossible to recycle (P. Liu et al., 2017), and requiring sophisticated and expensive repairing techniques to ensure their lifetime demands (Mishnaevsky, 2023). Meanwhile, (Nijssen et al., 2023) argues that the design of a blade is governed by fatigue and with it the amount of material required. As such, understanding the causes of fatigue in wind turbine blades may allow for a material reduction (Wang et al., 2016; Serafeim et al., 2022). Besides flutter and turbulent wind conditions, one important cause of fatigue damage is stall-induced instabilities (Holierhoek, 2023) during parked or idling conditions, which have lacked academic attention for modern multi-watt scale wind turbines. To combat the gap in the understanding of this phenomenon, the present thesis applies a fully non-linear time domain approach to shine light into the process of stall-induced instabilities and contemporary modelling limits thereof.

1.1. Research Questions

The research questions are substantiated in the literature review of Chapter 2. However, to aid the reader interested primarily in the results based on the thesis title, the research questions are stated up front. Questions 1.(a)–(c) are briefly investigated. Questions 2.–3.(b) are the primary focus. A complete answer to question 3.(c) exceeded the scope of the thesis. The conclusion can be found in Chapter 7.

1. What influence does using a dynamic stall model have on stall-induced instabilities of a blade section compared to using quasi-steady aerodynamics on
   (a) the inflow conditions causing unstable behaviour (instability regions),
   (b) the amplitude of anticipated limit cycle oscillations, and
   (c) the relative flow conditions during instability.
2. Can well-known and widely-used dynamic stall models be used to accurately simulate stall-induced oscillations?
   (a) If they predict instability, do the flow conditions remain in the model's validity range?

3. How do different dynamic stall models compare in aeroelastic damping?
   (a) What are the inflow conditions causing unstable behaviour?
   (b) What kind of instability do the models predict?
   (c) Which parts of each model's internal working cause differences and which cause similarities?

1.2. Document structure

For ease of navigation in this document, numerous hyperlinks are used. This includes all obvious references, important parameters in equations (linking to their definition in the nomenclature), and between paragraphs in Chapter 5. Additionally, long sections have individual abstracts to present information compactly for the reader who is interested only in the most crucial facts.

2

Literature Review

In this chapter, the baseline literature behind the objectives of the thesis is presented. This includes a brief history of the research on stall-induced instabilities of wind turbine blades, research on these instabilities during parked conditions of the wind turbine, and finally a direction to important publications investigating dynamic stall.

2.1. Stall-induced instability

The investigation of stall-induced instabilities on wind turbines dates back to before the 21st century. First, it occurred during the operation of stall-regulated wind turbines. With modern larger variable-pitch speed-regulated wind turbines, it became of concern during parked conditions. Insights from the literature are given in the next two sections.

2.1.1. General

The analysis of nonlinear stall-induced instabilities spans aspects of aeroelasticity, unsteady aerodynamics, structural modelling, and eigenvalue analysis in the linear and structural time integration in the nonlinear case. One of the first accounts of stall-induced instabilities, even though the cause was unknown then, was given by Moeller, 1997. Blades hit the tower and broke off during operation due to edgewise oscillations. Already then was it realised that the problem gained severity the longer the blades.

Following the incidents, research on the topic quickly gained traction. Petersen et al., 1998 developed a linearised analytical quasi-steady model for the 2D aeroelastic behaviour of a blade section. He concluded the main parameters controlling the vibrations are

1. the aerodynamic and structural characteristics of the blade (section),
2. the orientation of the principle bending axes, and
3. the properties of the supporting structures.

The first point includes especially the unsteady drag coefficient and unsteady lift coefficient behaviours and the mode shapes. The list underpins the multidisciplinary nature of stall-induced vibrations and the importance of analysing the whole wind turbine. However, the most fundamental finding is that during stall-induced vibrations, the aerodynamic forces supply energy to the structural oscillations, effectively acting as negative damping. Chaviaropoulos, 2001 extended the analysis by incorporating nonlinear effects to show that linearisation weakens the aerodynamic damping, resulting in too conservative approximations. To his surprise, quasi-steady aerodynamics yielded the highest damping compared to steady and unsteady cases. However, no structural damping was incorporated, the blade had a length of $17\,\mathrm{m}$ and belonged to a stall-regulated wind turbine, and no insights into the causes for larger damping applying non-linear, unsteady aerodynamics was given. Working on analysing the whole turbine, M. H. Hansen, 2003 published a linearised analytical quasi-steady model of a rotating wind turbine with which he substantiated the importance of incorporating the entire turbine. He did so by showing the

strong effects of the dynamics of the shaft, nacelle, and tower on the blade vibrations. Additionally, he explained that edgewise vibrations are aerodynamically less damped than flapwise vibrations and urged researchers to consider structural damping, too. A year later, Riziotis et al., 2004 backed the notion that linear models are too conservative but otherwise focused on a rotating wind turbine. However, already in 2004, they noted that the emergence of lighter blades thanks to advancements in fabrication and materials caused reduced structural damping – a trend still present today (Naeini et al., 2020). Approaching the end of the '00s, M. H. Hansen, 2007 summarises previous work on stall-induced vibrations and emphasises the above-listed findings of Petersen et al., 1998. Additionally, utilising a linearised aerodynamic force expression, he deduces that the aerodynamic damping is linearly proportional to the relative velocity (instead of the usual squared dependence for aerodynamic forces), drag always acts as positive damping, and negative lift gradients lower damping. At last, Chaviaropoulos et al., 2009 applied a fully unsteady aerodynamic model (based on the ONERA model) to edgewise stall-induced vibrations for an isolated blade. They analysed yaw-misalignment angles of $-20°$ to $40°$ and found that unsteady aerodynamics do not always increase the damping. However, no explanation was given.

The above research laid the foundation for stall-induced instabilities. However, as was the state of the art then, all of the analyses were done for stall-regulated rotating turbines, individual blades (sections), or using linearised theory. Analysis of instabilities during parked conditions was missing and instead was focused on stall-induced instabilities during normal operation (Wang et al., 2016).

2.1.2. Of the parked rotor

Wang et al., 2016 marks a paper on the research on the stall-induced instability of idling, modern-scale wind turbines. In their paper, they used the nonlinear time-domain model hGAST to investigate which yaw angles must be reached before stall-induced instabilities begin. Their model implemented finite element models for the blades, drive train, and tower as individual beam elements. They then used a linear model to calculate the mode shapes and eigenfrequencies at certain yaw angles to shed light onto the physics of the stall-induced instabilities. Subsequently, a blade motion was simulated based on a mode shape and frequency belonging to the blade to calculate the work done by the fluid flow. However, the imposed amplitude of the mode shape was $0.2\,\mathrm{m}$ at the tip of the DTU $10\,\mathrm{MW}$ reference wind turbine. In comparison, Totsuka et al., 2016 showed $6\,\mathrm{m}$ tip deflections of the same turbine. The analysis of Wang et al., 2016 is thus missing strong unsteady aerodynamic effects. This can be seen by their dynamic angle of attack having ranges of only $5°$ to $10°$.

Zou et al., 2015 developed a medium-fidelity free vortex wake model that is connected to a non-linear aeroelastic solver for a blade section. The vortex wake is allowed to detach at the trailing and leading edge. Their objective is to investigate vortex-induced and stall-induced vibrations. However, they only run simulations for yaw-misalignment angles of $\approx 90°$, skipping the $\pm 15°$ yaw-misalignment that occur during normal operation (Wang et al., 2016).

A flutter analysis of a parked floating wind turbine was performed by Naeini et al., 2020. A single blade is modelled that is allowed to bend and twist as a non-linear Euler-Bernoulli beam. The governing equations were obtained by coupling the Ritz method with the Lagrange equations. Theodorsen's theory of unsteady aerodynamics was used to model the aerodynamic forces and moment. In the end, the objectives focus on the influence of the floater motion on the flutter instability regions.

Wu et al., 2024 are that at high angles of attack, classical engineering methods like the blade element momentum theory fail to be accurate. Thus, they introduce a high-fidelity model in which they couple the geometrically accurate beam theory as the structure with computational fluid mechanics for the external forces. Their objectives are investigating the effect of different turbulent intensities and gravity on a single blade and a three-bladed rotor for $0°$ yaw-misalignment. For an inflow of $35\,\mathrm{m/s}$, they show edgewise oscillations for all blades of the rotor. Two blades are pitched to $90°$, one blade is pitched to $50°$. They find that gravity has an increasing and higher turbulence a decreasing effect on the edgewise oscillation amplitude. However, no insights into the development of the oscillations are given.

More research on stall-induced instabilities exists but few investigate the effects of changes in the dynamic stall modelling. Totsuka et al., 2016 used HAWC2 and FAST for time domain simulations with turbulent inflow to showcase that stall-induced instability of the DTU $10\,\mathrm{MW}$ can come from higher-order

structural modes. Jiang et al., 2014 used HAWC2 for the NREL $5\,\mathrm{MW}$ reference wind turbine to analyse the transient behaviour and its impacts on stability for shutdown events. Kwan, 2017 revisited Petersen et al., 1998's analytical model to adapt it from its original formulation for a rotating turbine to that of a parked turbine. In doing so, Kwan showed critical instability ranges for the yaw, rotor azimuth, and blade pitch angle and compared them to results obtained from a PHATAS model. His research emphasised the importance of investigating stall-induced instabilities having shown the conditions under which they arise while not addressing the underlying physics. Finally, W. R. Skrzypiński et al., 2014 showed using 2D RANS and 3D DES simulations the differences in aerodynamic stability limits between 2D and 3D conditions.

One contribution analysing the influences of changes in the dynamic stall modelling on blade vibrations was done by W. Skrzypiński et al., 2014. Other than analysing the influences of added mass terms, spring constant values, inertial heave-pitch coupling, and different aerodynamic polars on stall-induced vibrations, they alter the degree of lag the aerodynamic forces experience in unsteady conditions. Like other publications, they show how unsteady effects (by adding the lagging) can increase the aeroelastic damping significantly.

Even though the importance of incorporating unsteady aerodynamics into the investigation of stall-induced instabilities has been stated numerous times, no direct comparison of different dynamic stall models' influences on stall-induced vibrations could be found. In the literature, existing dynamic stall models are often implemented as a means to an end to analyse aeroelastic phenomena or to validate new dynamic stall models. Of course, this is a part of what they are intended to be used for. However, in the complex domain of aeroelasticity, small changes in the aerodynamic behaviour might result in significant changes in the aeroelastic behaviour. On one hand, aeroelastic tools like HAWC2 and openFAST (both tools are capable of a lot more than "just" aeroelasticity), offer many different dynamic stall models for aeroelastic simulations. On the other hand, researchers developing new dynamic stall models often only validate their new models against existing models based on the prediction of unsteady force and moment coefficients. For both cases, it would be valuable to have a direct comparison of the influences of the models on the aeroelastic behaviour. As such, a dynamic stall model from HAWC2, openFAST, an unpublished model intended to be used for the aeroelastic tool described in Meng et al., 2024, and a recently published model by Bangga et al., 2020 will be implemented and compared for their influence on the aeroelastic behaviour of a blade section.

2.2. Dynamic Stall

This section does not function as a complete explanation of the background knowledge for dynamic stall. Rather, it redirects the reader to sources explaining different aspects of it.

Bangga et al., 2020 gives a good overview of the phenomena involved in dynamic stall modelling and points to many well-known models. These include the Beddoes-Leishman (Leishman et al., 1989), Snel (Snel, 1997), ONERA (Tran et al., 1980), Boeing-Vertol (Tarzanin, 1972), and Øye (Øye, 1991) models. Another model that is extensively used in this thesis was published by (Morten Hartvig Hansen et al., 2004). It lies the foundation for the HAWC2 and openFAST models implemented for this thesis. For HAWC2, the correction from Pirrung et al., 2018 is added in comparison to the original model from Morten Hartvig Hansen et al., 2004. For openFAST, the original Morten Hartvig Hansen et al., 2004 model is changed as described in Branlard et al., 2022. Each publication can be used to learn about the implementation of the respective model.

Coincidentally, Bangga et al., 2020 is one of the few publications comparing fundamentally different dynamic stall models. They, too, developed a new model that tries to fit to higher harmonics of the unsteady drag, lift, and moment coefficient loops. As a consequence, their dynamic stall shows strong oscillations in each of the coefficient loops. Another comparison of dynamic stall models is given in Holierhoek et al., 2013. They found that different models predict vastly different unsteady loops and critique what this thesis tries to investigate: different dynamic stall might predict completely different aeroelastic behaviour. The paper by Holierhoek et al., 2013 is a good source for an overview of the dynamics related to dynamic stall, too. Lastly, another summary of the Beddoes-Leishman, Snel, and ONERA model (equations with brief explanations) can be found in Khan, 2018.

3

Set-up

This chapter goes to length explaining the implementation and validation of the blade section model that is used to research the thesis objectives. First, a holistic view of the software to research the thesis objectives is presented. An overview of the model's capabilities and the coding approach is given. Afterwards, the later so-called "section" model is detailed. This includes the definition of all aerodynamic, structural, and time integration algorithms and their validation. Post-processing algorithms are defined and validated, too.

Additional effort was put into concisely presenting the algorithms. In the best case, new and other researchers can benefit from them if they are interested in using one of the described algorithms.

3.1. Overview: coding approach, code structure, capabilities, and limitations

Section 3.1 abstract

The code was written focusing on modularity, conciseness, and sufficient comments. It is structured into five parts: project-wide defaults and utilities, the aeroelastic simulation tool, post-processing, plotting, and combining the previous four parts. The "section" model can simulate two-dimensional blade section aeroelastic behaviour for three degrees of freedom with inertial, damping, and stiffness coupling, and steady, quasi-steady, or dynamic stall-extended aerodynamics. Five dynamic stall models are implemented. Time integration is performed with an adapted HHT–α algorithm. A variety of post-processing and plotting capabilities are available. The model's limitations regarding real-world wind turbines are largely due to the 2D modelling approach and the accuracy of dynamic stall models for large effective angles of attack.

During the development of the model, significant emphasis was placed on writing clean, modular, and well-documented code, following object-oriented programming principles. This approach was chosen to ensure the code's adaptability, clarity, and reusability.

Modular code was prioritised to facilitate adjustments and repurposing. By establishing general input and output interfaces, a single block of code can be reused across various applications. It also simplifies the addition of new functionalities, which proved particularly beneficial in accommodating the numerous objective changes that required additional aerodynamic algorithms. Modular code furthermore enhances the ability to connect different functionalities consistently and predictably. This consistency reduces integration challenges, although it can introduce some overhead in developing "adaptors" between different parts of the code. Likewise, modularity ensures work done in this thesis can be easily transferred to other projects, provided the other interfaces are clear, and it supports unit testing on indi-

vidual components. However, modularity can increase the abstractness of core functionalities, as the code inside of modules may become distanced from direct input due to the abstraction layers. This can complicate both coding and future modifications, although this level of abstraction is often necessary in larger projects. Additionally, while establishing robust input/output interfaces can be time-consuming, the process often leads to more generalised and flexible core functionalities, which is beneficial in the long term. Lastly, negative changes to one module can impact all connected parts. Still, this risk is limited by implementing thorough unit testing.

Including insightful comments throughout the code was another key strategy to enhance understanding, particularly for complex or abstract sections. Well-documented code aids both the original developer and new users, especially when dealing with non-self-explanatory segments critical to the overall project structure. While writing these comments does require additional time, this investment is offset by the time saved during future code reviews and modifications.

Coding separate modules allows their reuse at relevant and potentially multiple parts; each functionality should ideally be only coded once. This prevents the project from becoming bloated as functionalities are reused, rather than rewritten, in different parts of the code. It also centralises updates, as any changes to a functionality need to be made in only one location. However, this approach can again introduce greater abstractness, and if a single case within a functionality needs to be modified without affecting others, the code may require further abstraction to handle individual cases separately.

Finally, object-oriented programming aided a clear structure for the code. object-oriented programming enables methods and attributes to be easily passed around via inheritance or instances, both within and outside of classes, leading to better-encapsulated code. This encapsulation helps define the scope and function of code segments more clearly, with a direct and understandable connection between objects and the methods that operate on them. While object-oriented programming can be intimidating for those unfamiliar with the approach, it is widely adopted in many modern programming languages, making it a valuable skill. Python, in particular, offers significant flexibility in how classes are used. While sometimes leading to more abstract code it allows for extensive generalisation of functionalities.

In conclusion, the advantages of investing time and effort into writing clean, well-documented, and modular code, utilising object-oriented principles, significantly outweigh the drawbacks.

A clear project structure is essential for clean code. To achieve this, the top-level code blocks were divided into five primary functionalities, as illustrated in Figure 3.1. This separation helps isolate the scope of each functionality, clarifying where and how each part of the code should be used. It also provides a clear, intuitive flow of information, making it easier to identify where to add new functionalities. However, this approach increases the number of files, though it is preferable to have more, smaller files than fewer, larger ones. Additionally, while establishing an initial structure requires effort, this process prompts early consideration of interfaces, which is beneficial in the long run. A poorly designed structure can hinder code development and usage, but regular evaluation and restructuring can mitigate this risk. Organising the top-level functionalities as shown in Figure 3.1 and their sub-files, the project structure promotes clean, maintainable code.

After all, it is the capabilities of code that make it useful. The functionalities directly related to the aeroelastic simulation and evaluation are briefly stated below. Further details are given in the respective Sections 3.2 to 3.5 and 3.7.

The model simulates time-domain aeroelastic behaviour in two dimensions, featuring three degrees of freedom (DOFs): two translational along perpendicular inertial axes and one rotational around a non-inertial axis that moves with the object. The aerodynamic behaviour can be steady, quasi-steady, or selected from five dynamic-stall models. Structural behaviour is modelled using a spring and damper for each DOF, with their forces acting along the direction of the corresponding axis. The model also allows for inertial, damping, and stiffness coupling. Time integration is handled using either an explicit Euler or an adapted HHT–α^{HHT} method. The method's α is usually named without the "HHT" superscript. It is added to avoid confusion with the geometric angle of attack (α). Each DOF can be individually set to a predetermined motion, and inflow conditions can vary over time. Most parts of the simulation and post-processing support adaptive time steps.

Automated multi-processing exists for simulations and post-processing for different combinations of

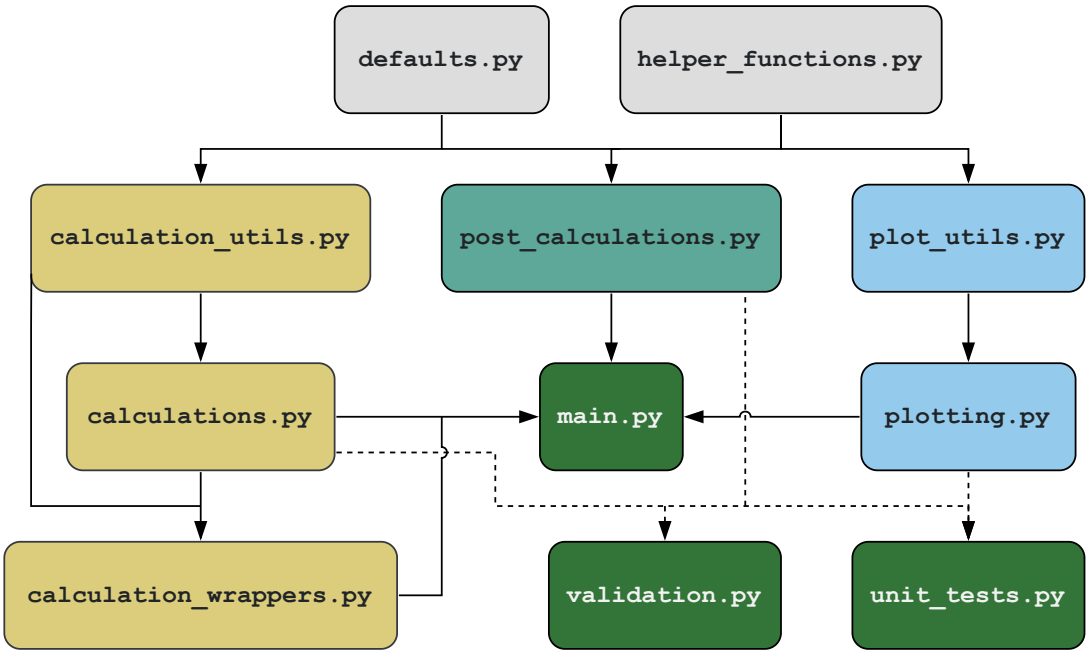

Figure 3.1: Top-level information flow of the developed software between different Python files. Arrows indicate the passing of classes (majority), stand-alone functions (few), and value definitions (rare). Five collections are highlighted by colour. Each collection serves a top-level task: setting defaults and core-level utilities for the whole code (grey), defining the aeroelastic analysis tool (ocker), post-calculations (turquoise), plotting (blue), and connecting all functionalities (green), respectively. Solid/dashed lines indicate information flow during normal/validation operations, respectively.

wind speed and yaw angle in free simulations (with no constraints on movement). The yaw angle here is synonymous to the geometric angle of attack of the blade section. The blade the section is taken from is assumed to point vertically up with a pitch of $90°$, i.e., the leading edge is facing into the incoming wind for a yaw angle of $0°$. Similarly, for simulations where movement is constrained to be cyclic, parallel simulations and post-processing are possible for different oscillation amplitudes and yaw angles. The model also allows for saving of full or partial time series of any simulation parameter. Energies, powers, and forces are calculated in both the inertial axis directions and the edgewise and flapwise directions. Structural, aerodynamic, and aeroelastic damping coefficients can be calculated over time.

Visualisation is supported through preconfigured plots and animations for positions, forces, energies, powers, and dynamic stall parameters using matplotlib with a full LaTeX backend or matplotlib's in-house MathTex. The model includes a predetermined plot for aeroelastic damping coefficients over oscillation amplitude, highlighting regions where the effective angle of attack exceeds various threshold values. Additionally, any combination of simulation parameters can be displayed using Lissajous curves with time encoded as a colour gradient of the curve. Consequently, the developed software has extensive capabilities for simulating 2D aeroelastic behaviour and visualising the data.

3.2. 2D aeroelastic blade "section" model

Section 3.2 abstract

The custom “section” model was developed because it was unclear whether academic/industrial tools could quickly simulate what is needed for the objectives and learning purposes. The model consists of a lumped mass with rotational inertia, two translational dampers and springs (oriented parallel to Euclidean axes), and a torsional damper and spring. The equation of motions are stated and the choice for the direction of the springs and dampers is given. Steady and quasi-steady flow angles and magnitudes are defined in this section. The “section” model code was developed with an emphasis on structure, object-oriented programming, and was coded in three layers of abstractness. This automates core functionalities, eases adding aeroelastic algorithms, and provides an intuitive interface for the user. At last, an algorithm to calculate the steady state with or without heave-pitch stiffness coupling and with or without a pre-defined geometric angle of attack is given.

The aeroelastic model created for this thesis is, for its descriptiveness, called “section”. Any plot lines labelled with “section” refer to data created with it. In Figure 3.1, the “section” model comprises the leftmost (ocker) collection (`calculation_utils.py`, `calculations.py`, and `calculation_wrappers.py`) and parts of `defaults.py`.

The choice to develop a custom model is based on the consideration of available aeroelastic tools. According to the objectives, the used model should simulate realistic wind turbine section behaviour with limited influential parameters, while maintaining a low computational cost (monetary, time, and environmental). Very high-fidelity 3D Computational Fluid Dynamics and medium-fidelity free-vortex-type simulations encompass a vast variety of influential parameters and a high computational cost, both outside the scope of this project. Thus, these approaches were discarded. The same issue applies to the medium-fidelity free-vortex wake model QBlade. If the results of this thesis argue for higher fidelity simulations, they can be used next. Multi-body tools like HAWC2 or openFAST that use the Blade Element Method and already provide dynamic stall models match the objectives closer. However, no information about simulating 2D blade sections using either tool could be found. Additionally, it was uncertain if every parameter of the simulation’s calculation could be accessed. This is important to determine the reasons for the potentially different simulation responses when using different dynamic stall models. Hence, a custom model was developed that is explained subsequently.

The “section” model uses a low-fidelity approach that is purposefully just able to simulate non-linear stall-induced vibrations as argued in the paragraph above. This encompasses linear modelling of structural damping and stiffness, non-linear time integration, and using non-linear dynamic stall models for the calculation of the aerodynamic forces and moment. For the analysis of induced vibrations in stall, Petersen et al., 1998 showed that negative aerodynamic damping can already occur for an airfoil solely allowed to move in edgewise direction (1D). However, in the same paper, the authors also stress the importance of allowing the airfoil to move in another direction than purely edgewise. Thus the “section” model received two translational degrees of freedom. A torsional degree of freedom was also added owing to the torsional flexibility of modern and upcoming, large wind turbines, that have shown torsional steady-state deflections up to $5.5\,°$ (Zahle et al., 2024). The degrees of freedom in this model are directly or indirectly coupled. Direct coupling here refers to inertial, damping, or stiffness coupling. Indirect here refers to the coupling that, all through aerodynamic forces vector (f_{aero}), arises because translational movement influences the torsional coordinate, which itself affects translational movement again. Even if torsional coordinate was fixed, translational movement affects f_{aero} which, in return, influences the translational movement again. The model performs discrete time integration of the three equation of motions derived from Figure 3.2, with the inclusion of external aerodynamic forces. The airfoil is modelled as a lumped mass with additional torsional inertia, damping, and stiffness. The damping and stiffness are linear, acting along the axes for forces and around the axis for the moment, as indicated by their respective indices. The springs are undeformed when their corresponding axis coordinate is zero. External aerodynamic forces are based on the airfoil’s polar, with modifications according to the chosen aerodynamic model (steady, quasi-steady, or dynamic stall), without considering induction

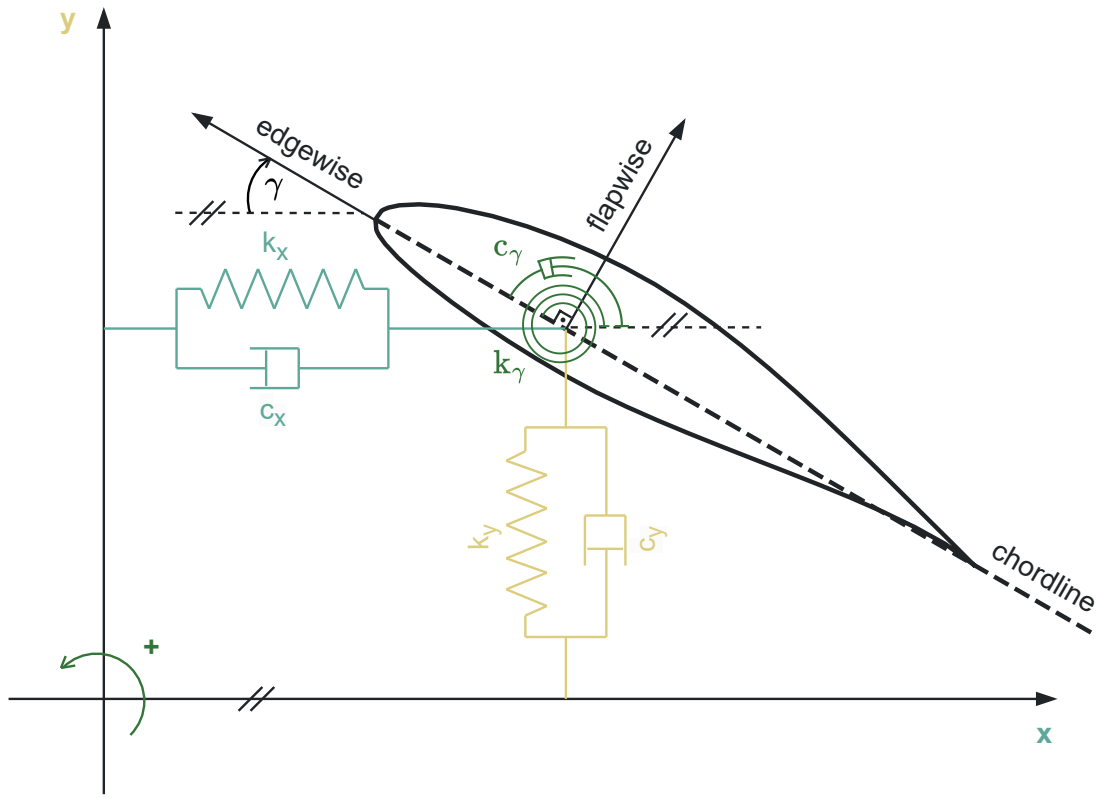

Figure 3.2: Schematic of the “section” model. The x- and y-axes create a Cartesian coordinate system. An additional γ-axis specifying rotation is placed on the chord line following the right-hand rule. Unless otherwise stated, it points through the quarter-chord point. The coordinate γ is measured from a line parallel to the x-axis to the chord line. Thus, in this schematic, $\gamma < 0$. The translational springs and dampers act parallel to the axes indicated by their index. The rotational spring’s and damper’s moment act around the γ-axis. The directions edgewise and flapwise are parallel and normal to the chord line, respectively.

effects from aerodynamic forces on the flow. With this setup, the model employs fundamental modelling approaches while accommodating self-induced vibration behaviour.

The equation of motions in their most general form used in this thesis are

$$\boldsymbol{M}\ddot{\boldsymbol{x}} + \boldsymbol{C}\dot{\boldsymbol{x}} + \boldsymbol{K}\boldsymbol{x} = \boldsymbol{f}_{\text{ext}} \tag{3.1}$$

$$\boldsymbol{x} = \begin{bmatrix} x \\ y \\ \gamma \end{bmatrix}, \quad \boldsymbol{f}_{\text{ext}} = \begin{bmatrix} f_{\text{aero},x} \\ f_{\text{aero},y} \\ M_{\text{aero}} \end{bmatrix} \tag{3.2}$$

$$\boldsymbol{M} = \begin{bmatrix} m & 0 & 0 \\ 0 & m & mr_{\text{cg}} \\ 0 & mr_{\text{cg}} & I \end{bmatrix}, \quad \boldsymbol{C} = \begin{bmatrix} C_{xx} & C_{xy} & C_{x\gamma} \\ C_{yx} & C_{yy} & C_{y\gamma} \\ C_{\gamma x} & C_{\gamma y} & C_{\gamma\gamma} \end{bmatrix}, \quad \boldsymbol{K} = \begin{bmatrix} K_{xx} & K_{xy} & 0 \\ K_{yx} & K_{yy} & K_{y\gamma} \\ K_{\gamma x} & K_{\gamma y} & K_{\gamma\gamma} \end{bmatrix} \tag{3.3}$$

with the mass (inertia) matrix in the xy coordinate system ($\boldsymbol{M}$), the damping matrix in the xy coordinate system ($\boldsymbol{C}$), the stiffness matrix in the xy coordinate system ($\boldsymbol{K}$), the positional coordinates ($\boldsymbol{x}$), and the external forces and moments vector ($\boldsymbol{f}_{\text{ext}}$). Dots over variables indicate differentiation in time. Hence, $\dot{\boldsymbol{x}}$ and $\ddot{\boldsymbol{x}}$ are the airfoil’s velocity and acceleration, respectively. Bold capital letters denote matrices, and bold lowercase letters vectors. The indices x, y, and γ (or combinations thereof) specify components in the respective direction (or coupling between the combined axes). This relation applies to letters that have a bold pendant. The displacements $\begin{bmatrix} x & y & \gamma \end{bmatrix}^T$. They are components of $\boldsymbol{x}$ without an additional index. This also holds for the time derivatives of $\boldsymbol{x}$. Most calculations performed do not include inertial or structural coupling, see Table 3.1. Then, $\boldsymbol{M}$, $\boldsymbol{C}$, and $\boldsymbol{K}$ are diagonal matrices.

Inertial and structural coupling can be intentional or indirect. Intentional coupling is done by setting

Table 3.1: Overview of the inertial and structural coupling applied throughout the thesis.

modelling of	Chapter 5: main results	Section 3.6: aeroelastic validation	Appendix B: body-fixed damping and stiffness
inertia	uncoupled	heave-pitch coupled	uncoupled
damping	uncoupled	uncoupled	lead/lag-pitch and heave-pitch coupled
stiffness	uncoupled	uncoupled	lead/lag-pitch and heave-pitch coupled

off-diagonal elements of the respective matrices to non-zero values. However, to reduce the number of influential parameters, the “section” model does not include inertial or structural coupling in the main investigation. Indirect structural coupling lies in the orientation of the structural damping and stiffness forces. As shown in Figure 3.2, the translational dampers and springs act parallel to their respective axes. Considerable effort was devoted to determining whether this approach or modelling them along the edgewise/flapwise directions was more realistic and suitable. Intuitively, the damping and stiffness forces should align with the edgewise/flapwise directions, reflecting the structural characteristics of the section. However, this approach introduces several complex phenomena:

1. If the airfoil is pinned to a point away from the origin, the approach from Figure 3.2 has one stable torsional coordinate (γ), $\gamma = 0\,°$. Without a torsional spring, all γ are neutrally stable. Defining the springs and dampers in edgewise and flapwise direction, choosing different values for the spring stiffness along e (k_e) and spring stiffness along f (k_f), and adding a torsional spring again, the stable γ is not $0\,°$. Furthermore, without the torsional spring, there is one stable, one unstable, and no neutrally stable γ.
2. Certain movements in the inertial xy coordinate system remain undamped despite the presence of damping.
3. Damping forces in x and y direction are influenced by the rotational velocity $\dot{\gamma}$.
4. Although the total damping work continues to always dissipate energy, individual components in the x or y directions can add energy.

The damping matrix in this alternative model would be fully populated, with six unique entries, and the stiffness matrix would have seven non-zero elements, six of which are unique. Given the complexity this introduces, it was decided against this modelling approach to minimise the number of phenomena under consideration. Furthermore, reducing the structural parameters of an entire blade to a section is unlikely to be as straightforward as assuming constant edgewise/flapwise stiffness and damping under torsional deformation. A derivation of the matrices and simulations demonstrating the listed behaviour is provided in Appendix B. To summarise, except where noted in Table 3.1, no inertial or structural coupling is modelled in this thesis; the inertial, damping, and stiffness matrices are then all diagonal.

Next, the basic aerodynamic equations needed for the “section” are explained. The involved angles and flow components are defined in Figure 3.3. Focusing on the angles (left side), the relations

$$\alpha = \phi - \gamma \tag{3.4}$$

$$\alpha_{\text{qs}} = \phi_{\text{qs}} - \gamma \tag{3.5}$$

are found for the geometric angle of attack (α) and quasi-steady angle of attack (α_{qs}) with the wind inflow (here also yaw misalignment) angle (ϕ) and relative quasi-steady inflow angle (ϕ_{qs}). Note the opposing measurement directions for positive angles between the aerodynamic and structural angles. Relating the blade section to a full rotor, $\gamma = 0°$ equals a twist-less blade pitched to $90\,°$. I.e. if a rotor is at stand-still without yaw-misalignment or any other influences on the blade’s positioning, e.g. cone, shaft tilt, etc., the chordline is parallel to the wind direction. γ is known from the time integration of the equation of motions. The ϕ and ϕ_{qs} are calculated from the velocities and their components shown on the right side of Figure 3.3. The wind inflow vector ($\boldsymbol{u_0}$) is due to wind, $\dot{\boldsymbol{\gamma}}\boldsymbol{r}_{\text{rot}}$ is due to the torsion rate of the airfoil, and $\dot{x}$ and $\dot{y}$ due to the translational velocity of the airfoil. Unless otherwise stated, $r_{\text{rot}} = 0.5c$ with the chord (c). This stems from defining the torsion around the quarter-chord point and measuring

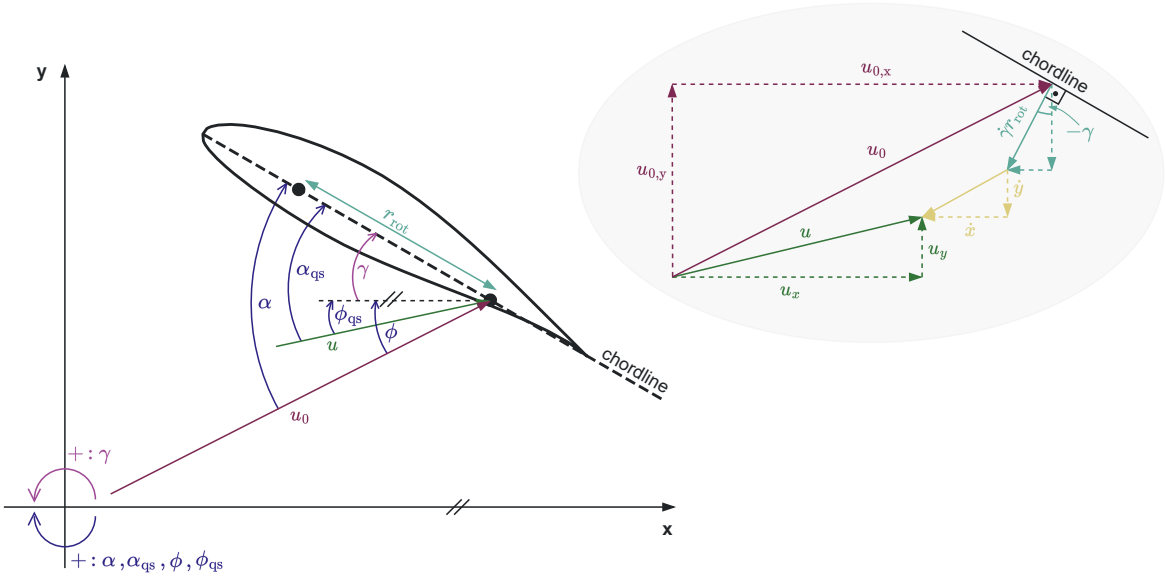

Figure 3.3: Basic angles, flow directions, and flow quantities of the "section" model. Flow quantities that are immediately available during the simulation (from inputs or simulation results) are denoted by their vectors. Vectors without named flow quantities require further calculations. The two black dots on the chordline display the quarter- and three-quarter-chord. The direction of positive measurements for the angles is shown at the origin. The direction of measurement for the angles is shown by their arrows. Thus, in this schematic, $\alpha > 0$, $\phi > 0$, and $\gamma < 0$.

ϕ_{qs} at the three-quarter-chord point. Adding these velocities yields the quasi-steady inflow vector ($\boldsymbol{u}$):

$$\boldsymbol{u} = \boldsymbol{u_0} + \dot{\boldsymbol{\gamma}}\boldsymbol{r}_{\text{rot}} + \dot{\boldsymbol{x}} \tag{3.6}$$

$$= \begin{bmatrix} u_{0,\text{x}} \\ u_{0,\text{y}} \end{bmatrix} + \dot{\gamma} r_{\text{rot}} \begin{bmatrix} \sin(-\gamma) \\ \cos(-\gamma) \end{bmatrix} + \begin{bmatrix} -\dot{x} \\ -\dot{y} \end{bmatrix} \tag{3.7}$$

$$\boldsymbol{u} = \begin{bmatrix} u_x \\ u_y \end{bmatrix} = \begin{bmatrix} u_{0,\text{x}} + \dot{\gamma} r_{\text{rot}} \sin(\gamma) - \dot{x} \\ u_{0,\text{y}} - \dot{\gamma} r_{\text{rot}} \cos(\gamma) - \dot{y} \end{bmatrix}. \tag{3.8}$$

Comparing the right and left side of Figure 3.3 shows that ϕ and ϕ_{qs} lie between the wind inflow magnitude (u_0) and $u_{0,\text{x}}$, and between the quasi-steady inflow magnitude (u) and u_x, respectively. Thus

$$\phi = \arctan\left(\frac{u_{0,\text{x}}}{u_{0,\text{x}}}\right), \text{ and} \tag{3.9}$$

$$\phi_{qs} = \arctan\left(\frac{u_x}{u_y}\right). \tag{3.10}$$

This concludes the calculations of $\boldsymbol{u}$, α, and α_{qs} which will lay the foundation for the aerodynamic calculations in Section 3.3.

As argued in Section 3.1, the code was developed with an emphasis on structure. To facilitate this, three abstractness levels of the code exist: user, developer, and core developer (sorted from intuitive to abstract). The user is presented with a pipeline of a few sensible steps to set up and run a simulation. The developer implements simulation algorithms, meaning any algorithm that calculates aerodynamic or structural forces or performs time integration. The core developer enforces the input/output interfaces for the simulation algorithms by means of Python's abstract base classes, defines the data handling before, during, and after a simulation, and catches errors for the developer while providing meaningful error messages. As a result, adding a new algorithm to the simulation solely requires the definition of the algorithm (and its initialisation if required) and naming the variables of the algorithm that should be saved. At no point does the core simulation code need adjustments. Developing software with this three-level approach is initially slow due to the added effort required for the layout/structure of the core code and the greater abstractness of it. However, the flexibility provided by this approach on the

developer level can quickly pay off. Adjusting to the multiple changes of the objectives during the thesis work was significantly eased by the automated core code. Projects of the size of the “section” model thus benefit strongly from well-structured code.

A structured code with core-level automation streamlines the user’s workflow for running simulations by making the process both efficient and intuitive. Core automation can handle tasks such as setting, combining, and creating values in multiple places based on a single definition. Flexibility for these automated values is maintained by providing default values that can be modified, allowing users full control when needed. Additionally, by automating back-end tasks like directory creation, data handling, and data type management, the user interface focuses solely on simulation-related steps, making the process more intuitive. This approach is illustrated in Figure 3.4, which outlines the simulation pipeline: the necessary components for running a simulation must exist (grey), the aerodynamic, structural, and time integration algorithms must be configured (ocker), the simulation must be executed (blue), and the results saved (red). This structure aligns with the expected steps for users familiar with aeroelastic simulations, ensuring a logical and user-friendly process.

The Python class `ThreeDOFsAirfoil` seen in the pipeline mainly combines the different engineering models into an aeroelastic simulation through the methods `simulate()` and `simulate_along_path()`. Their core concept is given in Algorithm 1. Mainly, both functions run the initialisation methods for the aerodynamic, structural, and time integration algorithm and then loop over the time array. During each time step, the aerodynamic and structural forces are calculated and fed into the time integration algorithm. For `simulate_along_path()`, the airfoil’s position and velocity are updated according to the specified $\boldsymbol{x}_{\text{set}}$ and $\dot{\boldsymbol{x}}_{\text{set}}$ at the beginning of each time step. If preferred, only the position or velocity can be predefined. During the calculations, the time series of all parameters are saved as instance attributes. The only other calculation task class `ThreeDOFsAirfoil` has is the optional calculation of the steady state. The simulations for this thesis use this often, so the reason and algorithm thereof are explained next.

For simulations targeting limit cycle oscillations (LCOs), the method `approximate_steady_state()` helps reduce the transient time from the airfoil’s initial position to the LCO state. Instead of placing the airfoil initially in the origin, the aim is to place it closer onto its converged LCO path by calculating the steady-state displacement with `approximate_steady_state()` and adding an edgewise (predominant LCO direction) offset. The method is termed an approximation because dynamic stall models that account for leading-edge vortex detachment can result in non-constant aerodynamic forces even under steady inflow conditions. Such models are, e.g., the original Beddoes-Leishman model from Leishman et al., 1989 or the two models defined in Sections 3.3.1.4 and 3.3.1.5. However, outside of dynamic stall effects, the approximation is accurate to the numerical precision of the forthcoming root-finding problems.

The method offers two aerodynamic modes: one finds the approximate steady state for given inflow conditions and the other finds the approximate steady state and required inflow angle for a given inflow speed and desired geometric angle of attack. Structurally, two modes are available: one with no structural coupling and another with heave-pitch stiffness coupling.

The calculation procedure is explained in the next paragraphs. The implementation is detailed thereafter in Algorithm 2. The only implementation difference to the “section” model code is that the aerodynamic force/moment is also returned, which is necessary to initialise the HHT–α^{HHT} algorithm properly. The calculations of the displacements $\boldsymbol{x}$ are based on Equations (3.1) to (3.3) for $\dot{\boldsymbol{x}} = 0\,\mathrm{m/s}$ and $\ddot{\boldsymbol{x}} = 0\,\mathrm{m/s^2}$, thus reading

$$K_{xx}x = f^{\text{steady}}_{\text{aero},x}(\alpha(\gamma,...),...) \tag{3.11}$$

$$K_{yy}y + K_{y\gamma}\gamma = f^{\text{steady}}_{\text{aero},y}(\alpha(\gamma,...),...) \tag{3.12}$$

$$K_{\gamma y}y + K_{\gamma\gamma}\gamma = M^{\text{steady}}_{\text{aero}}(\alpha(\gamma,...),...)\,. \tag{3.13}$$

As a reminder, only heave-pitch coupling can be modelled by `approximate_steady_state()`. As defined in Equation (3.4), the aerodynamic forces and moments are, amongst other parameters, indirectly dependent on the torsional coordinate (γ). This causes the need for root-finding algorithms for Equations (3.12) and (3.13) if the aerodynamic forces and moments are based on strongly non-linear

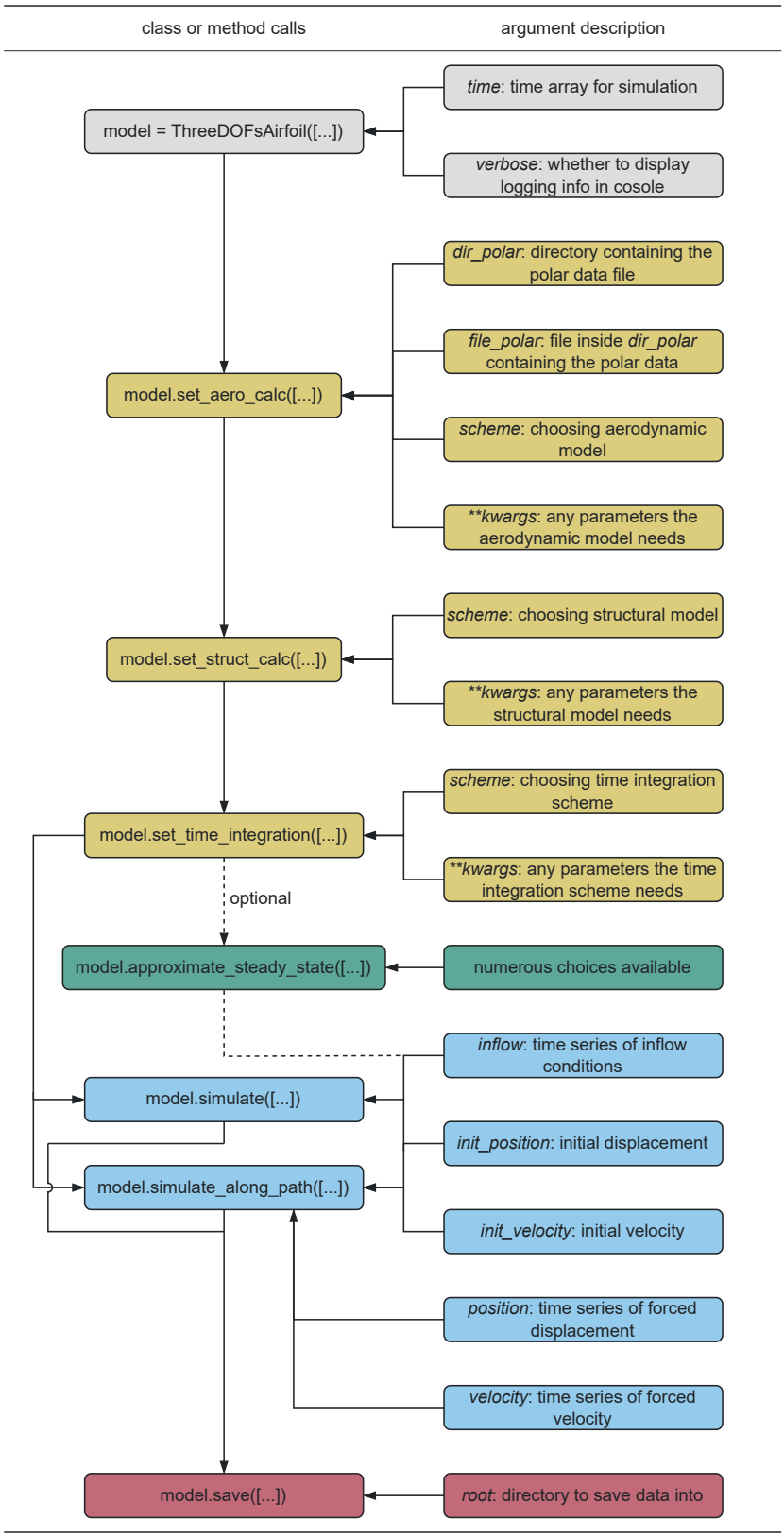

Figure 3.4: Top-level pipeline of running a simulation with the “section” model. The steps are categorised: initialisation of a model instance (grey), setting the simulation algorithms (ocker), an optional calculation of the steady state (green-blueish), running the simulation (blue), and saving it (red). The column “method calls” shows the necessary method calls. “[...]” is a placeholder for method arguments. The column “argument description” states the main argument names in italics and their meaning after the colon.

Algorithm 1 The main process of .simulate() and .simulate_along_path().

*The three method calls in **Require** internally save the aerodynamic, structural, and time integration algorithms. Additionally, they internally save the initialisation methods and the algorithm-specific parameters.*

Require:

1. class method .set_aero_calc() used
2. class method .set_struct_calc() used
3. class method .set_time_integration() used

Return:

1. general parameters (time, displacements, velocities, accelerations, ...) saved as object attributes
2. aerodynamic parameters (forces, dynamic stall parameters, ...) saved as object attributes
3. structural parameters (damping forces, stiffness forces, ...) saved as object attributes

function SIMULATE($\boldsymbol{u}_0$, $\boldsymbol{x}_{\text{init}}$, $\dot{\boldsymbol{x}}_{\text{init}}$)
  *Or: **function** simulate_along_path($\boldsymbol{u}_0$, x_{init}, $\dot{x}_{init}$, x_{set}, $\dot{x}_{set}$)*
  $\phi \leftarrow$ angle between components of $\boldsymbol{u}_0$
  $dt \leftarrow$ array of all time step sizes ▷ *The time array is defined during the instance initialisation.*
  add $\boldsymbol{u}_0$, ϕ, and dt to parameters that will be saved to a file
  $\boldsymbol{x}^0 \leftarrow \boldsymbol{x}_{\text{init}}$ ▷ *Superscript indices denote index-based location in an array.*
  $\dot{\boldsymbol{x}}^0 \leftarrow \dot{\boldsymbol{x}}_{\text{init}}$
  loop over and execute the initialisation methods for the aerodynamic, structural, and time integration algorithms

  for i in range(number of time steps minus 1)
    ▷ *If the function is simulate_along_path([...]):*
      $x^i \leftarrow x^i_{set}$
      $\dot{x}^i \leftarrow \dot{x}^i_{set}$
      In the actual implementation, individual components of x^i and $\dot{x}^i$ can be set. ◁
    $f^i_{\text{aero}} \leftarrow$ aerodynamic algorithm([...])
    $\boldsymbol{f}^i_{\text{damp}}, \boldsymbol{f}^i_{\text{stiff}} \leftarrow$ structural algorithm([...])
    $\ddot{\boldsymbol{x}}^{i+1}, \dot{\boldsymbol{x}}^{i+1}, \boldsymbol{x}^{i+1} \leftarrow$ time integration algorithm([...])
    ▷ *The inputs to the algorithm functions are always: complete state (all parameters that the simulation keeps track of) and history of the system, i, respective algorithm parameters*

  $\boldsymbol{f}^{\text{last}}_{\text{aero}} \leftarrow$ aerodynamic algorithm([...])
  $\boldsymbol{f}^{\text{last}}_{\text{damp}}, \boldsymbol{f}^{\text{last}}_{\text{stiff}} \leftarrow$ structural algorithm([...])

measurement data. For steady aerodynamics, those relations are given by

$$D^{\text{steady}} = \frac{1}{2}\rho c U^2 C_d(\alpha) \tag{3.14}$$

$$L^{\text{steady}} = \frac{1}{2}\rho c U^2 C_l(\alpha) \tag{3.15}$$

$$M^{\text{steady}}_{\text{aero}} = \frac{1}{2}\rho c^2 U^2 C_m(\alpha)\,. \tag{3.16}$$

In the steady case, the direction of the steady drag (D) and lift (L) are parallel and normal to $\boldsymbol{u_0}$, respectively. Hence,

$$\begin{bmatrix} f^{\text{steady}}_{\text{aero},x} \\ f^{\text{steady}}_{\text{aero},y} \\ M^{\text{steady}}_{\text{aero}} \end{bmatrix} = \boldsymbol{R} \begin{bmatrix} D^{\text{steady}} \\ L^{\text{steady}} \\ M^{\text{steady}}_{\text{aero}} \end{bmatrix} = \begin{bmatrix} \cos(-\phi) & \sin(-\phi) & 0 \\ -\sin(-\phi) & \cos(-\phi) & 0 \\ 0 & 0 & 1 \end{bmatrix} \begin{bmatrix} D^{\text{steady}} \\ L^{\text{steady}} \\ M^{\text{steady}}_{\text{aero}} \end{bmatrix}. \tag{3.17}$$

$\boldsymbol{R}$ is a passive planar rotation matrix that rotates around γ. It projects the vector $\begin{bmatrix} D^{\text{steady}} & L^{\text{steady}} \end{bmatrix}^T$ from the aerodynamic coordinate system that has one axis in the direction of $\boldsymbol{u_0}$ and the other axis

perpendicular to it (to the left when looking in the direction of $\boldsymbol{u_0}$) onto the xy coordinate system. Virtually, this is done by rotating the aerodynamic coordinate system clockwise by wind inflow (here also yaw misalignment) angle (ϕ) onto the xy coordinate system. Because counter-clockwise is defined as positive, see Figure 3.2, clockwise is negative. The signs in $\boldsymbol{R}$ are not simplified for clarity.

To summarise until this point, the force balances for the steady state are given by Equations (3.11) to (3.13). They include the steady aerodynamic forces and moments that are given by Equations (3.14) to (3.17). Once the aerodynamic forces and moments are known, the displacements can be calculated as seen in Algorithm 2, lines 15 to 17 and 36 to 40 for no heave-pitch coupling and with heave-pitch coupling, respectively. However, for given inflow conditions (i.e. the final geometric angle of attack (α) is not yet known), the aerodynamic moment (M_{aero}) influences the torsional coordinate (γ) which in turn influences M_{aero} (and the drag and lift). Thus, often by root-finding, the steady γ has to be acquired first. The case-dependent (with/without structural heave-pitch coupling and with/without a set geometric angle of attack (α)) approach to this calculation is stated next.

No stiffness coupling

If there is no heave-pitch coupling, only Equation (3.13) has γ on both sides of the equation and is thus enough to find γ. Under this condition, the equation reduces to

$$\gamma K_{\gamma\gamma} = M_{\text{aero}}^{\text{steady}}(\alpha(\gamma, \phi))\,. \tag{3.18}$$

Thus, after solving Equation (3.18), γ can be used to solve Equations (3.11) and (3.12) for x and y, respectively. Solving Equation (3.18) is done differently depending on the choice for geometric angle of attack (α).

Specific α wanted

In case a specific geometric angle of attack (α) is wanted, the wind inflow (here also yaw misalignment) angle (ϕ) has to become a variable. That is because for a given wind inflow magnitude (u_0) and α, M_{aero} and thus γ is fully defined. Since α is set already, the equation $\alpha = \phi - \gamma$ can only hold if ϕ is adjusted. Hence, using `approximate_steady_state()` with a set α will return ϕ that is needed to achieve the set α. To get γ, Equation (3.18) simplifies since α becomes independent of γ (α is set to a value already). γ can then immediately be calculated as seen in Algorithm 2, line 9 and ϕ as in line 10.

No specific α wanted

If no specific specific geometric angle of attack (α) is wanted, $\alpha = \phi - \gamma$ is used to calculate M_{aero}. However, M_{aero} influences γ in a strongly non-linear way. Hence, the root-finding problem for Equation (3.18) as shown in Algorithm 2, line 12 has to be solved.

Stiffness coupling

With heave-pitch coupling, the full Equations (3.12) and (3.13) have to be used. Independent of the choice of whether α is set or not, a root-finding problem has to be solved. This is derived now. First, rearrange Equation (3.12) for y and use Equation (3.17) to express $f_{\text{aero},y}^{\text{steady}}$.

$$y = \frac{f_{\text{aero},y}^{\text{steady}}(\alpha(\gamma, ...), ...) - K_{y\gamma}\gamma}{K_{yy}} \qquad \text{from Equation (3.12)} \tag{3.19}$$

$$y = \frac{D^{\text{steady}}(\phi - \gamma)\sin(\phi) + L^{\text{steady}}(\phi - \gamma)\cos(\phi) - K_{y\gamma}\gamma}{K_{yy}} \qquad \text{with Equation (3.17)} \tag{3.20}$$

Then, express Equation (3.13) as a root-finding problem and insert y.

$$0 = K_{\gamma y}y + K_{\gamma\gamma}\gamma - M_{\text{aero}}^{\text{steady}}(\alpha(\gamma, ...), ...) \qquad \text{from Equation (3.13)} \tag{3.21}$$

$$\begin{aligned} 0 = {} & \frac{K_{\gamma y}}{K_{yy}}\left(D^{\text{steady}}(\phi - \gamma)\sin(\phi) + L^{\text{steady}}(\phi - \gamma)\cos(\phi) - K_{y\gamma}\gamma\right) \\ & + K_{\gamma\gamma}\gamma - M_{\text{aero}}^{\text{steady}}(\phi - \gamma) \qquad \text{with Equation (3.20)} \end{aligned} \tag{3.22}$$

Equation (3.22) can now be used to find γ. Then, γ and Equation (3.20) is used to find y (see Algorithm 2, line 39).

Specific α wanted
If a specific α is wanted, the steady L, D, and M_{aero} are known. In Equation (3.22), $\phi = \alpha + \gamma$ is substituted and the whole equation solved as defined in Algorithm 2, lines 20 to 25.

No specific α wanted
If no specific α is wanted, $\alpha = \phi - \gamma$ has to be used for the calculation of the aerodynamic forces and moments. However, the directions of the aerodynamic forces are given by ϕ. The calculation of γ is shown in Algorithm 2, lines 28 to 33.

Algorithm 2 Calculating the approximate steady state of the airfoil for a given inflow.

Require:
1. functions polar lift coefficient $(C_l)(\alpha)$, polar drag coefficient $(C_d)(\alpha)$, polar moment coefficient $(C_m)(\alpha)$
2. structural parameters chord (c), stiffness matrix in the xy coordinate system $(\boldsymbol{K})$
3. air density (ρ)

Return:
1. approximated steady state displacements $\boldsymbol{x}$
2. wind inflow (here also yaw misalignment) angle (ϕ)

1: **function** APPROXIMATE_STEADY_STATE($\boldsymbol{u}$, α, stiffness coupling)
2: $u \leftarrow$ magnitude of $\boldsymbol{u}$
3: $\phi \leftarrow$ angle between the components of $\boldsymbol{u}$
4: $q \leftarrow 0.5\rho u^2$
5: $f_{\text{base}} \leftarrow qc$
6: $t_{\text{base}} \leftarrow -qc^2$
7: **if** stiffness coupling is `False`
8: **if** α is specified
9: $\gamma \leftarrow t_{\text{base}} C_m(\alpha)/K_{\gamma\gamma}$
10: $\phi \leftarrow \alpha + \gamma$
11: **else**
12: $\gamma \leftarrow \gamma$ that satisfies $0 = t_{\text{base}} C_m(\phi - \gamma) + \gamma K_{\gamma\gamma}$
13: $\alpha \leftarrow \phi - \gamma$
14: $\#M_{\text{aero}} \leftarrow t_{\text{base}} C_m(\alpha)$ ▷ *If wanted for output.*
15: $\boldsymbol{R} \leftarrow \begin{bmatrix} \cos(-\phi) & \sin(-\phi) \\ -\sin(-\phi) & \cos(-\phi) \end{bmatrix}$
16: $\boldsymbol{f}_{\text{aero}} \leftarrow \boldsymbol{R}\begin{bmatrix} f_{\text{base}} C_d(\alpha) & f_{\text{base}} C_l(\alpha) \end{bmatrix}^T$ ▷ $\boldsymbol{f}_{aero} = \begin{bmatrix} f_{aero,x} & f_{aero,y} \end{bmatrix}^T$
17: $\boldsymbol{x} \leftarrow \begin{bmatrix} f_{\text{aero,x}}/K_{xx} & f_{\text{aero,y}}/K_{yy} \end{bmatrix}$
18: **else** ▷ *Only considers heave-pitch stiffness coupling $K_{y\gamma}$.*
19: **if** α is specified
20: $L \leftarrow f_{\text{base}} C_l(\alpha)$
21: $D \leftarrow f_{\text{base}} C_d(\alpha)$
22: $M_{\text{aero}} \leftarrow t_{\text{base}} C_m(\alpha)$
23: **function** RESIDUE(γ)
24: **return** $K_{y\gamma}/K_{yy}\left(L\cos(\alpha+\gamma) + D\sin(\alpha+\gamma) - K_{y\gamma}\gamma\right) + K_{\gamma\gamma}\gamma - M_{\text{aero}}$
25: $\gamma \leftarrow \gamma$ that satisfies $0 = \texttt{residue}(\gamma)$
26: $\phi \leftarrow \alpha + \gamma$
Continuation on line line 27, next page.

This concludes the description of the top-level “section” model, its coding background, the equation of motions that are solved, the pipeline of running a simulation, and how the approximate steady state can be calculated. The next three sections explain the aerodynamic, structural, and time integration modelling used in the aeroelastic simulations.

Continued from line 26, previous page.

else
  function RESIDUE(γ)
    $\alpha \leftarrow \phi - \gamma$
    $f_{\text{aero,y}} \leftarrow f_{\text{base}} \left(C_l\left(\alpha\right)\cos\left(\phi\right) + C_d\left(\alpha\right)\sin\left(\phi\right)\right)$
    $M_{\text{aero}} \leftarrow t_{\text{base}} C_m\left(\alpha\right)$
    return $K_{y\gamma}/K_{yy}\left(f_{\text{aero,y}} - K_{y\gamma}\gamma\right) + K_{\gamma\gamma}\gamma - M_{\text{aero}}$
  $\gamma \leftarrow \gamma$ that satisfies $0 = \texttt{residue}(\gamma)$
  $\alpha \leftarrow \phi - \gamma$
$\#M_{\text{aero}} \leftarrow t_{\text{base}} C_m(\alpha)$ ▷ *If wanted for output.*
$\boldsymbol{R} \leftarrow \begin{bmatrix} \cos\left(-\phi\right) & \sin\left(-\phi\right) \\ -\sin\left(-\phi\right) & \cos\left(-\phi\right) \end{bmatrix}$
$\boldsymbol{f}_{\text{aero}} \leftarrow \boldsymbol{R}\begin{bmatrix} f_{\text{base}} C_d(\alpha) & f_{\text{base}} C_l(\alpha) \end{bmatrix}^T$ ▷ $\boldsymbol{f}_{aero} = \begin{bmatrix} f_{aero,x} & f_{aero,y} \end{bmatrix}^T$
$x \leftarrow f_{\text{aero,x}}/K_{xx}$
$y \leftarrow \left(f_{\text{aero,y}} - K_{y\gamma}\gamma\right)/K_{yy}$
$\boldsymbol{x} \leftarrow \begin{bmatrix} x & y \end{bmatrix}$

return $\begin{bmatrix} \boldsymbol{x} & \gamma \end{bmatrix}, \phi$ ▷ *Also return* $\begin{bmatrix} \boldsymbol{f}_{aero} & M_{aero} \end{bmatrix}$ *if needed for, e.g., time integration initialisation.*

3.3. Aerodynamic modelling

The aerodynamic modelling is concerned with the calculation of the aerodynamic drag (D), lift (L), and aerodynamic moment (M_{aero}). In the "section" model, these are the only external forces and moments acting on the blade section. After a short introduction to quasi-steady aerodynamics, the focus lies on unsteady aerodynamic models that are positioned at the core of the thesis objectives. Besides the initial descriptions and implementation algorithms, this section also shows the validation of their implementation in the "section" model.

3.3.1. Descriptions and implementations

Section 3.3 abstract

The calculation algorithms for quasi-steady aerodynamics and five dynamic stall (DS) models are presented and explained where interesting. The five dynamic stall models are: Stäblein (models unsteady attached flow), AEROHOR (models unsteady attached and unsteady separated flow, and leading-edge vortices), 1st-order IAG (same approach as AEROHOR, different implementation details), Hansen-Gaunaa-Madsen as it is implemented in openFAST (models unsteady attached and trailing-edge separated flow), and the Hansen-Gaunaa-Madsen corrected for large angles of attack (same approach as Hansen-Gauna-Madsen openFAST, different lagging of quasi-steady angle of attack (α_{qs})). Additionally, the Kirchhoff equations for trailing-edge separated flow are examined.

Five different models for the calculation of the unsteady aerodynamic force and moment are implemented. However, one of them, the here so-called Stäblein model, is only used for the aeroelastic validation of the "section" model. The other four can be categorised into two groups. The 1st-order IAG and AEROHOR models are based on the initial Beddoes-Leishman (Leishman et al., 1989) model, thus modelling unsteady attached flow, trailing-edge separated flow, and leading-edge vortex influences. The other two Hansen-Gaunaa-Madsen derivative models are based on the Hansen-Gaunaa-Madsen model (Morten Hartvig Hansen et al., 2004) that uses a different approach to modelling the unsteady attached and trailing-edge separated flow. leading-edge vortices are not modelled. Further explanations of the models are given in the respective sections. However, before working on unsteady aerodynamics, quasi-steady aerodynamics have to be discussed.

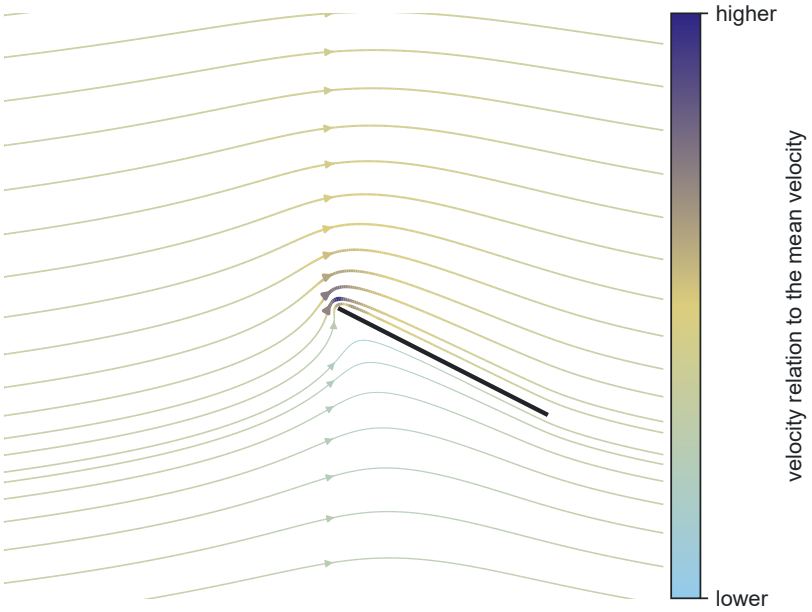

Figure 3.5: Steady near-field potential flow reconstruction of a flat plate at $15\,°$ geometric angle of attack and $1\,\mathrm{m/s}$ horizontal inflow. Velocity field data obtained from an unsteady, just-in-time compilation optimised Python panel code by the author. The simulation was done for a steady inflow with 200 equally-sized panels on the flat plate. The flow-field resolution is a grid of 100×47 (horizontal $\times$ vertical) equally-spaced points. Besides the colour bar, the line-width of the streamlines indicates the velocity relation of the streamline to the mean velocity (thin: lower, thick: higher).

Quasi-steady

Quasi-steady aerodynamics are understood as considering the influence of the motion of an airfoil (as a 2D model or as a section of a 3D blade or wing) on the angle of attack under potential flow conditions. This new angle of attack is called the quasi-steady angle of attack (α_{qs}). The definition of an angle of attack in the near-field is not trivial, see Figure 3.5. Different streamlines exhibit a multitude of inflow angles from negative values to very large positive values. In quasi-steady aerodynamics, the detailed influence of the motion of the airfoil on the near-field flow is not considered. Rather, it is assumed that the motion of the airfoil causes an apparent change in the far-field inflow conditions that the airfoil sees (the relative far-field inflow) (Larsen et al., 2007). Far-field flow refers to flow undisturbed by the presence of an object (here: the airfoil). The relative far-field inflow becomes a superposition of the (not relative) inflow conditions and the opposite-in-direction translational movement of a point on the airfoil. The rotational movement of the airfoil is translated into translational movement of points on the airfoil. Since this movement differs from point to point, a choice for a single point on the airfoil for which α_{qs} is calculated has to be made if the airfoil is allowed to rotate. In this thesis, unless otherwise stated, the axis of rotation is the quarter-chord point and, based on thin airfoil theory, α_{qs} is calculated for the three-quarter chord point. Interpreting a torsion rate to influence the quasi-steady angle of attack as if the whole airfoil had additional translational movement is, like many engineering models, not correct (Karbasian et al., 2022), but better than discarding the pitch rate altogether.

The α_{qs} is derived in Section 3.2, namely with Figure 3.3 and in Equations (3.5) to (3.8) and (3.10). As such, α_{qs} is calculated as

$$\alpha_{\mathsf{qs}} = \arctan\left(\frac{u_{0,\mathsf{x}} + \dot{\gamma} r_{\mathsf{rot}} \sin(\gamma) - \dot{x}}{u_{0,\mathsf{y}} - \dot{\gamma} r_{\mathsf{rot}} \cos(\gamma) - \dot{y}}\right) - \gamma\,, \tag{3.23}$$

or as seen in Algorithm 3. The aerodynamic forces and moment are then calculated by replacing α with α_{qs} in the steady aerodynamic Equations (3.14) to (3.16) and using the quasi-steady inflow magnitude (u) at the point of calculation of α_{qs} that considers the movement of the airfoil. Implementation details are given in Algorithm 4. There, the only additional step is the projection of the aerodynamic forces and moment onto the xy coordinate system.

Algorithm 3 Calculation of the quasi-steady angle of attack.

Require:
1. Input parameters for `quasi_steady_flow()`

Return:
1. Quasi-steady angle of attack (α_{qs})
2. quasi-steady inflow velocity components

function `QUASI_STEADY_FLOW`($\dot{\boldsymbol{x}}$, γ, $\boldsymbol{u}_0$, r_{rot})
- $v_{\text{pitch}} \leftarrow \dot{\boldsymbol{x}}_\gamma r_{\text{rot}} \begin{bmatrix} \sin(-\gamma) & \cos(\gamma) \end{bmatrix}^T$
- $u_x \leftarrow u_{0,x} - \dot{x}_x - v_{\text{pitch},x}$
- $u_y \leftarrow u_{0,y} - \dot{x}_y - v_{\text{pitch},y}$
- **return** $\arctan\left(\frac{u_y}{u_x}\right)$, u_x, u_y

Algorithm 4 Calculation of the quasi-steady aerodynamic coefficients, forces and moment.

Require:
1. functions `C_l`(α_{qs}), `C_d`(α_{qs}), `C_m`(α_{qs})
2. function `quasi_steady_flow_angle()` from Algorithm 3

Return:
1. quasi-steady aerodynamic forces and moment as a vector with components in $\begin{bmatrix} x & y & \gamma \end{bmatrix}$ direction

function `QUASI_STEADY`($\dot{\boldsymbol{x}}$, $\boldsymbol{x}$, $\boldsymbol{u}_0$, r_{rot}, c, ρ)
- $\phi_{\text{qs}}, u_x, u_y \leftarrow$ `quasi_steady_flow`($\dot{\boldsymbol{x}}$, x_γ, $\boldsymbol{u}_0$, $x_\alpha - x_{\text{pitch}}$)
- $u \leftarrow \sqrt{u_x^2 + u_y^2}$
- $\alpha_{\text{qs}} \leftarrow \phi_{\text{qs}} - x_\gamma$
- $\mathbf{c}_{\text{coeffs}} \leftarrow \begin{bmatrix} \texttt{C\_d}(\alpha_{\text{qs}}) & \texttt{C\_l}(\alpha_{\text{qs}}) & \texttt{C\_m}(\alpha_{\text{qs}}) \end{bmatrix}^T$
- $q \leftarrow \frac{1}{2}\rho u^2$
- $\boldsymbol{R} \leftarrow \begin{bmatrix} \cos(-\phi_{\text{qs}}) & \sin(-\phi_{\text{qs}}) & 0 \\ -\sin(-\phi_{\text{qs}}) & \cos(-\phi_{\text{qs}}) & 0 \\ 0 & 0 & -1 \end{bmatrix}$ ▷ *The "−" is based on coordinate system differences.*
- $\boldsymbol{D} \leftarrow \text{diag}\left(\begin{bmatrix} c & c & c^2 \end{bmatrix}\right)$ ▷ *Diagonal matrix with the stated values on the diagonal.*
- **return** $q\boldsymbol{D}\boldsymbol{R}\mathbf{c}_{\text{coeffs}}$

Stäblein

The Stäblein model is solely implemented to validate the aeroelastic behaviour of the "section" model. "Stäblein model" refers to the dynamic stall model used in the paper by Stäblein et al., 2017. In their paper, the authors use a linearised state-space approach to investigate the aerodynamic and aeroelastic damping of a blade section structurally coupled for heave-pitch and edge-pitch. How their results are used for validating the "section" model is explained in Section 3.6.

The Stäblein dynamic stall model incorporates unsteady attached flow and apparent mass terms that arise due to the acceleration of the airfoil. The implementation of the model is depicted in Algorithms 5 and 6. Algorithm-specific variables are the length from the leading-edge to the axis of rotation x_{pitch} and the length from the leading-edge to the point at which the quasi-steady angle of attack (α_{qs}) is calculated x_α. After some initial general calculations (Part 1), the quasi-steady angle of attack (α_{qs}) is lagged in time to calculate the effective angle of attack (α_{eff}) (Part 2). The paper's Equation (6), which defines the differential equation used for time-lagging values, is corrected to

$$\dot{z}_i + \frac{2W}{c}\left(b_i + \frac{c\dot{W}}{2W^2}\right) z_i = b_i A_i \frac{2W}{c}\alpha_{\text{qs}}\,, \tag{3.24}$$

Figure 3.6: Visualisation of the meaning of the time step indices for the time and the time steps. The arrow length represents the magnitude of the time step. The blocks with the variable t inside indicate a discrete time.

since it is missing the $+$ in the parenthesis. The time integration of Equation (3.24) in Part 2 is done based on the piece-wise constant discretisation from Morten Hartvig Hansen et al., 2004. The core part of calculating how much of an original value of a previous time step remains for the current time step is given in lines 13 and 14. The use of Δt^{i-1} is explained with the supporting Figure 3.6 because the author has encountered implementations unwary of this. If a value X is meant to be lagged in time from time t^{i-1} to t^i, Δt^{i-1} is used because it describes how much time has passed between the two states for X to change. If the time step values are not constant like in Figure 3.6, lagging X from t^{i-1} to t^i with Δt^i is unreasonable because it stands in no relation to the period in which X changed. Returning to Algorithms 5 and 6, Part 3 defines variables that are used repeatedly. Parts 4 to 6 are explained momentarily. Part 7 projects the aerodynamic forces and moment onto the xy coordinate system that the "section" model uses for its time integration.

The calculation of the lift (Part 4) is a sum of a circulatory, inertial (apparent mass), and centrifugal contribution. The circulatory lift (L_{circ}) is based on thin airfoil theory. The inertial lift (L_{iner}) "acts at mid-chord and equals the mass of air in a cylinder with the diameter of chord c times the vertical mid-chord acceleration"(Stäblein et al., 2017). More specifically, it is the mass per unit length along the axis of the defined cylinder. In its current implementation, L_{iner} assumes a small angle between the y-axis and the lift direction and a small x_γ. That is because L_{iner} is related to the flapwise movement of the mid-chord which is only approximated by movement along y for the given limitations. The final lift contribution, the centrifugal lift (L_{cent}), is the consequence of changing the orientation of the apparent mass (Stäblein et al., 2017).

The drag is calculated (Part 5) as the sum of the viscous and induced drag, and a torsional component. Adding an induced drag (D_{ind}) is one way of handling the directional change of the aerodynamic forces that occur when the wake behind an airfoil leaving the trailing-edge "induces" a downwash on the airfoil. This downwash tilts the inflow and with that by definition the direction of lift and drag. Either, this new direction is used to apply the forces to a body. Then, there is no induced drag because the lift and drag are perpendicular to each other. Or, if the tilt due to the downwash is small, the original angle of attack is used for the force directions and the lift (whose direction is still governed by the shifted angle of attack) is projected onto the old directions as

$$L \propto L_{\text{circ}}(\alpha_{\text{eff}}) \cos(\alpha_{\text{qs}} - \alpha_{\text{eff}}) \approx L_{\text{circ}}(\alpha_{\text{eff}}) \tag{3.25}$$

$$D \propto L_{\text{circ}}(\alpha_{\text{eff}}) \sin(\alpha_{\text{qs}} - \alpha_{\text{eff}}) \approx L_{\text{circ}}(\alpha_{\text{eff}}) (\alpha_{\text{qs}} - \alpha_{\text{eff}}) \ . \tag{3.26}$$

Here, α_{qs} is the angle of attack unaffected by the downwash and the effective angle of attack (α_{eff}) is the affected one. The first approach of using α_{eff} for the direction of the forces does not involve approximations. However, since the dynamic stalls models used for this thesis all employ the induced drag approach, so will their implementations in the "section" model. This will not remain without consequences. Lastly, the torsional component from line 31 is added. There are different approaches to calculating the aerodynamic force magnitude and direction, even for the quasi-steady case. A common approach is to use the angle of attack at the three-quarter chord point to determine the magnitude of the lift and drag, and to determine the direction of both. Then, an additional torsion rate term has to be added (Li et al., 2022). This modelling scheme is used in the "section" model. Based on thin airfoil theory, the torsion rate term is not needed when the magnitudes of the forces are based on the quasi-steady angle of attack at the three-quarter chord and the direction of them on the quarter-chord (Li et al., 2022). In Stäblein et al., 2017, this appears to be the case. It "appears" because it is stated that "The geometric angle of attack between chord and free-stream flow defines the direction of the aerodynamic forces" after which a quasi-steady angle of attack is defined that excludes the torsion rate (Equation (4) of the paper). Increasing ambiguity, the next page defines "the unsteady lift, which is perpendicular to α_E [the effective angle of attack]". It is therefore unclear what was chosen for the direction of the aerodynamic forces. To conclude, the "section" implementation of the Stäblein model

uses the quasi-steady angle of attack at the three-quarter chord for the direction and magnitude of the aerodynamic forces and adds the required torsional component.

As a brief note, using the word “induces” or “induction” to relate vortices as a cause for a velocity field (the effect) is a misnomer. The Biot-Savart law that is used to calculate the velocity field based on a vorticity distribution is a strictly kinematic, not dynamic, equation. While the idea of a vortex causing a velocity at a distance can be seen as intuitive to understand flow fields, it is not a physically correct conclusion (McLean, 2010). Rather, a velocity (or vorticity) field governed by its physical conservation equations might be converted into a vorticity (or velocity) field. However, this conversion does not represent a physical cause-and-effect relationship.

Back to the algorithm: in Part 6, the moment is calculated as a sum of the circulatory and inertial contributions and the moments created by the inertial and centrifugal lift parts. Differences in the signs between the paper and the implementation in the “section” model are due to different coordinate systems.

Algorithm 5 Implementation of the Stäblein model

Require:

1. function `quasi_steady_flow()` from Algorithm 4
2. functions `C_d()` and `C_m()` from polars

Return:

1. unsteady aerodynamic forces and moment as a vector with components in $\begin{bmatrix} x & y & \gamma \end{bmatrix}$ direction

arguments $\leftarrow (\boldsymbol{x},\ \dot{\boldsymbol{x}},\ \boldsymbol{u_0},$ ▷ *airfoil state*
$x_{\text{pitch}},\ x_\alpha,\ c,$ ▷ *lengths*
$C_{l,\alpha},\ \alpha_{0n,\text{inv}},$ ▷ *aerodynamic parameters*
$A_1,\ A_2,\ b_1,\ b_2)$ ▷ *general algorithm parameters*

function DYNAMIC_STALL_STÄBLEIN(i, arguments)
▷ *Part 1: general calculations* ◁
$\phi_{\text{qs}}\ , u_x\ , u_y \leftarrow$ `quasi_steady_flow`$(\dot{\boldsymbol{x}},\ x_\gamma,\ \boldsymbol{u}_0,\ x_\alpha - x_{\text{pitch}})$
$u^i \leftarrow \sqrt{u_x^2 + u_y^2}$
$\dot{u} \leftarrow \frac{u^i - u^{i-1}}{\Delta t^{i-1}}$
$\alpha_{\text{qs}}^i \leftarrow \phi_{\text{qs}} - x_\gamma$
$T_u^i \leftarrow \frac{c}{2u^i}$
▷ *Part 2: lagging for* α_{eff} ◁
$\bar{P}_1 \leftarrow b_1 \frac{u^i + u^{i-1}}{c} + \frac{\dot{u}^i + \dot{u}^{i-1}}{u^i + u^{i-1}}$
$\bar{P}_2 \leftarrow b_2 \frac{u^i + u^{i-1}}{c} + \frac{\dot{u}^i + \dot{u}^{i-1}}{u^i + u^{i-1}}$
$\bar{Q}_1 \leftarrow \frac{b_1 A_1}{c} u^{i-1} \alpha_{\text{qs}}^{i-1} + u^i \alpha_{\text{qs}}^i$
$\bar{Q}_2 \leftarrow \frac{b_2 A_2}{c} u^{i-1} \alpha_{\text{qs}}^{i-1} + u^i \alpha_{\text{qs}}^i$
$C_1 \leftarrow \exp(-\bar{P}_1 \Delta t^{i-1})$
$C_2 \leftarrow \exp(-\bar{P}_2 \Delta t^{i-1})$
$I_1 \leftarrow \frac{\bar{Q}_1}{\bar{P}_1}(1 - C_1)$
$I_2 \leftarrow \frac{\bar{Q}_2}{\bar{P}_2}(1 - C_2)$
$X_{\text{lag}}^i \leftarrow X_{\text{lag}}^{i-1} C_1 + I_1$
$Y_{\text{lag}}^i \leftarrow Y_{\text{lag}}^{i-1} C_2 + I_2$
$\alpha_{\text{eff}}^i \leftarrow \alpha_{\text{qs}}^i (1 - A_1 - A_2) + X_{\text{lag}}^i + Y_{\text{lag}}^i$
continuation on line 20 (next page)

Algorithm 6 Implementation of the Stäblein model – continued

continued from line 19

▷ *Part 3: useful variables* ◁

$m_{\text{app}} \leftarrow \rho \frac{\pi c^2}{4}$

$q \leftarrow \frac{\rho}{2} \left(u^i\right)^2$

$f_{\text{base}} \leftarrow qc$

▷ *Part 4: lift calculation* ◁

$L_c \leftarrow f_{\text{base}} C_{l,\alpha}(\alpha^i_{\text{eff}} - \alpha_{0,l,\text{inv}})$ ▷ *circulatory lift*

$L_{\text{iner}} \leftarrow -m_{\text{app}} \left(\ddot{x}^i_y + \left(\frac{c}{2} - x_{\text{pitch}}\right) \ddot{x}^i_\gamma\right)$ ▷ *inertial lift, $-\ddot{x}_\gamma$ because of coordinate system differences*

$L_{\text{cent}} \leftarrow -m_{\text{app}} u^i \dot{x}^i_\gamma$ ▷ *centrifugal lift*

▷ *Part 5: drag calculation* ◁

$D_{\text{visc}} \leftarrow f_{\text{base}} \texttt{C\_d}(\alpha^i_{\text{eff}})$ ▷ *lagged viscous drag*

$D_{\text{ind}} \leftarrow L_c \left(\alpha^i_{\text{qs}} - \alpha^i_{\text{eff}}\right)$ ▷ *induced drag*

$D_{\text{cent}} \leftarrow -L_c T^i_u \dot{x}^i_\gamma$ ▷ *torsional component*

▷ *Part 6: moment calculation* ◁

$M_s \leftarrow -f_{\text{base}} c \texttt{C\_m}(\alpha^i_{\text{eff}})$ ▷ *lagged moment*

$M_{\text{lift}} \leftarrow \frac{c}{2} \left(\frac{L_{\text{iner}}}{2} + L_{\text{cent}}\right)$ ▷ *moment due to L_{iner} and L_{cent}*

$M_{\text{iner}} \leftarrow \frac{m_{\text{app}} c^2}{32} \ddot{x}_\gamma$ ▷ *inertial moment*

▷ *Part 7: combining everything* ◁

$\boldsymbol{f}_{\text{aero}} \leftarrow \begin{bmatrix} L_c + L_{\text{iner}} + L_{\text{cent}} \\ D_s + D_{\text{ind}} \\ M_s + M_{\text{lift}} - M_{\text{iner}} \end{bmatrix}$ ▷ *In comparison to the other dynamic stall models: here, the moment already has the correct sign.*

$\boldsymbol{R} \leftarrow \begin{bmatrix} \cos\left(-\alpha_{\text{qs}} - x_\gamma\right) & \sin\left(-\alpha_{\text{qs}} - x_\gamma\right) & 0 \\ -\sin\left(-\alpha_{\text{qs}} - x_\gamma\right) & \cos\left(-\alpha_{\text{qs}} - x_\gamma\right) & 0 \\ 0 & 0 & 1 \end{bmatrix}$

return $\boldsymbol{R}\boldsymbol{f}_{\text{aero}}$

Kirchhoff flow modelling trailing-edge separation

The dynamic stall models explained in the next four Sections 3.3.1.4 to 3.3.1.7 all model the influence of trailing-edge separation. To avoid repetition in those sections, the main concept of all four modelling approaches is explained next.

The central equation is the potential flow Kirchhoff equation for trailing-edge separated flow

$$C_n = C_{n,\alpha} \left(\frac{1 + \sqrt{f_n(\alpha)}}{2}\right)^2 (\alpha - \alpha_0) \text{ or} \tag{3.27}$$

$$C_l = C_{l,\alpha} \left(\frac{1 + \sqrt{f_l(\alpha)}}{2}\right)^2 (\alpha - \alpha_0) \tag{3.28}$$

from Thwaites, 1961. Here, n or l denotes the normal (to the chord) or lift direction. Additional parameters are the lift slope ($C_{l,\alpha}$), the normal force slope ($C_{n,\alpha}$), and the zero lift angle of attack ($\alpha_{0,\text{l}}$). The newly introduced variable f is the separation point. It is the distance measured from the leading-edge of an airfoil to the point at which the flow separates from the airfoil, normalised on the chord. $f = 1$ hence means no separation, a decline in f means that the separation point is moving toward the leading-edge, and $f = 0$ means the flow around the airfoil is fully separated (separation point at the leading-edge). The use of n "or" l stems from different papers using the Kirchhoff equation either as Equation (3.27) or Equation (3.28). Leishman et al., 1989, e.g., uses the normal direction n, while HAWC2 (Morten Hartvig Hansen et al., 2004) and openFAST (Branlard et al., 2022) use the lift direction l. The author could not access Thwaites, 1961 to validate which is the original expression. C_n is the normal force coefficient that is calculated by

$$C_n(\alpha) = C_l(\alpha) \cos(\alpha) + C_d(\alpha) \sin(\alpha)\,. \tag{3.29}$$

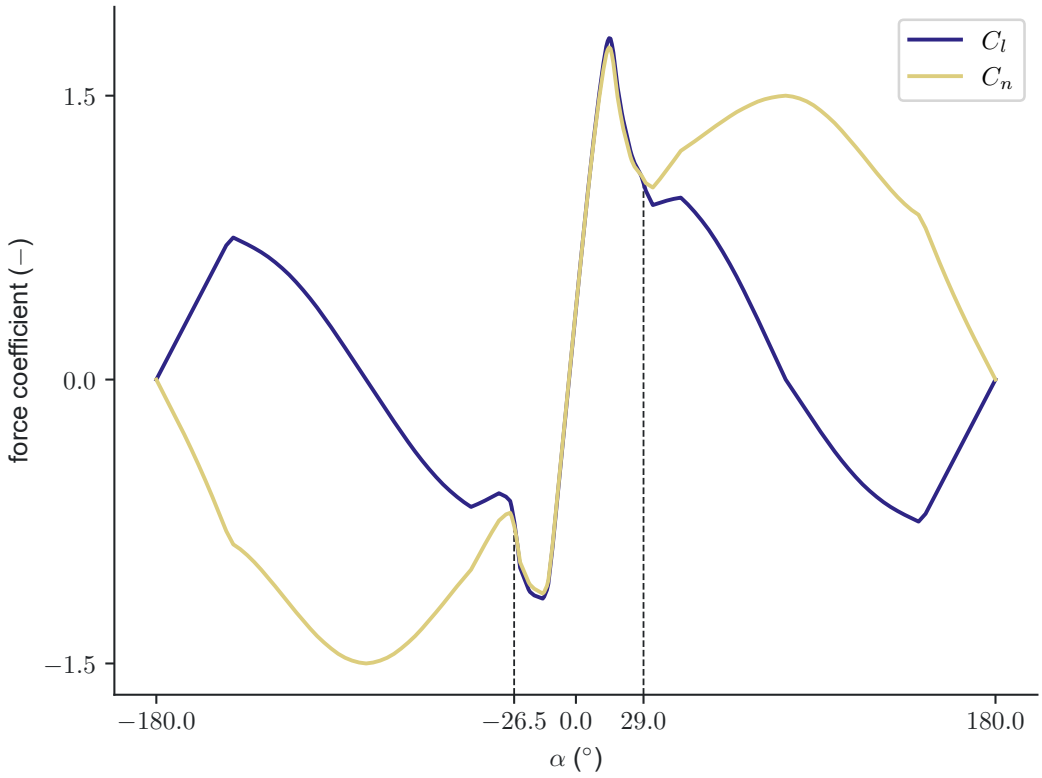

Figure 3.7: Steady lift and normal force coefficients as functions of the steady geometric angle of attack for an FFA-W3-221 airfoil. The two vertical lines indicate the angles of attack below and above of which the the flow is fully separated according to the Kirchhoff equation (for the lift) for potential flow from Thwaites, 1961.

As such, for $\alpha \to 0$ will also $C_n \to C_l$. Then, Equations (3.27) and (3.28) can be used interchangeably to a good approximation. However, for larger α, both force coefficients differ significantly as depicted in Figure 3.7. In the figure, the geometric angles of attack $-26.5°$ and $29°$ specify when Equation (3.28) predicts fully separated flow. Below and above those angles of attack neither of Kirchhoff's equations should be used (Larsen et al., 2007). Both equations are thus only valid inside the boundaries of $-26.5°$ and $29°$. Since C_n and C_l agree well in this region, Equations (3.27) and (3.28) can after all be used interchangeably for the FFA-W3-221 airfoil to a good approximation in the full α range that their are valid in.

As they stand, Equations (3.27) and (3.28) can be used to calculate C_l or normal force coefficient (C_n) for separated flow when separation point (f) is known. For that, both equations are rearranged for f as

$$f_n(\alpha) = \left(2\sqrt{\frac{C_n(\alpha)}{C_{n,\alpha}(\alpha - \alpha_0)}} - 1\right)^2 \tag{3.30}$$

$$f_l(\alpha) = \left(2\sqrt{\frac{C_l(\alpha)}{C_{l,\alpha}(\alpha - \alpha_0)}} - 1\right)^2 , \tag{3.31}$$

and (C_n,α) and (C_l,α) points from a polar are used.

The above examination of trailing-edge separated flow only considered the effect on C_n and C_l. A correction for tangential force coefficient (C_t) (and thus C_d) exist, too, in form of the equation

$$C_t = C_{n,\alpha}\,(\alpha - \alpha_0)\tan(\alpha)\sqrt{f_t}\,. \tag{3.32}$$

In X. Liu et al., 2015, this equation is again attributed to Kirchhoff although without specifying a source. C_t is calculated as

$$C_t(\alpha) = C_l(\alpha)\sin(\alpha) - C_d\cos(\alpha)\,. \tag{3.33}$$

Then signs follow the definition of α and that for $\alpha = 0°$, C_d and C_t face in opposite directions. To get f_t, the polar data is again used in combination with

$$f_t = \left(\frac{C_t}{C_{n,\alpha}(\alpha - \alpha_0)\tan(\alpha)}\right)^2. \tag{3.34}$$

Using Equation (3.33) is not as common as using Equations (3.27) and (3.28) and will only be used in the AEROHOR dynamic stall (DS) model implementation.

In the "section" model, `AeroForce()._adjust_f(sqrt_of_f, ...)` is used to calculate $f(\alpha)$. The argument `sqrt_of_f` is a function object for $\sqrt{f(\alpha)}$. `_adjust_f()` uses a Brent method to find the α at which the flow fully separates. In the fully separated region $f = 0$.

This concludes the foreword for the calculation of C_n, C_l, and C_t when using the respective Kirchhoff equations.

1st-order IAG

Bangga et al., 2020 developed the IAG model based on the original Beddoes-Leishman model (Leishman et al., 1989). Some of the original approaches are simplified or corrected and second-order differential equations for new state variables are added. These second-order additions are not implemented for the "section" model for simplicity's sake. The implementation of Bangga's model for the "section" model is thus called "1st-order IAG".

The 1st-order part of the IAG model was chosen because it represents an updated version of the well-known Beddoes-Leishman model. Hence, it includes modelling of unsteady attached, unsteady trailing-edge separated, and unsteady leading-edge separated flow. The leading-edge separation (also known as leading-edge vortex contribution) modelling is especially interesting for the comparison to the HGM-type dynamic stall models HAWC2 and openFAST use that do not include a leading-edge vortex contribution. Additionally, Larsen et al., 2007 supports incorporating leading-edge separation arguing that its effect is significant and to be expected during, e.g., active pitch control for vibrations and large deformations of modern flexible blades. Although the "section" model does not have pitch control, large deformations are expected during limit cycle oscillations.

The implementation of the 1st-order IAG model for the "section" model is detailed in Algorithm 7 and follows the description from Bangga et al., 2020 with some modifications. Bangga's paper describes the model in Sections 2.1 (original Beddoes-Leishman model with adaptations), 2.5.1 (additions/changes that make Bangga call it the IAG model), and 2.6 (corrections to be able to reconstruct the static polar). The implementation is split into parts. Each part is briefly commented on in the next paragraphs and changes to the original model from Bangga et al., 2020 are explained.

Part 1 performs general calculations. Bangga et al., 2020 does not explicitly state what their "α_n" are. For the implementation, it is assumed to be the quasi-steady angle of attack (α_{qs}) at the three-quarter chord point to account for the airfoil's movement. Additionally, the original model only uses the free-stream velocity to calculate the normalised distance s. In the implementation, the relative velocity at the three-quarter chord point including the airfoil's translational and rotational movement is used. Since s indicates the distance between the lag-inducing wake and the airfoil, the airfoil's movement should be incorporated.

Part 2 calculates the unsteady attached flow. First, α_{qs} is lagged in time to create effective angle of attack (α_{eff}). Compressibility effects (in the paper given by β) are neglected for the lagging of α_{qs}, i.e., $\beta = 1$. This is done because it is assumed that the relative flow velocities in the stand-still will be low enough. Additionally, the paper's term "$\Delta\alpha_n = \alpha_{n+1} - \alpha_n$" (Equation (4)) is changed to $\Delta\alpha_{\text{qs}} = \alpha^i_{\text{qs}} - \alpha^{i-1}_{\text{qs}}$. The paper's statement seems intentional since the following Equation (5) uses the difference between the current and last time step (for Δs^i). However, since α_{qs} for time step $i+1$ is not known at time step i in the "section" simulations, the change is kept. The calculation of the non-circulatory contribution in line 14 does not neglect compressibility effects. Assuming incompressibility

would cause "$D_n \to 0$" (due to "$M \to 0$"), however, the validation results omitting "D_n" are too far off the measurements. Lastly, and importantly, the time rate of change of the angle of attack is replaced by the torsion rate (Bergami et al., 2012).

Part 3 calculates the trailing-edge separated normal force coefficient (C_n). The lagging using Δs^{i-1} follows the same reasoning as explained for using Δt^{i-1} in Section 3.3.1.2. The if-else statement in lines 23 to 26 stems from Bangga's Section 2.6 and is based on a correction suggested by Larsen et al., 2007. Using line 24 for α_{eff} beyond values for which $f_n = 0$ causes a never-ending linear increase of $C_{n,\text{visc}}$. This does not reflect the steady polar. Hence, beyond $f_n = 0$, $C_{n,\text{visc}}$ is set to the polar's value. However, Bangga's use of the correction is not foolproof. In the paper's Section 2.6, Equation (85) is given as

$$C_{N_n}^{\text{INV}} = \begin{cases} \dfrac{dC_n}{d\alpha}\left(\alpha_n - \alpha_0^{\text{inv}}\right) & \text{if } f_n > 0 \\ 4C_n^{\text{VISC}} & \text{if } f_n = 0 \end{cases} \tag{3.35}$$

Yet, $C_{N_n}^{\text{INV}}$ is not used anywhere else in their paper. The only similar expression Bangga uses is the term of Equation (3.35) for the "if $f_n > 0$" case but with α_0^{visc} instead of α_0^{inv}. It is assumed that this is a typo in the paper because Bangga's correction would otherwise be in accord with Larsen's correction under the assumption that the "if $f_n = 0$" term replaces the "if $f_n > 0$" term in Bangga's Equation (18). Again, this assumption is made because $C_{N_n}^{\text{INV}}$ is not used except for its definition.

Part 4 calculates the leading-edge position utilising τ_v. The "if-else" condition is based on Section 2.5.1, Equation (74) in Bangga et al., 2020. There, however, the "$0.45\Delta tV/c$" must be corrected to "$0.45\Delta tV/(2c)$" (Leishman et al., 1989).

Parts 5, 6, and 7 do not deviate from Bangga et al., 2020 except for the changes described above and the rotation of the aerodynamic forces onto the xy coordinate system the "section" model uses for its momentum balance.

Algorithm 7 Implementation of the IAG 1st-order model

Require:

1. functions `C_d()`, `C_l()`, `C_m()` from polar
2. function `quasi_steady_flow()` from Algorithm 4
3. function `normal_separation_point()` from Equation (3.30) (or an interpolation function based on a pre-calculated set of (α,f_n) tuples)
4. function `C_t_visc()` from Equation (3.32)

Return:

1. unsteady aerodynamic forces and moment as a vector with components in $\begin{bmatrix} x & y & \gamma \end{bmatrix}$ direction or aerodynamic coefficients $\begin{bmatrix} C_d & C_l & C_m \end{bmatrix}$

arguments $\leftarrow (\boldsymbol{x}, \dot{\boldsymbol{x}}, \boldsymbol{u_0},$ ▷ *airfoil state*
$r_{\text{rot}}, c,$ ▷ *lengths*
$C_{n,\alpha}, \alpha_{0n,\text{inv}}, \alpha_{0n,\text{visc}},$ ▷ *aerodynamic parameters*
$A_1, A_2, b_1, b_2, K_\alpha, K_{\text{fc}}, K_v, a,$ ▷ *general algorithm parameters*
$T_p, T_{\text{bl}}, T_v, T_{v,\text{decay}}, T_{\text{mu}}, T_{\text{md}})$ ▷ *algorithm time constants*

1: **function** `DYNAMIC_STALL_FIRST_ORDER_IAG`(i, arguments)
2: ▷ *Part 1: general calculations* ◁
3: $\phi_{\text{qs}}, u_x, u_y \leftarrow$ `quasi_steady_flow`($\dot{\boldsymbol{x}}, x_\gamma, \boldsymbol{u}_0, r_{\text{rot}}$)
4: $u \leftarrow \sqrt{u_x^2 + u_y^2}$

continuation on line 5 (next page)

Implementation of the IAG 1st-order model – continued

continued from line 4 (previous page)

5: $\alpha^i_{\text{qs}} \leftarrow \phi_{\text{qs}} - x_\gamma$

6: $\Delta s^i \leftarrow \frac{2\Delta t^i u}{c}$

7: ▷ *Part 2: unsteady attached flow* ◁

8: $\Delta\alpha_{\text{qs}} \leftarrow \alpha^i_{\text{qs}} - \alpha^{i-1}_{\text{qs}}$

9: $X^i_{\text{lag}} \leftarrow X^{i-1}_{\text{lag}} \exp\left(-b_1 \Delta s^{i-1}\right) + \Delta\alpha_{\text{qs}} A_1 \exp\left(-0.5 b_1 \Delta s^{i-1}\right)$

10: $Y^i_{\text{lag}} \leftarrow Y^{i-1}_{\text{lag}} \exp\left(-b_2 \Delta s^{i-1}\right) + \Delta\alpha_{\text{qs}} A_2 \exp\left(-0.5 b_2 \Delta s^{i-1}\right)$

11: $\alpha_{\text{eff}} \leftarrow \alpha^i_{\text{qs}} - X^i_{\text{lag}} - Y^i_{\text{lag}}$

12: $C_{n,\text{c}} \leftarrow C_{n,\alpha}\left(\alpha_{\text{eff}} - \alpha_{0n,\text{inv}}\right)$ ▷ *Circulatory contribution; not a function call*

13: $D^i_i \leftarrow D^{i-1}_i \exp\left(\frac{-a\Delta t^i}{K_\alpha c}\right) - (\dot{x}^i_\gamma - \dot{x}^{i-1}_\gamma) \exp\left(\frac{-a\Delta t^i}{2K_\alpha c}\right)$ ▷ *-(...) because of coordinate system*

14: $C_{n,\text{i}} \leftarrow -\frac{4K_\alpha c}{u}\left(\dot{x}^i_\gamma + D^i_i\right)$ ▷ *Impulsive contribution;* $-\dot{x}_\gamma$ *because of coordinate system*

15: $C^i_{n,\text{pot}} \leftarrow C_{n,\text{c}} + C_{n,\text{i}}$ ▷ *Add circulatory and impulsive*

16: ▷ *Part 3: nonlinear trailing-edge separation* ◁

17: $D^i_p \leftarrow D^{i-1}_p \exp\left(-\frac{\Delta s^{i-1}}{T_p}\right) + (C^i_{n,\text{pot}} - C^{i-1}_{n,\text{pot}}) \exp\left(-\frac{\Delta s^{i-1}}{2T_p}\right)$

18: $C_{n,\text{sEq}} \leftarrow C^i_{n,\text{pot}} - D^i_p$

19: $\alpha_{\text{sEq}} \leftarrow C_{n,\text{sEq}}/C_{n,\alpha} + \alpha_{0n,\text{inv}}$

20: $f^i_n \leftarrow \texttt{normal\_separation\_point}(\alpha_{\text{sEq}})$

21: $D^i_{n,\text{bl}} \leftarrow D^{i-1}_{n,\text{bl}} \exp\left(-\frac{\Delta s^{i-1}}{T_{\text{bl}}}\right) + (f^i_n - f^{i-1}_n) \exp\left(-\frac{\Delta s^{i-1}}{2T_{\text{bl}}}\right)$

22: $f^i_{n,\text{Dp}} \leftarrow f^i_n - D^i_{n,\text{bl}}$

23: **if** $f^i_{n,\text{Dp}} \neq 0$ ▷ *Unsteady trailing-edge separated contribution*

24: $\quad C^i_{n,\text{visc}} \leftarrow C_{n,\alpha}(\alpha_{\text{eff}} - \alpha_{0n,\text{visc}}) \left(\frac{1+\sqrt{f_{n,\text{Dp}}}}{2}\right)^2$

25: **else**

26: $\quad C^i_{n,\text{visc}} \leftarrow \texttt{C\_l}(\alpha_{\text{eff}})$ ▷ *Function call.*

27: $C_{n,\text{f}} \leftarrow C^i_{n,\text{visc}} + C_{n,\text{i}}$

28: $C_{t,\text{f}} \leftarrow \texttt{C\_t\_visc}(\alpha_{\text{sEq}})$

29: ▷ *Part 4: leading-edge vortex position* ◁

30: $\tau^i_v \leftarrow \tau^{i-1}_v$

31: **if** $C_{n,\text{sEq}} > C_{n,\text{crit}}$

32: $\quad \tau^i_v \leftarrow \tau^i_v + 0.45\Delta s^{i-1}$

33: **else if** $C_{n,\text{sEq}} < C_{n,\text{crit}}$ **and** $\Delta\alpha_{\text{qs}} \geq 0$

34: $\quad \tau^i_v \leftarrow \tau^i_v \exp\left(-\Delta s^{i-1}\right)$

35: ▷ *Part 5: leading-edge vortex lift* ◁

36: $C^i_{n,\text{v,instant}} \leftarrow C_{n,\text{c}} \left(1 - \left(\frac{1+\sqrt{f^i_{n,\text{Dp}}}}{2}\right)^2\right)$

37: $C^i_{n,\text{v}} \leftarrow C^{i-1}_{n,\text{v}} \exp\left(\frac{-\Delta s^{i-1}}{T_v}\right)$ ▷ *Vortex contribution*

38: **if** $0 < \tau^i_v < T_{v,\text{decay}}$

39: $\quad C^i_{n,\text{v}} \leftarrow C^i_{n,\text{v}} + \left(C^i_{n,\text{v,instant}} - C^{i-1}_{n,\text{v,instant}}\right) \exp\left(-\frac{\Delta s^{i-1}}{2T_v}\right)$ ▷ *Vortex contribution*

continuation on line 40 (next page)

Implementation of the IAG 1st-order model – second continuation

continued from line 39 (previous page)

▷ *Part 6: moment coefficient* ◁

$C^i_{m,\mathsf{f}} \leftarrow \texttt{C\_m}(\alpha_{\mathsf{sEq}})$ ▷ *Polar contribution*

$r_p \leftarrow K_v \left(1 - \cos\left(\pi \tau^i_v / T_{v,\mathsf{decay}}\right)\right)$ ▷ *Idealised centre of pressure*

$C_{m,\mathsf{v}} \leftarrow -r_p C^i_{n,\mathsf{v}}$ ▷ *vortex contribution*

$C_{\mathsf{Pf}} \leftarrow K_{\mathsf{fc}} C_{n,\mathsf{crit}}$

if $\tau^i_v < T_{v,\mathsf{decay}}$ **and** $\Delta\alpha_{\mathsf{qs}} \geq 0$

  $\mathsf{tmp} \leftarrow C_{\mathsf{Pf}} \left(C^i_{n,\mathsf{v,instant}} - C^{i-1}_{n,\mathsf{v,instant}}\right)$

  $C^i_{m,\mathsf{c}} \leftarrow C^{i-1}_{m,\mathsf{c}} \exp\left(\frac{-\Delta s^{i-1}}{T_{\mathsf{mu}}}\right) - \mathsf{tmp} \exp\left(\mathsf{tmp}/2\right)$ ▷ *circulatory contribution; uses T_{mu}!*

else if $\Delta\alpha_{\mathsf{qs}} < 0$

  $\mathsf{tmp} \leftarrow C_{\mathsf{Pf}}(C^i_{n,\mathsf{v,instant}} - C^{i-1}_{n,\mathsf{v,instant}})$

  $C^i_{m,\mathsf{c}} \leftarrow C^{i-1}_{m,\mathsf{c}} \exp\left(\frac{-\Delta s^{i-1}}{T_{\mathsf{md}}}\right) - \mathsf{tmp} \exp\left(\mathsf{tmp}/2\right)$ ▷ *circulatory contribution; uses T_{md}!*

else

  $C^i_{m,\mathsf{c}} \leftarrow C^{i-1}_{m,\mathsf{c}}$ ▷ *circulatory contribution*

▷ *Part 7: combining everything* ◁

$$\boldsymbol{c}_{\mathsf{coeffs}} \leftarrow \begin{bmatrix} C_{t,\mathsf{f}} \\ C_{n,\mathsf{f}} + C^i_{n,\mathsf{v}} \\ C^i_{m,\mathsf{f}} + C_{m,\mathsf{v}} + C^i_{m,\mathsf{c}} \end{bmatrix}$$

$$\boldsymbol{R}_{\mathsf{dl}} \leftarrow \begin{bmatrix} -\cos\left(\alpha^i_{\mathsf{qs}}\right) & \sin\left(\alpha^i_{\mathsf{qs}}\right) & 0 \\ \sin\left(\alpha^i_{\mathsf{qs}}\right) & \cos\left(\alpha^i_{\mathsf{qs}}\right) & 0 \\ 0 & 0 & -1 \end{bmatrix}$$ ▷ *The "-1" is based on coordinate system differences.*

$\boldsymbol{c}_{\mathsf{coeffs}} \leftarrow \boldsymbol{R}_{\mathsf{dl}} \boldsymbol{c}_{\mathsf{coeffs}}$ ▷ *Now as $\begin{bmatrix} C_d & C_l & C_m \end{bmatrix}^T$*

if $c_{\mathsf{coeffs},d} < \texttt{C\_d}(\alpha_{\mathsf{sEq}})$ **and** $\alpha_{\mathsf{sEq}} < \alpha_{\mathsf{crit}}$

  $c_{\mathsf{coeffs},d} \leftarrow \texttt{C\_d}(\alpha_{\mathsf{sEq}})$

if return_coeffs is True

  return $\boldsymbol{c}_{\mathsf{coeffs}}$

$$\boldsymbol{R}_{\mathsf{xy}} \leftarrow \begin{bmatrix} \cos\left(-\phi_{\mathsf{qs}}\right) & \sin\left(-\phi_{\mathsf{qs}}\right) & 0 \\ -\sin\left(-\phi_{\mathsf{qs}}\right) & \cos\left(-\phi_{\mathsf{qs}}\right) & 0 \\ 0 & 0 & 1 \end{bmatrix}$$ ▷ *Projects $\begin{bmatrix} C_d & C_l & C_m \end{bmatrix}^T$ onto $\begin{bmatrix} C_x & C_y & C_m \end{bmatrix}^T$*

$q \leftarrow \frac{1}{2}\rho u^2$

$\boldsymbol{D} \leftarrow \mathsf{diag}\left(\begin{bmatrix} c & c & c^2 \end{bmatrix}\right)$ ▷ *Diagonal matrix with the stated values on the diagonal.*

return $q \boldsymbol{D} \boldsymbol{R}_{\mathsf{xy}} \boldsymbol{c}_{\mathsf{coeffs}}$

AEROHOR

The AEROHOR dynamic stall model is the unpublished dynamic stall model currently implemented for the aeroelastic tool AEROHOR from Meng et al., 2024. For the remainder of this thesis, AEROHOR does not refer to the overall aeroelastic tool but to the dynamic stall model it has implemented. The model combines the 1st-order IAG model described in Bangga et al., 2020 and X. Liu et al., 2015. Not all parts of the "section"s implementation of the 1st-order IAG model from Section 3.3.1.4 are used in the AEROHOR model. It is implemented to support the outlook stated in Meng et al., 2024 to investigate the influence of dynamic stall on stability analyses of floating offshore wind turbines. By applying the AERHOR model in an aeroelastic code on the section level the authors Meng et al., 2024 can assess their current dynamic stall's performance.

As an overview, the AEROHOR model includes unsteady attached, unsteady trailing-edge separated, and unsteady leading-edge separated vortex contributions. Compressibility effects are modelled for the lagging of the quasi-steady angle of attack (α_{qs}) and for impulsive force contributions. The model has a separation point (f) for the normal force coefficient (C_n) and tangential force coefficient (C_t) each. An aerodynamic moment is not calculated. The implementation for the "section" model is shown in Algorithm 8.

Part 1 calculates general parameters. The only difference between AEROHOR and the section's implementation is calculating Δs. In AEROHOR, this is done with the wind inflow magnitude (u_0). In the implementation, the movement of the airfoil is included by using the quasi-steady inflow magnitude (u). The calculation for K_α is from Leishman et al., 1989.

Part 2 first lags α_{qs} to obtain the effective angle of attack (α_{eff}) and then calculates the potential flow C_n and C_t. The calculation of potential flow tangential force coefficient ($C_{t,\text{p}}$) comes from X. Liu et al., 2015, the rest from Bangga et al., 2020. There exist multiple changes from AEROHOR to the implementation:

1. The lagging values X_{lag} and Y_{lag} are based on Δs^{i-1} (section) instead of Δs^i (AEROHOR). This is explained in Section 3.3.1.2 for Δt but the argumentation holds for Δs. Additionally, the change for s from Part 1 applies.
2. The impulsive normal force coefficient ($C_{n,\text{i}}$) is based on the pitch rate $\dot{x}_\gamma$ (Bergami et al., 2012) and quasi-steady inflow magnitude (u) instead of the rate of change of α_{qs} and the wind inflow magnitude (u_0). u is used to represent the actual travelled distance of the airfoil relative to the flow.
3. The airfoil's normal force slope ($C_{n,\alpha}$) is used instead of 2π.

Part 3 introduces the effects of trailing-edge separation using two separation points. The basic procedure to affect C_n with trailing edge separation stems from Bangga et al., 2020, Section 2.1.2. This was adapted in X. Liu et al., 2015, Section 1, to allow negative f_n values. The use of f_t comes from the same paper. In it, both are defined as

$$f_n = t_n^2 \operatorname{sgn}(t_n) \tag{3.36}$$

$$f_t = t_t^2 \operatorname{sgn}(t_t) \tag{3.37}$$

$$t_n = 2\sqrt{\frac{C_n(\alpha)}{C_{n,\alpha}(\alpha - \alpha_0)}} - 1 \tag{3.38}$$

$$t_t = \frac{C_t}{C_{n,\alpha}(\alpha - \alpha_0)\tan(\alpha)} \tag{3.39}$$

More information about the tangential separation point is given in Section 3.3.1.3. The AEROHOR model does not have a modelling approach for fully-separated flow. If the flow does become fully-separated the model continues using the Kirchhoff equations with the problems of doing so explained in Section 3.3.1.3. Lastly, also for the lagging of the separation points, Δs^{i-1} is used instead of Δs^i.

Parts 4 and 5 calculate the leading-edge vortex position and its influence on C_n. The condition to return τ_v to zero is taken from Pereira, 2010. At last, all force coefficients are combined in Part 6 and either returned as is or multiplied with the dynamic pressure (q) and the chord to return the aerodynamic forces along the x and y axis.

Algorithm 8 Implementation of the dynamic stall model used in AEROHOR

Require:

1. function `quasi_steady_flow()` from Algorithm 4
2. function `normal_separation_point()` from Equation (3.36) (or an interpolation function based on a pre-calculated set of (α,f_n) tuples)
3. function `tangential_separation_point()` from Equation (3.37) (or an interpolation function based on a pre-calculated set of (α,f_t) tuples)

Return:

1. unsteady aerodynamic forces and moment as a vector with components in $\begin{bmatrix} x & y & \gamma \end{bmatrix}$ direction or aerodynamic coefficients $\begin{bmatrix} C_d & C_l & 0 \end{bmatrix}$

arguments $\leftarrow (\boldsymbol{x},\ \dot{\boldsymbol{x}},\ \boldsymbol{u_0},$ ▷ *airfoil state*
$r_{\text{rot}},\ c,$ ▷ *lengths*
$C_{n,\alpha},\ \alpha_{0n,\text{inv}},\ \alpha_{0n,\text{visc}},$ ▷ *aerodynamic parameters*
$A_1,\ A_2,\ b_1,\ b_2,\ K_{\text{fc}},\ a,$ ▷ *general algorithm parameters*
$T_p,\ T_{\text{bl}},\ T_v,\ T_{v,\text{decay}})$ ▷ *algorithm time constants*

function DYNAMIC_STALL_AEROHOR(i, arguments)
▷ *Part 1: general calculations* ◁
$\phi_{\text{qs}}, u_x, u_y \leftarrow$ `quasi_steady_flow`$(\dot{\boldsymbol{x}},\ x_\gamma,\ \boldsymbol{u}_0,\ r_{\text{rot}})$
$u \leftarrow \sqrt{u_x^2 + u_y^2}$
$\alpha^i_{\text{qs}} \leftarrow \phi_{\text{qs}} - x_\gamma$
$\Delta s^i \leftarrow \frac{2\Delta t^i u}{c}$
$\beta \leftarrow \sqrt{1-(u/a)^2}$
$K_\alpha \leftarrow 0.75/(1 - u/a + \pi\beta^2(u/a)^2(A_1 b_1 + A_2 b_2))$
▷ *Part 2: unsteady attached flow* ◁
$\Delta\alpha_{\text{qs}} \leftarrow \alpha^i_{\text{qs}} - \alpha^{i-1}_{\text{qs}}$
$X^i_{\text{lag}} \leftarrow X^{i-1}_{\text{lag}} \exp\left(-b_1 \Delta s^{i-1}\beta^2\right) + \Delta\alpha_{\text{qs}} A_1 \exp\left(-0.5 b_1 \Delta s^{i-1}\beta^2\right)$
$Y^i_{\text{lag}} \leftarrow Y^{i-1}_{\text{lag}} \exp\left(-b_2 \Delta s^{i-1}\beta^2\right) + \Delta\alpha_{\text{qs}} A_2 \exp\left(-0.5 b_2 \Delta s^{i-1}\beta^2\right)$
$\alpha_{\text{eff}} \leftarrow \alpha^i_{\text{qs}} - X^i_{\text{lag}} - Y^i_{\text{lag}}$
$C_{n,\text{c}} \leftarrow C_{n,\alpha}\,(\alpha_{\text{eff}} - \alpha_{0n,\text{inv}})$ ▷ *Circulatory contribution; not a function call*
$D^i_i \leftarrow D^{i-1}_i \exp\left(\frac{-a\Delta t^{i-1}}{K_\alpha c}\right) - (\dot{x}^i_\gamma - \dot{x}^{i-1}_\gamma)\exp\left(\frac{-a\Delta t^{i-1}}{2K_\alpha c}\right)$ ▷ *-(...) because of coordinate system*
$C_{n,\text{i}} \leftarrow \frac{4K_\alpha c}{u}(-\dot{x}^i_\gamma - D^i_i)$ ▷ *Impulsive contribution; $-\dot{x}_\gamma$ because of coordinate system*
$C^i_{n,\text{pot}} \leftarrow C^i_{nc} + C^i_{n,\text{i}}$ ▷ *add circulatory and impulsive*
$C^i_{t,\text{pot}} \leftarrow C^i_{n,\text{pot}} \tan(\alpha_{\text{eff}})$
▷ *Part 3: trailing-edge separated flow* ◁
$D^i_p \leftarrow D^{i-1}_p \exp\left(-\frac{\Delta s^{i-1}}{T_p}\right) + (C^i_{n,\text{pot}} - C^{i-1}_{n,\text{pot}})\exp\left(-\frac{\Delta s^{i-1}}{2T_p}\right)$
$C_{n,\text{sEq}} \leftarrow C^i_{n,\text{pot}} - D^i_p$
$\alpha_{\text{sEq}} \leftarrow C_{n,\text{sEq}}/C_{n,\alpha} + \alpha_{0n,\text{inv}}$
$f^i_n \leftarrow$ `normal_separation_point`(α_{sEq})
$f^i_t \leftarrow$ `tangential_separation_point`(α_{sEq})
$D^i_{n,\text{bl}} \leftarrow D^{i-1}_{n,\text{bl}} \exp\left(-\frac{\Delta s^{i-1}}{T_{\text{bl}}}\right) + (f^i_n - f^{i-1}_n)\exp\left(-\frac{\Delta s^{i-1}}{2T_{\text{bl}}}\right)$
$D^i_{t,\text{bl}} \leftarrow D^{i-1}_{t,\text{bl}} \exp\left(-\frac{\Delta s^{i-1}}{T_{\text{bl}}}\right) + (f^i_t - f^{i-1}_t)\exp\left(-\frac{\Delta s^{i-1}}{2T_{\text{bl}}}\right)$
$f^i_{n,\text{Dp}} \leftarrow f^i_n - D^i_{n,\text{bl}}$
$f^i_{t,\text{Dp}} \leftarrow f^i_t - D^i_{t,\text{bl}}$
continuation on line 29 (next page)

Implementation of the AEROHOR model – continued

continued from line 28

29: $C_{n,\text{visc}} \leftarrow C^i_{nc}\left(\frac{1+\text{sgn}\left(f^i_{n,\text{Dp}}\right)\sqrt{|f^i_{n,\text{Dp}}|}}{2}\right)^2$ ▷ *Not a function call.*

30: $C^i_{n,\text{f}} \leftarrow C_{n,\text{visc}} + C^i_{n,\text{i}}$

31: $C_{t,\text{f}} \leftarrow C^i_{t,\text{pot}}\,\text{sgn}\left(f^i_{t,\text{Dp}}\right)\sqrt{|f^i_{t,\text{Dp}}|}$

32: ▷ *Part 4: leading-edge vortex position* ◁

33: **if** $C^i_{nsEq} \geq C_{n,\text{crit}}$

34: $\quad \tau^i_v \leftarrow \tau^{i-1}_v + 0.45\Delta s^{i-1}$

35: **else**

36: $\quad$ **if** $\Delta\alpha_{\text{qs}} \geq 0$

37: $\quad\quad \tau^i_v \leftarrow 0$

38: $\quad$ **else**

39: $\quad\quad \tau^i_v \leftarrow \tau^{i-1}_v + 0.45\Delta s^{i-1}$

40: ▷ *Part 5: leading-edge vortex lift* ◁

41: $C^i_{n,\text{v,instant}} \leftarrow C_{n,\text{c}}\left(1 - \frac{1}{4}\left(1 + \sqrt{f^i_{n,\text{Dp}}}\right)^2\right)$

42: $C^i_{n,\text{v}} \leftarrow C^{i-1}_{n,\text{v}}\exp\left(\frac{-\Delta s^{i-1}}{T_v}\right)$ ▷ *Vortex contribution*

43: **if** $0 < \tau^i_v$ **and** $\tau^i_v < T_{v,\text{decay}}$

44: $\quad C^i_{n,\text{v}} \leftarrow C^i_{n,\text{v}} + \left(C^i_{n,\text{v,instant}} - C^{i-1}_{n,\text{v,instant}}\right)\exp\left(-\frac{\Delta s^{i-1}}{2T_v}\right)$

45: ▷ *Part 6: combining everything* ◁

46: $\boldsymbol{c}_{\text{coeffs}} \leftarrow \begin{bmatrix} C_{t,\text{f}} \\ C_{n,\text{f}} + C^i_{n,\text{v}} \\ 0 \end{bmatrix}$ ▷ *The AEROHOR model does (currently) not implement an aerodynamic moment.*

47: $\boldsymbol{R}_{\text{dl}} \leftarrow \begin{bmatrix} -\cos(\alpha_{\text{qs}}) & \sin(\alpha_{\text{qs}}) & 0 \\ \sin(\alpha_{\text{qs}}) & \cos(\alpha_{\text{qs}}) & 0 \\ 0 & 0 & 0 \end{bmatrix}$

48: $\boldsymbol{c}_{\text{coeffs}} \leftarrow \boldsymbol{R}_{\text{dl}}\boldsymbol{c}_{\text{coeffs}} + \begin{bmatrix} C_{d,0} & 0 & 0 \end{bmatrix}^T$ ▷ *Now as* $\begin{bmatrix} C_d & C_l & C_m \end{bmatrix}^T$

49: **if** return_coeffs is True

50: $\quad$ **return** $\boldsymbol{c}_{\text{coeffs}}$

51: $\boldsymbol{R}_{\text{xy}} \leftarrow \begin{bmatrix} \cos(-\phi_{\text{qs}}) & \sin(-\phi_{\text{qs}}) & 0 \\ -\sin(-\phi_{\text{qs}}) & \cos(-\phi_{\text{qs}}) & 0 \\ 0 & 0 & 0 \end{bmatrix}$ ▷ *Projects* $\begin{bmatrix} C_d & C_l & 0 \end{bmatrix}^T$ *onto* $\begin{bmatrix} C_x & C_y & 0 \end{bmatrix}^T$

52: $q \leftarrow \frac{1}{2}\rho u^2$

53: $\boldsymbol{D} \leftarrow \text{diag}\left(\begin{bmatrix} c & c & 0 \end{bmatrix}\right)$ ▷ *Diagonal matrix with the stated values on the diagonal.*

54: **return** $q\boldsymbol{D}\boldsymbol{R}_{\text{xy}}\boldsymbol{c}_{\text{coeffs}}$

Hansen-Gaunaa-Madsen a lá openFAST

The here so-called Hansen-Gaunaa-Madsen a lá openFAST model, for the remainder called “HGM openFAST”, is the section’s implementation of the model described in Branlard et al., 2022 which is based on the model by Morten Hartvig Hansen et al., 2004 with some modifications. The HGM openFAST was implemented to represent a model that is widely accessible and potentially often used as part of openFAST. No changes were purposefully introduced in the implementation.

The HGM openFAST model models unsteady attached and unsteady trailing-edge separated flow. The state equations can be continuously integrated in time or discretised. The implementation uses the discretisation approach. The zero lift angle of attack ($\alpha_{0,\mathrm{l}}$) is found by linear interpolation of the polar values. The lift slope ($C_{l,\alpha}$) is the largest slope the C_l polar data has measured from $\alpha_{0,\mathrm{l}}$. Changes in the sign of values involving x_γ or $\dot{x}\gamma$ are due to coordinate system differences.

The implementation is detailed in Algorithm 9. Part 1 calculates general values. Part 2 calculates the unsteady attached potential flow lift coefficient ($C_{t,\mathrm{p}}$) including a torsion rate term. Part 3 calculates the lift coefficient affected by trailing edge separation. A torsion rate term is included, too. The handling of the separation influence is different from the previously explained 1st-order IAG and AEROHOR model. The Kirchhoff Equation (3.31) is again used to approximate the (unlagged) separation point based on the current equivalent steady angle of attack ($\alpha_{0,\mathrm{sEq}}$). However, the trailing-edge separated C_l is then calculated as an interpolation as seen in line 18. There, `C_l_fully_separated()` comes from

$$C_{l,\mathrm{sep}}(\alpha) = \begin{cases} \dfrac{C_l(\alpha) - C_{l,\alpha}(\alpha - \alpha_{0,\mathrm{l}}) f_{l,\mathrm{steady}}(\alpha)}{1 - f_{l,\mathrm{steady}}(\alpha)} & \text{if } 0 \leq f_{l,\mathrm{steady}}(\alpha) < 1 \\ \dfrac{C_l(\alpha)}{2} & \text{if } f_{l,\mathrm{steady}}(\alpha) = 1\,. \end{cases} \tag{3.40}$$

First, $f_{l,\mathrm{steady}}(\alpha)$ has to be calculated with Equation (3.31) and polar data. Then, Equation (3.40) is used to create the fully-separated polar. Exemplary plots can be seen in Section 3.3.2. Similar to the modelling approach in the 1st-order IAG model, the interpolation of the HGM openFAST model ensures that the Kirchhoff equation is not used outside of its validity range (refer to Section 3.3.1.3). In both modelling approaches, the polar lift coefficient is set to the polar value once $f_l = 0$. However, both approaches yield different results for fully separated flow, especially in the angle of attack range that is, under steady conditions, fully attached. Assuming an unsteady condition in which the flow is fully separated at an angle of attack that has $f_{l,\mathrm{steady}} = 1$ (around $\alpha_{0,\mathrm{l}}$), the Kirchhoff Equation (3.28) returns $C_l(\alpha_{\mathrm{eff}})/4$. The HGM openFAST model, however, returns $C_l(\alpha_{\mathrm{eff}})/2$. The author did not find literature about this large deviation of a factor two. A view of the deviation for a grid of angles of attack and separation points is given in Figure 3.8. As can be seen, the factor of two spans across the whole angle of attack range for $f_l = x_4 = 0$. The deviation is largest for angles of attack at the boundary of partially attached flow and for low separation point values irrespective of the angle of attack. However, the largest portion of the area shows a light green corresponding to a low deviation. Perhaps because of this, no greater focus has been placed on the issue.

Returning to the implementation, Parts 4 and 5 calculate the drag and moment coefficient, respectively. More information can be found in Morten Hartvig Hansen et al., 2004. At last, Part 6 combines all individual force and moment coefficients and returns them, or multiples the summed coefficients by the dynamic pressure (q) and the chord (c) (or c^2) to get the forces and moments. Those are then projected onto the coordinate system the “section” model uses for its momentum balance.

Algorithm 9 Implementation of the HGM a la openFAST model

Require:

1. functions `C_d()` and `C_m()` from polars
2. function `quasi_steady_flow()` from Algorithm 4
3. function `lift_separation_point()` from Equation (3.31)
4. function `C_l_fully_separated()` from Equation (3.40)

Return:

1. unsteady aerodynamic forces and moment as a vector with components in $\begin{bmatrix} x & y & \gamma \end{bmatrix}$ direction or aerodynamic coefficients $\begin{bmatrix} C_d & C_l & C_m \end{bmatrix}$

arguments $\leftarrow \big(\boldsymbol{x}, \dot{\boldsymbol{x}}, \boldsymbol{u_0},$ ▷ *airfoil state*
$r_{\text{rot}}, c,$ ▷ *lengths*
$C_{l,\alpha}, \alpha_{0n,\text{visc}},$ ▷ *aerodynamic parameters*
$A_1, A_2, b_1, b_2,$ ▷ *general algorithm parameters*
$T_p, T_f\big)$ ▷ *algorithm time constants*

function DYNAMIC_STALL_HGM_OPENFAST(i, arguments)

▷ *Part 1: general calculations* ◁

$\phi_{\text{qs}}, u_x, u_y \leftarrow$ `quasi_steady_flow`$(\dot{\boldsymbol{x}}, x_\gamma, \boldsymbol{u}_0, r_{\text{rot}})$

$u \leftarrow \sqrt{u_x^2 + u_y^2}$

$\alpha_{\text{qs}}^i \leftarrow \phi_{\text{qs}} - x_\gamma$

$T_u^i \leftarrow \frac{c}{2u}$

▷ *Part 2: unsteady attached flow* ◁

$\alpha_{\text{qs,avg}} \leftarrow 0.5\left(\alpha_{qs}^{i-1} + \alpha_{qs}^i\right)$

$X_{\text{lag}}^i \leftarrow X_{\text{lag}}^{i-1} \exp\left(-\frac{\Delta t^{i-1} b_1}{T_u^{i-1}}\right) + \alpha_{\text{qs,avg}} A_1 \left(1 - \exp\left(-\frac{\Delta t^{i-1} b_1}{T_u^{i-1}}\right)\right)$

$Y_{\text{lag}}^i \leftarrow Y_{\text{lag}}^{i-1} \exp\left(-\frac{\Delta t^{i-1} b_2}{T_u^{i-1}}\right) + \alpha_{\text{qs,avg}} A_2 \left(1 - \exp\left(-\frac{\Delta t^{i-1} b_2}{T_u^{i-1}}\right)\right)$

$\alpha_{\text{eff}} \leftarrow \alpha_{qs}^i(1 - A_1 - A_2) + X_{\text{lag}}^i + Y_{\text{lag}}^i$

$C_{l,\text{pot}}^i \leftarrow C_{l,\alpha}(\alpha_{\text{eff}} - \alpha_{0,l}) - \pi T_u^i \dot{x}_\gamma$ ▷ *Potential flow.*

▷ *Part 3: trailing-edge separated flow* ◁

$x_3^i \leftarrow x_3^{i-1} \exp\left(-\frac{\Delta t^{i-1}}{T_u^{i-1} T_p}\right) + 0.5\left(C_{l,\text{pot}}^{i-1} + C_{l,\text{pot}}^i\right)\left(1 - \exp\left(-\frac{\Delta t^{i-1}}{T_u^{i-1} T_p}\right)\right)$

$\alpha_{\text{eq}} \leftarrow \frac{x_3^i}{C_{l,\alpha}} + \alpha_{0,l}$

$f_l^i \leftarrow$ `lift_separation_point`(α_{eq})

$x_4^i \leftarrow x_4^{i-1} \exp\left(-\frac{\Delta t^{i-1}}{T_u^{i-1} T_f}\right) + 0.5\left(f_l^{i-1} + f_l^i\right)\left(1 - \exp\left(-\frac{\Delta t^{i-1}}{T_u^{i-1} T_f}\right)\right)$

$C_{l,\text{c}} \leftarrow x_4^i C_{l,\alpha}(\alpha_{\text{eff}} - \alpha_{0,l}) + (1 - x_4^i)$`C_l_fully_separated`$(\alpha_{\text{eff}})$ ▷ *Function call.*

$C_{l,\text{nc}} \leftarrow -\pi T_u^i \dot{x}_\gamma$ ▷ *Non-circulatory contribution*

▷ *Part 4: drag calculation* ◁

$C_d \leftarrow$ `C_d`(α_{eff}) ▷ *Function call.*

$C_{d,\text{sep}} \leftarrow (C_{d,\text{s}} - C_{d,0})\left(\left(\frac{\sqrt{f_l^i} - \sqrt{x_4^i}}{2}\right) - \left(\frac{f_l^i - x_4^i}{4}\right)\right)$

$C_{d,\text{c}} \leftarrow \left(\alpha_{\text{qs}} - \alpha_{\text{eff}} - T_u^i \dot{x}_\gamma\right) C_{l,\text{c}}$ ▷ *Induced (circulatory) contribution*

▷ *Part 5: moment calculation* ◁

$C_{m,\text{s}} \leftarrow$ `C_m`(α_{eff}) ▷ *Function call.*

$C_{m,\text{nc}} \leftarrow 0.5\pi T_u^i \dot{x}_\gamma$

continuation on line 27 (next page)

Implementation of the HGM a la openFAST model – continued

continued from line 26

27: ▷ *Part 6: combining everything* ◁

28: $\boldsymbol{c}_{\text{coeffs}} \leftarrow \begin{bmatrix} C_{l,\text{c}} + C_{l,\text{nc}} \\ C_{d,\text{s}} + C_{d,\text{c}} + C_{d,\text{sep}} \\ C_{m,\text{s}} + C_{m,\text{nc}} \end{bmatrix}$

29: **if** return_coeffs is True

30: **return** $\boldsymbol{c}_{\text{coeffs}}$

31: $\boldsymbol{R} \leftarrow \begin{bmatrix} \cos(-\alpha_{\text{qs}} - x_\gamma) & \sin(-\alpha_{\text{qs}} - x_\gamma) & 0 \\ -\sin(-\alpha_{\text{qs}} - x_\gamma) & \cos(-\alpha_{\text{qs}} - x_\gamma) & 0 \\ 0 & 0 & -1 \end{bmatrix}$ ▷ *The "−" is based on coordinate system differences.*

32: $q \leftarrow \frac{1}{2}\rho u^2$

33: $\boldsymbol{D} \leftarrow \text{diag}\left(\begin{bmatrix} c & c & c^2 \end{bmatrix}\right)$ ▷ *Diagonal matrix with the stated values on the diagonal.*

34: **return** $q\boldsymbol{D}\boldsymbol{R}\boldsymbol{c}_{\text{coeffs}}$

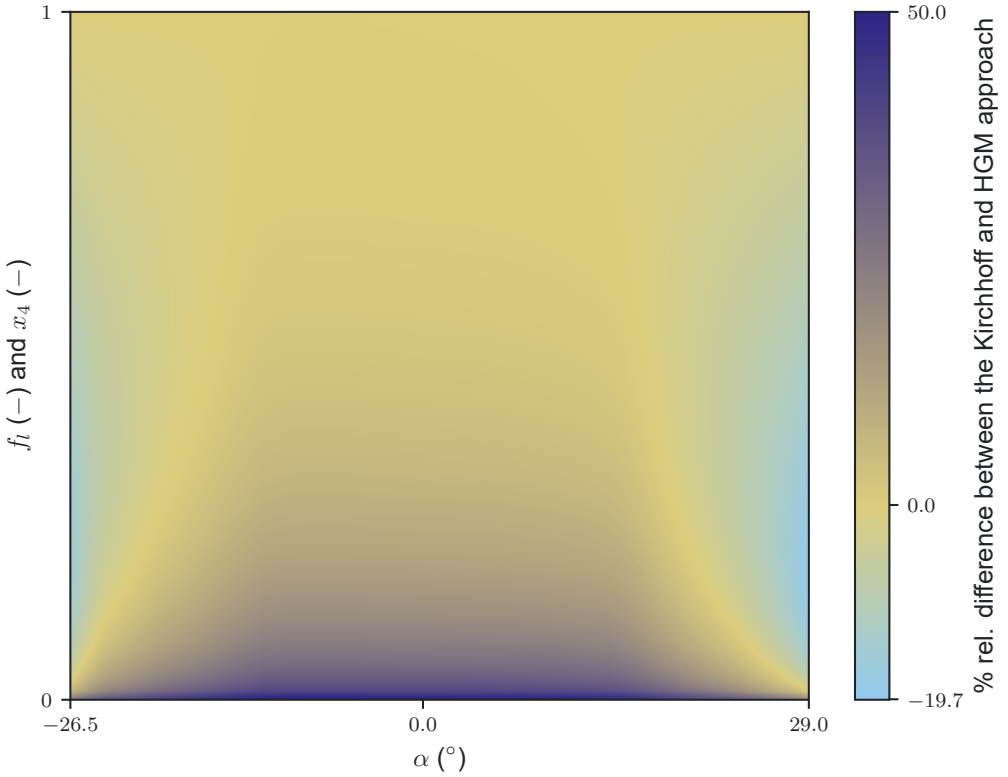

Figure 3.8: The relative difference between the trailing-edge separated lift coefficient using Kirchhoff's equation and the HGM approach for a grid of angles of attack and separation point values. The plotted values are $(C_{l,\text{HGM}} - C_{l,\text{Kirchhoff}})/C_{l,\text{HGM}}$ where $C_{l,\text{Kirchhoff}}$ comes from Equation (3.28) and $C_{l,\text{HGM}}$ from Algorithm 9, line 18. For the HGM approach, x_4 represents the separation point. The polar data is based on the FFA-W3-221 airfoil. Outside of the shown angle of attack range the flow is fully separated and hence the Kirchhoff equation is invalid.

Hansen-Gaunaa-Madsen f-scaled

The here so-called "HGM f-scaled" is the model described in Branlard et al., 2022 (and in Section 3.3.1.6) but the lagging of the quasi-steady angle of attack (α_{qs}) is done according to Pirrung et al., 2018. This model is implemented in HAWC2. Overall, the base model is again that of Morten Hartvig Hansen et al., 2004. As such, unsteady attached and unsteady separated flow are modelled. It was decided to implement this model after simulations using the HGM openFAST model showed unsteady lift coefficients ($C_{l,\text{us}}$s) and unsteady drag coefficients ($C_{d,\text{us}}$s) values in access of eight at effective angle of attacks (α_{eff}s) around $\alpha_{\text{eff}} = 90°$. This happens when a low degree of separation (large f) is carried to large α_{eff} quickly enough for f not to drop much. Then, the unsteady attached flow C_l contribution (Algorithm 9, first summand of line 18) becomes large. In the meantime, there were substantial differences between the quasi-steady angle of attack (α_{qs}) and effective angle of attack (α_{eff}) for high α_{qs} which gave rise to unrealistic large induced drag values. The next paragraphs analyse only the differences between the HGM f-scaled and HGM openFAST model. Hence, most of the HGM f-scaled explanation can be found in Section 3.3.1.6. The HGM f-scaled's implementation is detailed in Algorithm 10.

Interestingly, choosing a different modelling approach for the lagging of α_{qs} for α_{eff} to lower their difference can also reduce the unreasonable high $C_{l,\text{us}}$s. As stated in the paragraph above Equation (3.25), the vorticity in the wake causes the lagging between α_{qs} and α_{eff}. Pirrung et al., 2018 argue that different degrees of lagging between attached and fully separated flow should be considered because of wake differences. Thus, they propose to scale the lagging of α_{qs} for α_{eff} with the degree of separation as seen in Algorithm 10, lines 8 to 11. In essence, the difference between α_{qs} and α_{eff} is tried to be reduced at large separation conditions (small x_4 values) by decreasing the subtraction part $(X^i_{\text{lag}} - Y^i_{\text{lag}})/u^i$. This decreases the unrealistic large induced drag values. The reduction in the maximum $C_{d,\text{us}}$ and $C_{l,\text{us}}$ is more complex and dependent on the $f(\alpha)$ distribution and the lagging of Part 3. Hence, the effects are visualised in Figure 3.9 for a slow increase of α_{qs} and in Figure 3.10 for a fast increase in α_{qs}. As can be seen, decreasing the lagging between α_{qs} and α_{eff} has a considerable decreasing effect on the lagging between x_4 and α_{eff}. Thus, the maximum unsteady attached lift coefficient contribution decreases for large α_{eff}.

As stated, the connection between the lagging of α_{qs} for α_{eff} and the lagging between α_{eff} and x_4 is complex. A decrease in the lag between α_{qs} and α_{eff} might initially indicate greater unsteady attached lift coefficients (since α_{eff} will be larger) but the simultaneous faster decrease in f_l (which is based on α_{eff}) and thus x_4 seems to offset that. This effect is greater the slower the increase in α_{qs}. Without a detailed analysis, the author assumes that this is largely caused by the steep decrease of f_l after the separation process begins. This means a large decrease in f_l follows even a small increase in α_{qs}. The small increase in α_{qs} is exactly what is achieved with the HGM f-scaled model compared to the HGM openFAST model. A smaller f_l value decreases x_4 which further lowers the difference between α_{qs} and α_{eff}, thus closing the positive-feedback loop that lowers x_4 further. Increasing α_{qs} faster leaves this loop less time to unfold, hence decreasing the difference between the HGM openFAST and HGM f-scaled x_4 response. Nonetheless, even for α_{qs} changes of $\approx 60°$, the HGM f-scaled model reduces the unsteady attached lift force contribution considerably and reasonably.

Algorithm 10 Implementation of the HGM f-scaled model

Require:

1. functions `C_d()` and `C_m()` from polars
2. function `quasi_steady_flow()` from Algorithm 4
3. function `lift_separation_point()` from Equation (3.31)
4. function `C_l_fully_separated()` from Equation (3.40)

Return:

1. unsteady aerodynamic forces and moment as a vector with components in $\begin{bmatrix} x & y & \gamma \end{bmatrix}$ direction or aerodynamic coefficients $\begin{bmatrix} C_d & C_l & C_m \end{bmatrix}$

continuation on the next page

Implementation of the HGM f-scaled model – continued

continued from the previous page

arguments $\leftarrow (\boldsymbol{x},\, \dot{\boldsymbol{x}},\, \boldsymbol{u_0},$ ▷ *airfoil state*
$r_{\text{rot}},\, c,$ ▷ *lengths*
$C_{l,\alpha},\, \alpha_{0n,\text{visc}},$ ▷ *aerodynamic parameters*
$A_1,\, A_2,\, b_1,\, b_2,$ ▷ *general algorithm parameters*
$T_p,\, T_f)$ ▷ *algorithm time constants*

function DYNAMIC_STALL_HGM_F_SCALED(i, arguments)

▷ *Part 1: general calculations* ◁

$\phi_{\text{qs}}, u_x, u_y \leftarrow$ quasi_steady_flow($\dot{\boldsymbol{x}}$, x_γ, $\boldsymbol{u}_0$, r_{rot})

$u^i \leftarrow \sqrt{u_x^2 + u_y^2}$

$\alpha_{\text{qs}}^i \leftarrow \phi_{\text{qs}} - x_\gamma$

$T_u^i \leftarrow \frac{c}{2u^i}$

▷ *Part 2: unsteady attached flow lift* ◁

$U_{34} \leftarrow \alpha_{qs}^i u^i - \alpha_{qs}^{i-1} u^{i-1}$

$X_{\text{lag}}^i \leftarrow X_{\text{lag}}^{i-1} \exp\left(-\frac{\Delta t^{i-1} b_1}{T_u^{i-1}}\right) + U_{34} \frac{A_1}{b_1} \frac{T_u^{i-1}}{\Delta t^{i-1}} \left(1 - \exp\left(-\frac{\Delta t^{i-1} b_1}{T_u^{i-1}}\right)\right) x_4^{i-1}$

$Y_{\text{lag}}^i \leftarrow Y_{\text{lag}}^{i-1} \exp\left(-\frac{\Delta t^{i-1} b_2}{T_u^{i-1}}\right) + U_{34} \frac{A_2}{b_2} \frac{T_u^{i-1}}{\Delta t^{i-1}} \left(1 - \exp\left(-\frac{\Delta t^{i-1} b_2}{T_u^{i-1}}\right)\right) x_4^{i-1}$

$\alpha_{\text{eff}} \leftarrow \alpha_{qs}^i - \frac{X_{\text{lag}}^i + Y_{\text{lag}}^i}{u^i}$

$C_{l,\text{pot}}^i \leftarrow C_{l,\alpha}(\alpha_{\text{eff}} - \alpha_0) - \pi T_u^i \dot{x}_\gamma$ ▷ *Potential flow.*

▷ *Part 3: trailing-edge separated flow lift* ◁

$x_3^i \leftarrow x_3^{i-1} \exp\left(-\frac{\Delta t^{i-1}}{T_u^{i-1} T_p}\right) + 0.5 \left(C_{l,\text{pot}}^{i-1} + C_{l,\text{pot}}^i\right) \left(1 - \exp\left(-\frac{\Delta t^{i-1}}{T_u^{i-1} T_p}\right)\right)$

$\alpha_{\text{eq}} \leftarrow \frac{x_3^i}{C_{l,\alpha}} + \alpha_{0,l,\text{visc}}$

$f_l^i \leftarrow$ lift_separation_point(α_{eq})

$x_4^i \leftarrow x_4^{i-1} \exp\left(-\frac{\Delta t^{i-1}}{T_u^{i-1} T_f}\right) + 0.5 \left(f_l^{i-1} + f_l^i\right) \left(1 - \exp\left(-\frac{\Delta t^{i-1}}{T_u^{i-1} T_f}\right)\right)$

$C_{l,\text{c}} \leftarrow x_4^i C_{l,\alpha}(\alpha_{\text{eff}} - \alpha_0) + (1 - x_4^i) C_{l,\text{fs}}(\alpha_{\text{eff}})$ ▷ *Function call for $C_{l,fs}$*

$C_{l,\text{nc}} \leftarrow -\pi T_u^i \dot{x}_\gamma$ ▷ *Non-circulatory contribution*

▷ *Part 4: drag* ◁

$C_{d,\text{s}} \leftarrow C_d(\alpha_{\text{eff}})$ ▷ *Function call.*

$C_{d,\text{sep}} \leftarrow (C_{d,\text{s}} - C_{d,0}) \left(\left(\frac{\sqrt{f_l^i} - \sqrt{x_4^i}}{2}\right) - \left(\frac{f_l^i - x_4^i}{4}\right)\right)$

$C_{d,\text{c}} \leftarrow \left(\alpha_{\text{qs}} - \alpha_{\text{eff}} - T_u^i \dot{x}_\gamma\right) C_{l,\text{c}}$ ▷ *Induced (circulatory) contribution*

▷ *Part 5: moment* ◁

$C_{m,\text{s}} \leftarrow C_m(\alpha_{\text{eff}})$ ▷ *Function call.*

$C_{m,\text{nc}} \leftarrow 0.5\pi T_u^i \dot{x}_\gamma$

▷ *Part 6: combining everything* ◁

$\boldsymbol{c}_{\text{coeffs}} \leftarrow \begin{bmatrix} C_{l,\text{c}} + C_{l,\text{nc}} \\ C_{d,\text{s}} + C_{d,\text{c}} + C_{d,\text{sep}} \\ C_{m,\text{s}} + C_{m,\text{nc}} \end{bmatrix}$

if return_coeffs is True

  return $\boldsymbol{c}_{\text{coeffs}}$

continuation on line 31 (next page)

Implementation of the HGM f-scaled model – second continuation

continued from line 30 (previous page)

31: $\boldsymbol{R} \leftarrow \begin{bmatrix} \cos(-\alpha_{\text{qs}} - x_\gamma) & \sin(-\alpha_{\text{qs}} - x_\gamma) & 0 \\ -\sin(-\alpha_{\text{qs}} - x_\gamma) & \cos(-\alpha_{\text{qs}} - x_\gamma) & 0 \\ 0 & 0 & -1 \end{bmatrix}$ ▷ *The "−" is based on coordinate system differences.*

32: $q \leftarrow \frac{1}{2}\rho u^2$

33: $\boldsymbol{D} \leftarrow \text{diag}\left(\begin{bmatrix} c & c & c^2 \end{bmatrix}\right)$ ▷ *Diagonal matrix with the stated values on the diagonal.*

34: **return** $q\boldsymbol{D}\boldsymbol{R}\mathbf{c}_{\text{coeffs}}$

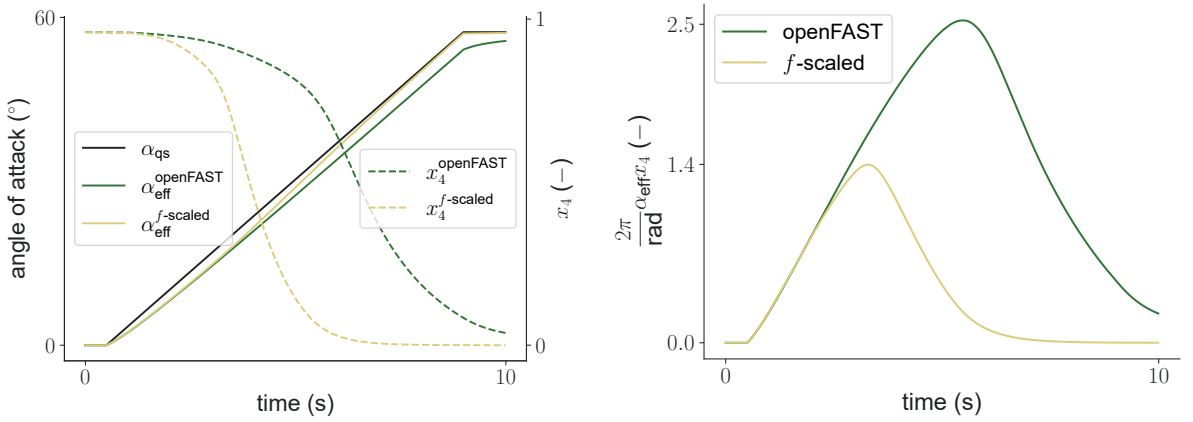

(a) Different angle of attacks and the separation point (here called x_4) as a time series in response to a predetermined ramp-up of α_{qs}.

(b) The unsteady attached C_l contribution based on α_{eff} and x_4 from Figure 3.9a for two respective lines. The plotted values correspond the first summand of Algorithm 9, line 18, for which here $C_{l,\text{slope}} = 2\pi\ 1/\text{rad}$ and $\alpha_{0,l} = 0°$ are assumed.

Figure 3.9: Comparison of the lagging of quasi-steady angle of attack (α_{qs}) and its effect from the HGM openFAST model and the HGM f-scaled model. α_{qs} is increased from $0\,\text{rad}$ to $1\,\text{rad}$ in $8.5\,\text{s}$. Data for the separation point (f) values is based on the FFA-W3-221 airfoil.

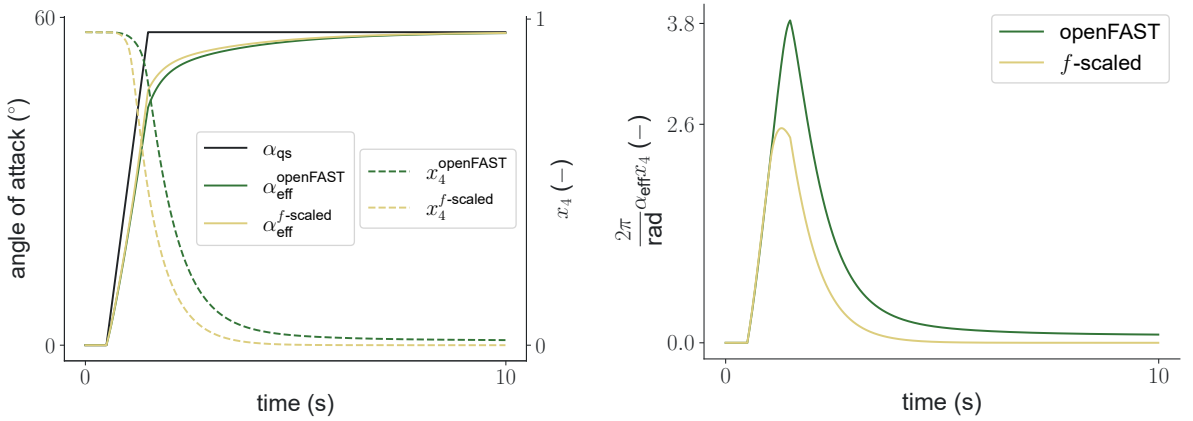

(a) Different angle of attacks and the separation point (here called x_4) as a time series in response to a predetermined ramp-up of α_{qs}.

(b) The unsteady attached C_l contribution based on α_{eff} and x_4 from Figure 3.9a for two respective lines. The plotted values correspond the first summand of Algorithm 9, line 18, for which here $C_{l,\text{slope}} = 2\pi\ 1/\text{rad}$ and $\alpha_{0,l} = 0°$ are assumed.

Figure 3.10: Comparison of the lagging of quasi-steady angle of attack (α_{qs}) and its effect from the HGM openFAST model and the HGM f-scaled model. α_{qs} is increased from $0\,\text{rad}$ to $1\,\text{rad}$ in $1\,\text{s}$. Data for the separation point (f) values is based on the FFA-W3-221 airfoil.

Table 3.2: Definition of the validation cases for the implemented dynamic stall models.

validation case	1	2	3
airfoil	S801	FFA-W3-221	FFA-W3-221
reduced frequency (k)	0.073	0.63	0.63
chord (c)	$0.457\,\mathrm{m}$	$3\,\mathrm{m}$	$3\,\mathrm{m}$
wind inflow magnitude (u_0)	$23.7\,\mathrm{m/s}$	$10\,\mathrm{m/s}$	$10\,\mathrm{m/s}$
oscillation amplitude	$10.85°$	$10°$	$10°$
oscillation mean	$19.25°$	$-5°$	$20°$

3.3.2. Validation

Section 3.3 abstract

The five dynamic stall models from Section 3.3.1 are validated using experimental data for the S801 airfoil and using HAWC2 and openFAST simulation results for the FFA-W3-221 airfoil. The implementation of the HGM openFAST model is visually indistinguishable from the openFAST implementation. The implementation of the 1st-order IAG model is close to the original implementation's result. Differences are attributed to algorithm constants. The AEROHOR model and the 1st-order IAG model match the experimental data for the S801 airfoil better than the HGM openFAST model and the HGM f-scaled model. This is attributed to specific parameter tuning of the former two models for the S801. For a high reduced frequency of $k = 0.63$, the four models show large differences in their polar drag coefficient and polar moment coefficient modelling. The results for the polar lift coefficient are similar. The main difference in the results is attributed to the extensive pitch-rate influence for the HGM-based models and the leading-edge vortex influence for the Beddoes-Leishman-based models. Lastly, the Stäblein model implementation is visually also indistinguishable from openFAST results at attached flow conditions.

The implementation algorithms presented in Section 3.3.1 are validated in this section. The airfoils S801 and FFA-W3-221 are used. For the former, measurement data was obtained from NREL for the grid-applied airfoil at a Reynolds number of $750\,000$. For the latter, HAWC2 and openFAST dynamic stall simulation data were visually extracted from Branlard et al., 2022 using automeris.io. The three validation cases are defined in Table 3.2. Since the Stäblein model is more primitive and only used for the aeroelastic validation of the section model, its validation is separated from the validation of the other dynamic stall models.

All validation simulations use the whole section model. The inflow is kept constant and the airfoil is moved along a predetermined path that corresponds to the oscillation definition. This goes to say that the aerodynamic core of the section model is validated and not a standalone implementation of the different algorithms.

Stäblein

The Stäblein model's lagging of the quasi-steady angle of attack (α_{qs}) in its unsteady attached flow model is based on Morten Hartvig Hansen et al., 2004. The only validation data based on the same time lagging are cases 2 and 3 from Table 3.2. However, since the Stäblein model only models unsteady attached flow, case 3 cannot be used. The validation is shown in Figures 3.11a to 3.11c. The implementation's results match exactly to the accuracy of retrieving the validation data. The acceleration terms present in the Stäblein model appear to be negligible since the openFAST model does not implement them.

1st-order IAG, AEROHOR, HGM openFAST, and HGM f-scaled

The implementations of the 1st-order IAG model and the HGM openFAST model can directly be compared to data from literature created with these models. This is done first. Then, all models are compared for cases 1 to 3 from Table 3.2.

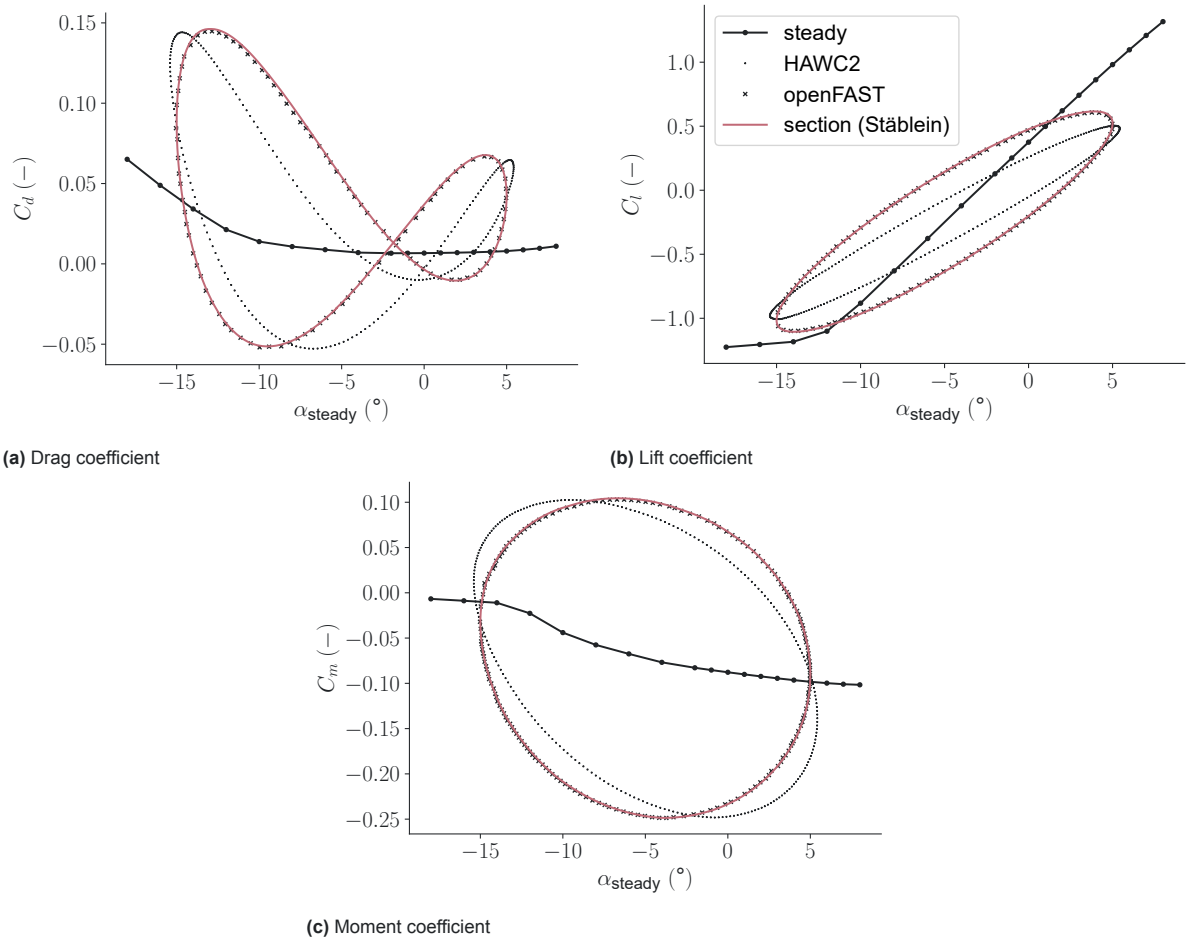

(a) Drag coefficient

(b) Lift coefficient

(c) Moment coefficient

Figure 3.11: Validation of the Stäblein model implementation against HAWC2 and openFAST dynamic stall (DS) simulations; validation data from Branlard et al., 2022. The simulation was performed for $k = 0.073$, $c = 0.457\,\mathrm{m}$, wind inflow magnitude of $23.7\,\mathrm{m/s}$, an oscillation amplitude of $10.85°$, and an oscillation mean of $19.25°$.

The implemented 1st-order IAG model results compared to the results of Bangga et al., 2020 are shown in Figures 3.12a to 3.12c. The section's implementation matches Bangga's well. Since both implementations show quantitatively very similar structures, the author believes the differences to stem from different ways of calculating the lift slope ($C_{l,\alpha}$), zero lift angle of attack ($\alpha_{0,\mathrm{l}}$), or different constant settings. In Bangga et al., 2020, it is not specifically stated which experimental case is compared to. The author of this thesis compared the different measurement results from NREL to those used in Bangga et al., 2020 to find which airfoil configuration (with or without leading-edge roughness) was used. However, the airfoil that was used in the experiment whose data Bangga used does have a critical angle of attack of $14.1°$ while Bangga claims $15.1°$. No matter the source of error, the focus lies not on a perfect implementation of the 1st-order IAG model. For the objectives of this thesis, the validation is considered as passed.

The analysis of the comparison of the the HGM openFAST model implementation to that of Branlard et al., 2022 is brief: they match almost completely, see Figures 3.13a to 3.13c. The minor differences are most likely related to the visual extraction of the validation data and that Branlard et al., 2022 use a continuous time integration for the state differential equations while the section implementation discretises the time integration.

Now, case 1 from Table 3.2 is examined. The results are shown in Figures 3.14a to 3.14c. Generally, the 1st-order IAG and AEROHOR models match the measurement results better (except for the AEROHOR moment which is not modelled). However, these two models' constants are specifically tuned for the S801 airfoil, while those of the HGM openFAST and HGM f-scaled are not.

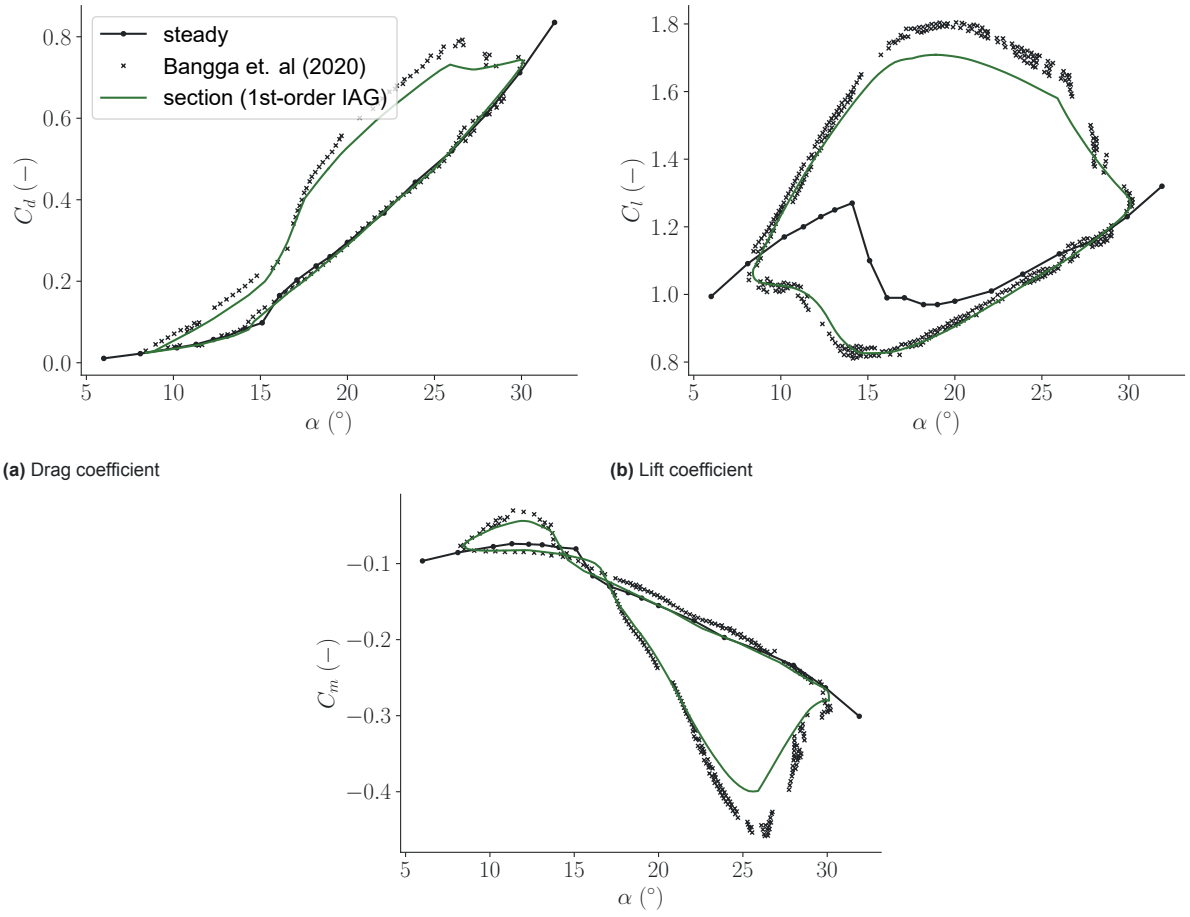

(a) Drag coefficient

(b) Lift coefficient

(c) Moment coefficient

Figure 3.12: Validation of the 1st-order IAG modelimplementation against that of Bangga et al., 2020. The simulation was performed for $k = 0.073$, $c = 0.457\,\mathrm{m}$, wind inflow magnitude of $23.7\,\mathrm{m/s}$, an oscillation amplitude of $10.85°$, and an oscillation mean of $19.25°$. The data from Bangga et al., 2020 is correctly not a single line; their implementation does not follow the same path for each oscillation.

Starting with a closer look at Figure 3.14b, the HGM openFAST and HGM f-scaled experience a significant drop in unsteady lift coefficient ($C_{l,\mathrm{us}}$) on the upper side of the loop around $\alpha \approx 15°$ because the flow experiences large separation. In the meantime, for the 1st-order IAG and AEROHOR models, the vortex lift modelling kicks in and maintains the difference to the other two models until α decreases again around $\alpha \approx 30°$. Before the upstroke (at the bottom side of the loop between α values of $5°$ to $20°$) all four models show the same qualitative shape. This is reasonable because there, all models are based more or less on the Kirchhoff equation to model the forces. The large deviations are thus most likely attributed to the unadjusted constants for the HGM openFAST and HGM f-scaled model.

Looking closer at Figure 3.14a, the influence of the modelled leading-edge vortex is again apparent, causing the large unsteady drag coefficient ($C_{d,\mathrm{us}}$) values for the 1st-order IAG and AEROHOR models. These two differ due to different unsteady tangential force coefficient ($C_{t,\mathrm{us}}$) modelling. For the AEROHOR model, the $C_{t,\mathrm{us}}$ (based on the Kirchhoff Equation (3.33)) reduces $C_{d,\mathrm{us}}$ stronger than in the case of the 1st-order IAG model that uses the steady C_t value at a lagged angle of attack. Because neither of the HGM models has the vortex contribution and the pitch rate is relatively low, their $C_{d,\mathrm{us}}$ values are close to the static polar.

Lastly, looking at Figure 3.14c, the leading-edge vortex influence is prominent for large α, causing the unsteady moment coefficient ($C_{m,\mathrm{us}}$) to drop significantly for the 1st-order IAG model. Otherwise, all except the AEROHOR model behave similarly.

Next, case 2 from Table 3.2 is examined. The results are shown in Figures 3.15a to 3.15c. The flow

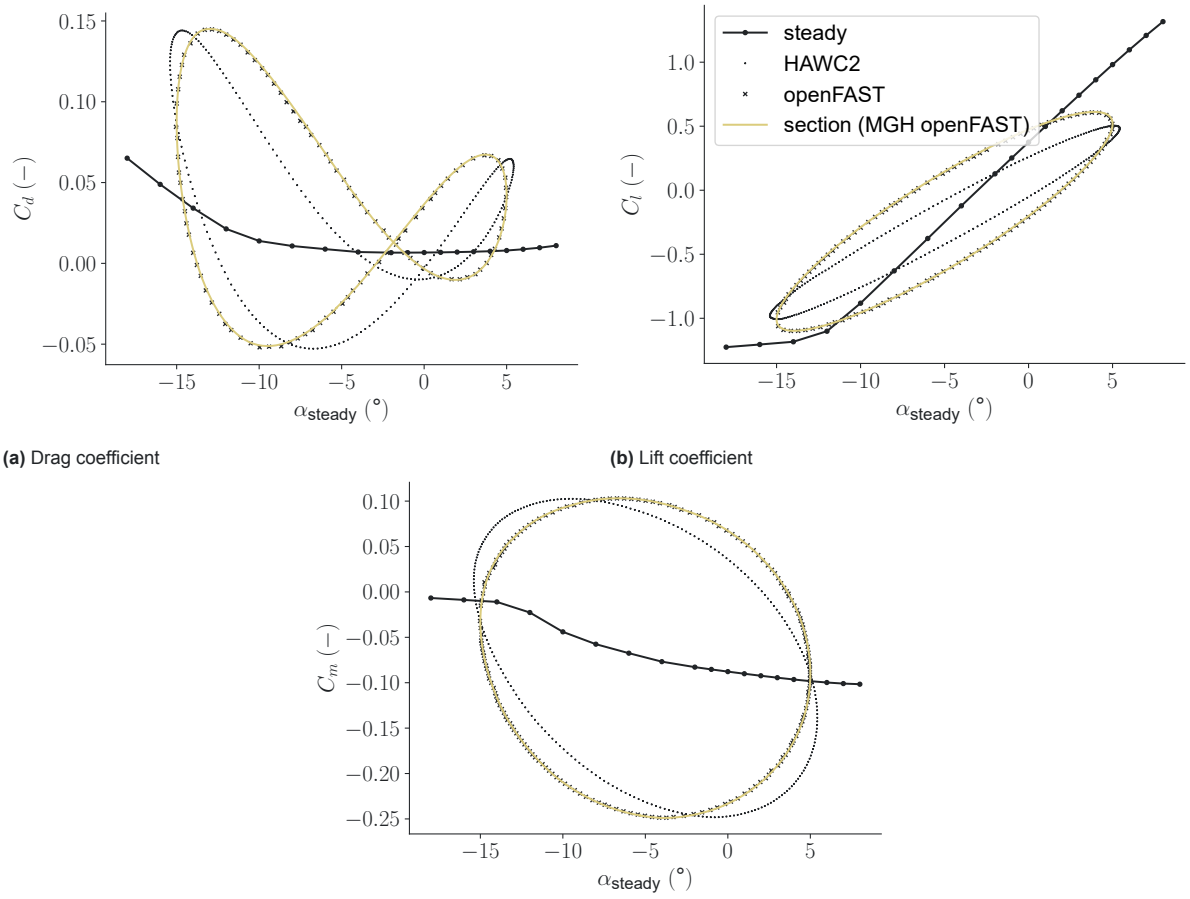

(a) Drag coefficient

(b) Lift coefficient

(c) Moment coefficient

Figure 3.13: Validation of the HGM openFAST modelimplementation against that of Branlard et al., 2022. The simulation was performed for $k = 0.63$, $c = 3\,\mathrm{m}$, wind inflow magnitude of $10\,\mathrm{m/s}$, an oscillation amplitude of $10°$, and an oscillation mean of $20°$. Back to the paragraph here.

in this case is fully or almost fully attached except for the lower end of α. Because of that, the models HGM openFAST and HGM f-scaled behave nearly identically (Pirrung et al., 2018) and will thus here be analysed as one model.

Starting with $C_{d,\text{us}}$ in Figure 3.15a, all models show the same qualitative loop. One peculiarity is adjusting the $C_{d,\text{us}}$ to C_d as defined in line 27, lines 57 and 58 for the 1st-order IAG model. The HGM models are governed by their pitch-rate and induced drag terms. The polar term has a small and almost constant value. The 1st-order IAG and AEROHOR drag components are overwhelmingly similar except for their $C_{t,\text{f}}$ (the polar contribution) modelling. The AEROHOR's $C_{t,\text{f}}$ becomes 1.5 times as large as the 1st-order IAG's and thus reduces $C_{d,\text{us}}$ stronger.

The $C_{l,\text{us}}$ loops from Figure 3.15b look similar. However, the underlying components are quite different. First, the lift contribution due to the torsion rate is, on average, half as large for the HGM-based models. Secondly, the trailing-edge separated unsteady C_l plays a significantly smaller role and loops clockwise for the HGM models, both in opposition to the other two models. The different directions of the loops come from the different approaches to lagging α_{qs} to get α_{eff} causing the α_{eff} loops to be in opposite directions. The final $C_{l,\text{us}}$ of all components loop in the same direction nonetheless.

At last, large differences in the unsteady moment coefficient ($C_{m,\text{us}}$) modelling are seen in Figure 3.15c. The counterclockwise loops of the HGM models are mainly caused by their torsion-rate terms while the polar contribution adds a relative constant offset. The 1st-order IAG lacks the torsion-rate contribution; its loops are almost completely based on the polar contributions. Additionally, the 1st-order IAG model loops $C_{m,\text{us}}$ in the opposite direction to the HGM-based models. The differences in the $C_{m,\text{us}}$ are large.

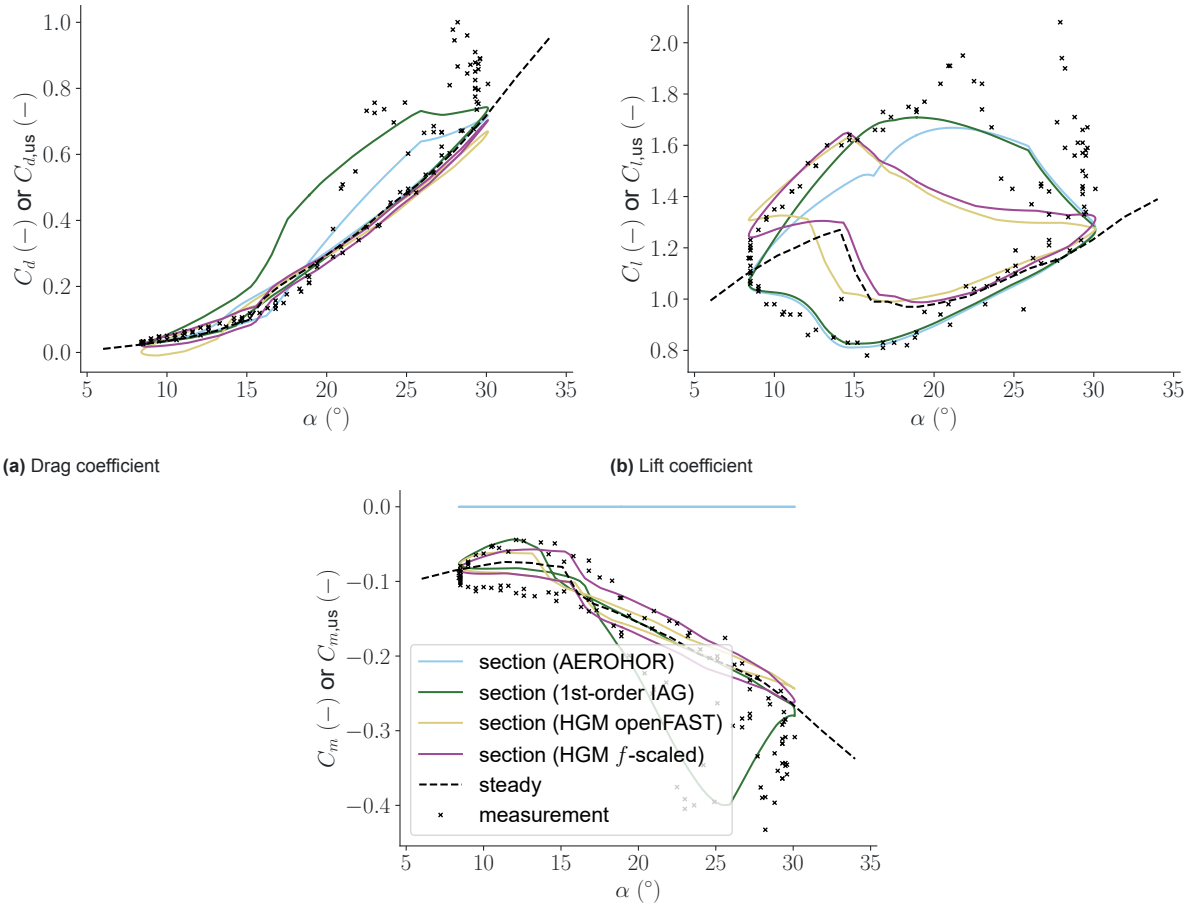

(a) Drag coefficient

(b) Lift coefficient

(c) Moment coefficient

Figure 3.14: Validation of the 1st-order IAG, AEROHOR, HGM openFAST, and HGM f-scaled implementations against measurement data from taken from NREL for the S801 airfoil. The simulation was performed for $k = 0.073$, $c = 0.457\,\mathrm{m}$, wind inflow magnitude of $23.7\,\mathrm{m/s}$, an oscillation amplitude of $10.85°$, and an oscillation mean of $19.25°$. Back to the paragraph here.

The results from the last validation case are shown in Figures 3.16a to 3.16c. A detailed analysis is not done here but in the later limit cycle oscillation (LCO) analyses. However, it is noteworthy that the correction for the $C_{d,\mathrm{us}}$ in the 1st-order IAG model introduces significant kinks. Additionally, at the high reduced frequency of $k = 0.63$ and the high mean α, the α_{eff} curve is so wide and flat that the conditions for vortex development for the 1st-order IAG and AEROHOR models are never satisfied (only one vortex is modelled that continuously travels downstream without the creation of a new one).

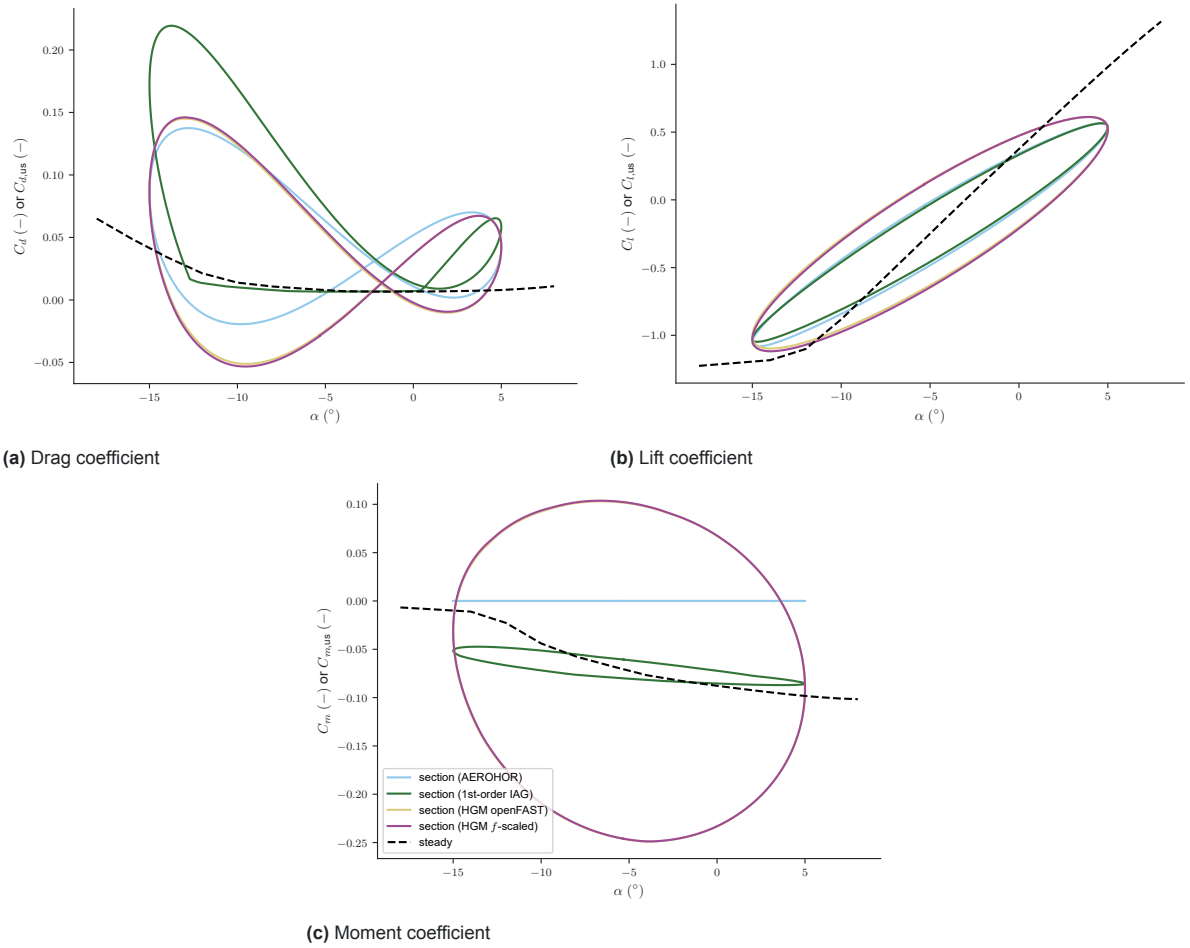

(a) Drag coefficient

(b) Lift coefficient

(c) Moment coefficient

Figure 3.15: Validation of the 1st-order IAG, AEROHOR, HGM openFAST, and HGM f-scaled implementations against measurement data from taken from Branlard et al., 2022. The simulation was performed for $k = 0.63$, $c = 3\,\mathrm{m}$, wind inflow magnitude of $10\,\mathrm{m/s}$, an oscillation amplitude of $10°$, and an oscillation mean of $-5°$. Back to the paragraph here.

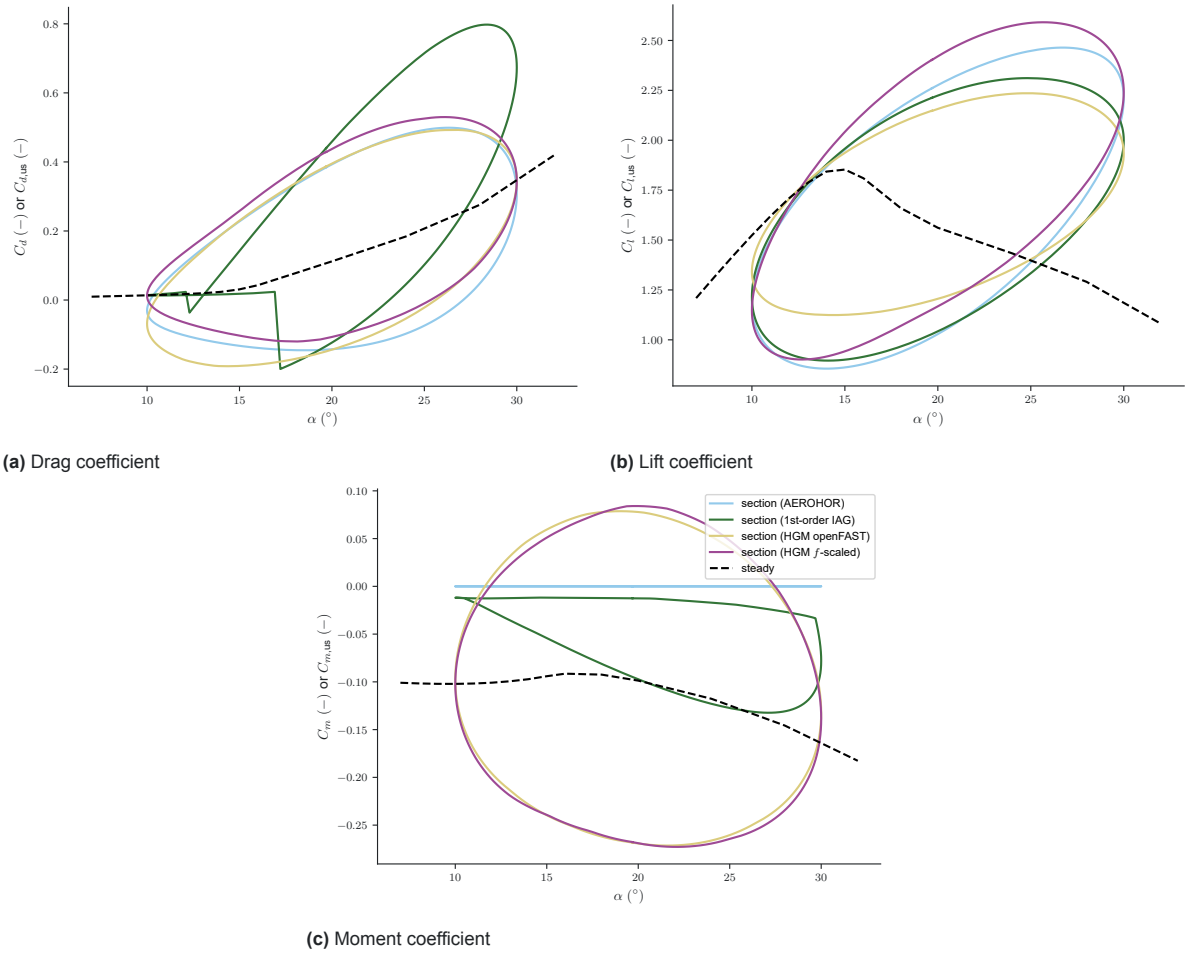

(a) Drag coefficient

(b) Lift coefficient

(c) Moment coefficient

Figure 3.16: Validation of the 1st-order IAG, AEROHOR, HGM openFAST, and HGM f-scaled implementations against measurement data from taken from Branlard et al., 2022. The simulation was performed for $k = 0.63$, $c = 3\,\mathrm{m}$, wind inflow magnitude of $10\,\mathrm{m/s}$, an oscillation amplitude of $10°$, and an oscillation mean of $20°$. Back to the paragraph here.

3.4. Structural modelling: Description and implementation

Section 3.4 abstract

The equations for the structural damping and stiffness forces and moments are given; both model their influence linearly. The structural parameters used to investigate the objects of the thesis are stated and reasoned; the data from $\approx 75\,\%$ span of the blade of the DTU $10\,\mathrm{MW}$ reference wind turbine is used without inertial or structural coupling.

Most of the structural modelling has been described in Section 3.1, where it was argued to model the translational dampers and springs parallel to the axes of the xy coordinate system. The consequences of choosing these dampers and springs as acting parallel and normal to the chord of the airfoil are explained in Appendix B. A rotational spring and damper acts with moments around the γ axis which moves with the airfoil. The structural damping and stiffness forces and moment are calculated at each time step i as

$$\boldsymbol{f}_c^i = \boldsymbol{C}\dot{\boldsymbol{x}}^i \text{, and} \tag{3.41}$$

$$\boldsymbol{f}_k^i = \boldsymbol{K}\boldsymbol{x}^i \tag{3.42}$$

respectively. In a steady-state, this means that a positive external force is balanced by a positive stiffness force. This goes back to the definition of the forces and moment in the equation of motions (EOMs) Equation (3.1). The implementation of Equations (3.41) and (3.42) is validated in energy, power, and work calculation validations in Section 3.7.2. The forces and moment calculated by Equations (3.41) and (3.42) are not used for the time integration because, as explained in Section 3.5, the time integration scheme does not have to (yet even cannot) use them. The damping matrix in the xy coordinate system ($\boldsymbol{C}$) and the stiffness matrix in the xy coordinate system ($\boldsymbol{K}$) are populated according to Table 3.1.

The structural parameters that are used for the simulations of the results Chapter 5 are shown in Table 3.3. Unless otherwise stated, $\boldsymbol{C}$ and $\boldsymbol{K}$ are thus

$$\boldsymbol{C} = \begin{bmatrix} 11.63\,\mathrm{Ns/m^2} & 0 & 0 \\ 0 & 7.31\,\mathrm{Ns/m^2} & 0 \\ 0 & 0 & 111.97\,\mathrm{N\,s\,rad^{-1}} \end{bmatrix}, \tag{3.43}$$

$$\boldsymbol{K} = \begin{bmatrix} 6931\,\mathrm{N/m^2} & 0 & 0 \\ 0 & 2982\,\mathrm{N/m^2} & 0 \\ 0 & 0 & 219\,050\,\mathrm{N\,rad^{-1}} \end{bmatrix}. \tag{3.44}$$

The units result from the section modelling forces per unit length. There are different methods to approximate 2D structural parameters based on a 3D blade. Performing a modal analysis or using the Ritz method to condense 3D blade structural parameters into 2D structural parameters was considered. However, due to the availability of the data from Stäblein et al., 2017, it was chosen to not use these methods. Stäblein et al., 2017 took the structural parameters at $\approx 75\,\%$ spanwise position (measured from the root) from the DTU $10\,\mathrm{MW}$ reference wind turbine (Bak et al., 2013). The $75\,\%$ position was chosen because it lies in the region where most aerodynamic power is extracted from the flow. The DTU $10\,\mathrm{MW}$ reference wind turbine can still be considered a modern reference wind turbine. The structural parameters are thus expected to give a reasonable approximation.

Table 3.3: Structural parameters used for the results Chapter 5. The parameters for the inertia, natural frequency, and damping ratios are taken from Stäblein et al., 2017. The damping and stiffness constants are shown for convenience and are based on the equations given in Stäblein et al., 2017.

axis	x	y	γ
inertia	$203\,\mathrm{kg/m}$	$203\,\mathrm{kg/m}$	$143.85\,\mathrm{kgm/rad}$
natural frequency ($\mathrm{rad\,s^{-1}}$)	0.93	0.61	6.66
damping ratio ($-$)	0.0049	0.0047	0.0093
damping constant	$11.63\,\mathrm{Ns/m^2}$	$7.31\,\mathrm{Ns/m^2}$	$111.97\,\mathrm{N\,s\,rad^{-1}}$
stiffness constant	$6931\,\mathrm{N/m^2}$	$2982\,\mathrm{N/m^2}$	$219\,050\,\mathrm{N\,rad^{-1}}$

3.5. Time integration

Section 3.5 abstract

The HHT–α^{HHT}–adapted algorithm is introduced, reasoned for, and its implementation is detailed. The algorithm is used for the time integration of the system state. The structural damping and stiffness forces and moments are an internal part of the HHT–α^{HHT}–adapted algorithm. Thus, only the external (aerodynamic) forces and moments have to be further supplied. The implementation is validated against the analytical solution of a mass-damper-spring system with multiple oscillatory external forces. The "-adapted" version is also compared to the original HHT–α^{HHT}. The HHT–α^{HHT}–adapted achieves a reasonable accuracy for twelve time steps per period and a high accuracy for 62.

This section describes which time integration scheme is used, details the implementation, and shows the validation of the implementation. As time integrator, the HHT–α^{HHT} algorithm from Hilber et al., 1977 and the implementation of Gavin, 2020. The HHT–α^{HHT} method is "at least second-order accurate and unconditionally stable" (Gavin, 2020) and can be used to artificially dampen high-frequency responses (Sherif et al., 2019) which is helpful if they are either not physical or can be neglected.

3.5.1. Description and implementation

The HHT–α^{HHT} algorithm is a time integration scheme for structural mechanics. This is because the calculation of the structural damping and stiffness forces and moments are an integral part of the algorithm itself. This allows for artificially adjusting the damping of high-frequency responses of the system using the damping parameter α^{HHT}. To achieve the above stated accuracy, α^{HHT} must be between (and including) 0 to 0.3 (Gavin, 2020). $\alpha^{\mathrm{HHT}} = 0$ means no damping of the high-frequency response and with increasing α^{HHT} does the damping increase. The section's implementation can be seen in Algorithm 11. This implementation differs from Gavin, 2020 by using the external forces at the current (k subscript) and last (l subscript) time step instead of the next (n subscript) and current time step. Since the external forces in the simulations using the section model are the aerodynamic forces that are dependent on $\ddot{\boldsymbol{x}}^i$, $\dot{\boldsymbol{x}}^i$, and $\boldsymbol{x}^i$, the HHT–α^{HHT} algorithm would need to be solved iteratively. Another approach would be to approximate the total (or partial) derivative of the current aerodynamic forces and linearly integrate those to assume their values at the next time step. Both options are left open for further research. In the section model, the time step is chosen small enough for the now so-called HHT–α^{HHT}–adapted to be accurate. The influence of the time step size is investigated in the validation section Section 3.5.2.

3.5.2. Validation

Since the main objective of this thesis is to analyse limit cycle oscillations (LCOs), the section's HHT–α^{HHT}–adapted algorithm is validated for a case with multiple oscillatory external forces. The validation data is based on the analytical solution for damped and excited oscillations from Thomson, 1993. The simulation is defined with a mass of $1\,\mathrm{kg}$, a natural frequency of $1\,\mathrm{rad\,s^{-1}}$, a damping coefficient of 0.1, an initial displacement of $1\,\mathrm{m}$, an initial velocity of $-4\,\mathrm{m\,s^{-1}}$, and five external oscillatory forces.

Algorithm 11 Implementation of the adapted HHT–α^{HHT} structural time integration.

Require:
1. damping parameter for the HHT-α^{HHT} algorithm (α^{HHT})
2. mass (inertia) matrix in the xy coordinate system ($\boldsymbol{M}$)
3. damping matrix in the xy coordinate system ($\boldsymbol{C}$)
4. stiffness matrix in the xy coordinate system ($\boldsymbol{K}$)

Return:
1. acceleration $\ddot{\boldsymbol{x}}^i$ at the next time step
2. velocity $\dot{\boldsymbol{x}}^i$ at the next time step
3. displacement $\boldsymbol{x}^i$ at the next time step

$\beta \leftarrow \left(\frac{1+\alpha^{\text{HHT}}}{2}\right)^2$
$\gamma \leftarrow 0.5 + \alpha^{\text{HHT}}$

$\boldsymbol{M}_n \leftarrow \boldsymbol{M} + \Delta t(1-\alpha^{\text{HHT}})\gamma\boldsymbol{C} + (\Delta t)^2(1-\alpha^{\text{HHT}})\beta\boldsymbol{K}$
$\boldsymbol{M}_k \leftarrow \Delta t(1-\alpha^{\text{HHT}})(1-\gamma)\boldsymbol{C} + (\Delta t)^2(1-\alpha^{\text{HHT}})(0.5-\beta)\boldsymbol{K}$
$\boldsymbol{C}_k \leftarrow \boldsymbol{C} + \Delta t(1-\alpha^{\text{HHT}})\boldsymbol{K}$
$\boldsymbol{K}_k \leftarrow \boldsymbol{K}$
$p_{k,\text{ext}} \leftarrow 1-\alpha$
$p_{l,\text{ext}} \leftarrow \alpha$

function HHT--α^{HHT}--ADAPTED($\ddot{\boldsymbol{x}}^i$, $\dot{\boldsymbol{x}}^i$, $\boldsymbol{x}^i$, $\boldsymbol{f}^i_{\text{ext}}$, $\boldsymbol{f}^{i-1}_{\text{ext}}$, Δt)
  $\boldsymbol{f} \leftarrow -\boldsymbol{M}_k\ddot{\boldsymbol{x}}^i - \boldsymbol{C}_k\dot{\boldsymbol{x}}^i - \boldsymbol{K}_k\boldsymbol{x}^i + p_{k,\text{ext}}\boldsymbol{f}^i_{\text{ext}} + p_{l,\text{ext}}\boldsymbol{f}^{i-1}_{\text{ext}}$

  $\ddot{\boldsymbol{x}}^{i+1} \leftarrow \boldsymbol{M}_n^{-1}\boldsymbol{f}$
  $\dot{\boldsymbol{x}}^{i+1} \leftarrow \dot{\boldsymbol{x}}^i + \Delta t\left((1-\gamma)\ddot{\boldsymbol{x}}^i + \gamma\ddot{\boldsymbol{x}}^{i+1}\right)$
  $\boldsymbol{x}^{i+1} \leftarrow \boldsymbol{x}^i + \dot{\boldsymbol{x}}^i\Delta t + (\Delta t)^2\left((0.5-\beta)\ddot{\boldsymbol{x}}^i + \beta\ddot{\boldsymbol{x}}^{i+1}\right)$
  return $\ddot{\boldsymbol{x}}^{i+1}$, $\dot{\boldsymbol{x}}^{i+1}$, $\boldsymbol{x}^{i+1}$

All forces have a magnitude of $1\,\text{N}$ but frequencies of $0.6\,\text{rad}\,\text{s}^{-1}$, $0.8\,\text{rad}\,\text{s}^{-1}$, $1\,\text{rad}\,\text{s}^{-1}$, $1.2\,\text{rad}\,\text{s}^{-1}$ and $1,4\,\text{rad}\,\text{s}^{-1}$. Using $1\,\text{N}$ for all forces is without loss of generality (for forces of this magnitude) since the different frequencies will cause different total force magnitudes. The stated values are used for all three axes x, y, and γ. Hence, all axes are validated for an inertial and structural uncoupled case. It is assumed that the implementation is correct and works for coupled cases, too, once the uncoupled case is validated.

The simulations use the section model as a whole with the external forces predefined as the aerodynamic forces. This goes to say that it is the core section model being validated and not a standalone HHT–α^{HHT}–adapted algorithm. The validation includes two cases with two different time step sizes. The results are shown in Figures 3.17a and 3.17b.

As can be seen, even for only twelve time steps per period both algorithms work well without (from a visual examination) an accumulating error over time. The initial error seems to persist. Increasing the time steps per period to 62 causes the simulations to visually almost perfectly overlap with the analytical solution. Assuming the limit cycle oscillation period to be around $2.5\,\text{s}$ (rounding down the natural frequency in the x direction of Table 3.3), 62 time steps require a time step duration of $0.04\,\text{s}$. Most of the simulations for the results Chapter 5 are performed with a time step duration of $0.001\,\text{s}$. Of course, different magnitudes for the structural and aerodynamic forces have to be considered, too.

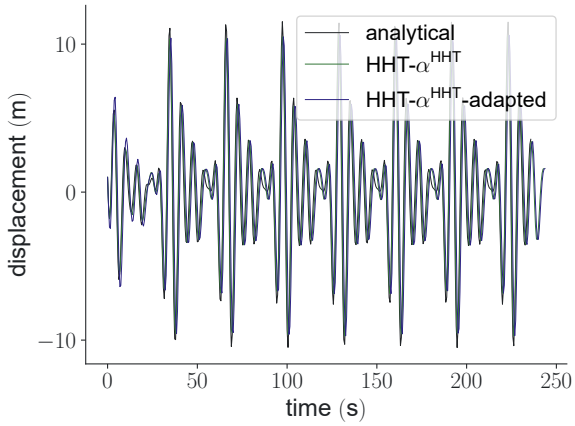

(a) Constant time step duration of $\approx 0.52\,\text{s}$. This means that there are on average 12 time steps per period.

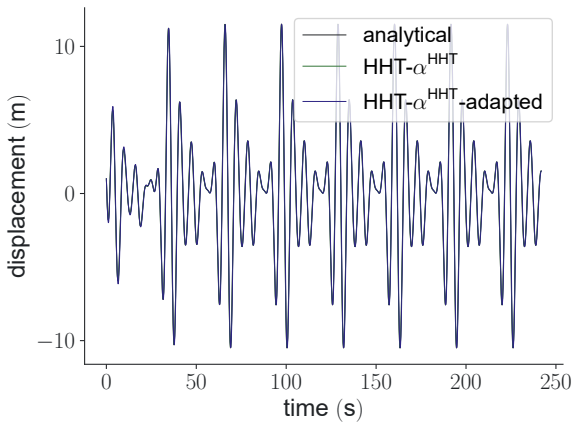

(b) Constant time step duration of $\approx 0.1\,\text{s}$. This means that there are on average 62 time steps per period.

Figure 3.17: Validation of the HHT–α^{HHT}–adapted time integration model against an analytical solution and the original HHT–α^{HHT} model for two time steps. Five oscillatory external forces with different frequencies but the same magnitude act on the mass-damper-spring one degree of freedom system. The initial displacement and velocity are non-zero.

3.6. Aeroleastic validation

Section 3.6 abstract

The aeroelastic behaviour of the section is validated for small oscillation amplitudes by means of the aeroelastic damping coefficient. From Stäblein et al., 2017, the aeroelastic damping coefficient for the given airfoil, inflow conditions, and structure, must lie between 0 to 0.01. The section model predicts ≈ 0.08. A convergence study for the time step is done. For the given validation simulation, the results showed insignificant changes for a time step duration of $0.001\,\text{s}$ and lower.

After the aerodynamic algorithms and the time integration have been separately validated in Sections 3.3.2 and 3.5.2, the combined aeroelastic behaviour is validated in this section. For that, a simulation with the same inflow and structural conditions as in Stäblein et al., 2017 is set and the results are compared. Instead of the linearised dynamic stall Stäblein uses, the section model uses the fully non-linear Stäblein model from Section 3.3.1.2. Since the results from Stäblein et al., 2017 are only valid for small oscillation amplitudes (because of their linearised state-space model), only the small amplitude response of the section can be validated.

The simulation setup is the following. The structural parameters are defined in Table 3.3. The damping matrix in the xy coordinate system ($\boldsymbol{C}$) and the stiffness matrix in the xy coordinate system ($\boldsymbol{K}$) are given in Equations (3.43) and (3.44), respectively. The mass (inertia) matrix in the xy coordinate system ($\boldsymbol{M}$) includes heave-pitch coupling as defined in Stäblein et al., 2017:

$$\boldsymbol{M} \approx \begin{bmatrix} 203\,\text{kg}\,\text{m}^{-1} & 0\,\text{kg}\,\text{m}^{-1} & 0\,\text{kg}\,\text{rad}^{-1} \\ 0\,\text{kg}\,\text{m}^{-1} & 203\,\text{kg}\,\text{m}^{-1} & 62\,\text{kg}\,\text{rad}^{-1} \\ 0\,\text{kg} & 62\,\text{kg} & 144\,\text{kg}\,\text{m}\,\text{rad}^{-1} \end{bmatrix}. \tag{3.45}$$

The wind inflow magnitude (u_0) is $u_0 = 45\,\text{m}\,\text{s}^{-1}$ and the steady-state geometric angle of attack (α) is $\alpha = 7°$. The airfoil has a constant lift slope of $7.15\,\text{rad}^{-1}$, a constant polar drag coefficient of 0.01, and a constant polar moment coefficient of -0.1. Algorithm 2 was used to find the wind inflow (here also yaw misalignment) angle corresponding to the needed geometric angle of attack and the initial steady-state position. The airfoil was then additionally displaced by $10\,\text{m}$ in the x-direction. The simulation was run for $300\,\text{s}$ for a convergence study of time step duration of $0.005\,\text{s}$, $0.0025\,\text{s}$, $0.001\,\text{s}$ and $0.0005\,\text{s}$.

The results from Stäblein et al., 2017 and the section are shown in Figures 3.18a and 3.18b, respectively. For the section results, hardly any differences could be distinguished between the time steps $0.001\,\text{s}$

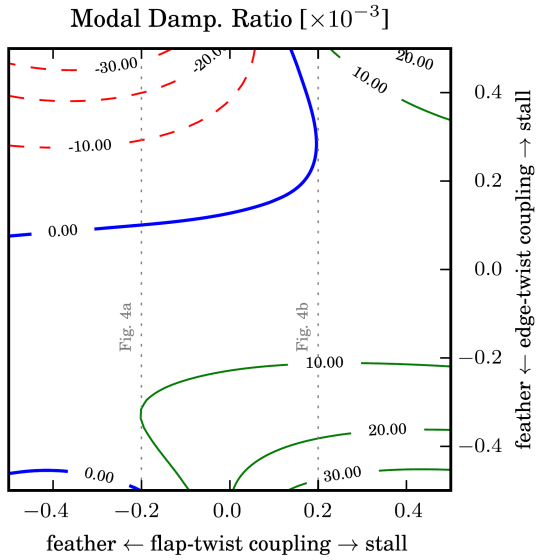

(a) Linearised state-space results, modified from Stäblein et al., 2017 Figure (3).

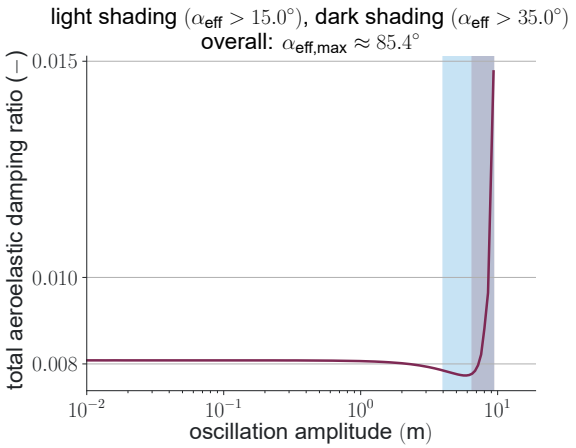

(b) Results of a $300\,\text{s}$ simulation using the section model and a time step duration of $0.001\,\text{s}$. Oscillation amplitudes below $1\,\text{cm}$ are not plotted but continue just above the aeroelastic damping of 0.008.

Figure 3.18: Aeroelastic validation of the section model. The inflow magnitude is $45\,\text{m}\,\text{s}^{-1}$ with a steady-state angle of attack of $7°$. A constant lift slope and drag and moment coefficient are assumed. No separation is modelled.

and $0.0005\,\text{s}$; hence the former case is shown. The results for each case can be seen in Figures A.1a to A.1d. In Stäblein et al., 2017, differently pronounced structural couplings are examined for their influence on the aeroelastic stability of a blade section. The data to validate the section model again is thus only the centre of Figure 3.18a where no structural coupling is modelled. There, the aeroelastic damping ratio lies between 0 to 0.01. Figure 3.18b shows the aeroelastic damping ratio as function of the oscillation amplitude for the section simulation. The light and dark-shaded areas indicate where the maximum effective angle of attack (α_{eff}) during one period exceeded a specific value. This is supposed to give insights into the validity of the results. Since the used Stäblein model does not account for any kind of separation (or an actual airfoil polar), periods during which $\alpha_{\text{eff}} > 15°$ occurs become inaccurate and periods for which $\alpha_{\text{eff}} > 15°$ cause wrong modelling. However, for small oscillation amplitudes, the section model correctly predicts an aeroelastic damping between 0 and 0.01. With this, the section model is assumed to yield reasonable aeroelastic simulation results.

3.7. Post-processing

Section 3.7 abstract

The section model works internally on the xy coordinate system. To aid analysing results, some parameters are projected in the edgewise and flapwise direction. The aerodynamic forces are also projected in the drag and lift direction. The rotation matrices for these operations are defined. Additionally, the calculation of the aerodynamic and structural damping power and work, and the calculation of the potential and kinetic energy are defined. At last, all of the stated calculations are validated by running a simulation with predefined aerodynamic forces. The results match the expected outcomes to high precision.

Simulations with the section model return most of the state variables related to the xy coordinate system. These include most notably the airfoil's velocity and displacement and aerodynamic and structural forces. For aided interpretation of the results, these are projected onto different coordinate systems to gain insights into the edgewise and flapwise motion or lift and drag forces. Additionally, energies, work, power, and damping coefficients are of interest. In this section, the calculation of the post-processing is explained.

3.7.1. Description and implementation

Most of the values need to be projected from the xy to the edgewise-flapwise ef coordinate system. Since the airfoil's torsion angle γ might change from one time step to the other, the directions edgewise and flapwise also change. Hence, each projection needs to account for the current time step's x_γ. The projection from the xy to the ef coordinate system is described by

$$\boldsymbol{R}^i_{xy\to ef} = \begin{bmatrix} \cos\left(x^i_\gamma\right) & \sin\left(x^i_\gamma\right) \\ -\sin\left(x^i_\gamma\right) & \cos\left(x^i_\gamma\right) \end{bmatrix} . \tag{3.46}$$

The torsional angle or other parameters connected to the γ-axis remain the same in both coordinate systems. Thus, the displacement, velocity, and structural damping and stiffness forces can be readily projected for each time step by

$$\boldsymbol{x}^i_{ef} = \boldsymbol{R}^i_{xy\to ef} \begin{bmatrix} x^i_x \\ x^i_y \end{bmatrix} \tag{3.47}$$

$$\dot{\boldsymbol{x}}^i_{ef} = \boldsymbol{R}^i_{xy\to ef} \begin{bmatrix} \dot{x}^i_x \\ \dot{x}^i_y \end{bmatrix} \tag{3.48}$$

$$\boldsymbol{f}^i_{k,ef} = \boldsymbol{R}^i_{xy\to ef} \begin{bmatrix} f^i_{k,x} \\ f^i_{k,y} \end{bmatrix} \tag{3.49}$$

$$\boldsymbol{f}^i_{c,ef} = \boldsymbol{R}^i_{xy\to ef} \begin{bmatrix} f^i_{c,x} \\ f^i_{c,y} \end{bmatrix} \tag{3.50}$$

The aerodynamic forces are of interest both in the ef coordinate system but also in the drag-lift dl coordinate system. The projection onto the ef coordinate system again follows

$$f^i_{\mathsf{aero},ef} = \boldsymbol{R}^i_{xy\to ef} \begin{bmatrix} f^i_{\mathsf{aero},x} \\ f^i_{\mathsf{aero},y} \end{bmatrix} . \tag{3.51}$$

For the projection into the dl coordinate system, the following is done for each time step:

$$\boldsymbol{R}^i_{xy\to dl} = \begin{bmatrix} \cos\left({\alpha_{\mathsf{qs}}}^i\right) & \sin\left({\alpha_{\mathsf{qs}}}^i\right) \\ -\sin\left({\alpha_{\mathsf{qs}}}^i\right) & \cos\left({\alpha_{\mathsf{qs}}}^i\right) \end{bmatrix} , \tag{3.52}$$

$$f^i_{\mathsf{aero},dl} = \boldsymbol{R}^i_{xy\to dl} \begin{bmatrix} f^i_{\mathsf{aero},x} \\ f^i_{\mathsf{aero},y} \end{bmatrix} . \tag{3.53}$$

The kinetic energy components can be calculated for the ef coordinate system for $M_{xx} = M_{yy}$ as

$$\boldsymbol{e}_{\mathsf{kin},ef} = \frac{1}{2} \begin{bmatrix} M_{xx} \left(\dot{x}^i_e\right)^2 \\ M_{yy} \left(\dot{x}^i_f\right)^2 \end{bmatrix} . \tag{3.54}$$

The potential energy, however, cannot be projected onto the ef coordinate system if the spring stiffness K_{xx} and K_{yy} are different. Thus, the potential energy is given in the xy coordinate system as

$$\boldsymbol{e}_{\mathsf{pot},xy} = \frac{1}{2} \begin{bmatrix} K_{xx} \left(x^i_x\right)^2 \\ K_{yy} \left(x^i_y\right)^2 \end{bmatrix} . \tag{3.55}$$

Next, the work done by the structural damping forces in the ef coordinate system are obtained. The work done by the structural stiffness forces is already reflected in the components of the potential energy. However, calculating the power when the coordinate systems' orientation changes with each time step introduces some peculiarities because the edgewise and flapwise directions change during the time step. Hence, it is assumed that the rotational change of the ef coordinate system is small between time steps. Assuming that the damping forces and velocities change linearly over the time step (see Algorithm 11 for the linear velocity increase), the average of both is taken and the power calculated as

$$\boldsymbol{p}^i_c = -\frac{\left(\boldsymbol{f}^i_{c,ef} + \boldsymbol{f}^{i+1}_{c,ef}\right)\left(\dot{\boldsymbol{x}}^i_{ef} + \dot{\boldsymbol{x}}^{i+1}_{ef}\right)}{2} , \tag{3.56}$$

where the vector multiplication means piece-wise multiplication. The minus is used so that power and work done by the structural damping forces and moment are negative. The minus is needed because of the definition of $\boldsymbol{f}_c$ in Equation (3.41).

A similar calculation approach is done for the power of the drag and lift. These, however, are in the dl coordinate system. Thus, first the velocity $\dot{\boldsymbol{x}}$ is projected onto the dl coordinate system.

$$\dot{\boldsymbol{x}}_{dl}^{i} = \boldsymbol{R}_{xy\to dl}^{i} \begin{bmatrix} \dot{x}_x^i \\ \dot{x}_y^i \end{bmatrix} \tag{3.57}$$

$$\boldsymbol{p}_{\text{aero}}^{i} = \frac{\left(\boldsymbol{f}_{\text{aero},dl}^{i} + \boldsymbol{f}_{\text{aero},dl}^{i+1}\right)\left(\dot{\boldsymbol{x}}_{dl}^{i} + \dot{\boldsymbol{x}}_{dl}^{i+1}\right)}{2} \tag{3.58}$$

Again, a vector product here means piece-wise multiplication. To get the work done by the individual forces, the power at time step i is multiplied by the time step duration at i.

$$\boldsymbol{w}_{\text{c}}^{i} = \boldsymbol{p}_{c}^{i}\Delta t^{i} \tag{3.59}$$

$$\boldsymbol{w}_{\text{aero}}^{i} = \boldsymbol{p}_{\text{aero}}^{i}\Delta t^{i} \tag{3.60}$$

Before a final validation, calculations regarding oscillations are explained. Potential oscillations are found by finding the local (in time) maxima of the displacement x_x for edgewise and x_y for flapwise oscillations. The torsional deflection in all simulations is smaller than $0.5°$. Hence, x_x represents edgewise and x_y flapwise displacement accurately. Assuming that the motion is indeed oscillatory, the work done by any power contribution is then the sum of the power over all time steps of one period multiplied by the time step duration at each time step. The amplitude A^i of the period i is calculated as half the distance between the local (in time) maxima and minima of x_x or x_y, depending on which amplitude is wanted. The damping ratio is then calculated as $\ln\left(A^{i-1}/A^{i}\right)(2\pi)^{-1}$, assuming the damping ratio is small. Scipy's `find_peaks()` is used to find the local maxima and minima.

3.7.2. Validation

At last, the projections and the calculations of the energies, power, and work are validated. The calculations of the amplitudes and damping ratios are not validated. This is done by simulating a simple intuitive case for which the expected values can be readily calculated analytically. The structure is defined as

$$\boldsymbol{M} = \begin{bmatrix} 3\,\mathrm{kg\,m^{-1}} & 0 & 0 \\ 0 & 1\,\mathrm{kg\,m^{-1}} & 0 \\ 0 & 0 & 2\,\mathrm{kg\,m\,rad^{-1}} \end{bmatrix} \tag{3.61}$$

$$\boldsymbol{C} = \begin{bmatrix} 2\,\mathrm{N\,s\,m^{-2}} & 0 & 0 \\ 0 & 1\,\mathrm{N\,s\,m^{-2}} & 0 \\ 0 & 0 & 2\,\mathrm{N\,s\,rad^{-1}} \end{bmatrix} \tag{3.62}$$

$$\boldsymbol{K} = \begin{bmatrix} 1\,\mathrm{N\,m^{-2}} & 0 & 0 \\ 0 & 2\,\mathrm{N\,m^{-2}} & 0 \\ 0 & 0 & 3\,\mathrm{N\,rad^{-1}} \end{bmatrix} \tag{3.63}$$

The external forces are defined in Table 3.4. The simulation is run for $160\,\mathrm{s}$ with a time step duration of $0.001\,\mathrm{s}$. The initial displacement and velocity are $0\,\mathrm{m}$ (rad) and $0\,\mathrm{m\,s^{-1}}$ $(\mathrm{rad\,s^{-1}})$.

The results can be seen in Figures 3.19 and 3.20 and in Table 3.4. An elaborate analysis is not written here. The HHT–α^{HHT}–adapted algorithm returned the expected displacements after steps of $20\,\mathrm{s}$ as seen in the displacement plot. The structural stiffness force and moment vector is correct, too, combining the definition of $\boldsymbol{K}$ and the displacements. The components of the potential energy display the values they should be for the given displacements-stiffnesses combinations. Validating the calculation of the damping forces cannot be done as easily visually without a reference calculation. Also, judging the implementation based on whether the damping forces dissipate the correct amount of energy does not work if the same implementation is used in the time integration of the simulation. Unless the damping forces are erroneously implemented to add energy, they will always dissipate the correct amount

Table 3.4: Definition of the external forces and moments per unit length for the validation of the energy, power, and work calculations of the post-processing. "Linearly increasing" is meant for the whole time frame. θ is linearly increasing from 0 to π. x, y, and γ specify the direction of the force or moment.

time frame (s)	x ($\mathrm{N\,m^{-1}}$)	y ($\mathrm{N\,m^{-1}}$)	γ (N)
0 to 20	1	0	0
20 to 40	1	2	0
40 to 60	0	0	0 to π, linearly increasing
60 to 80	0	0	π
80 to 100	0	2	π
100 to 120	$-\sin(\theta)$	$\cos(\theta)$	0
120 to 140	0	1	0
140 to 160	0	0	0

Table 3.5: Work of the external and structural damping forces and moments for each time frame of the validation of the calculation of the energy, power, and work. All values are rounded to the second decimal place and the forces and moments are per unit length.

time frame (s)	$w_{x,\text{aero}}$ (N)	$w_{y,\text{aero}}$ (N)	$w_{\gamma,\text{aero}}$ (N)	$w_{x,\text{c}}$ (N)	$w_{y,\text{c}}$ (N)	$w_{\gamma,\text{c}}$ (N)
0 to 20	1.00	0.00	0.00	-0.50	0.00	0.00
20 to 40	0.00	2.00	0.00	0.00	-1.00	0.00
40 to 60	0.00	0.00	4.89	-0.46	-1.04	-0.86
60 to 80	0.00	0.00	0.99	0.00	0.00	-0.07
80 to 100	0.00	2.00	0.00	0.00	-1.00	0.00
100 to 120	0.35	-0.47	0.00	-0.18	-0.21	-4.93
120 to 140	0.00	0.48	0.00	-0.49	-0.23	0.00
140 to 160	0.00	0.00	0.00	0.00	-0.25	0.00
sum	1.35	4.01	5.88	-1.63	-3.73	-5.86

as long as they oppose the movement. This is because even if the damping force is wrong, the drop in kinetic energy will be correct for the given wrong force provided everything else is correct. For a given kinetic energy, there is always the same amount that can be dissipated. However, in the section model, the time integration does not use the method to calculate the damping forces. Hence, the method can be validated with the simulation data by calculating the dissipated energy after all. The calculation of the damping force at a given time step now does not influence the kinetic energy at the next time step anymore. Thus, if the calculated damping force were larger or smaller than it should, energy conservation would be broken when calculating the work done by it. This means both the damping force calculation and power/work calculation are validated together as one validation. It is assumed that there is no error cancellation between the two calculations. Table 3.5 shows that the difference between the work of the external forces and moment and that of the damping forces and moment is $0.02\,\mathrm{N}$. Without the rounding done for Table 3.5, the difference is $\approx 0.0005\,\mathrm{N}$, i.e., $\approx 0.007\,\%$ of the maximum total energy that occurred during the simulation. The calculation of the power and work is hereby validated.

At last, the projection of the forces is also validated by the nonlinear change in edgewise and flapwise external force during rotation and the negative flapwise external and stiffness force when the airfoil is pulled in the positive y direction while being rotated to $180°$ (between $80\,\mathrm{s}$ to $100\,\mathrm{s}$).

This concludes the validation of the projections, energies, power, and work.

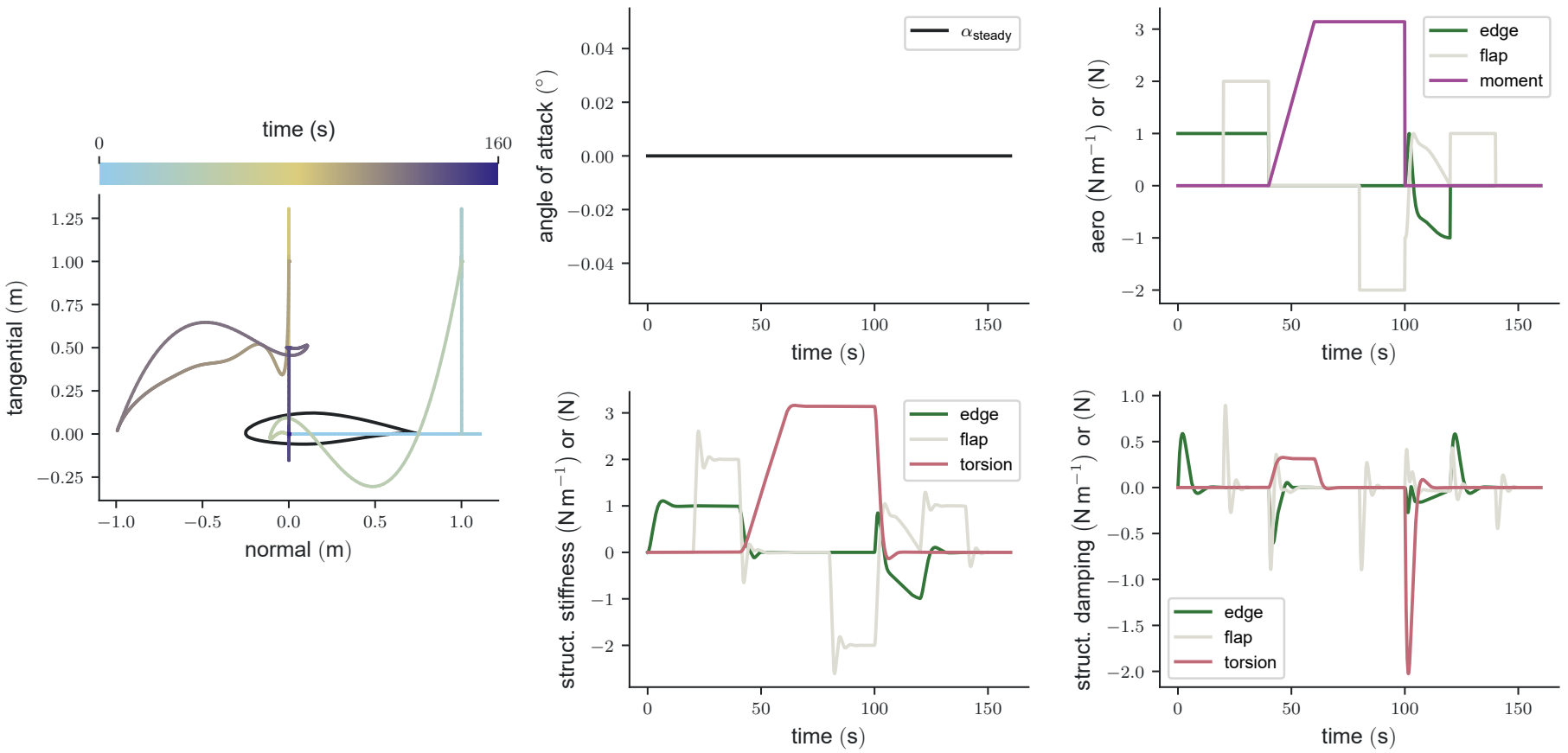

Figure 3.19: Time series of the displacement, angle of attack, and external and structural forces for the validation of the energy, power, and work calculations. All forces are per unit length.

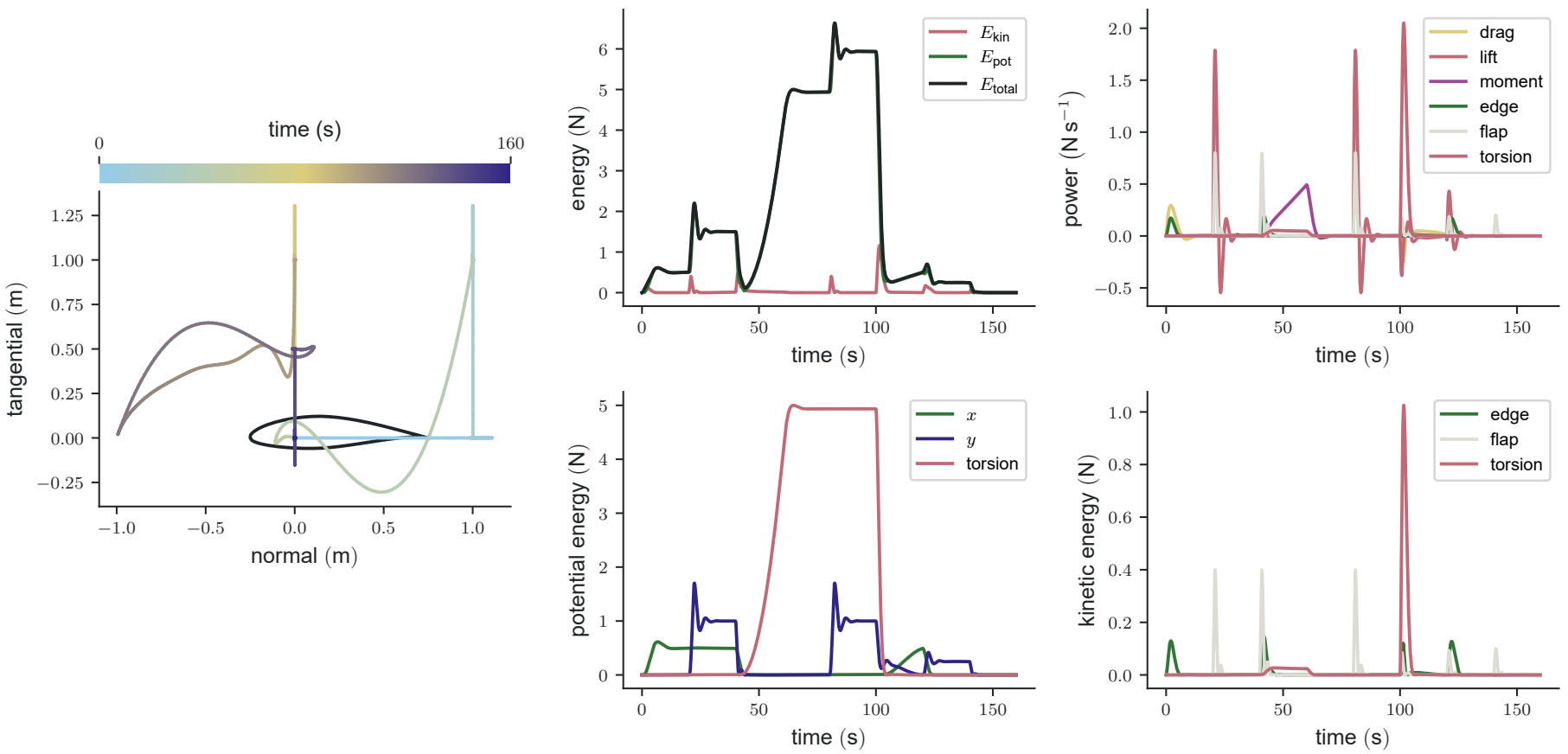

Figure 3.20: Time series of the displacement, kinetic and potential energies, and the power of the external and structural forces for the validation of the energy, power, and work calculations. All forces are per unit length. All energies and powers are per unit length.

4

Methodology

To sum up the research objectives from Section 1.1, first, the effect of employing dynamic stall models instead of quasi-steady aerodynamics during stall-induced instabilities is briefly investigated. Then, the major focus lies on comparing the results from the four implemented dynamic stall models of Sections 3.3.1.4 to 3.3.1.7 for stall-induced limit cycle oscillations. This includes not only the differences and similarities between the outputs of the models but also if the limit cycle oscillations dynamics even allow for a valid use of them.

All simulations are run with the section model that was purposefully developed with the objectives in mind and is extensively explained in Chapter 3. It models a 2D section (lumped mass-damper-spring system with additional torsional inertia, damping, and stiffness) aeroelasticity with an adapted HHT-α^{HHT} time integrator, linear damping and stiffness, and six aerodynamic models, four of which are the dynamic stall models that will be compared. The section is thought to be a slice of a 3D blade that belongs to a wind turbine rotor. The wind turbine is parked and the blade is pitched such that the section has a pitch of $90°$. The x and y directions from Figure 3.2 are thus called "normal" and "tangential", referring to the rotor plane. Post-processing exists to project forces in intuitive directions such as edgewise, flapwise, lift, and drag, calculate energies, and calculate the power and work done by the aerodynamic and damping forces. The implementation of the stated algorithms and methods has been validated. The section model allows for investigating the time series of every parameter used in the simulations because it keeps track of them all. At the end of a simulation, either the full-time series or time frames thereof can be saved. The model therefor allows for detailed investigations into the workings of the dynamic stall models. All simulations are run on a local machine. The calculations are sped up by the section model's automated multi-processing capabilities.

To answer the research questions, the following steps are taken

1. A specific combination of wind speed ($35\,\mathrm{m/s}$) and angle of attack ($20°$) is chosen for a time step convergence study for a simulation representative of the main simulations explained in the next steps. Used time step sizes are $0.01\,\mathrm{s}$, $0.005\,\mathrm{s}$, $0.001\,\mathrm{s}$ and $0.0005\,\mathrm{s}$. The simulation is run for $600\,\mathrm{s}$. The specific wind speed and angle of attack are chosen from preliminary simulations showing LCO for two of the dynamic stall models. The initial velocity is $\boldsymbol{u}_{\mathbf{0},\text{init}} = \begin{bmatrix} 0\,\mathrm{m\,s^{-1}} & 0\,\mathrm{m\,s^{-1}} & 0\,\mathrm{rad\,s^{-1}} \end{bmatrix}^T$. The initial position $\boldsymbol{x}_{\text{init}}$ is calculated with Algorithm 2. Then, $30\,\%$ of $x_{x,\text{init}}$ is added to itself: $x_{x,\text{init}} = 1.3 \times x_{x,\text{init}}$. This is to add a disturbance to the airfoil in the approximate edgewise direction. $30\,\%$ was chosen as an educated guess to cause a significant disturbance relative to the steady state. This way, either positive damping is captured for a significant amount of time or, if the system experiences negative damping, the time until the system enters a limit cycle oscillation state is reduced. The results are shown in Section 5.1.
2. $600\,\mathrm{s}$ simulations using the quasi-steady, 1st-order IAG, AEROHOR, HGM openFAST and HGM f-scaled models for a grid of wind speeds and angle of attacks (that approximately correspond to yaw-misalignment angles) are performed. 399 simulations are run for each model with wind speeds from $5\,\mathrm{m/s}$ to $50\,\mathrm{m/s}$ in steps of $2.5\,\mathrm{m/s}$ and steady-state angles of attack from $-25°$ to

$25°$ in steps of $2.5°$. The wind speed range was chosen to include normal operating wind speeds and extreme wind speeds. The angle of attack range is chosen to be larger than $\pm 15°$, which is "considered as normal idling conditions by wind turbine manufactures" (Wang et al., 2016), but not too large to keep a distance to fully separated flow. This is done to keep at least the steady inflow conditions inside the validity range of the dynamic stall models. The initial conditions are the same as in 1. Only the last $15\,\mathrm{s}$ of every simulation is saved. The time step size is is based on the results from 1. From the grid results, the limit cycle oscillation amplitudes, convergence criteria, and different maximum angles of attack per period are extracted.

3. Based on the results from 2., the amplitudes the quasi-steady model predicts are compared to those HGM openFAST predicts. HGM openFAST here acts as a general dynamic stall model to compare against quasi-steady aerodynamics. The results are shown in Section 5.2
4. Based on the results from 2., an analysis of the limit cycle oscillations amplitudes of each dynamic stall model is done and it is checked whether they operate in their validity range. Also, this is used to validate the assumption of using the HGM openFAST model as a baseline dynamic stall model from step 2. The results are shown in Section 5.3.
5. A specific wind speed and steady-state angle of attack combination from 2. is investigated in more detail to find similarities and differences between each model's predictions. The results are shown in Section 5.4.

No inertial or structural coupling is modelled. The structural and aerodynamic parameters are taken as those approximately at $75\,\%$ span of the DTU $10\,\mathrm{MW}$ reference wind turbine from Bak et al., 2013 as defined at the end of this chapter.

The analysis of the data is based on data visualisation and tables. The results for the grid simulations from step 1. are visualised as filled contour plots with accompanying colour bars. For specific contour plots, the colour bar scaling is kept the same to aid comparability. Light blue to ocker corresponds to the smallest negative value to zero. Ocker to dark blue corresponds to values from zero to the maximum positive. The results of step 4. are visualised as time series, Lissajous curves, damping coefficient functions of amplitudes, and tables of work done by the aerodynamic and damping forces and moments.

Lastly, the structural and aerodynamic data used are summarised. The structure is defined with the mass (inertia) matrix in the xy coordinate system ($\boldsymbol{M}$), damping matrix in the xy coordinate system ($\boldsymbol{C}$), stiffness matrix in the xy coordinate system ($\boldsymbol{K}$). The structural values are taken calculated from Stäblein et al., 2017:

$$\boldsymbol{M} = \begin{bmatrix} 203\,\mathrm{kg\,m^{-1}} & 0\,\mathrm{kg\,m^{-1}} & 0\,\mathrm{kg\,rad^{-1}} \\ 0\,\mathrm{kg\,m^{-1}} & 203\,\mathrm{kg\,m^{-1}} & 62\,\mathrm{kg\,rad^{-1}} \\ 0\,\mathrm{kg} & 62\,\mathrm{kg} & 144\,\mathrm{kg\,m\,rad^{-1}} \end{bmatrix}, \tag{4.1}$$

$$\boldsymbol{C} = \begin{bmatrix} 11.63\,\mathrm{Ns/m^2} & 0 & 0 \\ 0 & 7.31\,\mathrm{Ns/m^2} & 0 \\ 0 & 0 & 111.97\,\mathrm{N\,s\,rad^{-1}} \end{bmatrix}, \tag{4.2}$$

$$\boldsymbol{K} = \begin{bmatrix} 6931\,\mathrm{N/m^2} & 0 & 0 \\ 0 & 2982\,\mathrm{N/m^2} & 0 \\ 0 & 0 & 219\,050\,\mathrm{N\,rad^{-1}} \end{bmatrix}. \tag{4.3}$$

The DTU $10\,\mathrm{MW}$ reference wind turbine uses the FFA-W3-241 at $75\,\%$ span. Because the openFAST and HAWC2 validation data in Section 3.3.2 used the FFA-W3-221, this airfoil is used for the simulations instead. The steady polars are displayed in Figure 4.1.

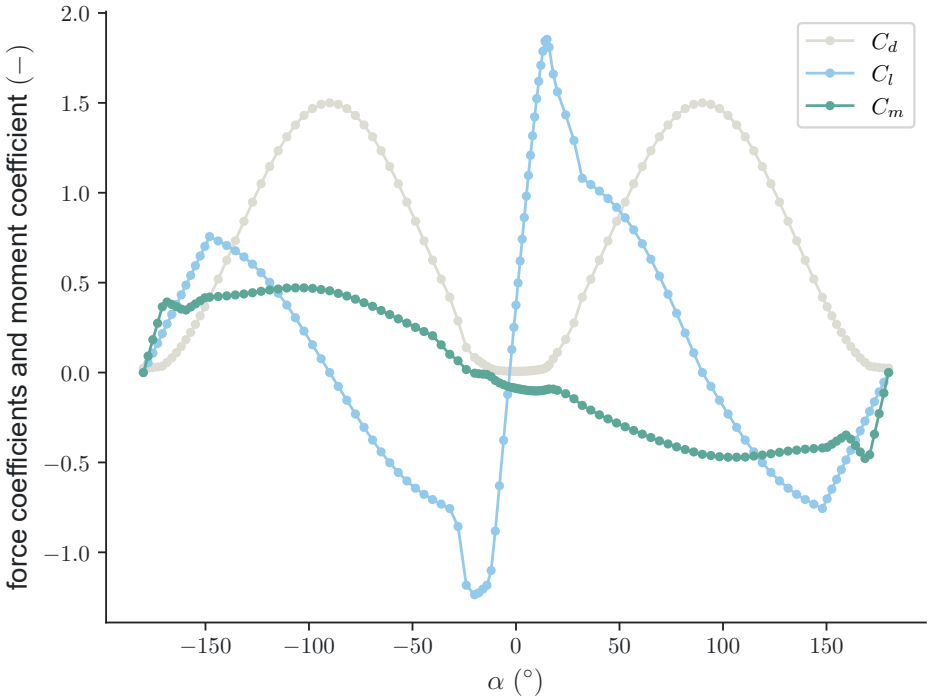

Figure 4.1: Steady drag, lift, and moment polars from for steady angle of attacks (α) from $-180°$ to $180°$ for the FFA-W3-221 airfoil.

5

Results

This chapter presents the results for the approach defined in Chapter 4.

5.1. Convergence study

Section 5.1 abstract

The dynamic behaviour predicted by the section model converges for finer time step duration sizes for all implemented dynamic stall models. A simulation with $35\,\mathrm{m/s}$ at a steady-state geometric angle of attack of $20°$ with time step durations of $0.01\,\mathrm{s}$, $0.005\,\mathrm{s}$, $0.001\,\mathrm{s}$ and $0.0005\,\mathrm{s}$ is used to investigate time step duration convergence after which $0.001\,\mathrm{s}$ is chosen for further simulations.

This section shows the convergence study for the time step size. The convergence study is defined as the first step in Chapter 4. The results are shown in Figures 5.1a to 5.1d. The time frames of the figures are chosen so that a noticeable oscillation is present. For the 1st-order IAG and AEROHOR model, no limit cycle oscillations develop and the time frame has to be placed early into the simulation before the oscillations are dampened out. Both HGM-based models show limit cycle oscillations. Hence, the time frames can be placed at the end of the simulation. The later the time frame, the more indicative the convergence study as deviations can accumulate. In both HGM-based results, there is a clear difference between the simulations using $0.01\,\mathrm{s}$ and $0.005\,\mathrm{s}$ time step sizes to using $0.001\,\mathrm{s}$ or $0.0005\,\mathrm{s}$. The same qualitative difference can be seen for the 1st-order IAG and AEROHOR simulations with smaller quantitative differences. As such, the simulations converge to a solution for finer time step sizes. Since the difference between the $0.001\,\mathrm{s}$ and $0.0005\,\mathrm{s}$ simulations is small but the computational effort is doubled for the $0.0005\,\mathrm{s}$ case, it is chosen to continue with a time step size of $0.001\,\mathrm{s}$ for the grid study.

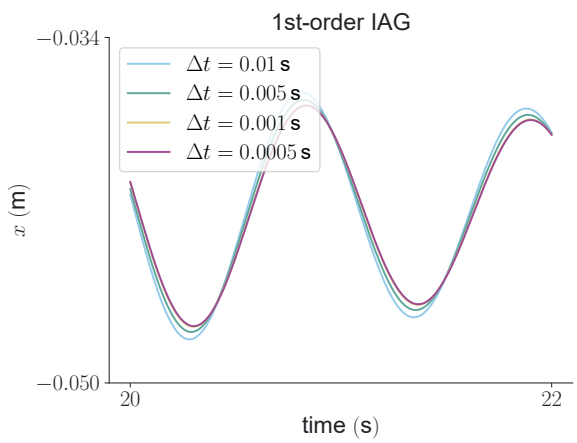

(a) Time frame of $20\,\mathrm{s}$ to $22\,\mathrm{s}$ of the results using the 1st-order IAG model.

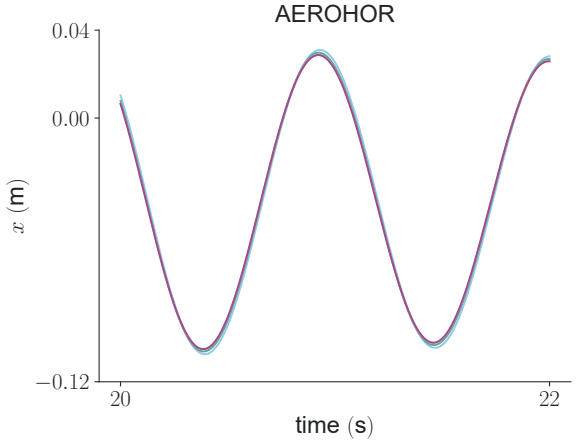

(b) Time frame of $100\,\mathrm{s}$ to $102\,\mathrm{s}$ of the results using the AEROHOR model.

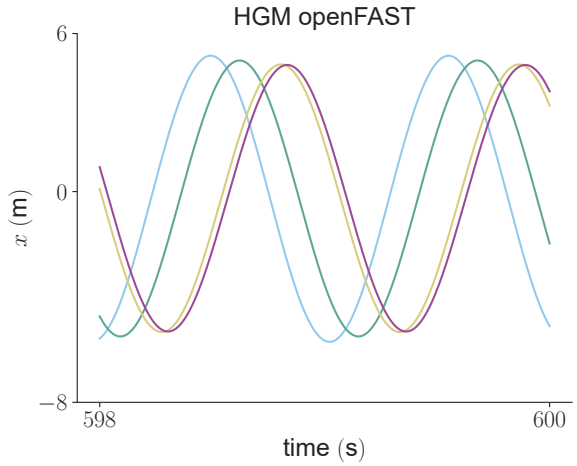

(c) Time frame of $598\,\mathrm{s}$ to $600\,\mathrm{s}$ of the results using the HGM openFAST model.

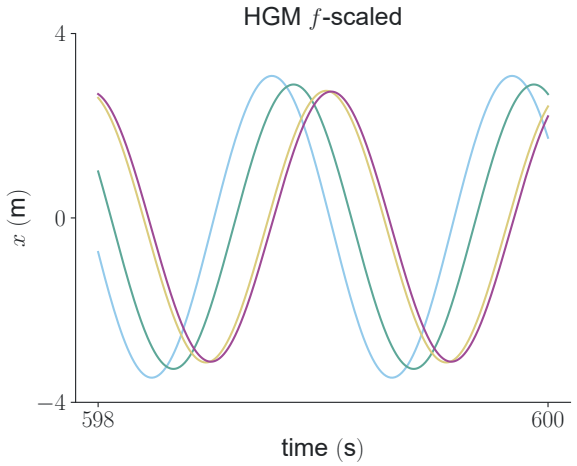

(d) Time frame of $598\,\mathrm{s}$ to $600\,\mathrm{s}$ of the results using the HGM f-scaled model.

Figure 5.1: Results of the time step size convergence study described in Chapter 4, step 1. Displacement in the x direction for an inflow velocity of $35\,\mathrm{m/s}$ at a steady-state angle of attack of $20°$. The initial position is the steady-state position plus a $30\,\%$ offset of the steady-state x displacement in the x direction. The line labels are the same in all sub-figures.

5.2. Wind speed – angle of attack grid (quasi-steady and HGM openFAST)

Section 5.2 abstract

The influence of using a dynamic stall model (the HGM openFAST model) in comparison to quasi-steady aerodynamics on the occurrence of limit cycle oscillations is shown. Inflow conditions are a grid of wind speeds from $5\,\mathrm{m/s}$ to $50\,\mathrm{m/s}$ at steady-state angles of attack from $-25°$ to $25°$. For a blade section similar to that at $75\,\%$ span of the DTU $10\,\mathrm{MW}$ reference wind turbine, quasi-steady aerodynamics predict limit cycle oscillations amplitudes up to $22.5\,\mathrm{m}$. Using the HGM openFAST model, amplitudes reach $7.2\,\mathrm{m}$. The regions of instability are similar but smaller using the HGM openFAST model.

This section shows the results of the grid simulations that is defined in Chapter 4, step 2, for the quasi-steady and HGM openFAST models. The colour bars are synchronised between both models.

The flapwise limit cycle oscillations amplitudes of each simulation's last period are shown in Figures 5.2a

and 5.2b. Using the quasi-steady model, no limit cycle oscillations occur between $-12.5°$ to $12.5°$ steady-state of attack. From $-25°$ to $-15°$ and $15°$ to $25°$, limit cycle oscillations occur and increase in amplitude with higher the wind speed. For the same angle of attack range, the limit cycle oscillation amplitudes increase with increasing magnitude of the angle of attack. At wind speeds of $50\,\mathrm{m/s}$, the amplitudes reach almost $22.5\,\mathrm{m}$. Using the HGM openFAST model, the region in which limit cycle oscillations occur for positive steady-state angles of attack is very similar but for negative ones, it is decreased in size. There, noticeable limit cycle oscillations only occur for higher wind speeds and angles of attack. In general, the amplitudes are significantly lower when using the HGM openFAST model. The trend of ever-increasing amplitudes for an increase in wind speed and or angle of attack is not as visible with the given colour bar scaling.

The relative change in edgewise amplitude between the second to last and last period of the simulation is shown in Figures 5.2c and 5.2d. Nearly all simulations show a converged solution. Exceptions are mainly at the border of the limit cycle oscillations regions. The only case exceeding the limits of $-3\,\%$ to $3\,\%$ is with the quasi-steady model for ($10\,\mathrm{m/s}$,$17.5°$). There, a complex oscillation with at least two different frequencies occurs, see Figure 5.4. The loop itself rotates around an axis normal to the plane over time causing the algorithm to calculate the change in amplitudes to be erroneous. No simulation around ($10\,\mathrm{m/s}$,$17.5°$) experiences a similar behaviour. For ($12.5\,\mathrm{m/s}$,$17.5°$) and ($10\,\mathrm{m/s}$,$20°$), there is a dominant edgewise oscillation. For ($7.5\,\mathrm{m/s}$,$17.5°$), there is a dominant flapwise oscillation. For ($10\,\mathrm{m/s}$,$15°$) the airfoil is, relative to the other now described oscillations, in its steady-state. A deeper analysis of the oscillation at ($10\,\mathrm{m/s}$,$17.5°$) is not part of the objectives and is thus not done.

The maximum quasi-steady angle of attack (α_{qs}) of each simulation's last period is shown in Figures 5.3a and 5.3b. For both models, the regions overlap with those of significant limit cycle oscillations amplitudes. For the quasi-steady model and positive steady-state angle of attack values, the quasi-steady angle of attacks are all of a similar magnitude. For the negative steady-state angles of attack, the magnitudes are more uneven. In the case of the HGM openFAST model, the quasi-steady angle of attacks are yet more uneven.

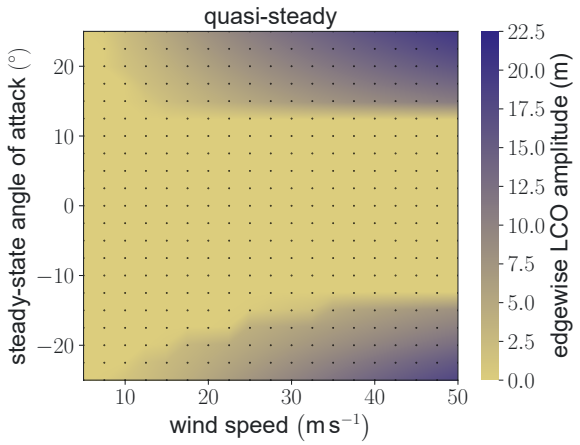

(a) Edgewise limit cycle oscillations using the quasi-steady model.

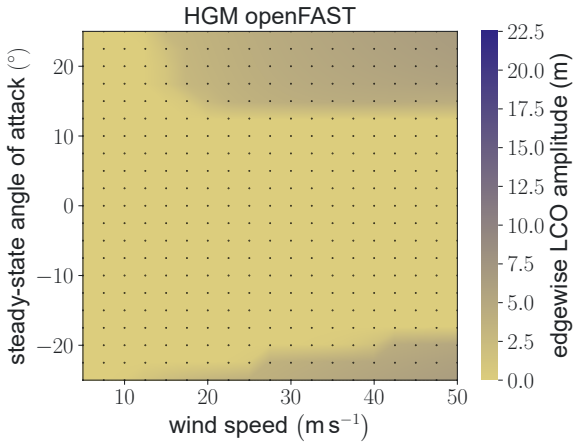

(b) Edgewise limit cycle oscillations using the HGM openFAST model.

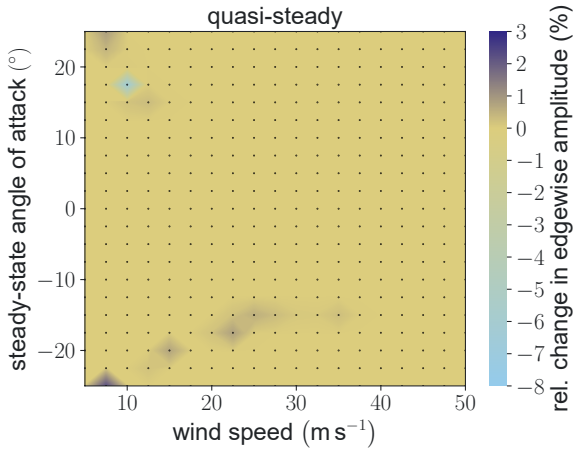

(c) Edgewise limit cycle oscillations convergence of the simulations using the quasi-steady model.

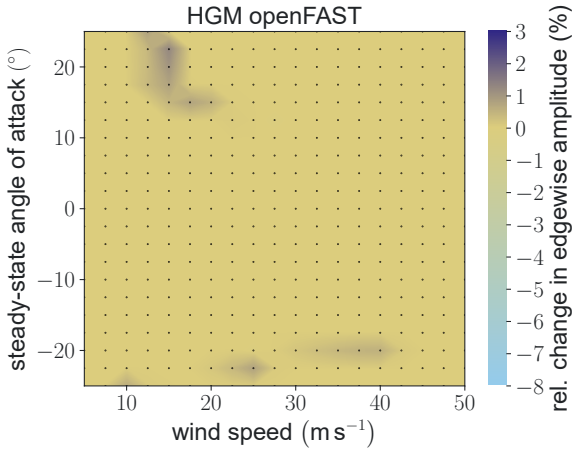

(d) Edgewise limit cycle oscillations convergence of the simulations using the HGM openFAST model.

Figure 5.2: Amplitude and convergence results of the grid calculations described in Chapter 4, step 2, for the quasi-steady and the HGM openFAST model. The convergence values are post-processed to be limited to a range from $-3\,\%$ to $3\,\%$. The black dots indicate pairs of angles of attack and wind speed for which a simulation was run.

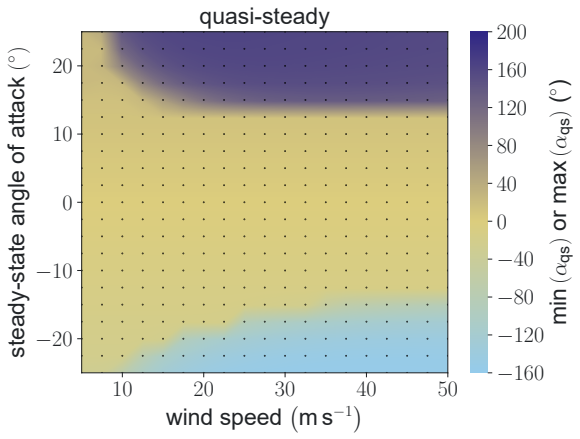

(a) Using the quasi-steady model.

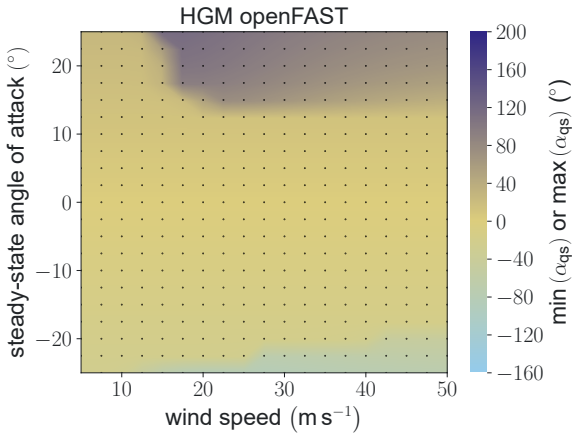

(b) Using the HGM openFAST model.

Figure 5.3: Smallest or largest quasi-steady angle of attack (α_{qs}) chosen by the greater magnitude during the last period of the grid calculations described in Chapter 4, step 2, for the quasi-steady and the HGM openFAST model. The black dots indicate pairs of angles of attack and wind speed for which a simulation was run.

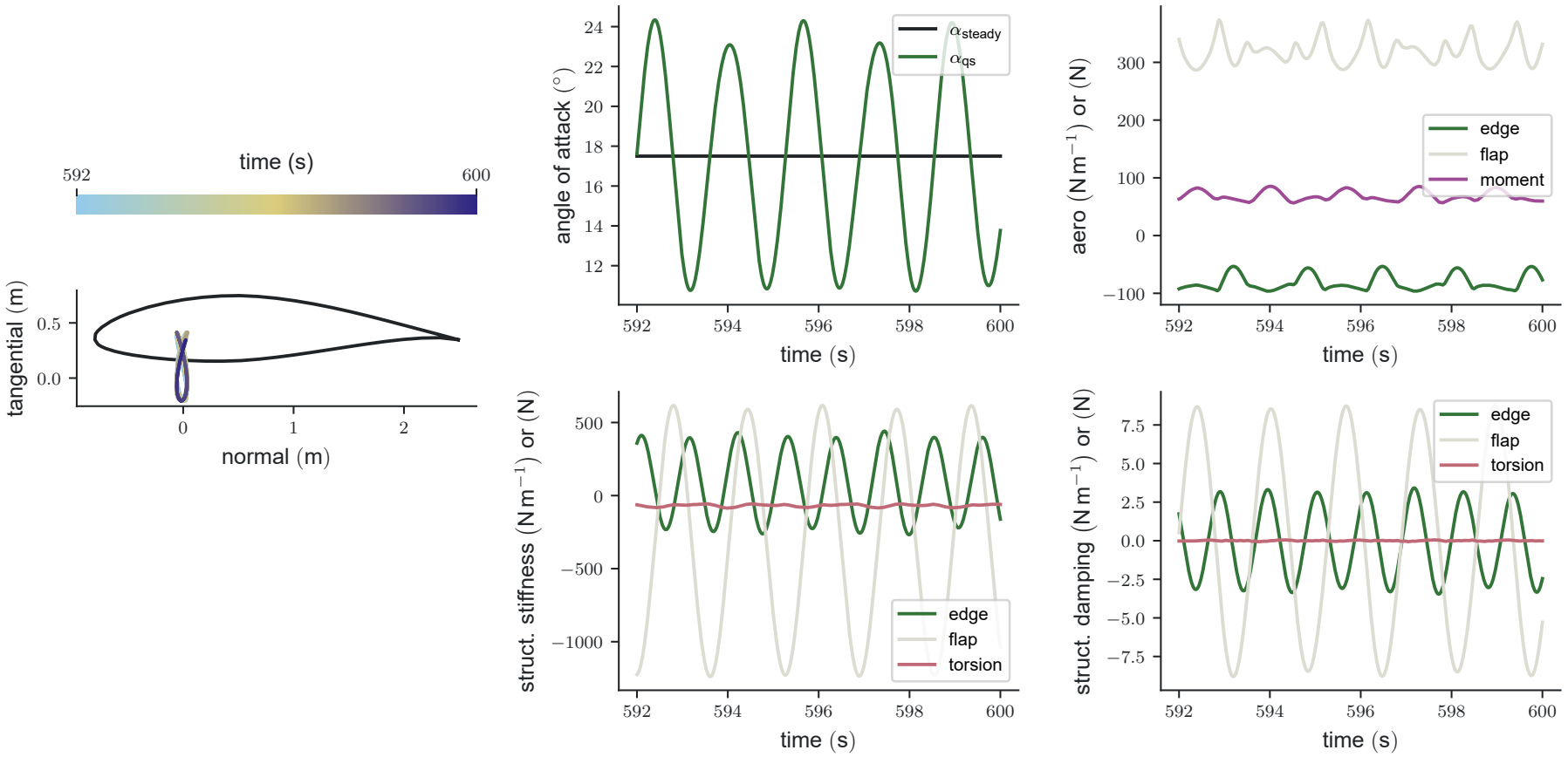

Figure 5.4: Time series of the displacement, angle of attacks, and external and structural forces for $10\,\mathrm{m/s}$ inflow at a steady-state angle of $17.5°$. The aerodynamic model is quasi-steady. All forces are per unit length.

At last, the flapwise limit cycle oscillations amplitudes are shown in Figures 5.5a and 5.5b. The regions overlap with those of the edgewise limit cycle oscillations amplitudes. However, the flapwise amplitudes are an order of magnitude lower than the edgewise's.

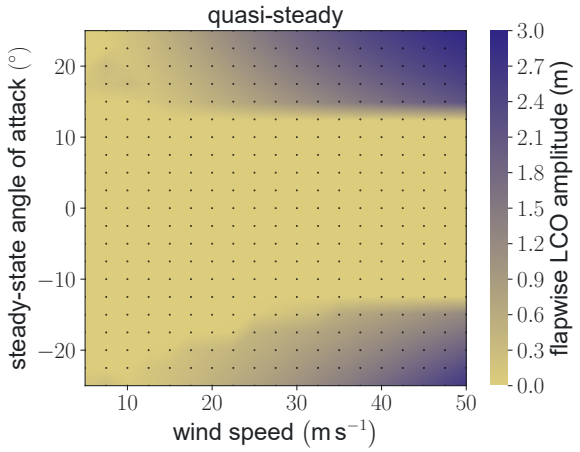

(a) Flapwise limit cycle oscillations using the quasi-steady model.

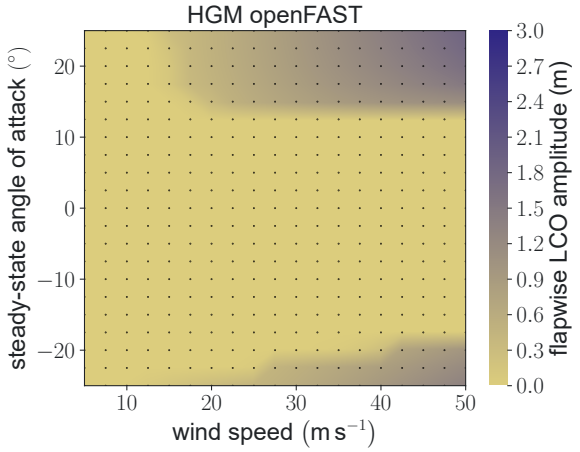

(b) Flapwise limit cycle oscillations using the HGM openFAST model.

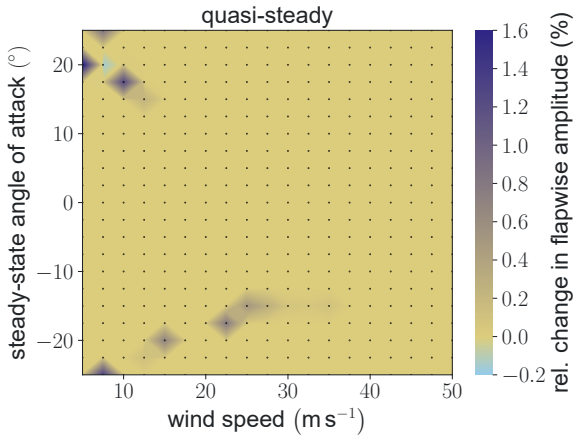

(c) Flapwise limit cycle oscillations convergence of the simulations using the quasi-steady model.

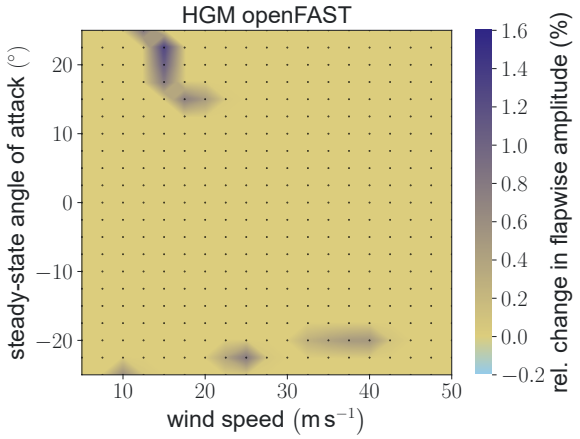

(d) Flapwise limit cycle oscillations convergence of the simulations using the HGM openFAST model.

Figure 5.5: Amplitude and convergence results of the grid calculations described in Chapter 4, step 2, for the quasi-steady and the HGM openFAST model. The black dots indicate pairs of angles of attack and wind speed for which a simulation was run.

5.3. Wind speed – angle of attack grid (1st-order IAG, AEROHOR, HGM openFAST, HGM f-scaled)

Section 5.3 abstract

The four dynamic stall models are compared for their influence on instability by analysing the amplitudes of the converged simulations. Inflow conditions are a grid of wind speeds from $5\,\mathrm{m/s}$ to $50\,\mathrm{m/s}$ at steady-state angles of attack from $-25°$ to $25°$. For a blade section similar to that at $75\,\%$ span of the DTU $10\,\mathrm{MW}$ reference wind turbine, both HGM-based models predict limit cycle oscillations that are dominant in the edgewise direction with an incidental flapwise component. The instability region and amplitudes predicted by the HGM f-scaled model are smaller than those predicted by the HGM openFAST model. Neither the 1st-order IAG model nor the AEROHOR model predict edgewise vibrations but flapwise limit cycle oscillations. However, these occur only for a few inflow conditions and have a small magnitude compared to the edgewise limit cycle oscillations predicted by the other two models.

This section shows the results of the grid simulations that are defined in Chapter 4, step 2, for the 1st-order IAG, AEROHOR, HGM openFAST and HGM f-scaled models. The colour bars are synchronised between all models. Non-synchronised plots can be found in Appendix A.2.

The edgewise limit cycle oscillations amplitudes of each simulation's last period are shown in Figures 5.6a to 5.6d. Both the 1st-order IAG model and the AEROHOR model do not show limit cycle oscillations using the given colour bar scaling. The flapwise amplitudes of the HGM openFAST model are already described in Section 5.2. The HGM f-scaled model's limit cycle oscillations regions are similar to those of the HGM openFAST model but decreased in extend. Noticeable limit cycle oscillations do not start above and below $-20°$ and $15°$ for the respective regions. Furthermore, for a given steady-state angle of attack, limit cycle oscillations occur at higher wind speeds (given they do occur) than what the HGM openFAST model predicts. The maximum amplitudes simulated with the HGM f-scaled model are reduced, too.

The relative change in edgewise amplitude between the second to last and last period of the simulation is shown in Figures 5.7a to 5.7d. Nearly all simulations show a converged solution. Exceptions are mainly at the border of the limit cycle oscillations regions. The only cases exceeding the limits of $-3\,\%$ to $3\,\%$ are with the AEROHOR model and the 1st-order IAG model. For the AEROHOR model, this happens for the conditions $([42, 5\,\mathrm{m/s}, 50\,\mathrm{m/s}], -25°)$ and $([45\,\mathrm{m/s}, 50\,\mathrm{m/s}], 17.5°)$. For the 1st-order IAG model, this happens for the conditions $([45\,\mathrm{m/s}, 50\,\mathrm{m/s}], 17.5°)$. All of these simulations are converged, too, but their edgewise responses contain multiple oscillations with different frequencies or phase shifts. The algorithm to calculate the amplitude change is based on the assumption of a single oscillation and thus returns erroneous values. An example of these simulations using the AEROHOR model is shown in Figure 5.8.

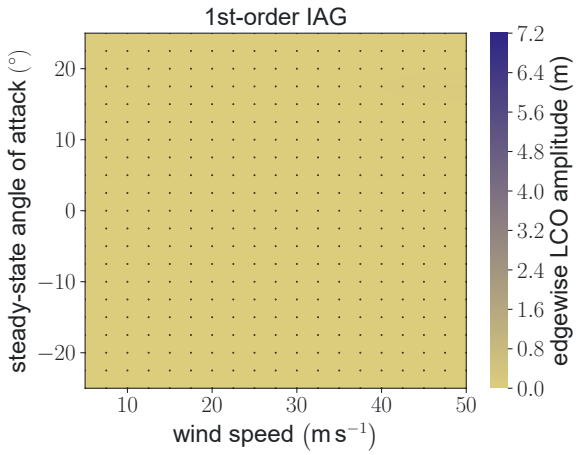

(a) Edgewise limit cycle oscillations amplitudes using the 1st-order IAG model.

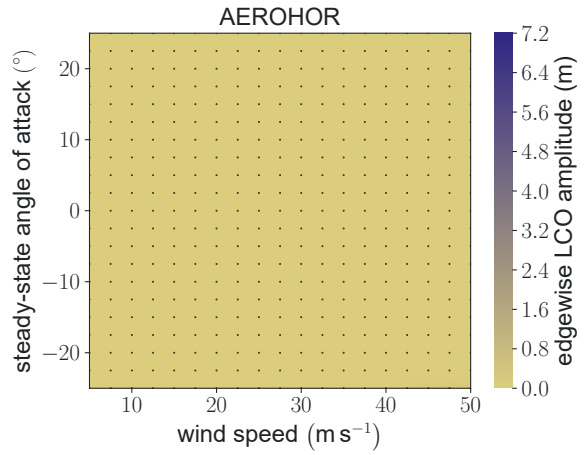

(b) Edgewise limit cycle oscillations amplitudes using the AEROHOR model.

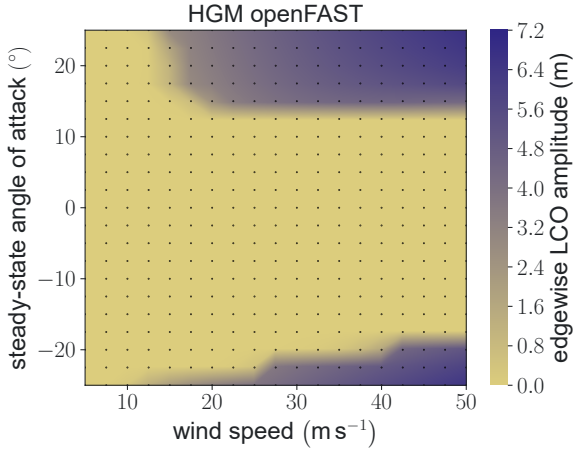

(c) Edgewise limit cycle oscillations amplitudes using the HGM openFAST model.

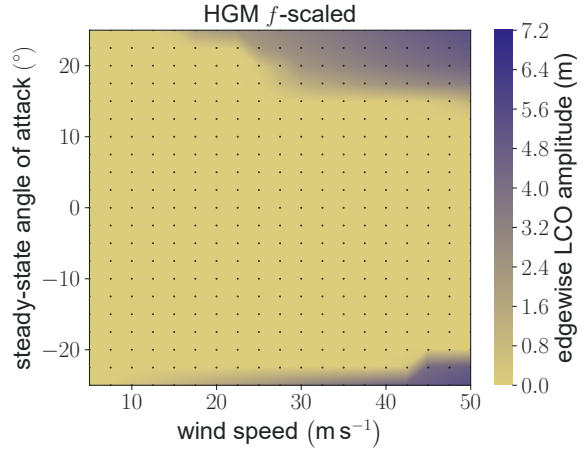

(d) Edgewise limit cycle oscillations amplitudes using the HGM f-scaled model.

Figure 5.6: Edgewise amplitude results of the grid calculations described in Chapter 4, step 2, for the four dynamic stall models. The black dots indicate pairs of angles of attack and wind speed for which a simulation was run. The same results with individual colour bar scaling can be seen in Figures A.2a to A.2d

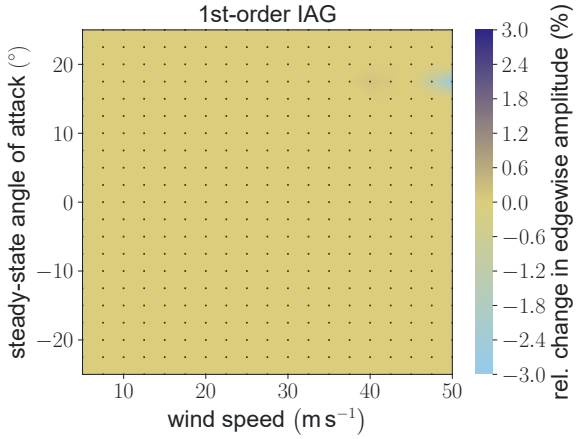

(a) Edgewise limit cycle oscillations convergence of the simulations using the 1st-order IAG model.

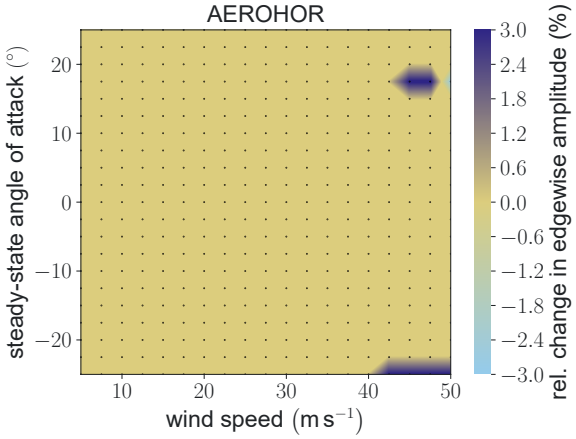

(b) Edgewise limit cycle oscillations convergence of the simulations using the AEROHOR model.

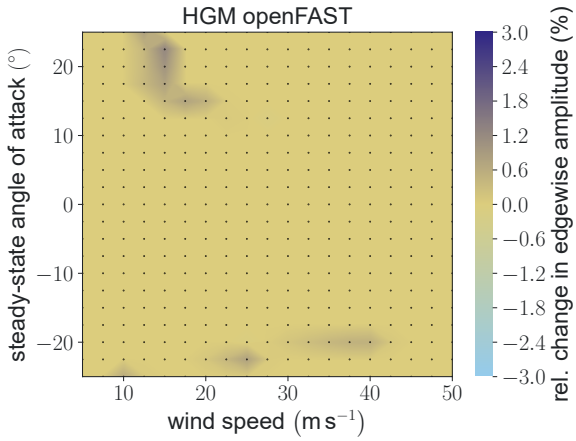

(c) Edgewise limit cycle oscillations convergence of the simulations using the HGM openFAST model.

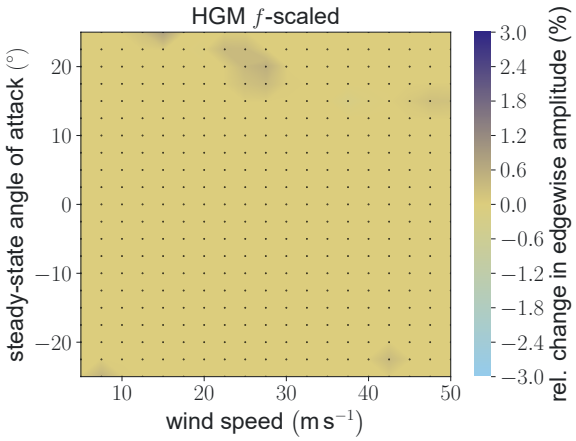

(d) Edgewise limit cycle oscillations convergence of the simulations using the HGM f-scaled model.

Figure 5.7: Edgewise convergence results of the grid calculations described in Chapter 4, step 2, for the four dynamic stall models. The values are post-processed to be limited to a range from $-3\,\%$ to $3\,\%$. The black dots indicate pairs of angles of attack and wind speed for which a simulation was run.

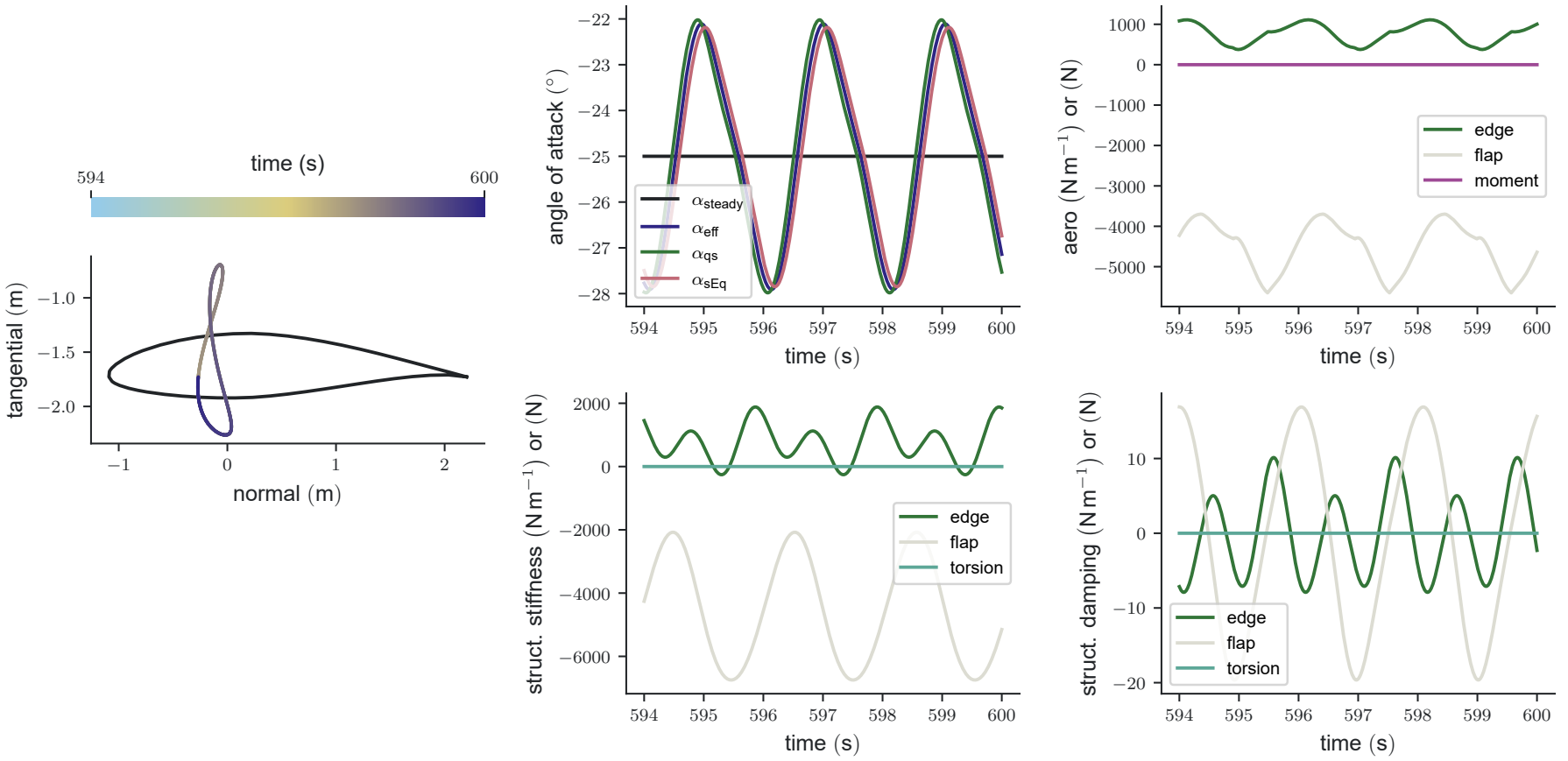

Figure 5.8: Time series of the displacement, angle of attacks, and external and structural forces for $45\,\mathrm{m/s}$ inflow at a steady-state angle of $-25°$. The aerodynamic model is AEROHOR. All forces are per unit length. The edgewise response shows multiple oscillation components. This can be seen in the displacement plot and the structural stiffness and damping forces plots.

The smallest or largest effective angle of attack (α_{eff}) of each simulation's last period is shown in Figures 5.9a to 5.9d. For both HGM-based models, the regions with increased effective angle of attack magnitude overlap with those of significant limit cycle oscillations amplitudes. For the HGM openFAST model, the largest effective angles of attack appear around $20\,\mathrm{m/s}$ to $22.5\,\mathrm{m/s}$ inflow velocities at steady-state angles of attack of $17.5°$ to $25°$ with the upper angle of attack limit given by the grid boundaries. For higher inflow velocities, the maximum effective angles of attack decrease. In the region of limit cycle oscillations in the negative steady-state angle of attack range, the magnitude of the maximum amplitude of the effective angles of attack seems to increase with higher inflow velocities, too. The same prominent decrease in the effective angle of attack with increasing inflow velocities in the limit cycle oscillations regions does not appear for the HGM f-scaled model. The maximum and minimum effective angles of attack for the 1st-order IAG model and the AEROHOR model are governed by the steady-state angle of attack values.

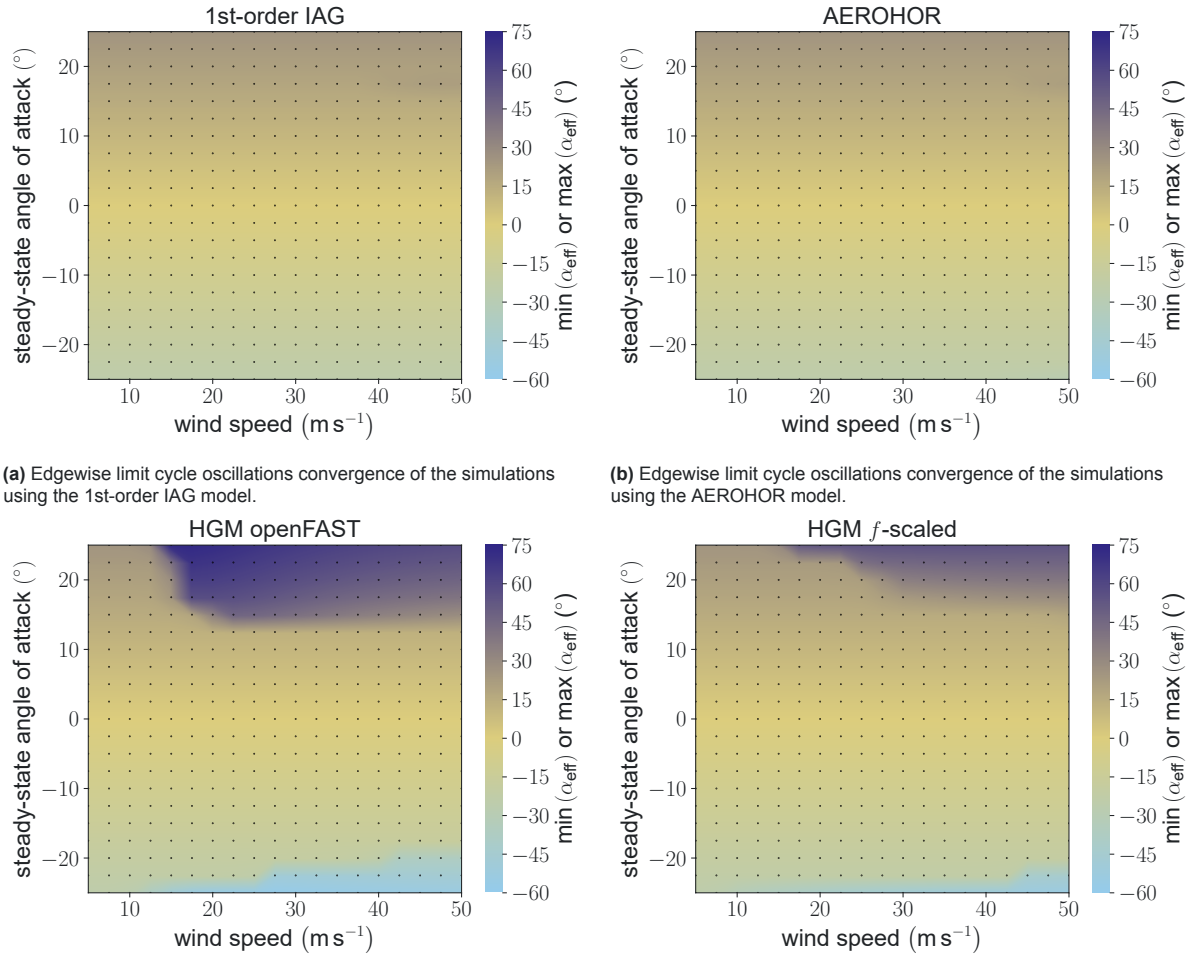

(a) Edgewise limit cycle oscillations convergence of the simulations using the 1st-order IAG model.

(b) Edgewise limit cycle oscillations convergence of the simulations using the AEROHOR model.

(c) Edgewise limit cycle oscillations convergence of the simulations using the HGM openFAST model.

(d) Edgewise limit cycle oscillations convergence of the simulations using the HGM f-scaled model.

Figure 5.9: Smallest or largest effective angle of attack (α_{eff}) chosen by the greater magnitude during the last period of the grid calculations described in Chapter 4, step 2, for the four dynamic stall models. The black dots indicate pairs of angles of attack and wind speed for which a simulation was run. The same results with individual colour bar scaling can be seen in Figures A.3a to A.3d

The flapwise limit cycle oscillations amplitudes of each simulation's last period are shown in Figures 5.10a to 5.10d. In contrast to the edgewise amplitudes from Figure 5.6, the 1st-order IAG and the section model show noticeable flapwise limit cycle oscillations relative to both HGM-based models. The former two model's flapwise limit cycle oscillations are constrained to a steady-state angle of attack of $-25°$ and $17.5°$ and wind speeds $> 35\,\mathrm{m\,s^{-1}}$ for the IAG model and $> 40\,\mathrm{m/s}$. However, it must be noted that simulations for $-25°$ lie on the boundary of the grid. The region of flapwise limit cycle oscillations is

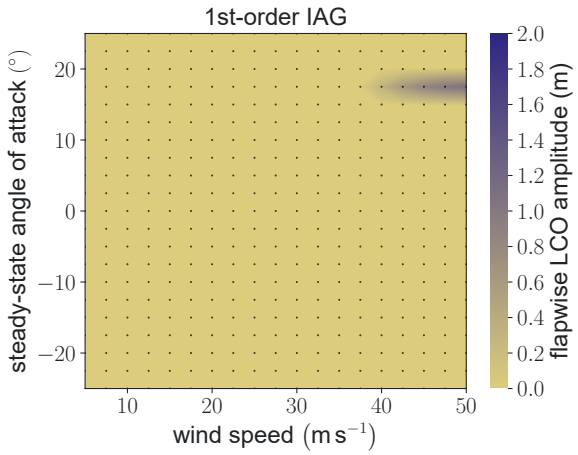

(a) Flapwise limit cycle oscillations amplitudes using the 1st-order IAG model.

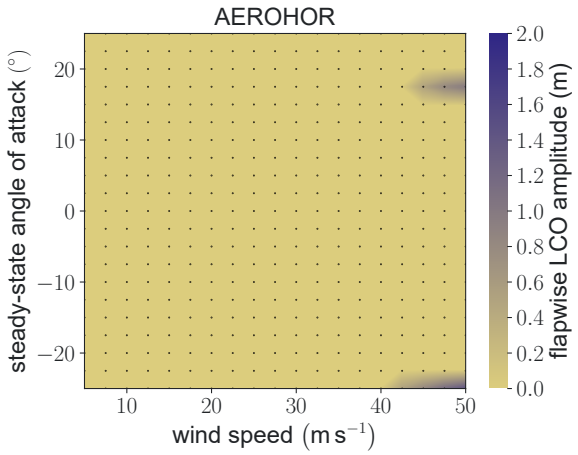

(b) Flapwise limit cycle oscillations amplitudes using the AEROHOR model.

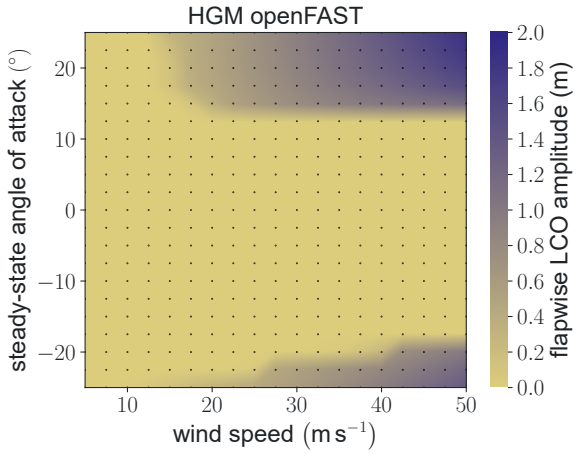

(c) Flapwise limit cycle oscillations amplitudes using the HGM openFAST model.

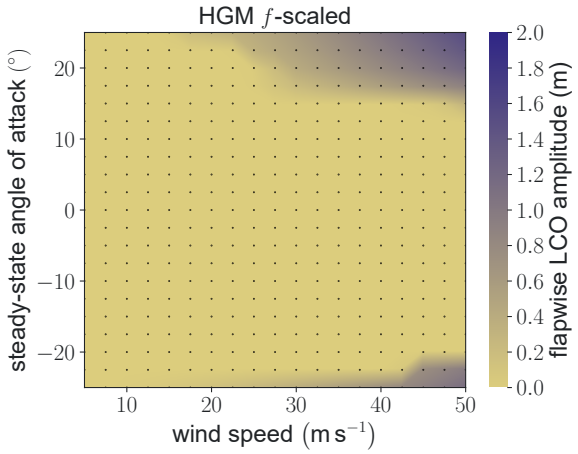

(d) Flapwise limit cycle oscillations amplitudes using the HGM f-scaled model.

Figure 5.10: Flapwise amplitude results of the grid calculations described in Chapter 4, step 2, for the four dynamic stall models. The black dots indicate pairs of angles of attack and wind speed for which a simulation was run. The same results with individual colour bar scaling can be seen in Figures A.4a to A.4d

smaller and with decreased amplitudes for the AEROHOR model compared to the 1st-order IAG model. The flapwise limit cycle oscillations for both HGM-based models are the same as for their edgewise limit cycle oscillations. The amplitudes are an order of magnitude lower.

The relative change in flapwise amplitude between the second to last and last period of the simulation is shown in Figures 5.11a to 5.11d. Nearly all simulations show a converged solution. Exceptions are mainly at the border of the limit cycle oscillation regions. The only special case is with the 1st-order IAG modelfor the conditions $(47.5\,\mathrm{m/s}, 17.5°)$). This simulation is converged, too, but the flapwise response is a superposition of multiple oscillation components. As explained earlier, multiple oscillation components cause the algorithm to calculate the change in amplitude to be erroneous. For brevity, data for this special case is not shown but is similar to that of Figure 5.8.

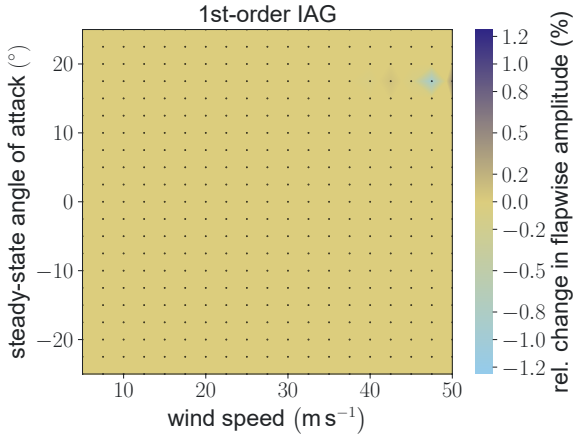

(a) Flapwise limit cycle oscillations convergence of the simulations using the 1st-order IAG model.

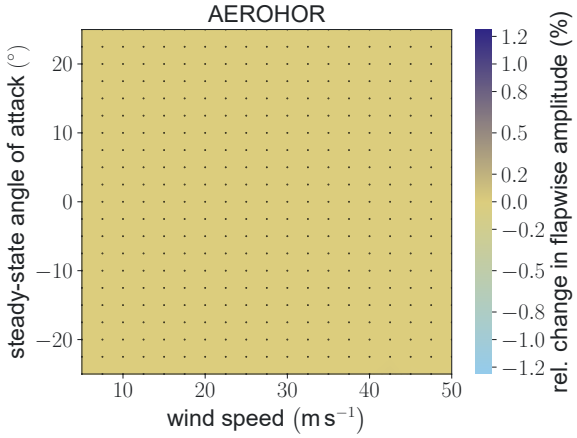

(b) Flapwise limit cycle oscillations convergence of the simulations using the AEROHOR model.

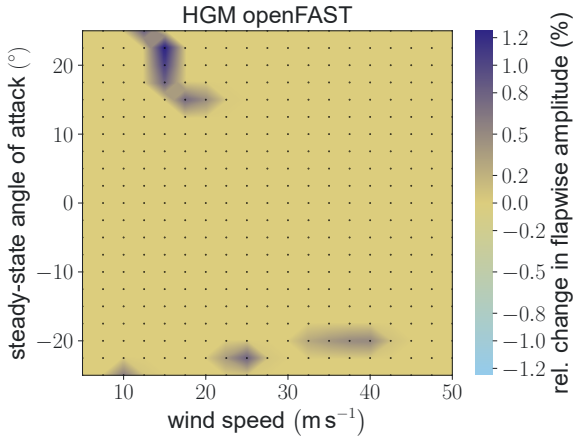

(c) Flapwise limit cycle oscillations convergence of the simulations using the HGM openFAST model.

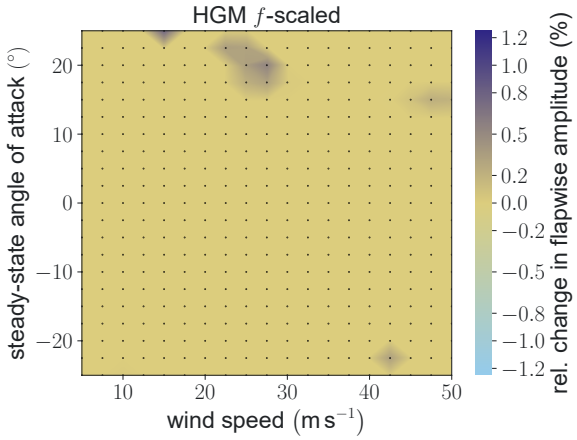

(d) Flapwise limit cycle oscillations convergence of the simulations using the HGM f-scaled model.

Figure 5.11: Flapwise convergence results of the grid calculations described in Chapter 4, step 2, for the four dynamic stall models. The black dots indicate pairs of angles of attack and wind speed for which a simulation was run.

Table 5.1: Approximate limit cycle oscillations (LCOs) amplitudes for an inflow velocity of $45\,\mathrm{m/s}$ at a steady-state angle of attack of $17.5°$.

	1st-order IAG	AEROHOR	HGM openFAST	HGM f-scaled
edgewise LCO amplitude (m)	0	0	5.8	4
flapwise LCO amplitude (m)	0.8	0.5	1.5	1

5.4. Detailed analysis for $25\,\mathrm{m/s}$ wind speed, $20°$ steady-state angle of attack (1st-order IAG, AEROHOR, HGM openFAST, HGM f-scaled)

Section 5.4 abstract

The four dynamic stall models are compared for their influence on instability by analysing time series of energies, powers, forces, and dynamic stall parameters, as well as by analysing the aeroelastic damping ratio, unsteady aerodynamic coefficient loops, and the work per period of the aerodynamic and structural forces per amplitude. Inflow conditions are a grid of wind speeds from $5\,\mathrm{m/s}$ to $50\,\mathrm{m/s}$ at steady-state angles of attack from $-25°$ to $25°$. No data is found that explains each model's behaviour in a trivial way. Limit cycle oscillation occur for the 1st-order IAG model and the AEROHOR model because the magnitude of the negative aerodynamic damping decreases at larger amplitudes. For the HGM-based models, the negative aerodynamic damping continues to grow in magnitude and limit cycle oscillations occurs when the structural damping catches up to balance the aerodynamic work. For the 1st-order IAG model and the AEROHOR model, the major-axes of the unsteady lift coefficient loops align with the negative lift slope of the steady polar in detached flow conditions. Both HGM-based models do not; their unsteady lift coefficient loops' major-axes correspond to a positive lift slope.

Based on the edgewise and flapwise limit cycle oscillations amplitude plots from Figures 5.6 and 5.10 the case $(45\,\mathrm{m/s}, 17.5°)$ is chosen for a detailed analysis. These conditions are especially interesting because of the different system responses of each model, see Table 5.1. While edgewise is the dominant limit cycle oscillation direction for the HGM-based models, it is flapwise for the 1st-order IAG and AEROHOR models. The latter do not show any significant oscillations in the edgewise direction. Additionally, the amplitudes using the HGM openFAST model are almost $1.5\times$ larger than those using the HGM f-scaled model. The analysis will be twofold:

1. Obtain an overview of the similarities and differences between the entire simulations. First, data for local extremes (maxima and minima) of different angles of attack, aerodynamic and structural forces are shown. The local (in time) extremes create an envelope showing which maxima and minima the respective parameters obtain during the oscillations. Then, the aeroelastic damping ratios are visualised as functions of the oscillation amplitude. For different amplitudes, the loops of the unsteady drag coefficient and unsteady lift coefficient are plotted over the steady polar. At last, the work done by the aerodynamic drag, lift, aerodynamic moment, and structural damping as functions of the amplitude are displayed. Unlike most other plots of this chapter, the plots for work are based on simulations with a time step duration of $0.0005\,\mathrm{s}$ (instead of $0.001\,\mathrm{s}$). Figure 5.1 shows barely any difference in the simulated system response. However, the post-processing calculations for the work done by the aerodynamic and structural forces and moments are more sensitive to the time step duration.
2. A more detailed analysis of the initial transient time is done for each simulation. The time frame is chosen small enough so that individual time series can be investigated yet still large enough to capture the different developments.

A lot of data is visualised which causes many pages to be filled with plots. In the caption of all of the following figures, there are hyperlinks to return to the paragraph that references them. The time series

of some data is visualised by connecting local (in time) maxima to maxima and minima to minima. The local extremes are found using scipy's find_peaks. The area encompassed by the maxima and minima line is shaded with the same colour as the lines. For the plots of the aerodynamic and structural forces and moments, the labels indicate the direction.

First, Figure 5.12 is described. The results are obtained with the 1st-order IAG model. Initially, the amplitude of the edgewise oscillations decreases until $\approx 10\,\mathrm{s}$, after which it slightly increases again. The amplitude of the flap-wise oscillations increases immediately until the system enters limit cycle oscillations. This convergence is reached after $\approx 50\,\mathrm{s}$. The differences between the quasi-steady angle of attack and effective angle of attack are very small throughout the simulation. The converged angle of attack range is $\approx 14°$ to $21°$. The converged oscillation is dominant in the flapwise direction and the displacement loop is almost symmetric. At last, all parameters except for the edgewise and flapwise structural stiffness forces are visibly affected by higher-frequency oscillations.

In Figure 5.13, different parameters regarding the damping are shown. The damping ratio and work are calculated based on peaks of the y displacement because of the eventually dominant flapwise oscillation. The y and flapwise direction are approximately the same for small torsional angles. Figure 5.13a shows an increase in the damping ratio from initial ≈ -0.03 to 0 with increasing oscillation amplitude. The slope of the damping ratio is relatively constant for amplitudes between $0.2\,\mathrm{m}$ to $0.6\,\mathrm{m}$ and then increases until close to reaching the limit cycle oscillation amplitude. Figure 5.13b shows the work done by different forces and moments. The work done by the aerodynamic drag and lift first increase while the former is constantly dissipating energy and the latter is adding energy. The drag's work starts to decrease earlier than the lift's work. The aerodynamic moment's work contribution is negligible. The total aerodynamic work first increases and starts to decrease between (amplitude-wise) the decrease of the drag and lift work. The structural damping work first decreases slightly before continuously increasing. At the largest oscillation amplitude, the total aerodynamic and total structural work has the same magnitude but different signs. The loops of the unsteady drag coefficient and unsteady lift coefficient from Figures 5.13c and 5.13d, respectively, contain high-frequency oscillations on top of their loops. Most of the loops do not close exactly. The effective angle of attack increases with increasing oscillation amplitude and the loops become wider. The unsteady drag coefficient loops rotate clockwise slightly with increasing amplitude. Such a trend is not as apparent for the unsteady lift coefficient loops. However, both the unsteady drag coefficient and unsteady lift coefficient loop shapes are vaguely parallel to the steady polar of the same effective angle of attack range.

In Figure 5.14 the results using the AEROHOR model are shown. Again, there is an initial decrease in the amplitude of edgewise oscillations. However, in comparison to the 1st-order IAG model, the flapwise oscillation amplitude decreases initially, too. This development lasts until $\approx 40\,\mathrm{s}$. There, the damping ratio reaches its minimum of just under -0.08. Then, the flapwise amplitudes increase while the edgewise amplitudes continue to decrease. Throughout the whole simulation, the differences between the quasi-steady angle of attack (α_{qs}) and effective angle of attack (α_{eff}) are very small. The maximum ranges of the aerodynamic forces in the edge- and flapwise direction first decrease until $\approx 40\,\mathrm{s}$ and then increase. Convergence is reached after $\approx 150\,\mathrm{s}$. The converged angle of attack range is $\approx 16°$ to $19°$. The converged oscillation is overall narrow in the edgewise direction and slightly less symmetric as predicted by the 1st-order IAG model. At the bottom (smaller flapwise displacement) of the oscillation, the edgewise displacement changes are smaller than at the top (larger flapwise displacement) of the oscillation. The maximum-minimum ranges of the angles of attack, forces, and moments are smaller than what is predicted with the 1st-order IAG model.

Figure 5.15 shows parameters related to the damping, still for the AEROHOR model. The damping ratio and work are calculated based on peaks of the y displacement because of the eventually dominant flapwise oscillation. With regards to the initial $40\,\mathrm{s}$ described in the above paragraph, the amplitude at which $40\,\mathrm{s}$ have passed is specified in the damping and work plots Figures 5.15a and 5.15b. Below $40\,\mathrm{s}$, both damping and work show strong nonlinearities even for small amplitudes. After $40\,\mathrm{s}$, the work done by the lift increases before displaying a significant decrease $\rightarrow$ small increase $\rightarrow$ smaller decrease behaviour. In comparison, the work done by the drag decreases more evenly until the largest amplitudes. This decrease in drag first halts the increase in total aerodynamic work from low to medium amplitudes and then decreases it until the structural and aerodynamic work cancels each other. The structural work first decreases until $40\,\mathrm{s}$ and then increases. With an increase in oscillation amplitude, the loops

of the unsteady drag coefficient increase in their effective angle of attack range but hardly widen. In contrast, the unsteady lift coefficient loops increase in their effective angle of attack range and widen significantly. While initially not exactly closed and with an uneven shape, the unsteady lift coefficient loops become increasingly elliptical and connect to themselves for increasing amplitude. The loop shapes of both the unsteady drag coefficient and unsteady lift coefficient are on average pointed in the same direction as the steady polar for the same range of effective angle of attack.

Figure 5.16 shows the results using the HGM openFAST model. No initial decrease of the amplitude of the edgewise or flapwise oscillation is apparent. Rather, the edgewise oscillation grows immediately. The flapwise and torsional oscillations start growing in amplitude significantly at $\approx 50\,\mathrm{s}$ and $80\,\mathrm{s}$, respectively. The oscillation is converged after $\approx 150\,\mathrm{s}$. The differences between the quasi-steady angle of attack and effective angle of attack is significant. The converged range of their values is $\approx -18°$ to $60°$ and $\approx -12°$ to $36°$ for the quasi-steady angle of attack and effective angle of attack, respectively. The oscillation's displacement appears to be an ellipse with the semi-major axis dominantly in edgewise direction. The ranges from maximum to minimum for all angles of attack, forces, and moments are significantly larger than those predicted by the 1st-order IAG model and the AEROHOR model. The maximum values for the aerodynamic force in flapwise direction and the moment are further from their mean than the minimum values. For the aerodynamic force in the edgewise direction, the opposite occurs.

Data for the damping, work, and coefficient loops is visualised in Figure 5.17. The damping ratio and work are calculated based on peaks of the x displacement because of the dominant edgewise oscillation. The amplitude at which $30\,\mathrm{s}$ of the simulation has passed is marked. The reason will become apparent when analysing this time frame closer in step 2. In this initial time, the damping ratio has a mean of just under -0.08. After that, the damping ratio in Figure 5.17a appears to grow exponentially before reaching the lightly-shaded region. In this region, the damping ratio continues to grow linearly before increasing its growth just before reaching the darkly-shaded region after which the slope does not further increase significantly. During the limit cycle oscillations, the effective angle of attack exceeds $25°$ for $39\,\%$ and $35°$ for $20\,\%$ of the time of each period. In Figure 5.17b it can be seen that first, i.e. from smaller to larger amplitudes, both the aerodynamic drag's and lift's work per period increases. After entering the lightly-shaded region, the lift's work decreases drastically while the drag's work continues to grow. The use of drag and lift is not accidentally switched. The structural damping work grows (negatively) with increasing amplitude until it cancels the added energy from the aerodynamic forces and moment. The loops of both the unsteady drag coefficient and unsteady lift coefficient significantly grow in size and change shape. During the limit cycle oscillations, unsteady drag coefficient values of 1.75 and unsteady lift coefficient values of 4 are reached. A major difference to the results predicted with the 1st-order IAG model and the AEROHOR model is that the unsteady lift coefficient loop shape does not match with the direction of the steady polar for values effective angle of attack larger than $\approx 15°$. Similarly, for the limit cycle oscillation state, the unsteady drag coefficient loop shape direction differs from the steady polar, too.

At last, Figure 5.18 shows the results obtained with the HGM f-scaled model. The core development is the same as predicted with the HGM openFAST model. However, the oscillation is converged only after $\approx 250\,\mathrm{s}$. Additionally, the differences between quasi-steady angle of attack and effective angle of attack and all other maximum-minimum ranges are decreased. The differences between the maximum-mean and minimum-mean for the aerodynamic forces and moment are smaller than those predicted with the HGM openFAST model and the structural stiffness and damping forces and moments are approximately halved. The displacement loop is again an ellipse, this time with it's semi-major axis almost identical to the edgewise direction.

The results for the damping ratio, work and unsteady coefficient loops is visualised in Figure 5.19. The damping ratio and work are again calculated based on peaks of the x displacement because of the dominant edgewise oscillation. The amplitude at which $50\,\mathrm{s}$ of the simulation has passed is marked. The reason will become apparent when analysing this time frame closer in step 2. The initial damping ratio as seen in Figure 5.19a has a mean of ≈ -0.06. Then, the slope increases until an amplitude of $\approx 1.5\,\mathrm{m}$ after which it appears constant. The largest effective angle of attack to occur during the simulation is $27.4°$. During the limit cycle oscillations, the effective angle of attack exceeds $25°$ for $20\,\%$ of the time of each period. Figure 5.19b shows the contribution of different forces and moments to the

work done on the system. Both the aerodynamic drag's and lift's work increase increase continuously after $50\,\mathrm{s}$ while being positive. The drag's work slope increases but the lift's work slope decreases, turning into a negative slope at approximately the beginning of the lightly-shaded region. After that, the lift's contribution sinks. However, the still-occurring increase of the drag's work outweighs this decrease causing the total aerodynamic work to increase. Limit cycle oscillations are reached only once the structural damping work has caught up to the total aerodynamic work. The loops of both the unsteady drag coefficient and unsteady lift coefficient grow in size and change shape. During the limit cycle oscillations, unsteady drag coefficient values of 0.3 and unsteady lift coefficient values of 2.7 are reached. Like predicted by the HGM openFAST model but in contrast to the 1st-order IAG model and the AEROHOR model, the unsteady lift coefficient loop shape does not match the steady polar direction for effective angle of attack values larger than $\approx 15°$. In comparison to the HGM openFAST model however, the unsteady drag coefficient loop shape matches its steady polar better.

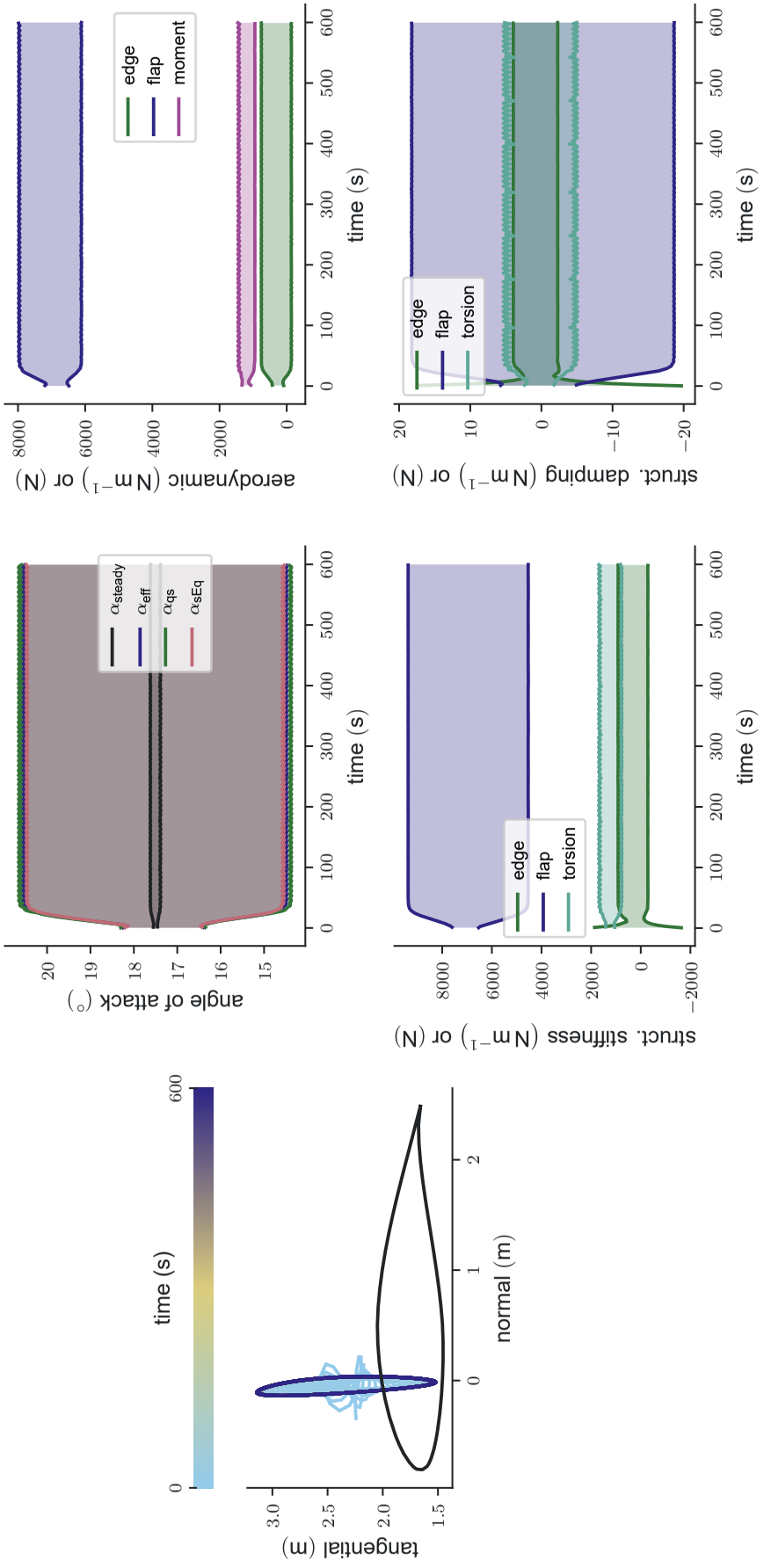

Figure 5.12: Time series of the displacement and the maximum and minimum of different angle of attacks and external and structural forces for 45 m/s inflow at a steady-state angle of 17.5°. The aerodynamic model is the 1st-order IAG. All forces are per unit length. The displacement plot is affected by a limited time resolution causing the loops to appear thicker and more discontinuous than they are. It's axes refer to the rotor plane (airfoil is pitched to 90° in stand-still).. Back to the paragraph here.

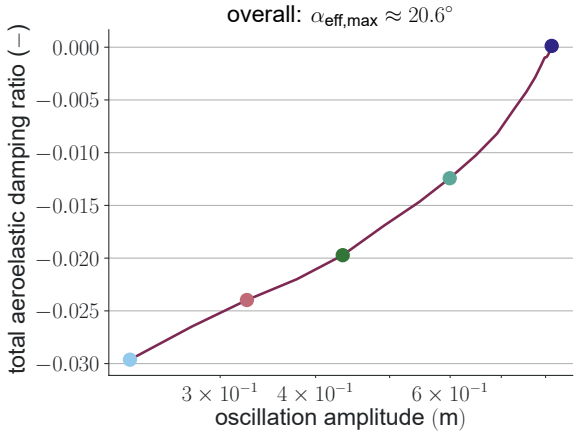

(a) The amplitude axis is log-scaled. $\alpha_{\text{eff,max}}$ denotes the effective angle of attack that occurred during the simulation. The coloured dots define amplitudes for which the unsteady unsteady drag coefficient and unsteady lift coefficient are plotted in Figures 5.13c and 5.13d, respectively.

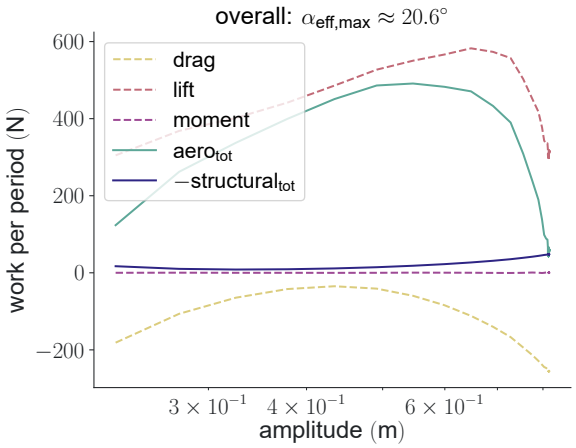

(b) Work per period of the aerodynamic drag, lift, and aerodynamic moment and of the structural damping forces and moment ($\text{structural}_{\text{tot}}$. The work is per unit length.

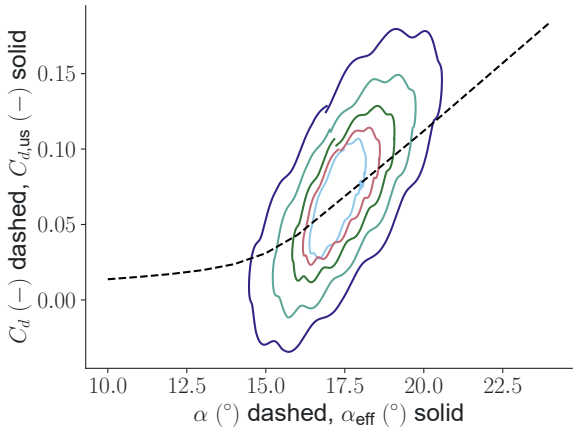

(c) Loops of the unsteady drag coefficient ($C_{d,\text{us}}$) at different oscillation amplitudes. The colours of the loops correspond to the colours of the dots in Figure 5.13a. The steady polar is shown as the black dashed line.

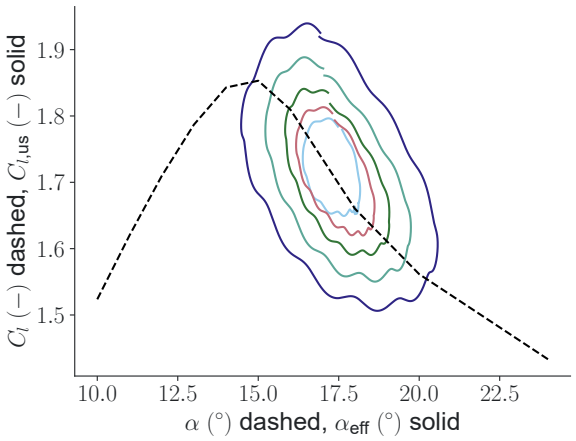

(d) Loops of the unsteady lift coefficient ($C_{l,\text{us}}$) at different oscillation amplitudes. The colours of the loops correspond to the colours of the dots in Figure 5.13a. The steady polar is shown as the black dashed line.

Figure 5.13: Different parameters from a simulation using the 1st-order IAG model with for an inflow velocity of $45\,\text{m}\,\text{s}^{-1}$ at a steady-state angle of attack of $17.5°$. The simulation was run for $100\,\text{s}$ with a time step duration of $0.0005\,\text{s}$. The first $3\,\text{s}$ of the simulation are not incorporated in this plot. The damping and work calculations are based on peaks of the y displacement. Back to the paragraph here.

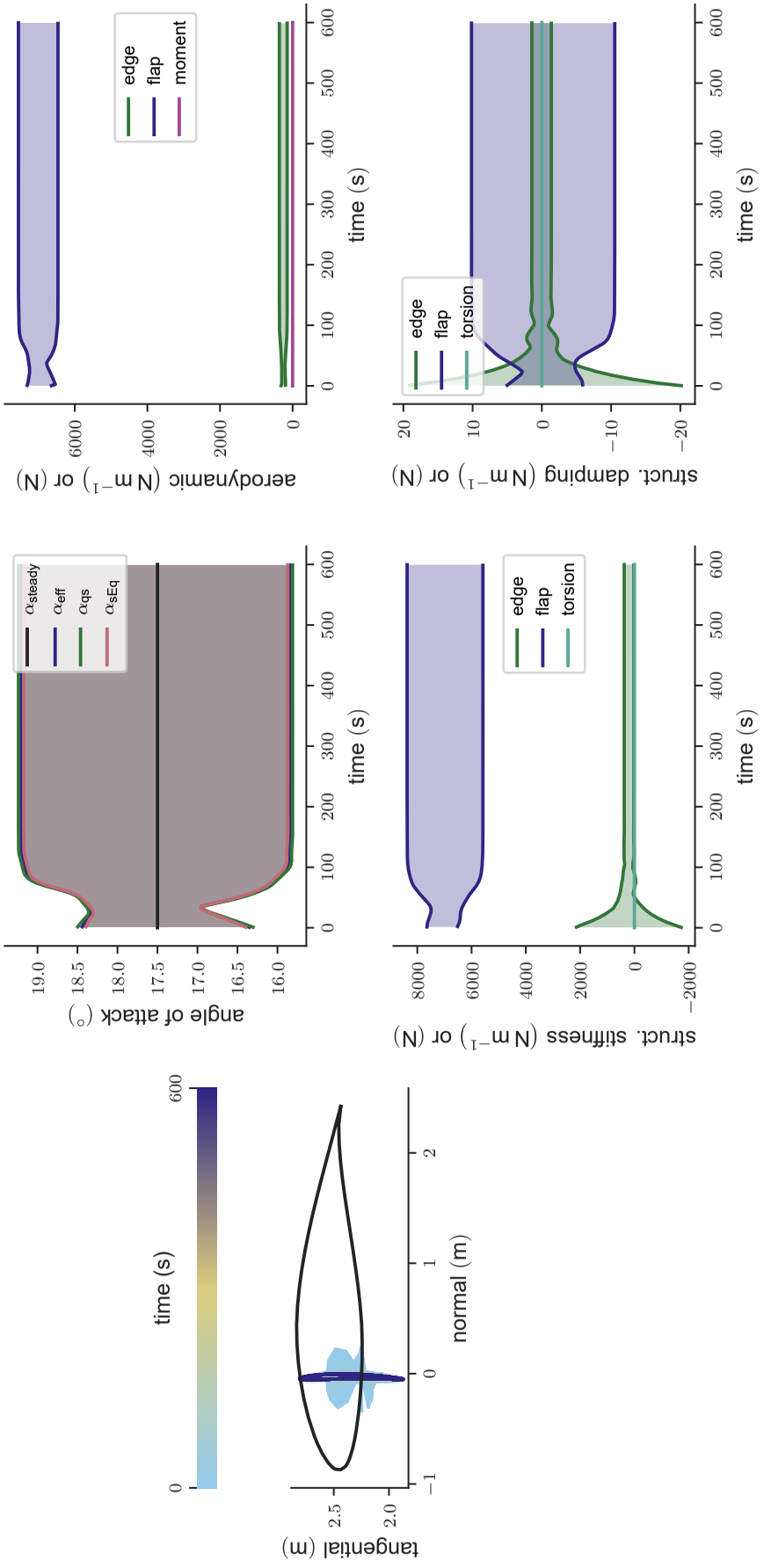

Figure 5.14: Time series of the displacement and the maximum and minimum of different angle of attacks and external and structural forces for 45 m/s inflow at a steady-state angle of 17.5°. The aerodynamic model is AEROHOR. All forces are per unit length. The displacement plot is affected by a limited time resolution causing the loops to appear thicker and more discontinuous than they are. It's axes refer to the rotor plane (airfoil is pitched to 90° in stand-still). Back to the paragraph here.

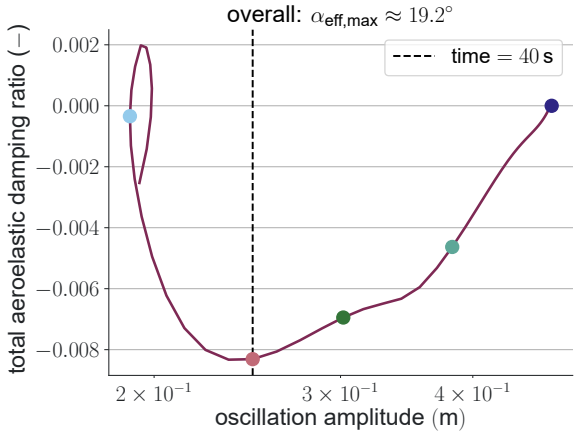

(a) The amplitude axis is log-scaled. $\alpha_{\text{eff,max}}$ denotes the effective angle of attack that occurred during the simulation. The coloured dots define amplitudes for which the unsteady unsteady drag coefficient and unsteady lift coefficient are plotted in Figures 5.15c and 5.15d, respectively.

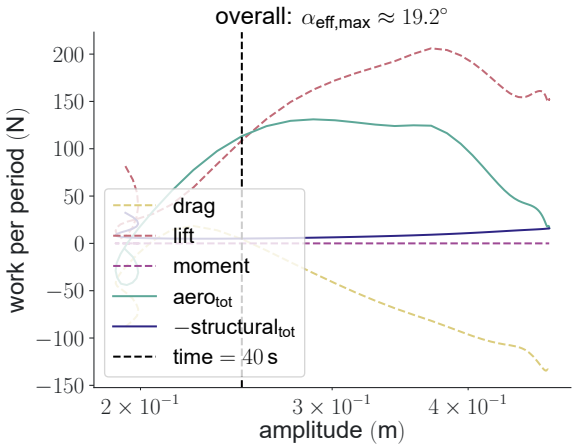

(b) Work per period of the aerodynamic drag, lift, and aerodynamic moment and of the structural damping forces and moment ($\text{structural}_{\text{tot}}$. The work is per unit length.

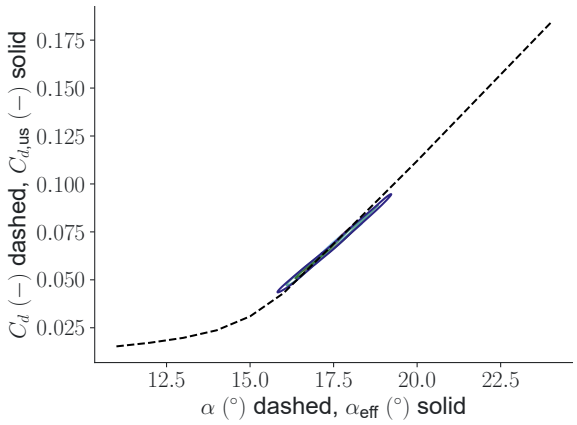

(c) Loops of the unsteady drag coefficient ($C_{d,\text{us}}$) at different oscillation amplitudes. The colours of the loops correspond to the colours of the dots in Figure 5.15a. The steady polar is shown as the black dashed line.

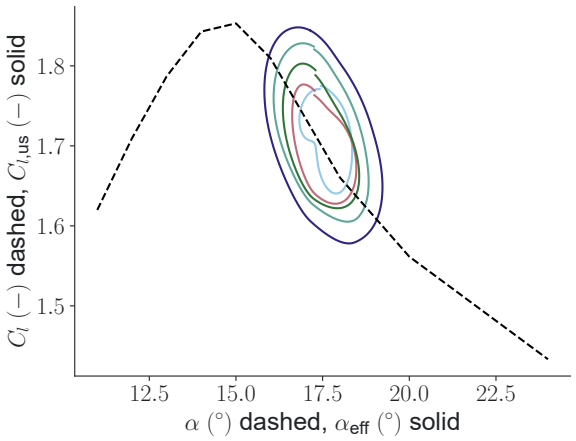

(d) Loops of the unsteady lift coefficient ($C_{l,\text{us}}$) at different oscillation amplitudes. The colours of the loops correspond to the colours of the dots in Figure 5.15a. The steady polar is shown as the black dashed line.

Figure 5.15: Different parameters from a simulation using the AEROHOR model with for an inflow velocity of $45\,\text{m}\,\text{s}^{-1}$ at a steady-state angle of attack of $17.5°$. The simulation was run for $200\,\text{s}$ with a time step duration of $0.0005\,\text{s}$. The first $3\,\text{s}$ of the simulation are not incorporated in this plot. The amplitude at which $40\,\text{s}$ of the simulation has passed is marked. The damping and work calculations are based on peaks of the y displacement. Back to the paragraph here.

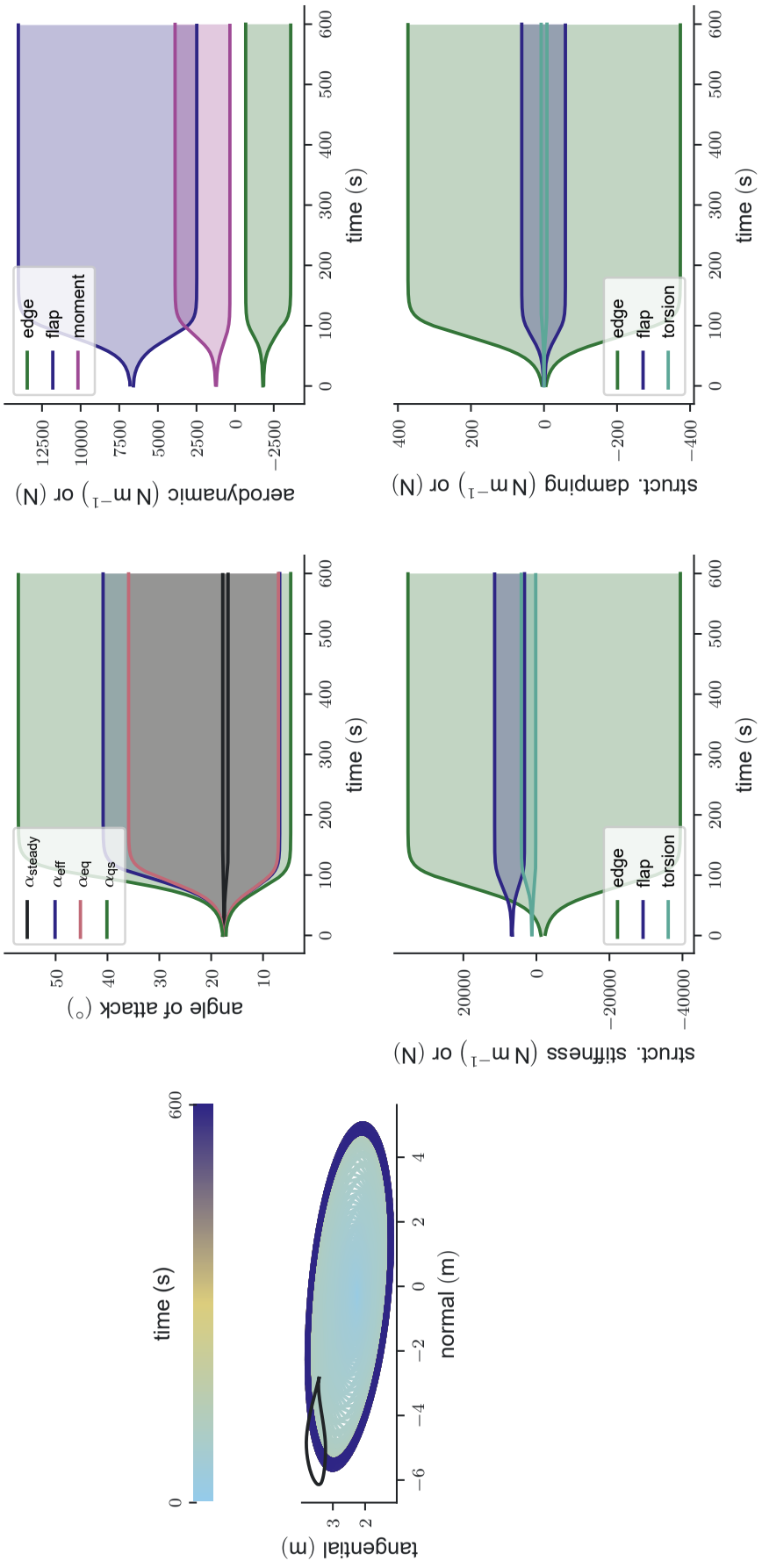

Figure 5.16: Time series of the displacement and the maximum and minimum of different angle of attacks and external and structural forces for 45 m/s inflow at a steady-state angle of 17.5°. The aerodynamic model is HGM openFAST. All forces are per unit length. The displacement plot is affected by a limited time resolution causing the loops to appear thicker and more discontinuous than they are. It's axes refer to the rotor plane (airfoil is pitched to 90° in stand-still). Back to the paragraph here.

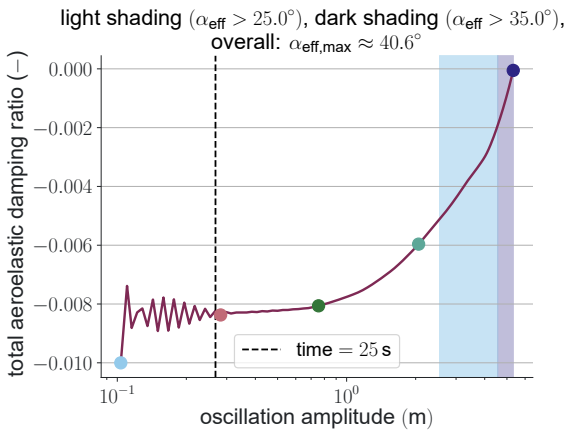

(a) The amplitude axis is $\log$-scaled. $\alpha_{\text{eff,max}}$ denotes the effective angle of attack that occurred during the simulation. The coloured dots define amplitudes for which the unsteady unsteady drag coefficient and unsteady lift coefficient are plotted in Figures 5.17c and 5.17d, respectively. Shaded regions indicate that a threshold effective angle of attack is exceeded at least once per period.

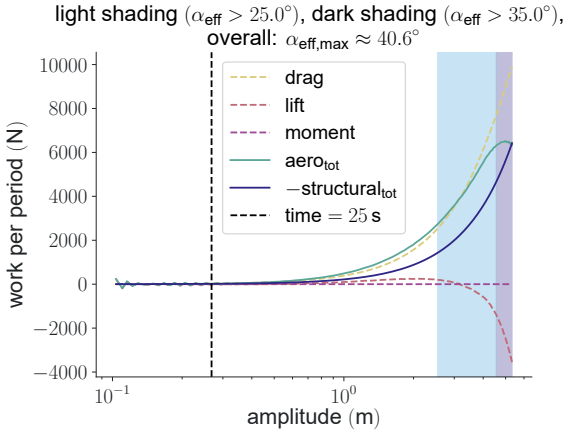

(b) Work per period of the aerodynamic drag, lift, and aerodynamic moment and of the structural damping forces and moment (structural$_{\text{tot}}$. The work is per unit length. Shaded regions indicate that a threshold effective angle of attack is exceeded at least once per period.

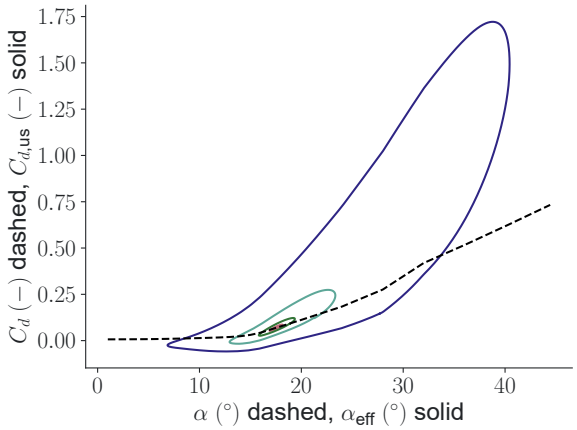

(c) Loops of the unsteady drag coefficient ($C_{d,\text{us}}$) at different oscillation amplitudes. The colours of the loops correspond to the colours of the dots in Figure 5.17a. The steady polar is shown as the black dashed line.

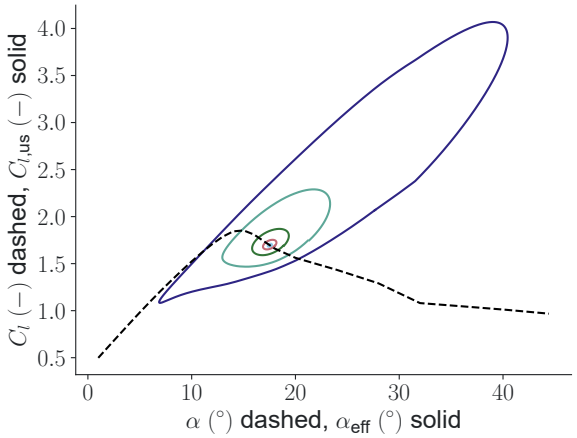

(d) Loops of the unsteady lift coefficient ($C_{l,\text{us}}$) at different oscillation amplitudes. The colours of the loops correspond to the colours of the dots in Figure 5.17a. The steady polar is shown as the black dashed line.

Figure 5.17: Different parameters from a simulation using the HGM openFAST model with for an inflow velocity of $45\,\text{m}\,\text{s}^{-1}$ at a steady-state angle of attack of $17.5°$. The simulation was run for $150\,\text{s}$ with a time step duration of $0.0005\,\text{s}$. The first $5\,\text{s}$ of the simulation are not incorporated in this plot. The amplitude at which $25\,\text{s}$ of the simulation has passed is marked. The damping and work calculations are based on peaks of the x displacement. Back to the paragraph here.

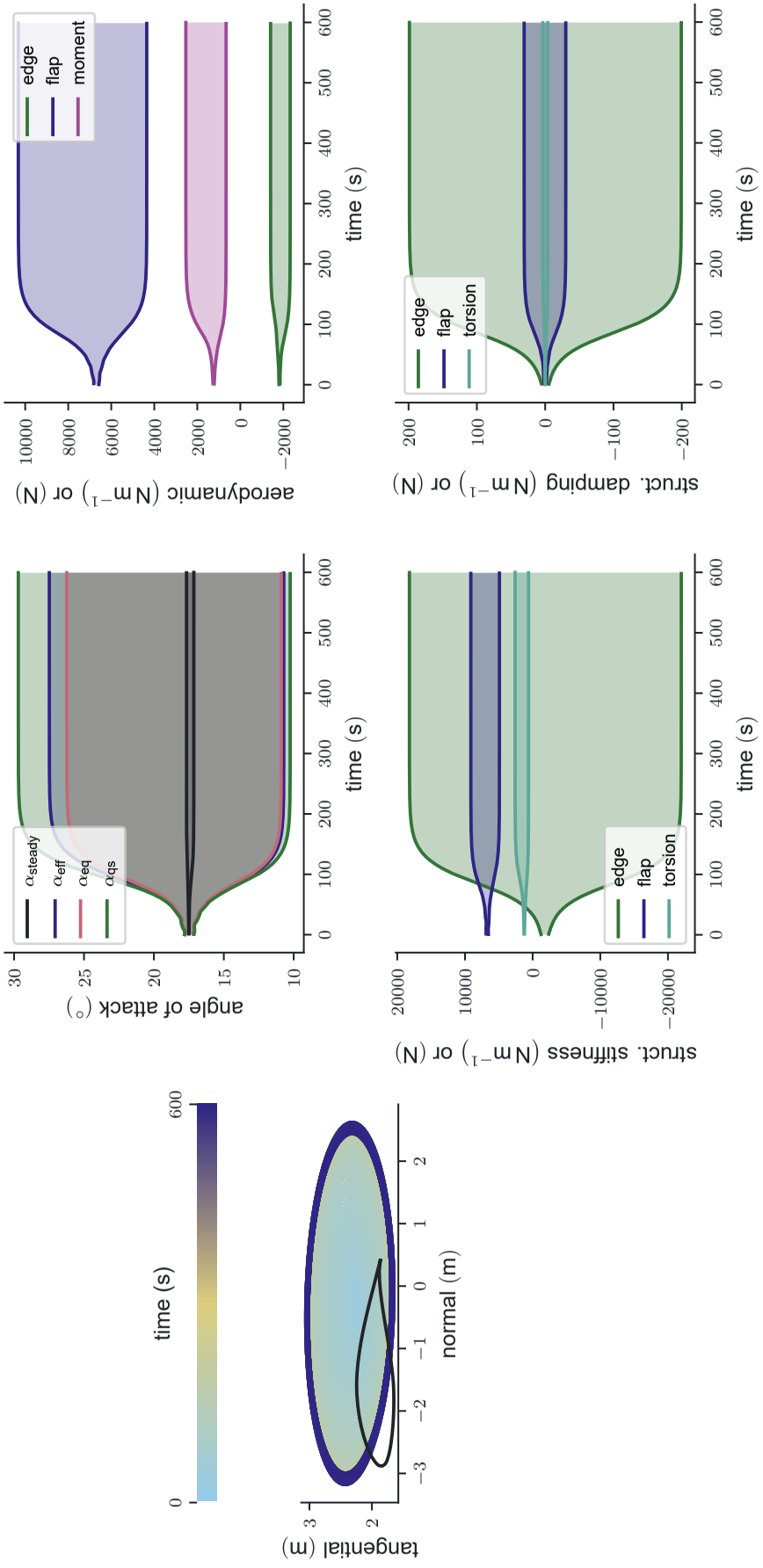

Figure 5.18: Time series of the displacement and the maximum and minimum of different angle of attacks and external and structural forces for 45 m/s inflow at a steady-state angle of 17.5°. The aerodynamic model is HGM f-scaled. All forces are per unit length. The displacement plot is affected by a limited time resolution causing the loops to appear thicker and more discontinuous than they are. It's axes refer to the rotor plane (airfoil is pitched to 90° in stand-still). Back to the paragraph here.

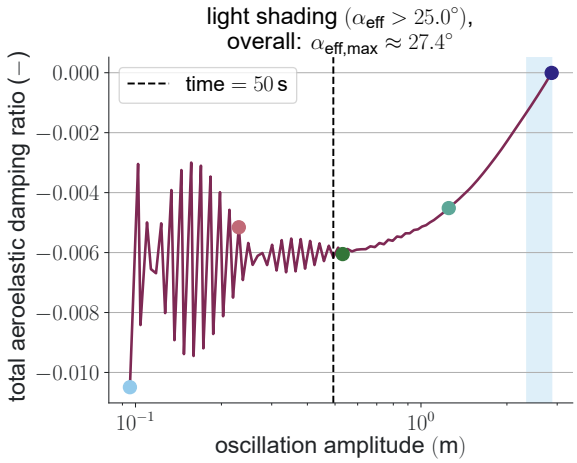

(a) The amplitude axis is log-scaled. $\alpha_{\text{eff,max}}$ denotes the effective angle of attack that occurred during the simulation. The coloured dots define amplitudes for which the unsteady unsteady drag coefficient and unsteady lift coefficient are plotted in Figures 5.19c and 5.19d, respectively. Shaded regions indicate that a threshold effective angle of attack is exceeded at least once per period.

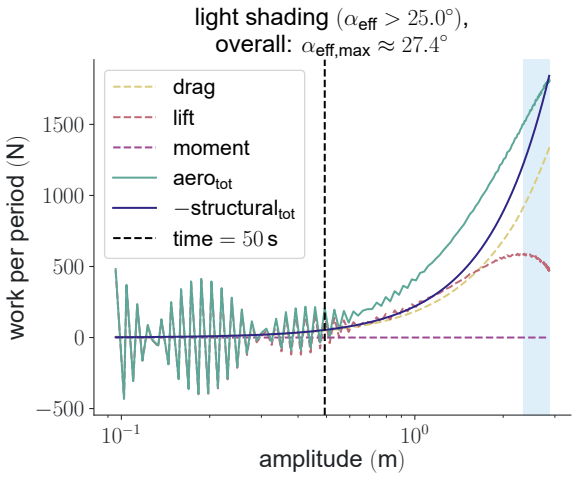

(b) Work per period of the aerodynamic drag, lift, and aerodynamic moment and of the structural damping forces and moment (structural$_{\text{tot}}$. The work is per unit length. Shaded regions indicate that a threshold effective angle of attack is exceeded at least once per period.

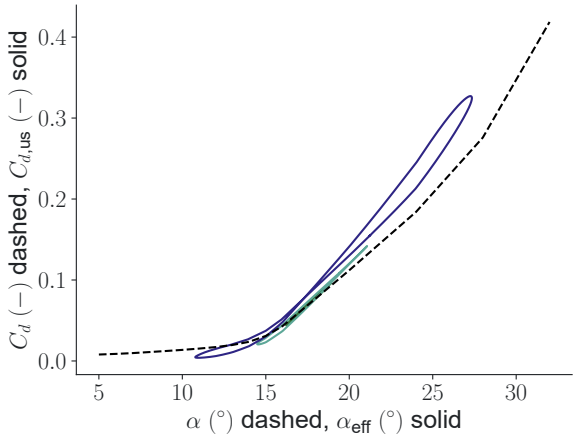

(c) Loops of the unsteady drag coefficient ($C_{d,\text{us}}$) at different oscillation amplitudes. The colours of the loops correspond to the colours of the dots in Figure 5.19a. The steady polar is shown as the black dashed line.

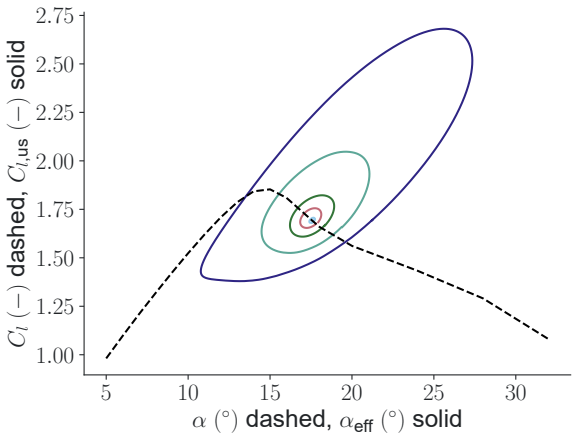

(d) Loops of the unsteady lift coefficient ($C_{l,\text{us}}$) at different oscillation amplitudes. The colours of the loops correspond to the colours of the dots in Figure 5.19a. The steady polar is shown as the black dashed line.

Figure 5.19: Different parameters from a simulation using the HGM f-scaled model with for an inflow velocity of $45\,\text{m}\,\text{s}^{-1}$ at a steady-state angle of attack of $17.5°$. The simulation was run for $300\,\text{s}$ with a time step duration of $0.0005\,\text{s}$. The first $5\,\text{s}$ of the simulation are not incorporated in this plot. The amplitude at which $50\,\text{s}$ of the simulation has passed is marked. The damping and work calculations are based on peaks of the x displacement. Back to the paragraph here.

With the overview of the whole simulation results given, a more detailed analysis of the initial transient periods is described next. The data used is of energy components and power contributions from the forces and the individual components of the dynamic stall models. This time, individual time series are visualised. The time frames for the plots are chosen to balance visual clarity (shorter time frames) against capturing the most changes (longer time frames). Again, the data visualisation requires a lot of space. Hyperlinks for the figures and back to the paragraphs are provided.

First, the transient behaviour of the 1st-order IAG model is analysed from Figures 5.20 and 5.21. In the former, it can be seen that the edgewise oscillations are damped out during the first $10\,\mathrm{s}$. Around the same time of $10\,\mathrm{s}$, the flapwise oscillation amplitude starts growing until $\approx 40\,\mathrm{s}$. As analysed from the Figure 5.13b (no return hyperlink from the figure), only the lift provides the net positive energy fed into the system. The flapwise kinetic energy shows that the airfoil moves faster up than down or vice-versa; most likely faster up than down because of the acceleration due to the lift.

Next, the individual contributions of the 1st-order IAG model are investigated with Figure 5.21. Only coefficients that directly influence the unsteady force and moment coefficient are plotted; intermediate coefficients are not. The transient period of the first $10\,\mathrm{s}$ is visible in all plots. Because the 1st-order IAG model operates with tangential and normal force coefficients, each coefficient is projected onto the drag and lift direction as done in lines 54 to 56. The total unsteady drag coefficient ($C_{d,\mathsf{us}}$), unsteady lift coefficient ($C_{l,\mathsf{us}}$), and unsteady moment coefficient ($C_{m,\mathsf{us}}$) are additionally plotted; they are the sum of the respective contributions. Trivial insights explaining the change from an initial edgewise to a flapwise oscillation are not apparent. The oscillations of the viscous tangential $C_{t,\mathsf{f}}$ and viscous normal $C_{n,\mathsf{visc}}$ force coefficient increase. So do the oscillations of the viscous moment $C_{m,\mathsf{f}}$ and circulatory moment $C_{m,\mathsf{C}}$. The latter shows strong discontinuities in its slope. At last, no leading-edge vortex is present. This is because $C_{n,\mathsf{sEq}}$ (intermediate coefficient; not plotted) that is used to reset the leading-edge vortex position never falls below the critical normal force coefficient of ≈ 2.17. This is required to indicate the creation of a new leading-edge vortex in the 1st-order IAG model. The smallest $C_{n,\mathsf{sEq}}$ during the whole simulation is ≈ 2.21.

Next, the initial transient period as predicted by the AEROHOR model is analysed with Figures 5.22 and 5.23. For both, the time frame is shifted from $[0\,\mathrm{s}, 40\,\mathrm{s}]$ as used for the 1st-order IAG model to $[10\,\mathrm{s}, 50\,\mathrm{s}]$. This is done to capture the transition from the edgewise to flapwise oscillation better. In Figure 5.22, it can be seen that the edgewise oscillation is damped slower than in the 1st-order IAG case. The AEROHOR's edgewise oscillation frequency is significantly higher than the flapwise's. There are multiple oscillation components visible in the flapwise movement. The two main components are of different amplitude in the beginning, then decrease until $\approx 25\,\mathrm{s}$ after which the smaller (amplitude-wise) component starts to increase in amplitude. At $40\,\mathrm{s}$, this component's amplitude surpasses that of the previously larger component. After that, both components increase together and the system appears to have passed the most non-linear period. It is because of this that the time $40\,\mathrm{s}$ is marked in Figures 5.19a and 5.19b (no return link). With increasing time, the work done by the lift appears to be increasingly governed by a single frequency. Interesting but not further investigated is the difference in the development of the maxima and minima peaks of the lift work.

In the dynamic stall Figure 5.23, the reasons for the behaviour are again not obvious. The drag and lift are governed by the viscous contributions again. These change only slightly in their maxima-minima range but develop from containing multiple frequencies to being governed by one. As for the 1st-order IAG model, no leading-edge vortex develops because the airfoil is in a position that shed one vortex already and the condition to develop a new one is not met. Simulations that start at an angle of attack that would shed a vortex are initialised with that vortex far downstream.

Now, the initial transient period as predicted by the HGM openFAST model is analysed with Figures 5.24 and 5.25. The time frame is changed to $[0\,\mathrm{s}, 30\,\mathrm{s}]$ as that is sufficient to capture the initial development. In Figure 5.24, the instability in the edgewise direction is visible as the growth in the average edgewise kinetic and potential energy. From $0\,\mathrm{s}$ to $20\,\mathrm{s}$, the y (approximately flapwise) potential energy oscillation and from $0\,\mathrm{s}$ to $25\,\mathrm{s}$ the lift work's oscillation contain multiple components. After that, both parameters appear to be governed by a single oscillation. It is for that reason that the time $25\,\mathrm{s}$ is marked in Figures 5.17a and 5.17b (no return link). Finally, the increase in edgewise amplitude is followed by an increase in flapwise amplitude.

The dynamic stall contributions are shown in Figure 5.25. The initial multiple components of the flapwise oscillation are apparent in the first $25\,\mathrm{s}$ of the angle of attack visualisation. In comparison to the results predicted with the AEROHOR model, the contributions to the force and moment coefficients are smoother. The edgewise instability is seen by the increase in the range of the different contributions. Even for the relatively small edgewise oscillation amplitude, the induced drag has a considerable influence on the total drag.

At last, the HGM f-scaled model is analysed for its influence on the initial $[0\,\mathrm{s}, 40\,\mathrm{s}]$ with Figures 5.26 and 5.27. The time frame is chosen longer again because the y component of the potential energy and the work done by the lift contain multiple oscillation components for longer. See Figure 5.26. The response starts to show only one oscillation component after $\approx 50\,\mathrm{s}$; hence the $50\,\mathrm{s}$ mark in Figures 5.19a and 5.19b (no return link). Otherwise, the system response is similar to that predicted by the HGM openFAST model.

The behaviour seen in Figure 5.27 can be mostly explained in the previous two paragraphs. The major difference is the reduced induced drag predicted by the HGM f-scaled model: the first time a quasi-steady angle of attack of $18.5°$ is reached, the HGM openFAST model predicts an induced drag coefficient of 0.009 while the HGM f-scaled model predicts 0.0026.

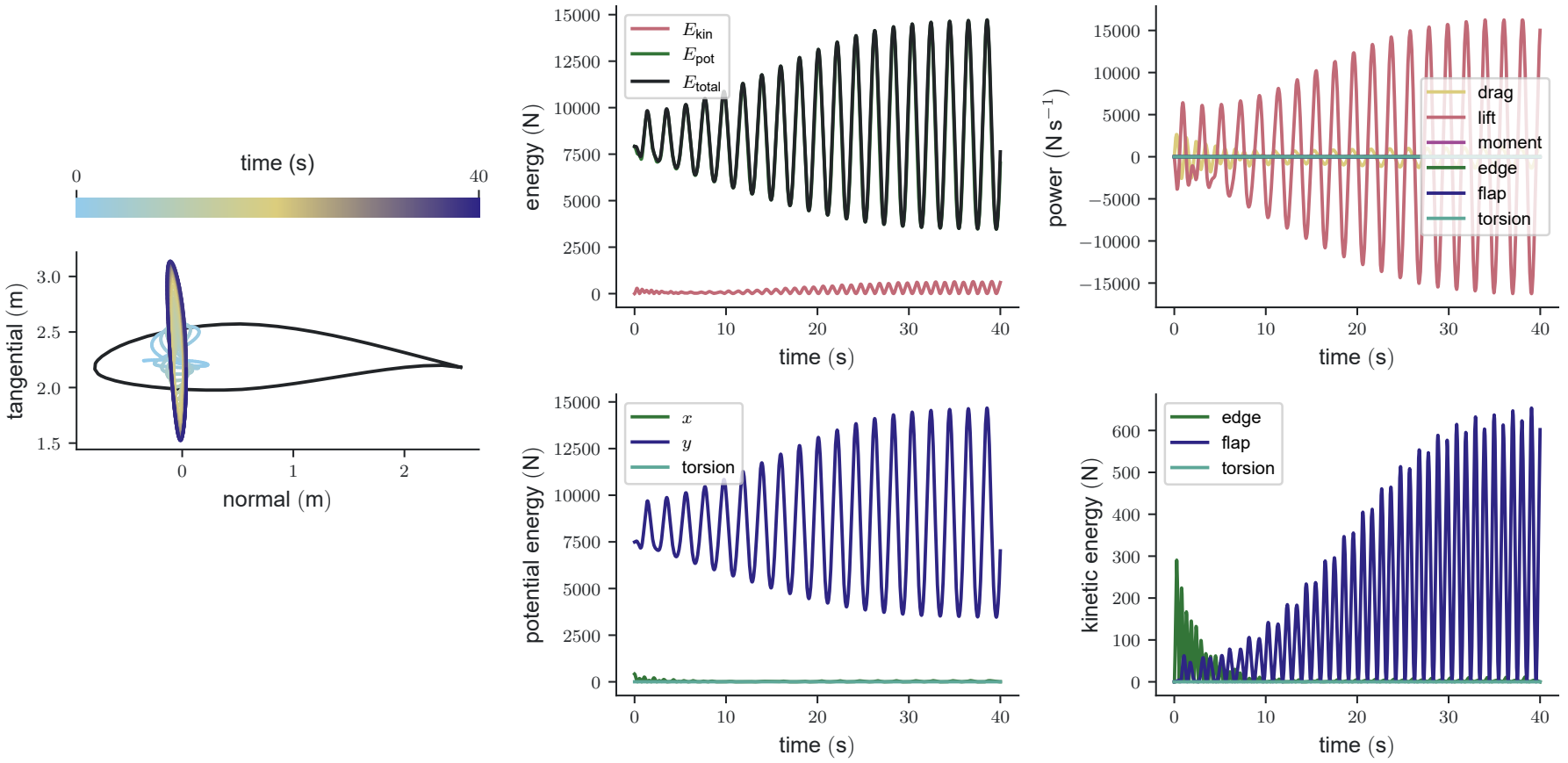

Figure 5.20: Time series of the displacement, energies, and power for $45\,\mathrm{m/s}$ inflow at a steady-state angle of $17.5°$. The aerodynamic model is the 1st-order IAG. All energies and powers are per unit length. The displacement axes refer to the rotor plane (airfoil is pitched to $90°$ in stand-still). Back to the paragraph here.

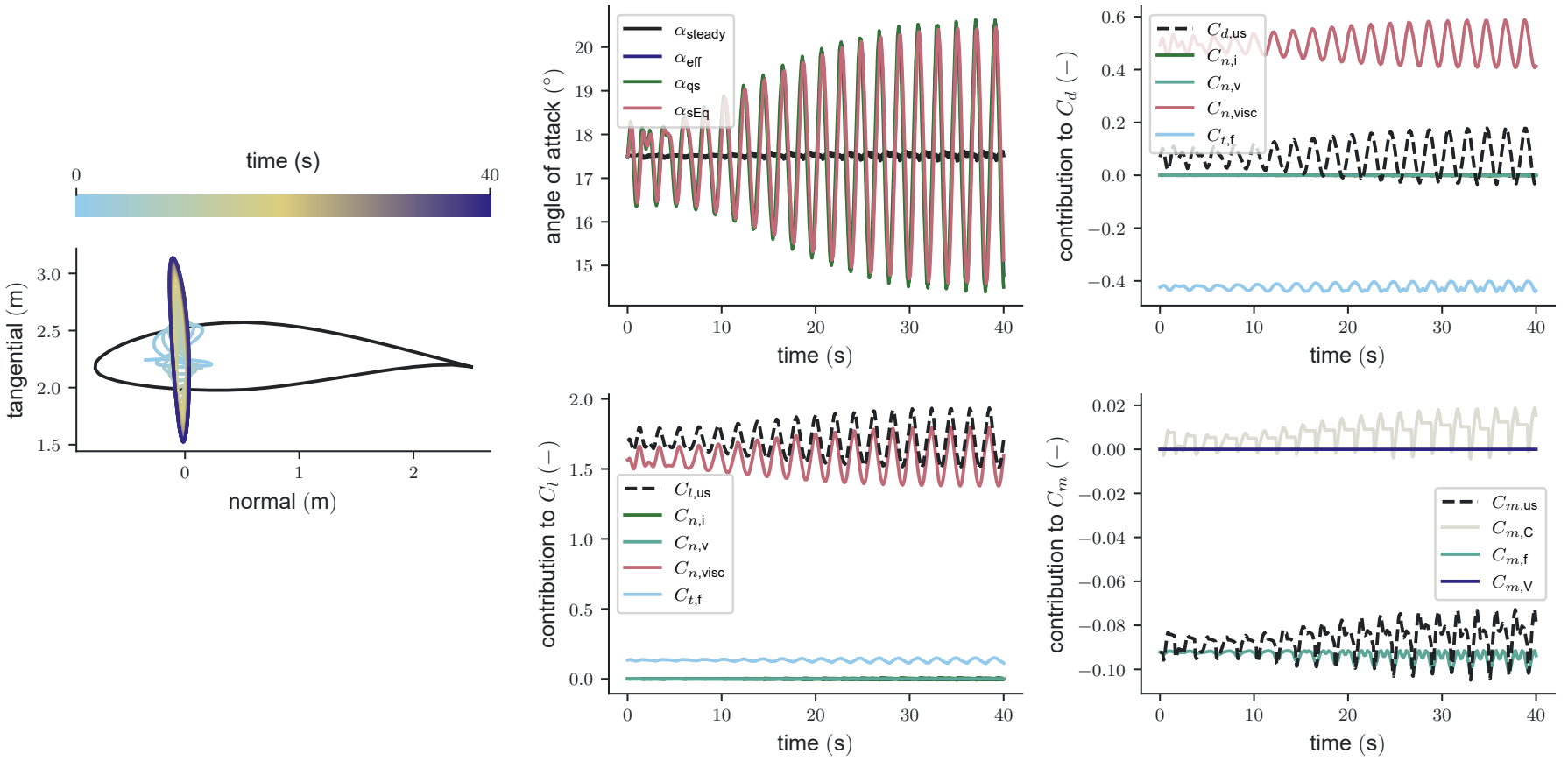

Figure 5.21: Time series of the displacement and dynamic stall parameters for $45\,\mathrm{m/s}$ inflow at a steady-state angle of $17.5°$. The aerodynamic model is the 1st-order IAG. All energies and powers are per unit length. The displacement axes refer to the rotor plane (airfoil is pitched to $90°$ in stand-still). Back to the paragraph here.

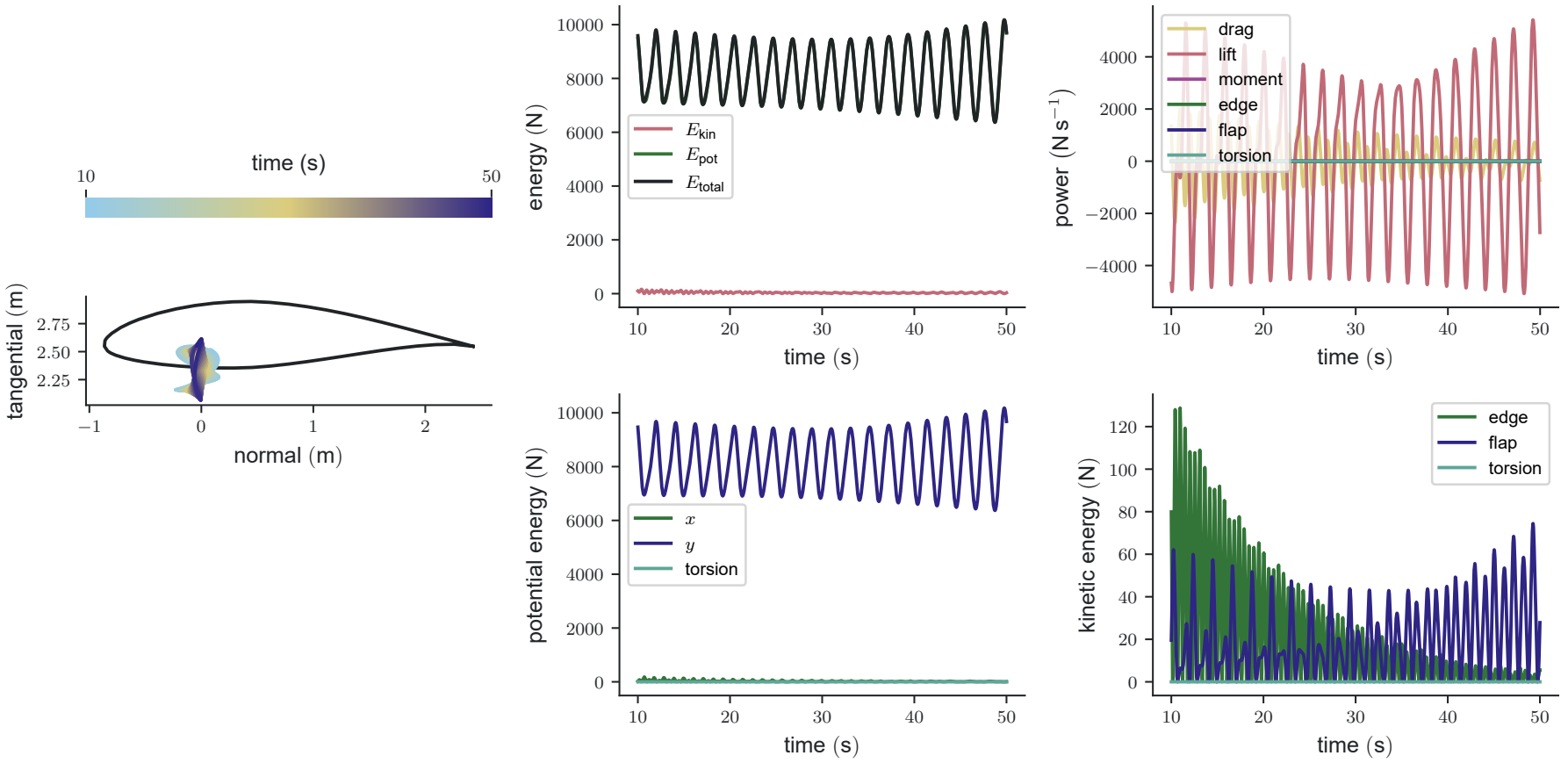

Figure 5.22: Time series of the displacement, energies, and power for $45\,\mathrm{m/s}$ inflow at a steady-state angle of $17.5°$. The aerodynamic model is AEROHOR. All energies and powers are per unit length. The displacement axes refer to the rotor plane (airfoil is pitched to $90°$ in stand-still). Back to the paragraph here.

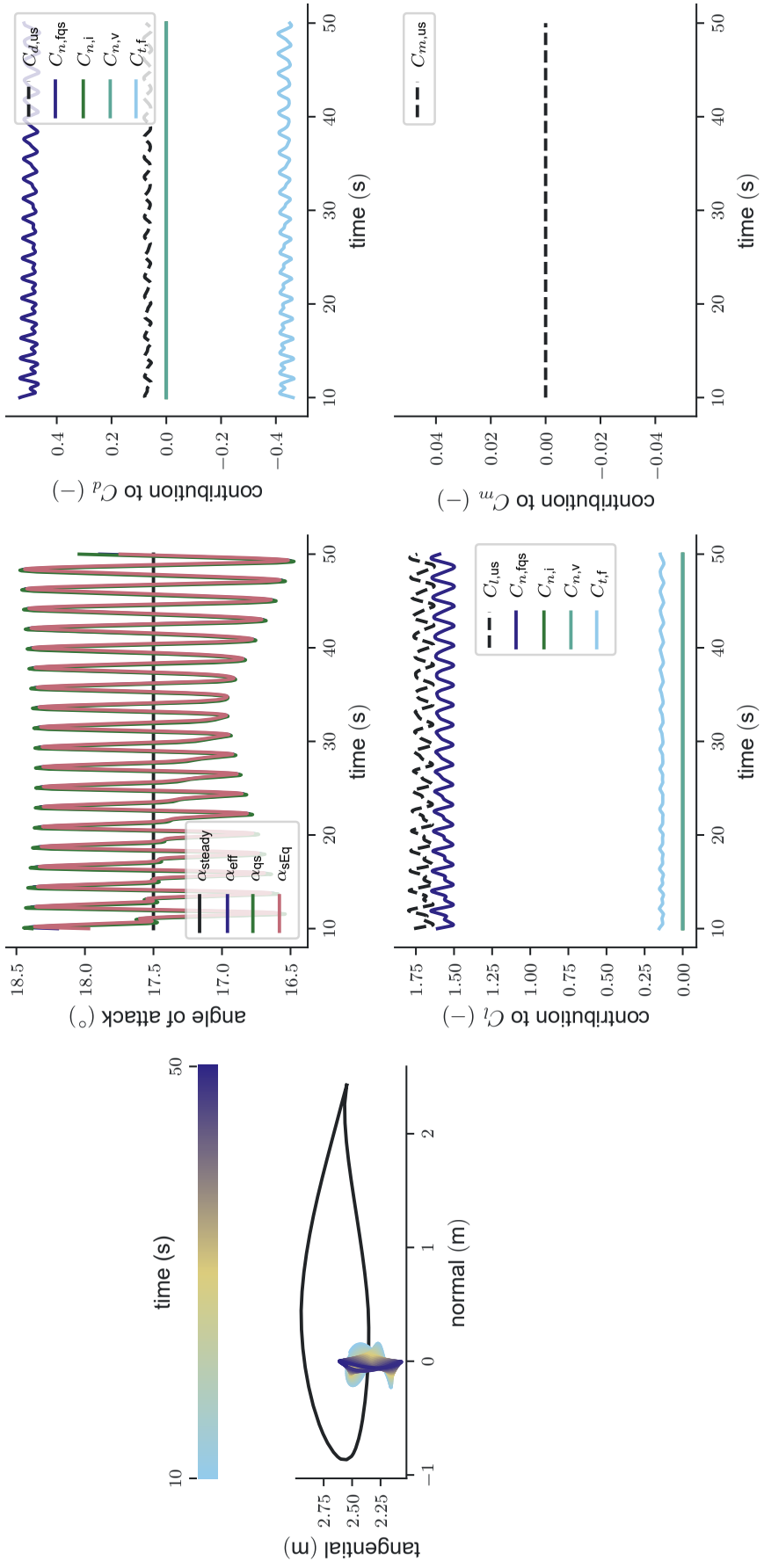

Figure 5.23: Time series of the displacement and dynamic stall parameters for 45 m/s inflow at a steady-state angle of 17.5°. The aerodynamic model is AEROHOR. All energies and powers are per unit length. The displacement axes refer to the rotor plane (airfoil is pitched to 90° in stand-still). Back to the paragraph here.

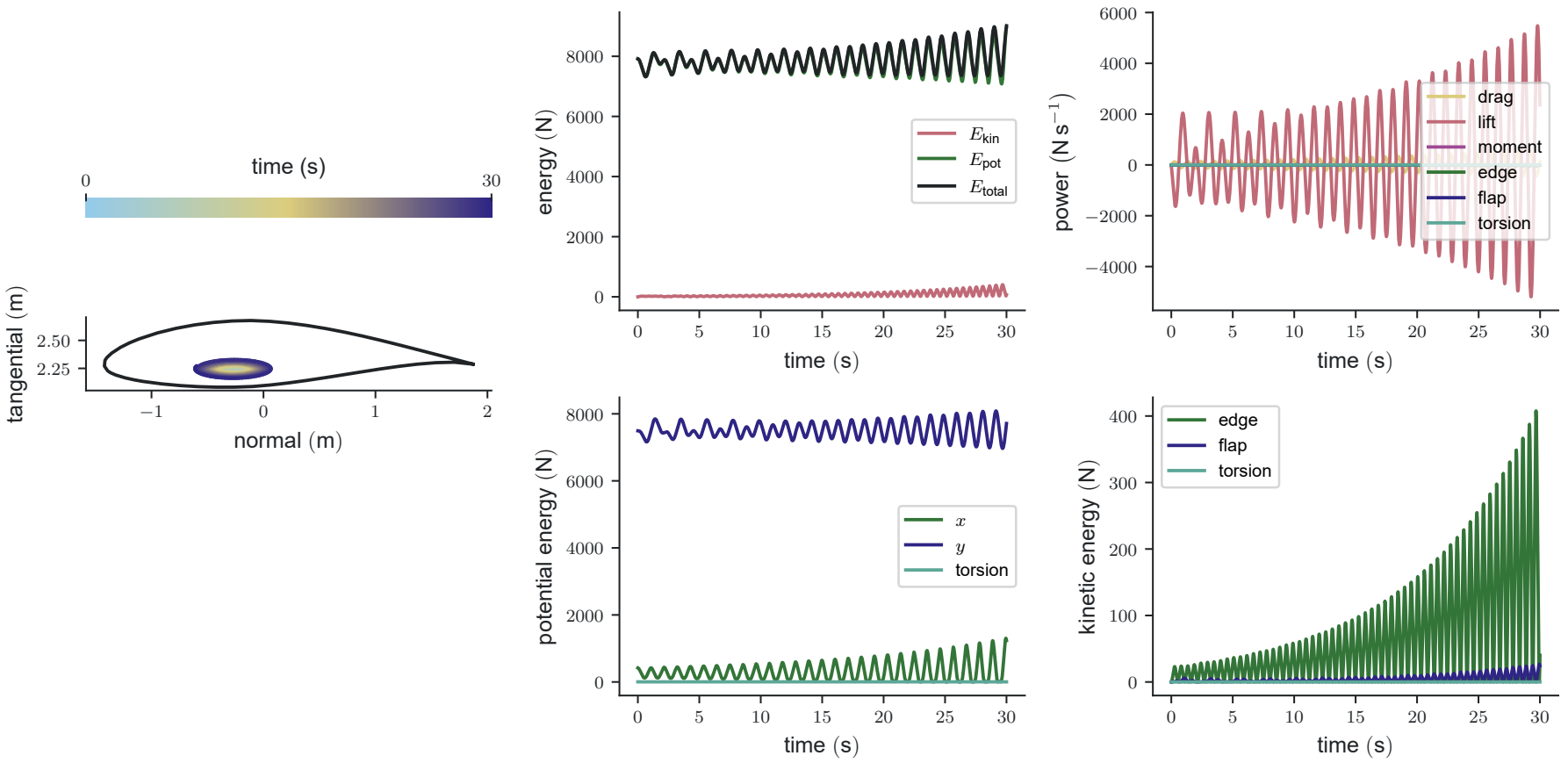

Figure 5.24: Time series of the displacement, energies, and power for $45\,\mathrm{m/s}$ inflow at a steady-state angle of $17.5°$. The aerodynamic model is HGM openFAST. All energies and powers are per unit length. The displacement axes refer to the rotor plane (airfoil is pitched to $90°$ in stand-still). Back to the paragraph here.

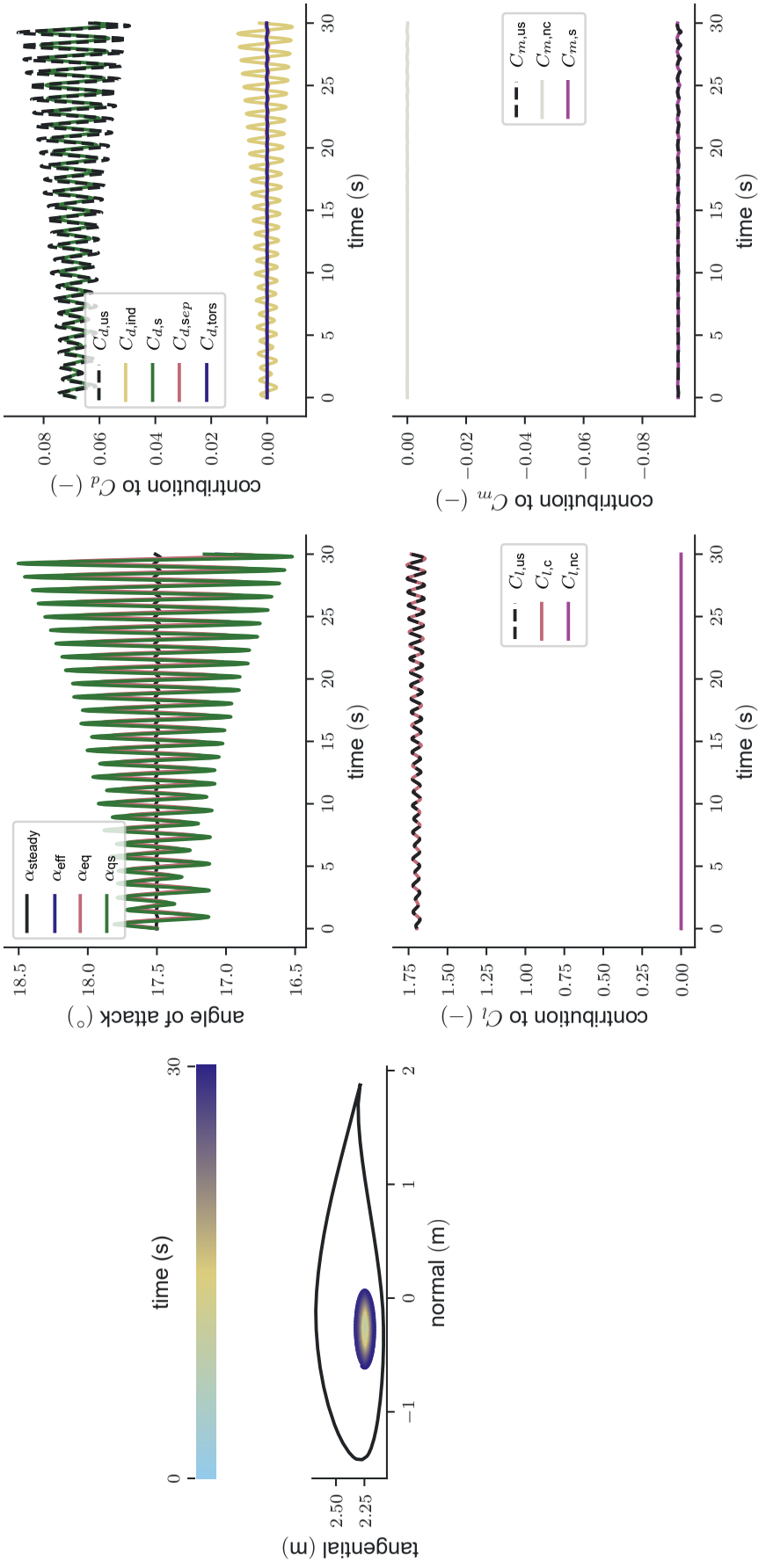

Figure 5.25: Time series of the displacement and dynamic stall parameters for 45 m/s inflow at a steady-state angle of 17.5°. The aerodynamic model is HGM openFAST. All energies and powers are per unit length. The displacement axes refer to the rotor plane (airfoil is pitched to 90° in stand-still). Back to the paragraph here.

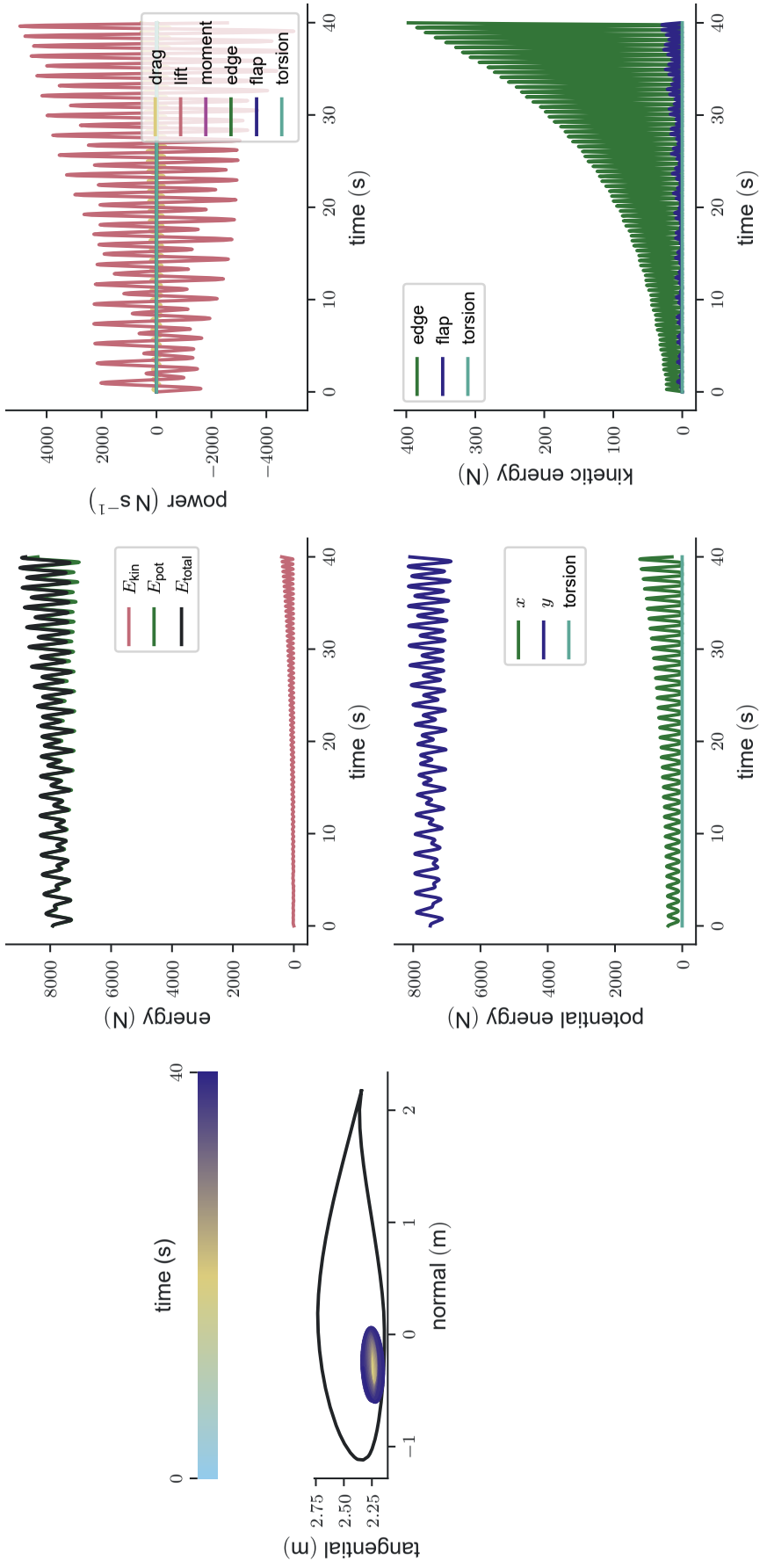

Figure 5.26: Time series of the displacement, energies, and power for 45 m/s inflow at a steady-state angle of 17.5°. The aerodynamic model is HGM f-scaled. All energies and powers are per unit length. The displacement axes refer to the rotor plane (airfoil is pitched to 90° in stand-still). Back to the paragraph here.

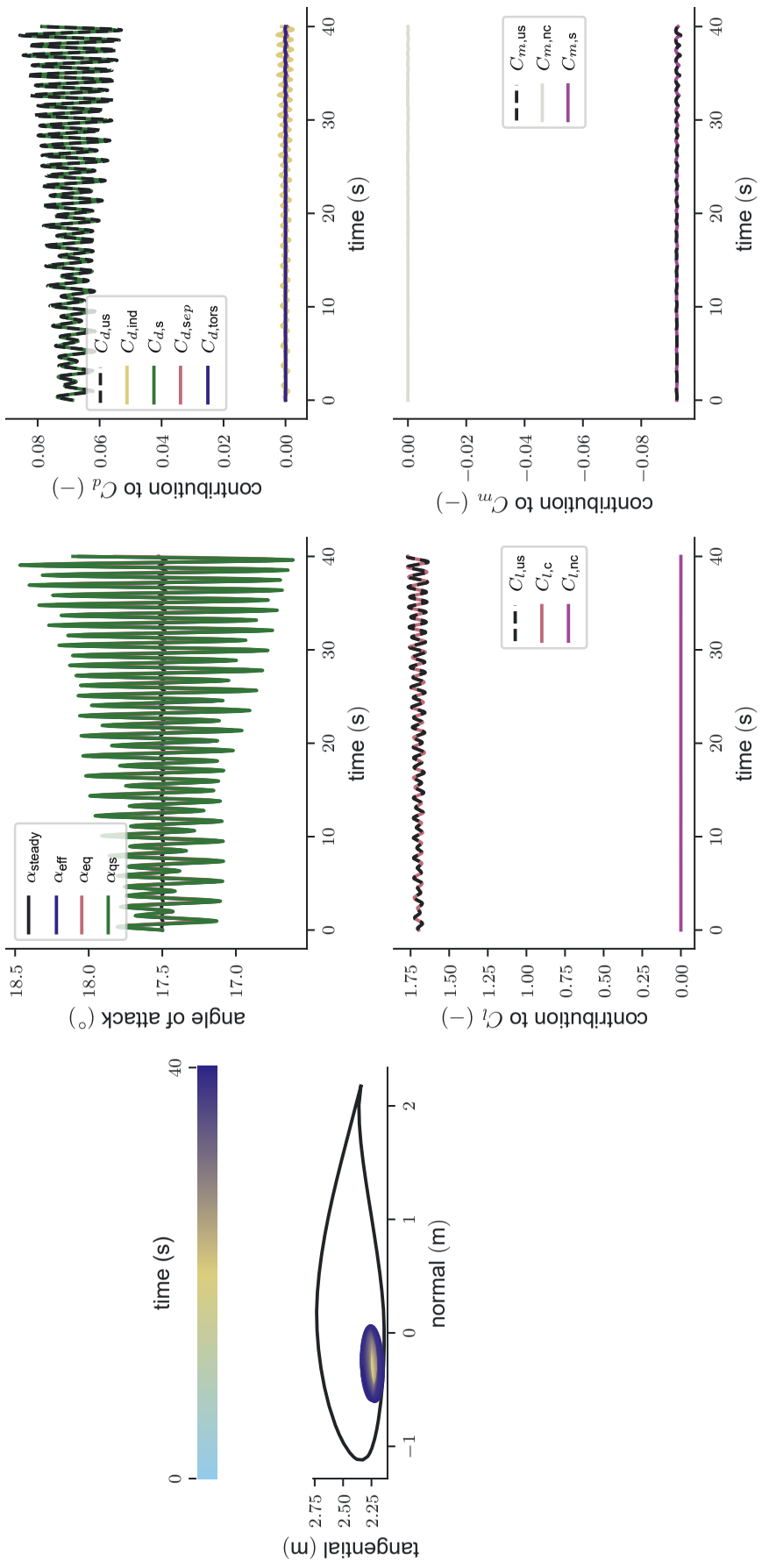

Figure 5.27: Time series of the displacement and dynamic stall parameters for 45 m/s inflow at a steady-state angle of 17.5°. The aerodynamic model is HGM f-scaled. All energies and powers are per unit length. The displacement axes refer to the rotor plane (airfoil is pitched to 90° in stand-still). Back to the paragraph here.

6

Discussion and outlook

This chapter discusses the results for the steps defined Chapter 4. Hence, the results of the time step convergence study are considered first. Then the limit cycle oscillations amplitudes and maximum quasi-steady angles of attack predicted with quasi-steady aerodynamics are compared to those predicted with the dynamic stall model HGM openFAST. Afterwards, the same analysis is done considering the 1st-order IAG model, the AEROHOR model, the HGM openFAST model, and the HGM f-scaled model. At last, the initial transient behaviour predicted with the four dynamic stall models is analysed for one specific inflow condition.

It is a good sign that the section model's simulations converge for smaller time step durations as seen in Section 5.1. The time step size thus has a smaller influence on the uncertainty of the results which are then as accurate as the different engineering modelling approaches are accurate. Additionally, the simulations are fairly accurate even for relatively large time step durations. Looking at the numerical data behind the case in Figure 5.1d and setting the time step duration of $0.0005\,\mathrm{s}$ as a baseline, the case with $0.01\,\mathrm{s}$ only deviates in amplitude by $\approx 12.4\,\%$ and lags behind by $\approx 0.27\,\mathrm{s}$ – both values are relatively small considering the simulation has run for almost $600\,\mathrm{s}$ at that time and required only $5\,\%$ of the computational steps.

Using a dynamic stall model significantly increases the aerodynamic damping in comparison to using quasi-steady aerodynamics, see Section 5.2 and especially Figures 5.2a and 5.2b. Quasi-steady aerodynamics predict limit cycle oscillation behaviour with α_{qs} values up to $200°$. There, quasi-steady aerodynamics do not deliver reasonable results:

1. The complete separation that starts at angles around $40°$ is not modelled other than by the values of the steady polar. However, both measurement and CFD polar data for angles above are error-prone (W. R. Skrzypiński et al., 2014).
2. The core concept of lagging the aerodynamic forces that is present in any unsteady aerodynamic models is missing.
3. No other dynamic effects as induced drag or leading-edge vortices are modelled.

Incorporating these effects by means of using a dynamic stall model shows that limit cycle oscillations can still occur, but at smaller amplitudes. Using the HGM openFAST model as a representation of dynamic stall model, the inflow conditions that cause limit cycle oscillation instabilities largely overlap with those conditions causing instabilities when using quasi-steady aerodynamics. This is unlikely a coincidence.

The range of inflow conditions causing instabilities starts at steady-state angles of attack after which the steady lift slope becomes negative; both at positive and negative steady-state angles of attack. This was also found by Wang et al., 2016. As for flapwise oscillations, this makes sense as a requirement for edgewise oscillations. During such, the energy flowing into the system is governed by the aerodynamic forces acting in edgewise direction: $\approx L\sin(\phi)\dot{x}_e \approx -L\phi\dot{x}_e$ and $\approx -D\cos(\phi)\dot{x}_e \approx D\dot{x}_e$ with lift (L), drag (D), the inflow angle (ϕ), the velocity in edgewise direction $\dot{x}_e$, and assuming no torsion of the

airfoil. For positive $\dot{x}_e$, the inflow angle decreases and thus the contribution $L\phi\dot{x}_e$. For negative $\dot{x}_e$, the opposite happens. This alone dampens edgewise oscillations. However, if the lift slope for the given inflow angles is negative, the lift increases for positive $\dot{x}_e$ and decreases for negative $\dot{x}_e$, potentially outweighing the direct effect of the factor ϕ. However, the maximum quasi-steady angle of attack values of $200°$ as predicted with the quasi-steady model suggest that a continuously negative lift slope is not necessary during one period. A deeper analysis into force directions, magnitudes, and powers of the aerodynamic forces for limit cycle oscillations with quasi-steady aerodynamics can reveal the process.

The few simulations at the border of the limit cycle oscillation regions that are not converged after 600 make sense. There, the aerodynamic damping is only slightly negative. The simulations thus need more time for the instability to develop. Judging by the surrounding converged simulations, it seems implausible that the simulations that are not yet converged would develop into something other than limit cycle oscillations.

Lastly, that the regions of increased edgewise oscillation amplitude overlap with those of increased flapwise oscillation is plausible. With increased edgewise oscillation amplitudes increases and decreases the maximum and minimum inflow magnitude as seen by the airfoil. Since a large part of the aerodynamic force acts in the flapwise direction, it experiences increased amplitudes, too.

The comparison of the limit cycle oscillations predicted by the four different dynamic stall models in Section 5.3 (see especially Figure 5.6) showed significant discrepancies. All four models predicted different results. The 1st-order IAG model and the AEROHOR model on one hand and the HGM openFAST model and the HGM f-scaled model on the other hand predicted similar results. Stating which of the two types of results is more correct is outside of the author's experience and available data. As for the dynamic stall models, the similarity between the respective cases shows that the backbones of the modelling approaches are robust; changes in some parts of the models do not cause the models to predict completely different behaviours. Still, the 1st-order IAG model and the AEROHOR model do not predict any edgewise limit cycle oscillations while showing small flapwise limit cycle oscillation for very specific inflow conditions. In contrast, the HGM openFAST model and the HGM f-scaled model show mainly edgewise limit cycle oscillations for which flapwise oscillations are incidental. Hence, for the sake of modelling limit cycle oscillations, the the HGM openFAST model and the HGM f-scaled model can be used. For the former, however, some oscillations cause effective angles of attack in the deep stall region. These results should be viewed with care since deep stall aerodynamics are not modelled other than based on the polar.

In relation to the statement of the methodologies if this thesis' results call for simulations with of higher fidelity, the answer is yes. Not to perform a grid study as presented here, but to create more ways to validate dynamic stall models. Current dynamic stall validation data for attached or partially separated is not sufficient compared to the large effective angles of attack that are shown to occur during limit cycle oscillations. Likewise, airfoil measurement data for these ranges would be valid, too.

The convergence plots for the amplitudes exemplify again that the 1st-order IAG modeland the AEROHOR modelcause large positive damping. Except for the few flapwise oscillations, not a single inflow condition caused even slight negative damping. In contrast, using the HGM-based models, there are multiple simulations that were not converged due to small negative damping that could not fully develop.

At last, the flapwise limit cycle oscillation predicted with the 1st-order IAG modeland the AEROHOR modelhave relatively small amplitudes of $< 2\,\mathrm{m}$. Their influence on structural integrity and fatigue damage is thus significantly smaller than the $7\,\mathrm{m}$ and $5.4\,\mathrm{m}$ amplitudes predicted by the HGM openFAST model and the HGM f-scaled model, respectively. Hence, using the HGM openFAST model to represent a dynamic stall model is a conservative approach to instability analysis.

Finally, the detailed results from Section 5.4 are discussed. First, general observations concerning all dynamic stall models are stated. The open loops of the unsteady drag coefficient and unsteady lift coefficient as seen for the 1st-order IAG model and the AEROHOR model in Figures 5.13c, 5.13d, 5.15c and 5.15d are caused by the negative aeroelastic damping at those amplitudes. After a period, the system does not return to the same state it began the period with. Thus, the unsteady drag or lift coefficient can be different at the end and the beginning of each loop. The unconnected loops also

happen for the HGM openFAST model and the HGM f-scaled model but are less visible because of the larger axes scaling.

In the work plots of Figures 5.13b and 5.15b from the 1st-order IAG model and the AEROHOR model, the structural damping component initially decreases with increasing amplitude of the oscillations. This is because the structural damping work considers all directions: edgewise, flapwise, and torsional. The amplitude, however, is only based (in these cases) on the y (approximately flapwise) displacement. Because the simulation is initialised with a displacement in the edgewise direction and the aerodynamic forces to not add energy in that direction, the structural damping dissipates the edgewise oscillation. This dissipation happens faster than the increase in the amplitude of the flapwise oscillation. Once that has increased, the overall structural damping work increases, too, as it dissipates energy from that oscillation.

Continuing with the AEROHOR model and adding the HGM-based models, each damping ratio plot shows either discontinuities or initially unexpected results. This is because the calculation of the damping ratio and oscillation amplitude considers only one dimension of the system. In the AEROHOR case the y axis and in the HGM-based cases the x axis. If a system has oscillations in different directions, this approach is only useful for describing the damping behaviour if one direction dominates the others in terms of amplitude and net work received. In the AEROHOR case, see Figure 5.15a, the damping ratio in the time period $[0\,\mathrm{s}, 40\,\mathrm{s}]$ shows a behaviour that is difficult to translate into the dynamics in the y direction. This is because during that period, the airfoil experiences damped oscillations in the x direction. These occur only because the initial displacement is chosen to facilitate edgewise oscillations. After $40\,\mathrm{s}$, the motion is dominated by flapwise movement and the damping ratio curve is sensible. Another restriction of the damping ratio and amplitude calculations is that they are based on the values of successive local peaks in the respective displacement direction. This works for oscillations that have a single component that is increasing or decreasing monotonously. However, in the cases of the HGM openFAST model and the HGM f-scaled model, see Figures 5.17 and 5.19, the x displacement time series oscillation contains multiple components. This is visible by zooming in on the edgewise kinetic energies in Figures 5.24 and 5.26. An additional visualisation is provided in Figures A.5a and A.5b. There, it is clearly visible that the amplitudes do not grow monotonously. This behaviour is also caused by the initial conditions. Even though both models predict edgewise oscillations and the initial displacement is set accordingly, the initial velocity is not. The initial translational velocity is initialised as $0\,\mathrm{m/s}$, but the velocity at the maximum edgewise displacements is nonzero in the flapwise direction. Thus, the flapwise oscillation that follows the edgewise oscillation needs to develop first. This can be seen in the time series of the y potential energy component in Figures 5.24 and 5.26. Additionally, this transient behaviour of the flapwise velocity causes a transient behaviour of the lift power (by first affecting the angle of attack, which affects the lift, and by dictating the flapwise velocity). This effect is stronger with the the HGM f-scaled model and is reflected in the discontinuities of the work plot in Figure 5.19b. As a last note, the data of the very beginning ($< 5\,\mathrm{s}$) of each simulation was omitted from the plots of the damping ratio, work, and unsteady loop coefficients to exclude the most severe effects that are only caused by the displacement and velocity initialisation.

Now, some details for each model are discussed. The 1st-order IAG model converges the fastest, showing the largest (magnitude-wise) negative damping of all models. While the other dynamic stall models predicted damping rations between -0.06 and -0.08, the 1st-order IAG model started with -0.3. This is interesting because in the edgewise and flapwise amplitude plots, the 1st-order IAG model shows the smallest regions of instability. The low damping ratio is not because of larger aerodynamic forces (those are very similar to those of AEROHOR in the beginning), but the direction of the forces must align better with the movement direction. Indeed, the initial edgewise oscillation quickly transforms into a dominant flapwise oscillation. There, the negative lift slope causes negative damping. The flapwise amplitude increases and with it the range of the effective angle of attack. Since the maximum flapwise velocity also increases, the unsteady drag coefficient and unsteady lift coefficient widen. Even though the unsteady drag coefficient and unsteady drag coefficient loops look similar for the two biggest amplitudes (the underlying polar values have roughly the same slope), the work done by the drag drops continuously and that of the lift abruptly. The main difference between the loops at the different amplitudes is the size – the underlying polar values are very similar. At the low range of the effective angle of attack values, almost fully-attached (under steady flow) conditions are achieved. However, whether this is the sole cause for the drastic decrease in added energy from the aerodynamic forces is

questionable.

Lastly, for the 1st-order IAG model, high-frequency components of the unsteady loops are explained by looking at the detailed force time series. The circulatory moment contribution ($C_{m,\mathrm{C}}$) shows a slope with discontinuities; thus the aerodynamic moment's change in time has discontinuities, too. This directly affects the structural damping and stiffness torque and indirectly all aerodynamic forces by influencing the effective angle of attack via the torsion angle. This unsteadiness also explains why the unsteady coefficient loops even in the case of zero aeroelastic damping do not perfectly close.

Looking at the AEROHOR model, the edgewise oscillations are damped slower than with the 1st-order IAG model. Additionally, the flapwise oscillations grow later. Since the AEROHOR's damping ratio is smaller in magnitude, this is expected. The unsteady lift coefficient loops at the two smallest amplitudes are similar in size and effective angle of attack range, yet they, too, cause drastically different aeroelastic damping: ≈ 0 and ≈ -0.008. In contrast to the largest loop predicted with the 1st-order IAG model, the largest loop now does not enter the fully attached region of the polar. Hence, this cannot be the governing factor decreasing the aerodynamic work added to the flow. Rather, it seems that the most fundamental approach to analysing the force and velocity vectors has to be used.

The results predicted by the HGM openFAST model are governed by a probable overestimation of the unsteady attached polar lift coefficient causing the overall unsteady lift coefficient to reach values of 4 at effective angle of attack of $40°$. Yet, the specific inflow conditions for the simulation of the detailed analysis did not even cause the largest effective angle of attack. During the grid simulations, effective angles of attack of $75°$ were obtained. This is far outside the validity range of the HGM openFAST model. Back to the detail simulation, the drag is the almost sole source of adding energy into the system. Judging from its maximum value of 1.75 and the modelling used in the HGM openFAST model, the induced drag most likely causes both the large positive drag work and the large unsteady drag coefficient values. As Pirrung et al., 2018 states, this is nonphysical.

Finishing the analysis, the the HGM f-scaled model successfully lowered the excessive effective angle of attack and induced drag values. The maximum unsteady lift coefficient approaches 2.75 and the maximum unsteady drag coefficient 0.35. The total aerodynamic work is given equally by the lift and lift at amplitudes up to $1.5\,\mathrm{m}$. For higher amplitudes, the drag work is dominant again. The effective angles of attack reached with the HGM f-scaled model are in a range for which the model is still considered valid.

The results and the discussion have to be assessed considering the limitations of the section modeland of the methodology. In relation to a whole wind turbine, the section modeldoes not include any 3D aerodynamic effects, does not calculate aerodynamic induction on the flow velocities, and models the structural damping and stiffness linearly. Choosing no structural or inertial coupling further increases the shortcomings of representing a full blade as a section. The interactions of the dynamics of the blade with the drivetrain, nacelle, tower, or floating structures are also not accounted for. For near-field aerodynamics, the shortcomings include inaccurate polars for large angles of attack (W. R. Skrzypiński et al., 2014), the difficulties of modelling dynamic stall, no modelled effects of surface roughness, and a constant inflow velocity. As for the methodology, the inflow velocity and steady-state angle of attack ranges cover only so much; while much larger inflow velocities are not expected in reality, larger yaw-misalignment angles (these correspond to the steady-state angles of attack) are expected. Likewise, the structural parameters chosen for the section modelare only one specific set of inertial, stiffness and damping values.

However, for the analysis of aeroelasticity dynamics on a sectional level, the section modelis highly capable, validated, automated, and multi-processing-enabled, and is equipped with a multitude of post-processing calculations and data visualisation schemes. As such, it is not only valuable for the research done in this thesis but is well-prepared for engineering model additions and further investigations. Based on the current capabilities of the section model, the following topics could be treated next:

1. How do limit cycle oscillations predicted with quasi-steady aerodynamics work?
2. (a) Which effects does the polar have on the limit cycle oscillations?

(b) i. Why do all limit cycle oscillations have very similar maximum quasi-steady angle of attack values despite different inflow conditions?

ii. Why do all limit cycle oscillations not have very similar minimum quasi-steady angle of attack values despite having very similar maximum values?

iii. How deep into the negative lift slope region does the inflow have to be to cause instabilities?

iv. How much does the polar drag coefficient polar influence the instability?

(c) How much does the structural damping affect the necessary inflow speed to start unstable behaviour?

(d) Which assumptions of quasi-steady aerodynamics are the main drivers of the large LCOs amplitudes?

(e) How quickly do limit cycle oscillations develop that pose significant structural damage?

(f) i. Based on an initial displacement in the edgewise or flapwise direction.

ii. Based on the yaw-misalignment angle.

iii. Under turbulent inflow conditions.

3. Analysing second by second, when and how do predictions with dynamic stall models start to deviate from predictions with quasi-steady aerodynamics?
4. (a) For different dynamic stall models, which modelling aspects cause the deviation (lagging of forces, separation modelling, leading-edge vortex modelling, ...)?

   (b) Which polar characteristics amplify the dynamic stall models' damping?
5. Based on the above analysis or by itself, where and why exactly deviate different dynamic stall models so extensively in their aerodynamic damping?
6. Why do limit cycle oscillation occur for dynamic stall models similar to the 1st-order IAG model and the AEROHOR model because the energy flow into the structure predicted by these models decreases with larger amplitude, but not for the HGM-based models for which limit cycle oscillations happen once the structural damping catches up?
7. Why does the maximum effective angle of attack during limit cycle oscillations for the HGM openFAST model decrease with larger inflow velocity? Why does it not for the HGM f-scaled model?
8. How sensitive are the limit cycle oscillation amplitudes to structural damping?
9. How sensitive are the limit cycle oscillation amplitudes to the constants of each DS model?
10. How sensitive are the limit cycle oscillation amplitudes to different amounts of turbulence intensity?
11. How sensitive are the limit cycle oscillation amplitudes to the frequency of their displacement?
12. How sensitive are the limit cycle oscillation amplitudes and instability regions to different inertial, damping, and stiffness coupling?
13. How easily can the development of limit cycle oscillations be detected and mitigated by active pitching of the blade?

Furthermore, the section model could be extended to:

1. Provide and analyse additional state-of-the-art dynamic stall models.
2. Tune each dynamic stall model for the used airfoil.
3. Implement deep-stall models.
4. Implement the time-continuous versions of the dynamic stall models.

7

Conclusion

An aeroelastic model designed to analyse dynamics on the level of a, in this context, wind turbine blade section, has been developed, explained, and validated. The structural parameters of the blade section are those of $75\,\%$ span of the DTU $10\,\mathrm{MW}$ reference wind turbine defined in Bak et al., 2013. No inertial or structural coupling is modelled for the core objectives but for validation purposes. The airfoil used is the FFA-W3-221. The implemented dynamic stall models are the 1st-order corrected IAG model from Bangga et al., 2020, the dynamic stall model currently implemented (but unpublished) for the AEROHOR model described in Meng et al., 2024, the reimplementation of the "HGM" (Morten Hartvig Hansen et al., 2004) model in openFAST described in Branlard et al., 2022, and a model based on the "HGM" model but corrected for large quasi-steady angle of attack changes as described in Pirrung et al., 2018.

The model was first used to run a grid of inflow velocities and steady-state angles of attack using quasi-steady aerodynamics and a dynamic stall model (openFAST's reimplementation of HGM) to assess instability conditions. 399 simulations were run for each case with wind velocitys from $5\,\mathrm{m/s}$ to $50\,\mathrm{m/s}$ in steps of $2.5\,\mathrm{m/s}$ and steady-state angles of attack from $-25°$ to $25°$ in steps of $2.5°$. In relation to a full wind turbine rotor, the steady-state angle of attack equals a good approximation of the yaw-misalignment of a vertical blade. The difference between the two is the torsion angle created by aerodynamic moment which is smaller than $0.26°$ in all simulations. Time convergence of the simulations was ensured. The airfoil is initially placed in the steady-state position plus an offset in the edgewise direction and is at rest. Using quasi-steady aerodynamics, the first edgewise stall-induced limit cycle oscillation instability occurs for wind velocities at $10\,\mathrm{m/s}$ for a steady-state angles of attack of $20°$. For all wind velocitys above $15\,\mathrm{m/s}$, edgewise stall-induced limit cycle oscillations occur for steady-state angles of attack of $15°$ and larger. A similar instability region exists for negative steady-state angles of attack. The edgewise oscillations are accompanied by flapwise oscillations an order of magnitude smaller. The edgewise limit cycle oscillations amplitudes reach $22.5\,\mathrm{m}$ with quasi-steady angle of attack values of $200°$. Quasi-steady aerodynamics are thus inappropriate to model stall-induced limit cycle oscillation. The results using the dynamic stall model showed similar inflow conditions causing instability but with maximum edgewise limit cycle oscillations amplitudes of $7.2\,\mathrm{m}$ and maximum effective angle of attack values of $75°$. The flapwise amplitudes reached $2\,\mathrm{m}$. This dynamic stall model thus provided increased aerodynamic damping, especially for edgewise oscillations compared to using quasi-steady aerodynamics. However, the effective angle of attack values obtained exceed the validity of the dynamic stall model.

After comparing one of the dynamic stall models to quasi-steady aerodynamics, all dynamic stall models were compared to one another by running the grid study defined above for each of them. Both HGM-based models showed similar instability regions. However, the model by Pirrung et al., 2018 increased damping further, lowering the maximum edgewise limit cycle oscillation amplitudes to $5.4\,\mathrm{m}$ and lowering the maximum obtained effective angle of attack to $60°$. This effective angle of attack value is still outside the validity range of the model but also only occurred for the most severe limit cycle oscillation. Stall-induced limit cycle oscillation cases modelled well inside valid conditions exist for the

model. The model from Bangga et al., 2020 and AEROHOR showed similar results to one another but completely different results compared to the HGM-based models. Bangga's and AEROHOR's do not predict any edgewise stall-induced limit cycle oscillations. Their aerodynamic damping for cases of edgewise oscillations is thus even larger. For few inflow conditions (four for Bangga's model, seven for AEROHOR's model) at inflow velocities above $40\,\mathrm{m/s}$, flapwise limit cycle oscillation are predicted. These do not exceed an amplitude of $1.5\,\mathrm{m}$ and are thus smaller than the incidental flapwise oscillations that occur during the edgwise oscillations predicted by the HGM-based models.

As shown, simulating stall-induced edgewise or flapwise limit cycle oscillations for the sake of simulating them is possible. However, with the four models predicting generally two completely opposing behaviours, the validity of the results for real-world conclusions is questionable. For any inflow velocity in fully attached flow conditions, all dynamic stall models agree to predict no instability. The same holds for lightly and strongly separated flow conditions during inflow velocities below $10\,\mathrm{m/s}$. However, even for slightly separated flow at $15°$ steady-state angle of attack, the two general result types increasingly disagree with increasing inflow velocity. Accurately simulating stall-induced instabilities thus appears to primarily need advances in dynamic stall modelling.

At last, an effort was made to analyse the differences and similarities between the dynamic stall models during the initial $0\,\mathrm{s}$ to $40\,\mathrm{s}$ for one specific inflow condition. At an inflow velocity of $45\,\mathrm{m/s}$ at $17.5°$, both HGM-based models predict dominantly edgewise stall-induced limit cycle oscillations while the other two models predict flapwise stall-induced limit cycle oscillations. Even though each simulation starts with edgewise oscillations due to the initial conditions, these oscillations were quickly (in a matter of $10\,\mathrm{s}$) damped by Bangga's model and slowly (in a matter of $40\,\mathrm{s}$) damped by the AEROHOR model. While damping the edgewise oscillation, both entered flapwise oscillations. In the HGM-based cases, the initial edgewise oscillation was intensified from the beginning. Drawing detailed conclusions based on every dynamic stall parameter present in the models to provide a definite answer for their different behaviours turned out to be outside the time scope of the thesis. Nonetheless, the developed model is well-equipped for such an analysis.

With the present research done for stall-induced instabilities that all manifested as limit cycle oscillations, it was hoped to gain insights into phenomena causing fatigue damage that could be used to reduce the amount of materials needed for wind turbine blades (Wang et al., 2016; Serafeim et al., 2022). Methods based on quasi-steady aerodynamics most likely overestimate the fatigue damage caused by stall-induced instabilities. If fatigue damage is the structural driver (Nijssen et al., 2023), more material is consumed for a blade than necessary. However, the present results also indicate that there are further steps required to model stall-induced instabilities accurately enough with dynamic stall models to predict trustworthy loads that can be used during the structural design of a blade.

References

Bak, Christian et al. (2013). *Description of the DTU 10 MW Reference Wind Turbine*.

Bangga, Galih, Thorsten Lutz, and Matthias Arnold (May 2020). "An improved second order dynamic stall model for wind turbine airfoils". In: *Wind Energy Science*. doi: 10.5194/wes-2020-75. url: https://doi.org/10.5194/wes-2020-75.

Behrend, Bettina (2022). *Don't plunder the rainforest for wind energy!* url: https://www.rainforest-rescue.org/petitions/1255/dont-plunder-the-rainforest-for-wind-energy.

Bergami, Leonardo and Mac Gaunaa (2012). *ATEFlap Aerodynamic Model, a dynamic stall model including the effects of trailing edge flap deflection*.

Branlard, E. et al. (June 2022). "Dynamic inflow and unsteady aerodynamics models for modal and stability analyses in OpenFAST". In: *Journal of Physics: Conference Series*. Vol. 2265. Institute of Physics. doi: 10.1088/1742-6596/2265/3/032044.

Chaviaropoulos, P. K. (Oct. 2001). "Flap/lead–lag aeroelastic stability of wind turbine blades". In: *Wind Energy* 4 (4), pp. 183–200. issn: 1095-4244. doi: 10.1002/we.55.

Chaviaropoulos, P. K. et al. (2009). *Stability analysis of parked wind turbine blades*. url: https://www.researchgate.net/publication/229053423.

Gavin, Henri P. (2020). *Numerical Integration in Structural Dynamics*.

Gielen, Dolf et al. (Apr. 2019). "The role of renewable energy in the global energy transformation". In: *Energy Strategy Reviews* 24, pp. 38–50. issn: 2211467X. doi: 10.1016/j.esr.2019.01.006.

Hansen, M. H. (2003). "Improved modal dynamics of wind turbines to avoid stall-induced vibrations". In: *Wind Energy* 6 (2), pp. 179–195. issn: 10954244. doi: 10.1002/we.79.

– (2007). "Aeroelastic instability problems for wind turbines". In: *Wind Energy* 10 (6), pp. 551–577. issn: 10991824. doi: 10.1002/we.242.

Hansen, Morten Hartvig, Mac Gaunaa, and Helge Aagaard Madsen (May 2004). *A Beddoes-Leishman type dynamic stall model in state-space and indicial formulations*.

Hilber, Hans M, Thomas J R Hughes, and Robert L Taylor (1977). *IMPROVED NUMERICAL DISSIPATION FOR TIME INTEGRATION ALGORITHMS IN STRUCTURAL DYNAMICS*.

Holierhoek, J. G. (Jan. 2023). "Aeroelastic design of wind turbine blades". In: Elsevier, pp. 169–189. isbn: 9780081030073. doi: 10.1016/B978-0-08-103007-3.00010-0.

Holierhoek, J. G. et al. (2013). "Comparing different dynamic stall models". In: *Wind Energy* 16 (1), pp. 139–158. issn: 10991824. doi: 10.1002/we.548.

Hutchinson, Mark and Fengh Zhao (Mar. 2023). *GLOBAL WIND REPORT 2023*.

Jiang, Zhiyu, Madjid Karimirad, and Torgeir Moan (Aug. 2014). "Dynamic response analysis of wind turbines under blade pitch system fault, grid loss, and shutdown events". In: *Wind Energy* 17 (9), pp. 1385–1409. issn: 10991824. doi: 10.1002/we.1639.

Karbasian, Hamid Reza et al. (Sept. 2022). "Numerical analysis of wind turbines blade in deep dynamic stall". In: *Renewable Energy* 197, pp. 1094–1105. issn: 18790682. doi: 10.1016/j.renene.2022.07.115.

Khan, Muhammad Arsalan (July 2018). "Dynamic stall modelling for wind turbines". In: url: http://repository.tudelft.nl/..

Kwan, Garry Yuan (July 2017). "INVESTIGATION OF IDLING INSTABILITIES IN WIND TURBINE SIMULATIONS". In.

Larsen, J. W., S. R.K. Nielsen, and S. Krenk (Oct. 2007). "Dynamic stall model for wind turbine airfoils". In: *Journal of Fluids and Structures* 23 (7), pp. 959–982. issn: 08899746. doi: 10.1016/j.jfluidstructs.2007.02.005.

Leishman, J. G. and T. S. Beddoes (July 1989). *A Semi-Empirical Model for Dynamic Stall*.

Li, Ang et al. (July 2022). "How should the lift and drag forces be calculated from 2-D airfoil data for dihedral or coned wind turbine blades?" In: *Wind Energy Science* 7 (4), pp. 1341–1365. issn: 23667451. doi: 10.5194/wes-7-1341-2022.

Liu, Pu and Claire Y. Barlow (Apr. 2017). “Wind turbine blade waste in 2050”. In: *Waste Management* 62, pp. 229–240. issn: 18792456. doi: 10.1016/j.wasman.2017.02.007.

Liu, Xiong et al. (Mar. 2015). “Dynamic stall simulation of wind turbine airfoils”. In: *Gongcheng Lixue/Engineering Mechanics* 32 (3), pp. 203–211. issn: 10004750. doi: 10.6052/j.issn.1000-4750.2014.03.0165.

Lynas, Mark, Benjamin Z. Houlton, and Simon Perry (Nov. 2021). *Greater than 99% consensus on human caused climate change in the peer-reviewed scientific literature*. doi: 10.1088/1748-9326/ac2966.

McLean, Doug (2010). *UNDERSTANDING AERODYNAMICS*.

Meng, Qingshen et al. (2024). *Stall-induced aeroelastic instability of floating offshore wind turbines*.

Mishnaevsky, Leon (Jan. 2023). “Maintenance and repair of wind turbine blades”. In: Elsevier, pp. 475–484. isbn: 9780081030073. doi: 10.1016/B978-0-08-103007-3.00003-3.

Moeller, T (May 1997). *Blade cracks signal new stress problem, preventative investment needed on turbines with large LM blades*. url: https://www.windpowermonthly.com/article/958000/blade-cracks-signal-new-stress-problem-.

Naeini, Saeid Fadaei et al. (Sept. 2020). “Flutter Stability Analysis of Parked Floating Wind Turbine Blades”. In: *Proceedings of the Canadian Society for Mechanical Engineering International Congress 2020*. Robertson Library, University of Prince Edward Island. doi: 10.32393/csme.2020.1238.

Nijssen, R. P.L. and P. Brøndsted (Jan. 2023). “Fatigue as a design driver for composite wind turbine blades”. In: Elsevier, pp. 217–248. isbn: 9780081030073. doi: 10.1016/B978-0-08-103007-3.00006-9.

Øye, Stig (1991). “Dynamic Stall simulated as time lag of separation”. In: *Proceedings of the 4th IEA Symposium on the Aerodyanmics of Wind Turbines*.

Pereira, Ricardo (2010). *Validating the Beddoes-Leishman Dynamic Stall Model in the Horizontal Axis Wind Turbine Environment*.

Petersen, Jørgen Thirstrup et al. (May 1998). *Prediction of dynamic loads and induced vibrations in stall*.

Pirrung, Georg R., Helge A. Madsen, and Scott Schreck (2018). “Trailed vorticity modeling for aeroelastic wind turbine simulations in standstill”. In: *Wind Energy Science* 3 (2), pp. 521–532. issn: 23667451. doi: 10.5194/wes-2-521-2017.

Riziotis, V. A. et al. (2004). “Aeroelastic stability of wind turbines: The problem, the methods and the issues”. In: *Wind Energy*. Vol. 7. John Wiley and Sons Ltd, pp. 373–392. doi: 10.1002/we.133.

Ruijven, Bas J. van, Enrica De Cian, and Ian Sue Wing (Dec. 2019). “Amplification of future energy demand growth due to climate change”. In: *Nature Communications* 10 (1). issn: 20411723. doi: 10.1038/s41467-019-10399-3.

Serafeim, Giannis P. et al. (June 2022). “Optimized blade mass reduction of a 10MW-scale wind turbine via combined application of passive control techniques based on flap-edge and bend-twist coupling effects”. In: *Journal of Wind Engineering and Industrial Aerodynamics* 225. issn: 01676105. doi: 10.1016/j.jweia.2022.105002.

Sherif, Karim et al. (June 2019). “A modified HHT method for the numerical simulation of rigid body rotations with Euler parameters”. In: *Multibody System Dynamics* 46 (2), pp. 181–202. issn: 1573272X. doi: 10.1007/s11044-019-09672-6.

Skrzypiński, Witold and Mac Gaunaa (Mar. 2014). “Wind turbine blade vibration at standstill conditions - The effect of imposing lag on the aerodynamic response of an elastically mounted airfoil”. In: *Wind Energy* 18 (3), pp. 515–527. issn: 10991824. doi: 10.1002/we.1712.

Skrzypiński, Witold Robert et al. (2014). “Self-induced vibrations of a DU96-W-180 airfoil in stall”. In: *Wind Energy* 17 (4), pp. 641–655. issn: 10991824. doi: 10.1002/we.1596.

Snel, H (1997). “Heuristic modelling of dynamic stall characteristic”. In: *Proceedings of the European Wind Energy Conference*.

Stäblein, Alexander R., Morten H. Hansen, and Georg Pirrung (Jan. 2017). “Fundamental aeroelastic properties of a bend–twist coupled blade section”. In: *Journal of Fluids and Structures* 68, pp. 72–89. issn: 10958622. doi: 10.1016/j.jfluidstructs.2016.10.010.

Tarzanin, F. (1972). “Prediction of control loads due to blade stall”. In: *Journal of the American Helicopter Society* 17, pp. 33–46.

Thomson, William T. (1993). *Theory of Vibrations with Applications*. Taylor&Francis.

Thwaites, Brian (1961). *Incompressible Aerodynamics*. Cambridge University Press.

Totsuka, Yoshitaka, Hiroshi Imamura, and Anders Yde (2016). “DYNAMIC BEHAVIOR OF PARKED WIND TURBINE AT EXTREME WIND SPEED”. In: *First International Symposium on Flutter and its Application*, pp. 575–584.

Tran, C and D Petot (1980). “Semi-empirical model for the dynamic stall of airfoils in view of the application to the calculation of responses of a helicopter blade in forward flight”. In.

Wang, Kai, Vasilis A. Riziotis, and Spyros G. Voutsinas (Oct. 2016). “Aeroelastic Stability of Idling Wind Turbines”. In: *Journal of Physics: Conference Series*. Vol. 753. Institute of Physics Publishing. doi: 10.1088/1742-6596/753/4/042008.

Wu, Xianyou et al. (July 2024). “Numerical Simulation Method for the Aeroelasticity of Flexible Wind Turbine Blades under Standstill Conditions”. In: *Energies* 17 (14), p. 3395. issn: 19961073. doi: 10.3390/en17143395.

Zahle, F ; et al. (2024). “Definition of the IEA Wind 22-Megawatt Offshore Reference Wind Turbine”. In: *Citation*. doi: 10.11581/DTU.00000317. url: https://doi.org/10.11581/DTU.00000317.

Zou, F. et al. (Dec. 2015). “Analysis of vortex-induced and stall-induced vibrations at standstill conditions using a free wake aerodynamic code”. In: *Wind Energy* 18 (12), pp. 2145–2169. issn: 10991824. doi: 10.1002/we.1811.

A

Supplementary results

This appendix chapter shows supplementary results. These can be results that are claimed in the main matter but are not important enough to be shown there or they are results that visualise some data better than presented in the main matter.

A.1. Aeroelastic validation

In the main matter, it was claimed that there was only a small difference left between the simulations with time step durations of $0.001\,\mathrm{s}$ and $0.0005\,\mathrm{s}$. The results are shown in Figure A.1.

A.2. Grid study

To compare the results of the grid study in the main matter, all colour bars used the same scaling. This, however, means that details of results that have a small magnitude compared to the colour bar scaling is lost. Hence, the results of the grid study are presented again for which every colour bar is scaled according to its accompanying figure. The maximum edgewise limit cycle oscillation amplitudes are shown in Figure A.2. The maximum and minimum effective angle of attack are shown in Figure A.3. The maximum flapwise limit cycle oscillation amplitudes are shown in Figure A.2.

Additionally, in the discussion Chapter 6, it is stated that during the initial time of two simulations using the the HGM openFAST model and the HGM f-scaled model models the edgewise amplitudes have oscillations in its growth. This is shown in Figure A.5.

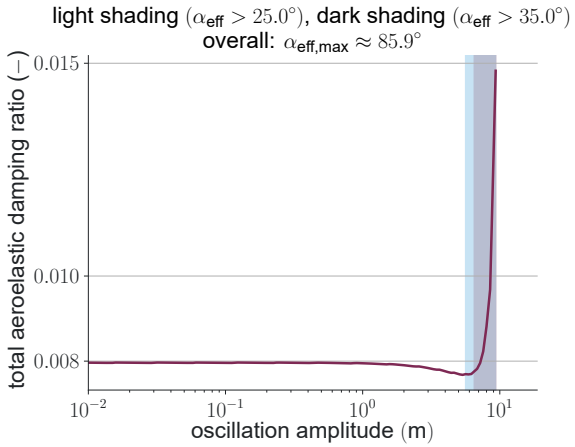

(a) Results with a time step duration of $0.005\,\text{s}$.

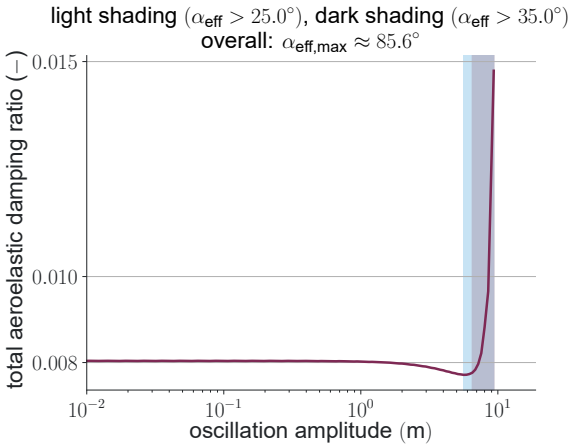

(b) Results with a time step duration of $0.0025\,\text{s}$.

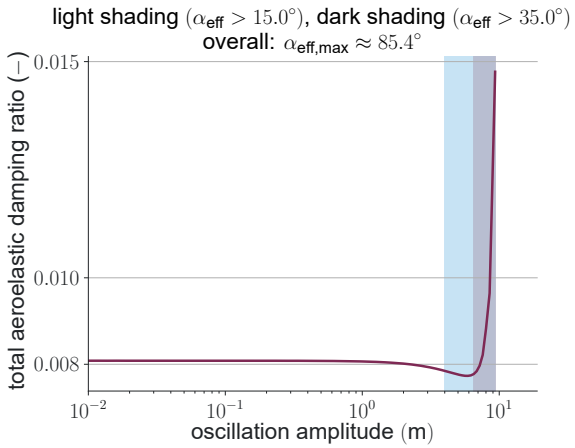

(c) Results with a time step duration of $0.001\,\text{s}$.

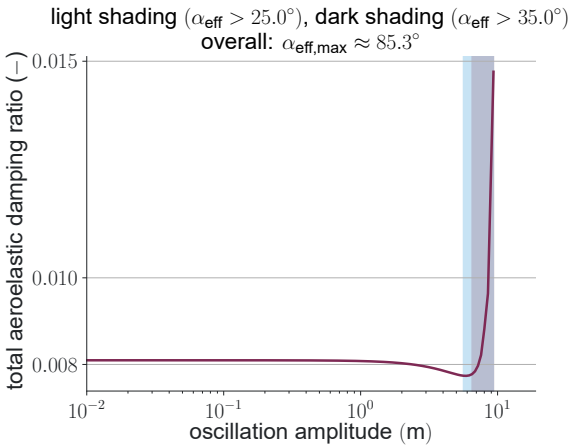

(d) Results with a time step duration of $0.0005\,\text{s}$.

Figure A.1: Aeroelastic damping ratio prediction to validate the aeroelastic behaviour of the section model. The aeroelastic validation is discussed in Section 3.6.

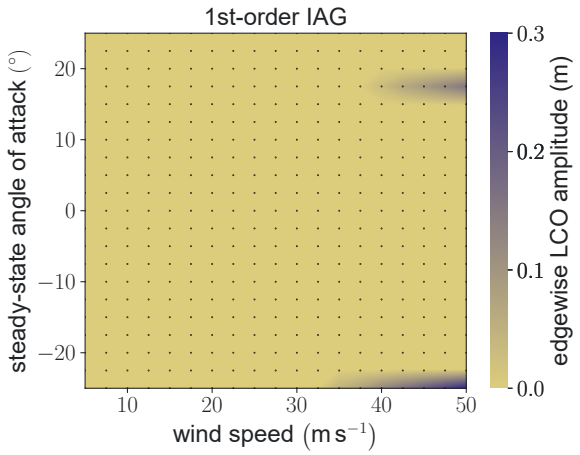

(a) Edgewise limit cycle oscillations amplitudes using the 1st-order IAG model.

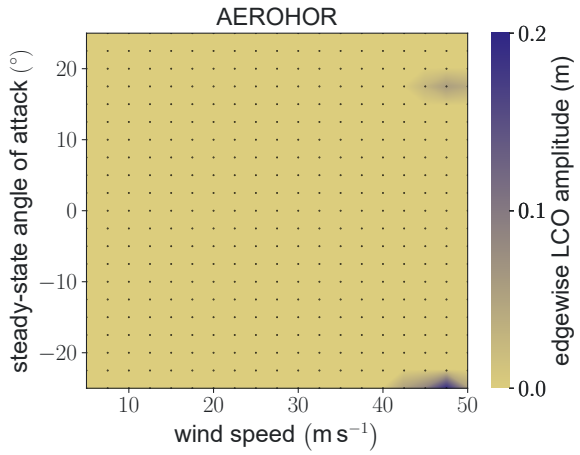

(b) Edgewise limit cycle oscillations amplitudes using the AEROHOR model.

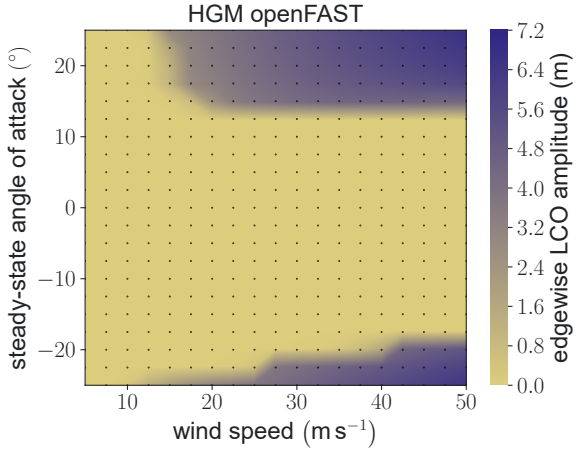

(c) Edgewise limit cycle oscillations amplitudes using the HGM openFAST model.

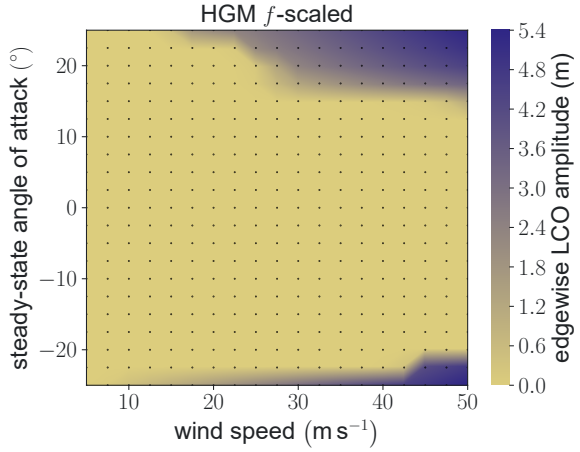

(d) Edgewise limit cycle oscillations amplitudes using the HGM f-scaled model.

Figure A.2: Edgewise amplitude results of the grid calculations described in Chapter 4, step 2, for the four dynamic stall models. The black dots indicate pairs of angle of attack and wind speed for which a simulation was run. Individual scaling of the colour bars.

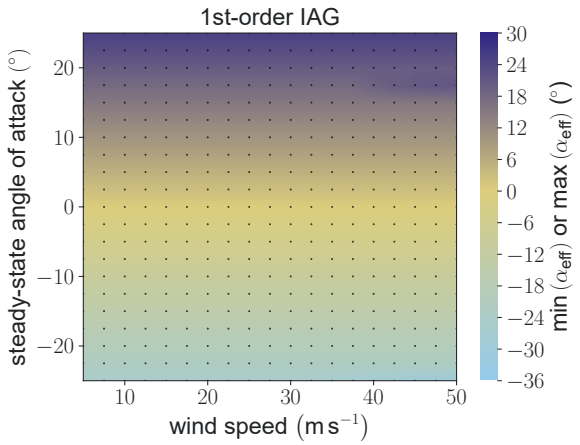

(a) Edgewise limit cycle oscillations convergence of the simulations using the 1st-order IAG model.

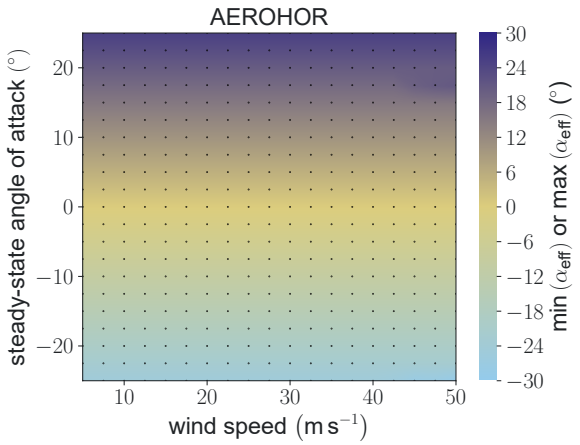

(b) Edgewise limit cycle oscillations convergence of the simulations using the AEROHOR model.

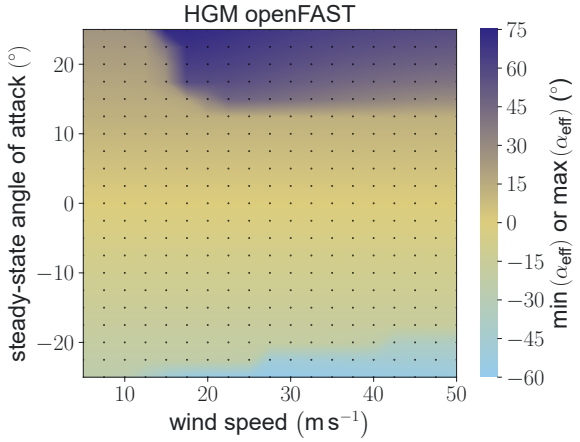

(c) Edgewise limit cycle oscillations convergence of the simulations using the HGM openFAST model.

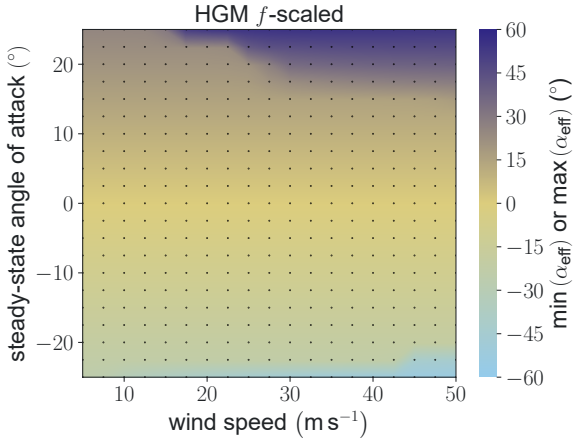

(d) Edgewise limit cycle oscillations convergence of the simulations using the HGM f-scaled model.

Figure A.3: Smallest or largest effective angle of attack (α_{eff}) chosen by the greater magnitude during the last period of the grid calculations described in Chapter 4, step 2, for the four dynamic stall models. The black dots indicate pairs of angle of attack and wind speed for which a simulation was run. Individual scaling of the colour bars.

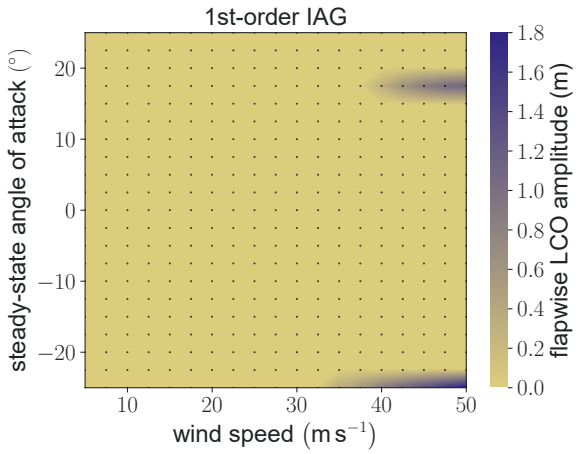

(a) Flapwise limit cycle oscillations amplitudes using the 1st-order IAG model.

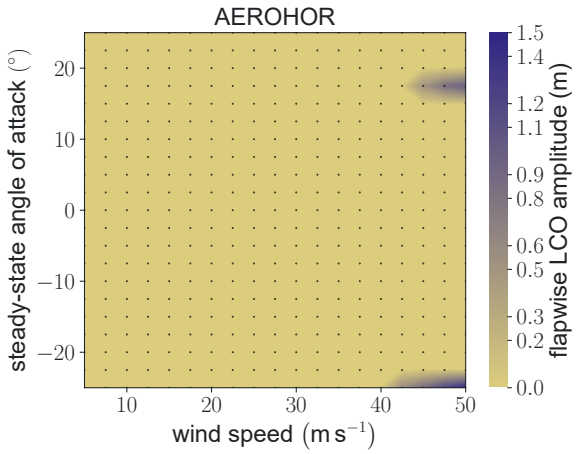

(b) Flapwise limit cycle oscillations amplitudes using the AEROHOR model.

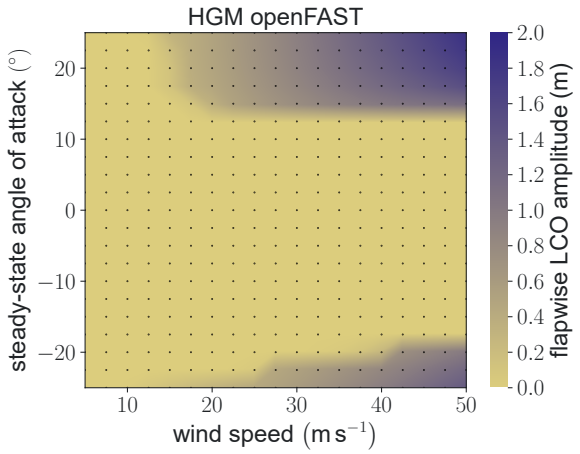

(c) Flapwise limit cycle oscillations amplitudes using the HGM openFAST model.

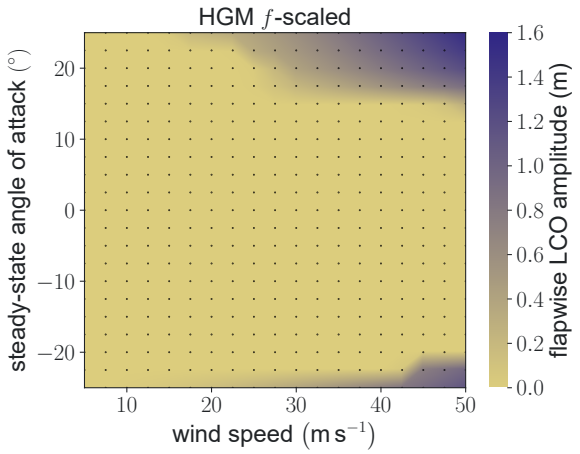

(d) Flapwise limit cycle oscillations amplitudes using the HGM f-scaled model.

Figure A.4: Flapwise amplitude results of the grid calculations described in Chapter 4, step 2, for the four dynamic stall models. The black dots indicate pairs of angle of attack and wind speed for which a simulation was run. Individual scaling of the colour bars.

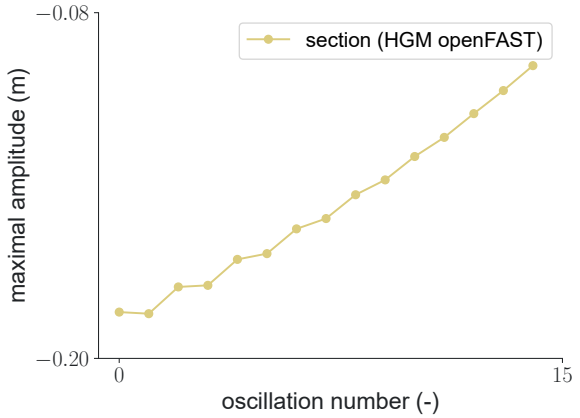

(a) Response as simulated with the HGM openFAST model.

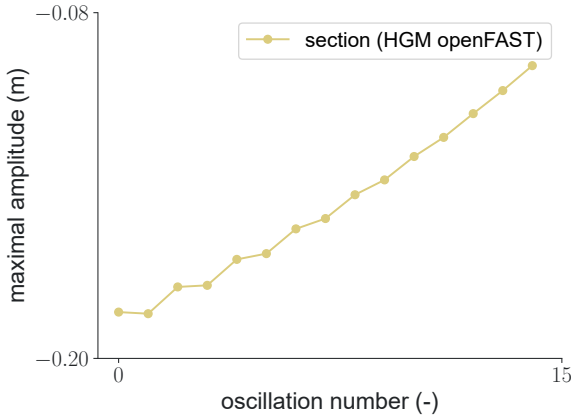

(b) Response as simulated with the HGM f-scaled model.

Figure A.5: Maximum x (edgewise) amplitudes of the first few oscillations for simulations with an inflow velocity of $45\,\mathrm{m/s}$ at a steady-state angle of attack of $17.5°$. The initial conditions are defined in the grid study definition in Chapter 4.

B

Simulating 2D objects with body-fixed structural parameters

Throughout the main matter, it is stated a few times that the translational structural damping and stiffness are modelled acting parallel to the coordinate axes x and y. During the development of the section model, this was not always the case. After an early version of the section modelstarted to be useful for aeroelastic simulations, it was decided to model the translational damping and stiffness forces acting parallel and normal to the chord. This seemed reasonable to keep constant edgewise and flapwise structural parameters.

Before this thesis, the author had not worked with finite element models on the implementation level. The initial objectives of this thesis were based on using the AEROHOR finite element wind turbine model described in Meng et al., 2024. To understand the dynamics, the author read the better half of Logan, 2017. There, it is shown that projecting damping and stiffness matrices from a coordinate system ef onto a xy coordinate system works by

$$\boldsymbol{R}_{xy\to ef} = \begin{bmatrix} \cos(\gamma) & \sin(\gamma) & 0 \\ -\sin(\gamma) & \cos(\gamma) & 0 \\ 0 & 0 & 1 \end{bmatrix}, \tag{B.1}$$

$$\boldsymbol{C} = \boldsymbol{R}_{xy\to ef}^{T} \boldsymbol{C}_{ef} \boldsymbol{R}_{xy\to ef}, \tag{B.2}$$

$$\boldsymbol{K} = \boldsymbol{R}_{xy\to ef}^{T} \boldsymbol{K}_{ef} \boldsymbol{R}_{xy\to ef}. \tag{B.3}$$

$\boldsymbol{C}$ and $\boldsymbol{K}$ are the damping and stiffness matrix in the xy coordinate system. $\boldsymbol{C}_{ef}$ and $\boldsymbol{K}_{ef}$ are here defined as matrices in which the structural parameters for the edgewise e and flapwise f are defined along the diagonal:

$$\boldsymbol{C}_{ef} = \begin{bmatrix} C_{ee} & 0 & 0 \\ 0 & C_{ff} & 0 \\ 0 & 0 & C_{\gamma\gamma} \end{bmatrix}, \tag{B.4}$$

$$\boldsymbol{K}_{ef} = \begin{bmatrix} K_{ee} & 0 & 0 \\ 0 & K_{ff} & 0 \\ 0 & 0 & K_{\gamma\gamma} \end{bmatrix}. \tag{B.5}$$

For simplicity, no structural coupling exists in the ef coordinate system. For convenience, the structural definition for the torsion is already given by the $\gamma\gamma$ component. In Equations (B.2) and (B.3), this component is not changed. The angle γ denotes the rotation differentiating both coordinate systems as shown in Figure B.1. Equations (B.2) and (B.3) were then used to calculate the projected damping and stiffness matrices at every time step to solve the equation of motions in the *inertial* coordinate system xy. The projection is only necessary because the author's missing background in structural mechanics

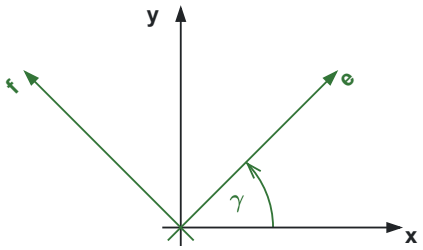

Figure B.1: xy and ef coordinate system.

prevented adapting the HHT–α^{HHT} to solve the equation of motions in the *non-inertial* reference frame ef. However, under some circumstances, simulations did not conserve energy. After many analyses, the simplest case of non-conserved energy was for

1. no external forces,
2. no structural damping,
3. non-zero initial displacement (otherwise there is no movement),
4. $K_{ee} \neq K_{ff} \neq 0$, and
5. a non-zero torsion rate $\dot{\gamma}$.

The potential energy was calculated based on x_e, x_f, and γ, and the kinetic energy based on $\dot{x}_e$, $\dot{x}_f$, and $\dot{\gamma}$. The breaking of conservation of energy happened both using an explicit Euler and the HHT–α^{HHT} for time integration.

Even though aeroelastic section modelling lies arguably the foundation of aeroelasticity and is used in many publications, the author could not find solutions in the literature. However, modelling constant edgewise and flapwise structural parameters seemed reasonable.

In the modelling of the section, the violation of conservation of energy comes from Equations (B.2) and (B.3) not coupling the torsion with the edgewise and flapwise displacement and velocity. A simple thought experiment shows this: assuming that the airfoil is pinned on the x-axis and $K_{ee} \neq K_{ff}$, even with $K_{\gamma\gamma} = 0$ and no structural damping, a rotation of the airfoil causes the potential energy to change. If $\gamma = 0°$ initially, only the edgewise spring is under tension. Thus, the potential energy equals $0.5K_{ee}x_x^2$. However, if the airfoil is rotated to $\gamma = 90°$, only the flapwise spring is under tension. The potential energy is now $0.5K_{ff}x_x^2$. However, $K_{ee} \neq K_{ff}$, $K_{\gamma\gamma} = 0$, and no structural damping were assumed. Thus, no work had to be done to rotate the airfoil (no damping and $K_{\gamma\gamma} = 0$), but the potential energy changed. This shows the need for a coupling between the rotation and displacement in the ef coordinate system.

Indeed, deriving the displacement $\boldsymbol{x}_{ef}$ and velocity $\dot{\boldsymbol{x}}_{\boldsymbol{ef}}$ in the ef coordinate system shows that exact coupling:

$$\boldsymbol{x}_{ef} = \boldsymbol{R}_{xy\to ef}\boldsymbol{x}_{xy} = \begin{bmatrix} \cos(\gamma) & \sin(\gamma) & 0 \\ -\sin(\gamma) & \cos(\gamma) & 0 \\ 0 & 0 & 1 \end{bmatrix} \begin{bmatrix} x \\ y \\ \gamma \end{bmatrix} = \begin{bmatrix} \cos(\gamma)x + \sin(\gamma)y \\ -\sin(\gamma)x + \cos(\gamma)y \\ \gamma \end{bmatrix} \tag{B.6}$$

Even if x and y are constant but non-zero, a rotation causes a displacement in the ef coordinate system. For the velocity as seen in $ef\ dotx_{ef} \neq \boldsymbol{R}_{xy\to ef}\dot{x}$. Rather,

$$\dot{\boldsymbol{x}}_{ef} = \dot{\boldsymbol{x}_{ef}} = \begin{bmatrix} \cos(\gamma)\dot{x} + \sin(\gamma)\dot{y} + (-\sin(\gamma)x + \cos(\gamma)y)\,\dot{\gamma} \\ -\sin(\gamma)\dot{x} + \cos(\gamma)\dot{y} + (-\cos(\gamma)x - \sin(\gamma)y)\,\dot{\gamma} \\ \dot{\gamma} \end{bmatrix} \tag{B.7}$$

At this point, it is important to note that there is a difference between the movement in flapwise and edgewise direction as defined in Figure 3.2 and along the flapwise and edgewise axis as defined in

Figure B.1. For once, the edgewise direction faces in the opposite direction as the edgewise axis. However, even if they pointed in the same direction their velocities would generally not be the same. Besides defining the velocities along the edgewise and flapwise axis, Figure B.1 gives a set of partial differential equations that describe movement in the xy coordinate system that does not result in translational movement in the ef coordinate system.

To ease the solution process, $\dot{\boldsymbol{x}}_{ef}$ is projected onto the xy coordinate system with $\boldsymbol{R}_{ef\to xy} = \boldsymbol{R}_{xy\to ef}^{T}$ to get $\dot{\boldsymbol{x}}^{ef}$. This is the velocity of the airfoil seen in the xy coordinate system when it moves in the ef coordinate system. The result is

$$\dot{\boldsymbol{x}}^{ef} = \begin{bmatrix} \dot{x} + y\dot{\gamma} \\ \dot{y} - x\dot{\gamma} \\ \dot{\gamma} \end{bmatrix} . \tag{B.8}$$

Now, if

$$\dot{x} + y\dot{\gamma} = 0\,, \text{ and} \tag{B.9}$$
$$\dot{y} - x\dot{\gamma} = 0 \tag{B.10}$$

the translation velocity of $\dot{\boldsymbol{x}}^{ef}$ has to be zero because the rotation matrix $\boldsymbol{R}_{ef\to xy}$ is orthonormal; it cannot project a vector of non-zero magnitude in one coordinate system onto a vector of zero magnitude in another. The solution to Equations (B.9) and (B.10) is quickly found as either case

$$\text{a) } x = \cos(t)\,, y = \sin(t)\,, \gamma = t \text{ or} \tag{B.11}$$
$$\text{b) } x = \sin(t)\,, y = \cos(t)\,, \gamma = t\,. \tag{B.12}$$

Both cases have an intuitive explanation of why they do not cause movement in the ef coordinate system: the airfoil always points with the same orientation to the origin while keeping a constant distance. This also explains why the velocity along the, e.g, flapwise axis is not the same as the velocity in the flapwise direction. Most importantly, it gives the reason why a damped system seemingly can have undamped motion. The motion only exists in the xy coordinate system but not in the coordinate system responsible for damping forces.

The previous last sentence is what the derivation of the coupled damping and stiffness matrices are based on. All considerations of work have to be derived in the ef coordinate system because that is where they happen.

The linear springs store the same energy no matter if viewed in the ef or xy coordinate system. Hence

$$E_{\text{pot}}^{xy} = E_{\text{pot}}^{ef}\,, \text{and} \tag{B.13}$$
$$dE_{\text{pot}}^{xy} = dE_{\text{pot}}^{ef}\,. \tag{B.14}$$

dE is the work done for potential energy. In the section model, this only happens due to stiffness forces. Thus

$$f_{kx}dx + f_{ky}dy + f_{k\gamma}d\gamma = K_{ee}x_e dx_e + K_{ff}x_f dx_f + K_{\gamma\gamma}x_\gamma dx_\gamma\,. \tag{B.15}$$

Everything on the right-hand side is known. The forces and moment f_{kx}, f_{ky} $f_{k\gamma}$ define the diagonal of the stiffness matrix $\boldsymbol{K}$ in the xy coordinate system. Doing all of the algebra results in

$$\boldsymbol{K}_{xy} = \begin{bmatrix} K_{ee}\cos(\gamma)^2 + K_{ff}\sin(\gamma)^2 & \cos(\gamma)\sin(\gamma)\left(K_{ee} - K_{ff}\right) & 0 \\ \cos(\gamma)\sin(\gamma)\left(K_{ee} - K_{ff}\right) & K_{ee}\cos(\gamma)^2 + K_{ff}\sin(\gamma)^2 & 0 \\ \left(K_{ee} - K_{ff}\right)\left(-\cos(\gamma)\sin(\gamma)x + y\left(\cos(\gamma)^2 - \sin(\gamma)^2\right)\right) & \left(K_{ee} - K_{ff}\right)\cos(\gamma)\sin(\gamma)y & K_{\gamma\gamma} \end{bmatrix} \tag{B.16}$$

The same holds for the linear dampers. No matter from which coordinate system they are viewed, if they dissipate energy it always has to be the same. A similar approach as in Equation (B.15) yields

$$\boldsymbol{C}_{xy} = \begin{bmatrix} C_{ee}c^2 + C_{ff}s^2 & 0 & 0 \\ cs\left(C_{ee} - C_{ff}\right) & 0 & 0 \\ C_{ee}c\left(-sx + cy\right) - C_{ff}s\left(-cx - sy\right) & 0 & 0 \end{bmatrix} \tag{B.17}$$

$$+ \begin{bmatrix} 0 & cs\left(C_{ee} - C_{ff}\right) & 0 \\ 0 & C_{ee}c^2 + C_{ff}s^2 & 0 \\ 0 & C_{ee}s\left(-sx + cy\right) + C_{ff}c\left(-cx - sy\right) & 0 \end{bmatrix} \tag{B.18}$$

$$+ \begin{bmatrix} 0 & 0 & C_{ee}c\left(-sx + cy\right) - C_{ff}s\left(-cx - sy\right) \\ 0 & 0 & C_{ee}s\left(-sx + cy\right) + C_{ff}c\left(-cx - sy\right) \\ 0 & 0 & C_{ee}\left(-sx + cy\right)^2 + C_{ff}\left(-cx - sy\right)^2 + c_{\varphi} \end{bmatrix} \tag{B.19}$$

Here, $s = \sin(\gamma)$ and $c = \cos(\gamma)$.

References for the Appendix

Logan, Daryl L. (2017). *A First Course in the Finite Element Method*.
Meng, Qingshen et al. (2024). *Stall-induced aeroelastic instability of floating offshore wind turbines*.